Unraveling the Crystal Structure of Gamma-Alumina through Correlated Experiments and Simulations of a Model System

by

Henry Ayoola

B. Sc. Chemical Engineering, University of Maryland Baltimore County, 2013

Submitted to the Graduate Faculty of the

Swanson School of Engineering in partial fulfillment

of the requirements for the degree of

Doctor of Philosophy

University of Pittsburgh

2020

UNIVERSITY OF PITTSBURGH

SWANSON SCHOOL OF ENGINEERING

This dissertation was presented

by

Henry Ayoola

It was defended on

October 5, 2020

and approved by

Ioannis Bourmpakis, Ph.D., Associate Professor
Department of Chemical and Petroleum Engineering

James R. McKone, Ph. D., Assistant Professor
Department of Chemical and Petroleum Engineering

Dissertation Co-Director: Wissam A. Saidi, Ph. D., Associate Professor
Department of Mechanical Engineering and Materials Science

Dissertation Director: Judith C. Yang, Ph. D., Professor
Department of Chemical and Petroleum Engineering

Unraveling the Crystal Structure of Gamma-Alumina through Correlated Experiments and Simulations of a Model System

Henry O. Ayoola, PhD

University of Pittsburgh, 2020

Gamma-alumina (γ-Al_2O_3) is a metastable alumina phase possessing useful properties, such as inherently high surface area and acidic surface sites. As a result, it is an important material for heterogeneous catalysis, with applications in oil refining, vehicle exhaust catalytic conversion, and the oxidation of methane—a major greenhouse gas. However, despite the widespread use and study of γ-Al_2O_3, its precise atomic structure is still not fully understood. This has led to conflicting predictions of γ-Al_2O_3 properties and resulting catalytic behavior. A major contributor to the uncertainty in the γ-Al_2O_3 structure has been the use of commercial samples for structural studies. Commercially available γ-Al_2O_3 is chemically and morphologically inhomogeneous which leads to inconsistent characterization results. The overall aim of my research was to contribute towards full resolution of the γ-Al_2O_3 structure by unambiguously resolving the space group and Al atom arrangement. In contrast to previous studies, I utilized chemically pure, morphologically well-defined, highly crystalline "model" γ-Al_2O_3 which I synthesized by controlled thermal oxidation of NiAl. I then studied the atomic structure of the model γ-Al_2O_3 using synergistic experimental and simulated selected-area electron diffraction (SAED) and high-resolution electron energy-loss spectroscopy (EELS). My results revealed that the cubic spinel-based model was the most accurate γ-Al_2O_3 structural model. Additionally, I resolved the Al vacancy distribution within the cubic spinel-based model using quantitative analysis of reflection intensities in the correlated experimental and simulated SAED, revealing that 50-80% of vacancies are found on tetrahedral

Al sites. Experimental high-resolution cryo-EELS correlated with EELS simulations performed using FEFF (a real-space multiple scattering code) confirmed the presence of vacancies primarily on tetrahedral sites. The synergistic approach of using a model γ-Al_2O_3 combined with the characterization methodology used in this project could be applied to other structurally complex materials.

In addition, this research has also advanced knowledge on the mechanisms of electron beam damage in γ-Al_2O_3 and their suppression, and on the interfacial bonding of Pt on γ-Al_2O_3 (111). Ultimately, a more accurate approach to modeling γ-Al_2O_3 structure as revealed in this project will accelerate catalyst design and discovery of catalytic applications for such a promising catalyst material as γ-Al_2O_3.

Table of Contents

List of Tables

List of Figures

Appendix Figure 28. Configurations of Pt atom adsorption on the γ-Al_2O_3 (111) surface.211

Preface

First of all, I would like to render my utmost gratitude to my dissertation advisor Dr. Judith Yang for agreeing to take me on as a student, for her guidance and support, and for her willingness to go out of her way to provide opportunities to broaden my research and professional horizons. No less, I would like to thank my co-advisor Dr. Wissam Saidi, who took it upon himself to become a second advisor and mentor for me and to give so much of his time and effort to help me reach this point. I am also grateful to Drs. James McKone and Yanni Mpourmpakis for serving as my committee members and for their helpful and insightful feedback.

I would like to thank the Meyerhoff program at UMBC, Keith Harmon, and Lamont Tolliver (RIP), and my fellow Meyerhoff scholars, without whose support and belief I would not have even attempted this path in the first place. Hold fast to dreams.

I would also like to thank the NFCF staff, Drs. Susheng Tan and Dan Lamont, Mike McDonald, and Matt France for their help with training and technical support, not to mention for being awesome people.

I would like to thank my post-doctoral mentors, Drs. Cecile Fittz and Stephen House, for their immeasurable help and patience. I would like to thank Dr. Brian Gleeson for his support and for his expertise and collaboration that enriched my graduate experience. I would like to acknowledge my colleagues at Pitt, Dr. Qing Zhu, Dr. Meng Li, Dr. Matthew Curnan, Dr. Christopher Andolina, Dr. Lianfeng Zou, Dr. Hao Chi, Ross Grieshaber, Michael Gresh-Sill, and my all-grown-up undergraduate mentee Matthew McCann for their insights and help with my research.

I would like to thank Dr. Roldan-Cuenya for the opportunity to work in her lab at Ruhr Universität Bochum, as well as my colleagues there; Dr. Miguel Lopez, Sebastian Kunze, Clara, Dr. Ilya Sinev, and Dr. Nuria, who helped to make my brief stay in their lab a fruitful and amazing experience.

I had some great luck to work with some amazing collaborators all over the USA. My sincere gratitude to (soon-to-be Dr.) Cheng-Han Li and Dr. Joerg Jinschek at OSU, and Drs. Joshua Kas and John Rehr at UW. Thanks for all the help, without which my publications wouldn't exist.

Lastly but by no means least, I would like to thank my family for their patience and support. They have been there for me every step of the way and my gratitude for them knows no bounds.

1.0 Introduction

The motivation and broader impacts of this project as well as the background information necessary to contextualize the scientific studies reported in later chapters are presented in this chapter.

1.1 Background and Significance

A catalyst is a material that increases the rate of a chemical reaction. The catalyst usually remains chemically unchanged at the end of the reaction process, allowing it to be reused for further chemical reactions. Generally, a catalyst modifies the reaction pathway, thereby reducing the overall energy (i.e. activation energy) required for the chemical reaction to occur and increasing the reaction rate [1]. Though a certain combination of reactants and reaction conditions may lead to a desired product (i.e. the product is thermodynamically favored), the reaction rate (i.e. kinetics) may be so slow or the reaction path so unselective and wasteful that the process to synthesize said reaction product is rendered industrially unfeasible. Therefore, catalysts are extremely useful materials; in fact, a vast number of industrial processes would be completely impractical if not for the existence of effective catalysts. Many of the groundbreaking chemical processes that have been developed over the last century such as pharmaceutical manufacturing, polymer manufacturing, crude oil refining, fertilizer synthesis, and even margarine production depend heavily on catalysis [2-8].

Catalysis—due to its critical importance in a great number of industrial processes and technologies—has a far-reaching impact on society. It is estimated that over 85% of all industrially produced chemicals rely on catalysis in some form [9]. The commercial value of catalysts produced annually is about $14 billion [10]. Close to 20% of all economic activities in industrialized countries depend on catalysis and it has been estimated that about 35% of the world's gross domestic product (GDP) is influenced by catalysis [10, 11]. Catalysis is also important for the environment. By increasing the efficiency of reaction processes, catalysis significantly reduces potentially harmful waste [12]. This importance is exemplified by the 3x order of magnitude lower waste-to-product ratio for the oil industry, in which almost all reactions are catalyzed, compared to the pharmaceutical industry, in which most reactions are based on traditional multistep organic chemistry [9]. Catalysis is expected to take on even greater importance in the coming years, as it is critical in the development of more sustainable, greener manufacturing processes and renewable, cleaner energy [12, 13].

Therefore, it is vitally important to not only improve existing catalysts, but to also develop new catalysts for future applications. This endeavor is predicated on a cooperative approach to research and exploration using both experiments and modeling, which in turn requires a fundamental understanding of catalysis and catalyst materials. Such research is thus highly relevant, a fact further evinced by the conferring of the Nobel Prize in Chemistry to Gerhard Ertl in 2007 for his seminal work on describing the catalytic mechanisms of the Haber process for ammonia production, a critically important step in fertilizer synthesis [14, 15].

1.2 Heterogeneous Catalysis

Catalysts are divided into homogeneous and heterogeneous varieties based on the phases of the reacting chemicals. Homogeneous catalysts are those that exist in the same phase as the reactants, whereas heterogeneous catalysts are a different phase from the reactants (usually solid-state catalyst materials in a gas or liquid reaction medium). While in both cases the catalyst is usually reusable, heterogeneous catalysts have the added benefit of not requiring difficult, costly separations from the reactant and product mixture after the reaction is completed, which is ideal for industrial processes.

Industrial heterogeneous catalysts often consist of an active phase material which performs the actual reaction catalysis, such as a transition metal micro- or nanoparticle (NP), dispersed on a nominally inert, high surface-area oxide support [16]. The active phase material usually possesses specific active sites on its surface where the catalyzed reaction takes place. Generally, the steps of the catalyzed reaction include reactants adsorbing onto the catalyst active site, the reaction taking place, and then the products desorbing from the active sites [17]. Hence, the nanoparticulate sizes of the active phase material coupled with the high surface-area provided by the support for dispersion of the active catalyst generally maximize the number of active sites and enhance the performance of the catalyst [18]. The high surface area of the supports and the nanoscale catalyst particle sizes also minimize the amount of active phase material required. This is a valuable outcome since the most effective catalysts are often precious, costly metals such as cobalt, gold and platinum [9].

Heterogeneous catalysis is a technologically and economically important subset of catalysis. About 90% of commercially available chemicals rely on heterogeneous catalysts for production. As an example, the production of fertilizer is heavily reliant on ammonia synthesis,

which is generally catalyzed by solid iron-based heterogeneous catalysts [7]. This ammonia synthesis process, named the Haber-Bosch process after its developers, is estimated to consume about 1% of the world's industrial energy budget [19]. Other important industrial processes such as hydrogenation for petroleum reforming (solid platinum and rhenium catalysts) and for margarine production (solid nickel) also rely on heterogeneous catalysts [2, 4].

1.3 Heterogeneous Catalyst Design

There are several attributes that render a heterogeneous catalyst effective for a given reaction. They can be summarized as follows [11, 17, 18]:

- The catalyst should be highly active for the desired reaction. Activity in this context means the presence of the catalyst should increase the rate of the reaction significantly. The higher the increase in reaction rate, the more active the catalyst. Since the activity increases with the number of active sites, the intrinsic activity of a catalyst material can be revealed by normalizing the activity by the number of active sites. This normalized activity is sometimes represented by the turnover frequency (TOF) which represents the rate of a given catalyzed reaction at a specific active site. Additionally, the morphology of the catalyst or support should not obscure or block active sites from reactant access, which would reduce the overall catalyst activity.
- The catalyst should exhibit acceptable selectivity for the desired reaction products. In most practical reaction processes, the reactants can produce a wide range of products through various pathways. A selective catalyst increases the reaction rates of reaction

pathways that produce the desired products, thereby reducing the number and amount of undesired by-products.

- The catalyst should be stable under required reaction conditions for long periods of time. Active sites should not be lost in significant amounts during the catalyzed reaction, which can happen via particle sintering, surface poisoning, etc. The active catalyst material should also be non-volatile and well-anchored on the support material of choice at the elevated temperatures and pressures commonly used in industrial processes.

These catalytic properties of activity, selectivity, and stability depend on the structure and morphology of the catalyst system as well as the materials of choice for both the catalyst and the support.

1.3.1 Rational Catalyst Design Approach

For many years the selection of a heterogeneous catalyst for a reaction was largely based on a trial-and-error approach predicated on experiential know-how. With the rapid advancement of synthesis techniques [20], characterization techniques [21-26], and computational tools [27-29], catalysis research is now able to study in detail the roles of the structural features of catalysts and the connection of these features to catalytic behavior. The vast amount of research in catalysis has shown that the factors of size, shape, atomic structure, and metal-support interaction significantly influence the activity and selectivity of a heterogeneous catalyst [20, 30, 31]. Additionally, these structural factors are dynamic under reaction conditions, and the dynamics must be accounted for to gain an accurate understanding of the catalytic behavior.

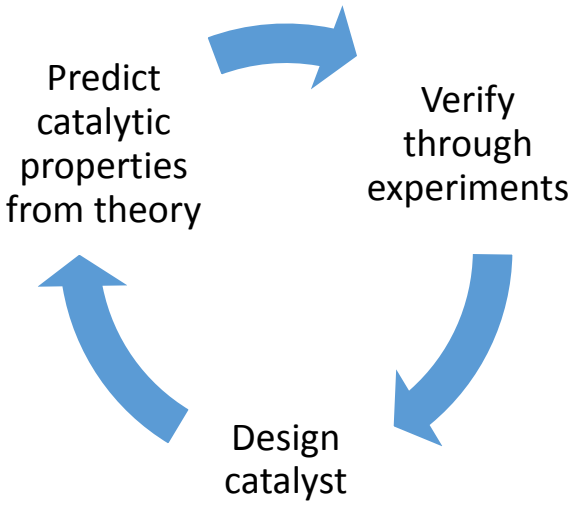

Figure 1. Flow diagram of the iterative process of rational catalyst design.

The rational catalyst design paradigm requires fundamental understanding of structure-property relationships of catalyst to predict and design efficient catalysts for given reactions of interest, through an iterative process (as depicted in Figure 1). This approach therefore requires correlative interplay between theory-based computational work and well-designed experiments. Importantly, the models being used in predictive simulations must be relatively accurate to reality in order for the predictive simulation results to be of any value.

1.3.2 Model System-Based Studies of Heterogeneous Catalysts

The rational design of catalysts requires predictive modeling tools that can be verified with experiments. However, the development of such models is limited by complexity in material samples that makes direct correlation between experimental and theoretical results difficult, creating the so-called "theory-experiment gap" or "materials" gap [32]. Properties of conventional

catalysts such as impurities and variable distributions of crystal orientation, which are difficult to represent in theory, can significantly impact catalyst behavior. To facilitate the correlation of experiment and theory, the catalyst system being studied experimentally should be uniform, structurally well-defined, and replicable.

For heterogeneous catalysts consisting of a supported metal active phase, model catalysts of well-dispersed NPs deposited on planar single-crystal or thin film supports have been used to bridge the materials gap [33]. Figure 2 provides an idealized schematic of such a model catalyst system. These model systems can provide valuable insight into the interplay of physical and electronic structure, adsorption, and active sites, while localizing the acquired insights to individual nanoparticle facets, edges or interfaces [34].

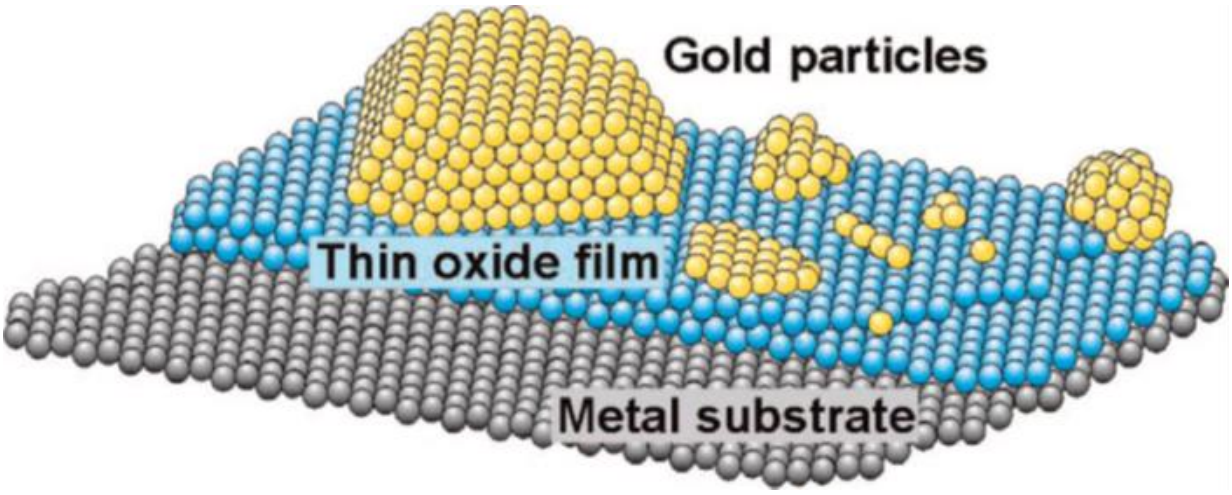

Figure 2. Schematic of supported Au model catalyst with planar thin film oxide support [35].

One of the most prominent examples of a catalyst for which a model system has enabled exceptionally detailed fundamental study is Au/TiO_2 [36]. For example, Wahlström et al. studied

a model system of Au/TiO_2 (110) with scanning transmission electron microscopy (STEM) in combination with density functional theory (DFT) calculations to find that Au nanoparticles nucleate at oxygen vacancies on the TiO_2 (110) surface [37]. Wörz et al. used infrared spectroscopy on model Au/TiO_2 combined with DFT calculations to describe the charge transfer associated with CO adsorption on reduced or oxidized TiO_2 supports [38]. The model catalyst approach of metal NPs deposited on planar single-crystalline supports has also been applied successfully to other metal/metal oxide catalyst systems including Ag/CeO_2, Rh/MgO, etc. [39-42]. These examples highlight the advantages of having a well-defined model catalyst for fundamental catalysis studies.

1.4 Gamma-Alumina: An Important Heterogeneous Catalyst Material

Gamma-alumina (γ-Al_2O_3) is a transitional phase of aluminum oxide that possesses naturally high surface area, high porosity, and acidic surface properties. As a result, it is an extremely important material in heterogeneous catalysis [43-46]. It is widely used as either a catalyst support or standalone catalyst in many industrial applications including oil refining and catalytic exhaust conversion. It is also seeing growing usage as a catalyst/support in methane oxidation, alcohol dehydration, and carbon monoxide oxidation reactions [47-50], all of which are vitally important for green and sustainable chemistry. The presence of undercoordinated acidic Al^{3+} sites on the γ-Al_2O_3 surface [51, 52] makes it an interesting material for myriad emerging catalysis applications. γ-Al_2O_3 also has shown promise in other applications unrelated to catalysis, such as ammonia absorption [46], also because of its inherently high porosity and surface area. Thus, the outcomes of this research project will potentially enable better predictive modeling of γ-Al_2O_3 properties for a wide variety of applications.

1.4.1 What is Gamma-Alumina (γ-Al_2O_3)?

To understand what is being referred to as γ-Al_2O_3, the concept of transitional alumina polymorphs must be introduced. Alumina in this context refers to the oxide of aluminum with the chemical formula Al_2O_3. This definition is important because the term "alumina" has been historically used to denote various aluminum compounds including aluminum hydroxide. It was discovered that alumina exists as several metastable polymorphs with the same stoichiometry but different crystal structures. These polymorphs were originally differentiated by powder X-ray diffraction and denoted by adding a Greek letter prefix to Al_2O_3 [43].

The transitional alumina polymorphs were discovered through observation of the continuous alumina phase transformation that occurs with increasing temperature during the Bayer process. The Bayer process was invented in 1889 by Carl Josef Bayer as a means to obtain pure alumina for aluminum metal production, starting from bauxite ore. Bauxite is the most common aluminum ore, a naturally occurring mixture of hydrated aluminum oxides that typically includes gibbsite ($2(Al(OH)_3)$), boehmite (γ-AlO(OH)) and diaspore (α-AlO(OH)). Even today, nearly all commercially produced alumina relies on the Bayer process, with the Hall-Heroult process then used to convert much of that alumina into aluminum metal.

The transitional aluminas are also called "metastable" aluminas because the thermodynamically stable polymorph is α-Al_2O_3 (corundum) [43]. The transitional aluminas however are stable at temperatures below their formation temperature and their phase transitions are irreversible. Typically, when a material is simply referred to as alumina, the material in question is the α-Al_2O_3 phase, which has a hexagonal close-packed (hcp) structure. Additionally, some commercially manufactured alumina formulations consisting of several metastable alumina polymorphs are called activated alumina [53]. α-Al_2O_3 is not normally included in activated

alumina formulations since its surface is not as chemically active as that of the metastable aluminas.

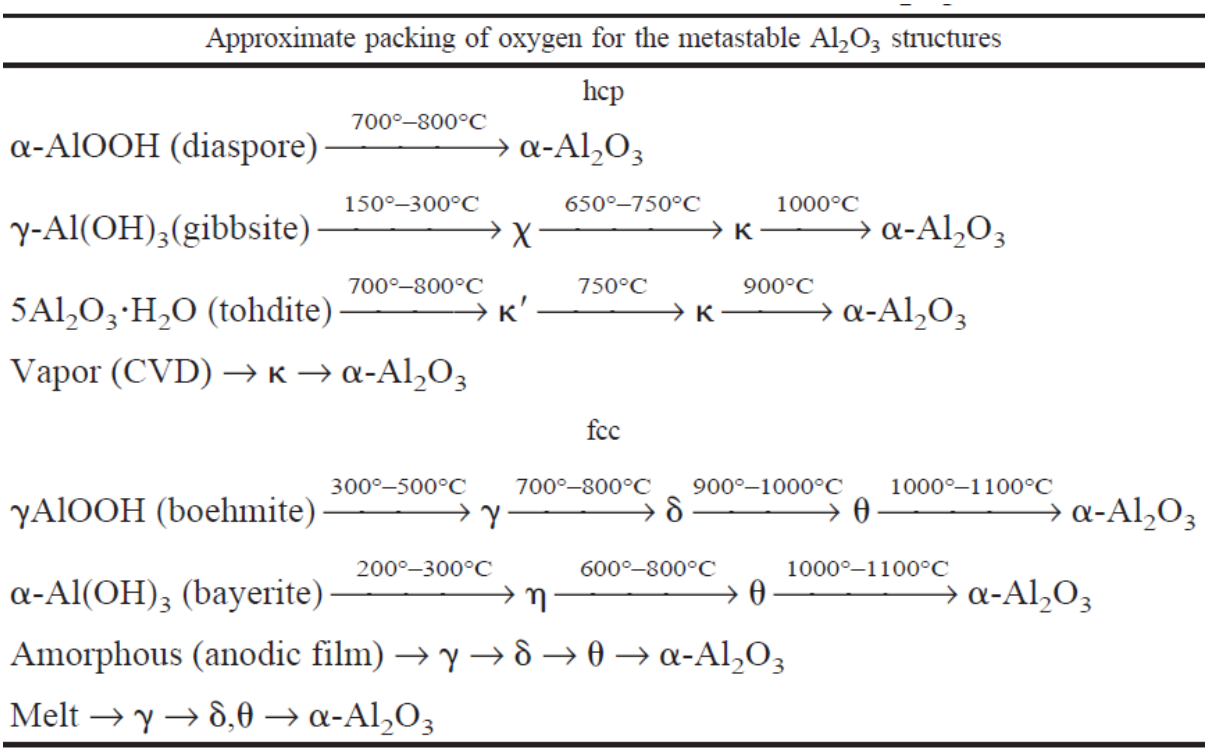

Figure 3. Sequences of phase transformation during common thermal treatment processing paths resulting in the formation of different transitional aluminas [43, 54].

γ-Al_2O_3 was the name given to the first transitional alumina polymorph formed between 300 °C and 500 °C during the dehydration of boehmite, which transforms with increasing temperature along the processing path: Boehmite → γ → δ → θ → α [43, 54]. Each transitional phase in this sequence was distinguished by its distinct powder XRD pattern, indicating a different crystal structure for each phase. The name γ-Al_2O_3 is now used to describe alumina with that same crystal structure regardless of the synthesis pathway, since alumina with the same structure is now being synthesized from a variety of different precursors with different processing paths, as shown

in Figure 3. There has been some confusion about the alumina nomenclature because the γ label has been historically used to refer to any alumina polymorph with cubic symmetry. However, it is now known that other phases of alumina such as η-Al_2O_3 also possess cubic symmetry [55]. η-Al_2O_3 is specifically used to denote the cubic alumina phase that derives from a bayerite precursor, which has a similar structure to γ-Al_2O_3 but different cation arrangement (nonspinel). These cubic phases of alumina can be differentiated by diffraction and other characterization methods.

As shown in Figure 3, γ-Al_2O_3 can also be produced starting from amorphous or melt precursors, but these synthesis pathways are not of particular industrial interest [54]. It has been demonstrated that the crystallinity of the precursor affects that of the γ-Al_2O_3 produced [56]. Though it may not be immediately obvious in Figure 3, the transitions between alumina polymorphs are not abrupt, and it is quite common for phases to overlap at a given temperature.

There has also been uncertainty about the structure of several metastable aluminas besides γ-Al_2O_3. All the metastable aluminas are known to have a face-centered cubic (FCC) oxygen arrangement that is consistent through the phase transitions up to and including α-Al_2O_3 [46]. The overall symmetry of the polymorph is thus determined by the placement and ordering of Al in the lattice. It has been observed based on the sharpness of powder diffraction peaks that the degree of Al ordering in the alumina structure increases along the boehmite processing path, with γ-Al_2O_3 having the most disordered structure [45, 55, 57]. The structure of δ-Al_2O_3 has also been heavily debated. It has been described as a slightly ordered supercell of γ-Al_2O_3 possessing orthorhombic symmetry, with 1-2 nm domains of tetrahedral Al ordering [57]. Kovarik et al. found that the δ-Al_2O_3 structure actually consists of two nearly identical structural variants, both orthorhombic with 38% of Al atoms on tetrahedral sites [58]. The structure of θ-Al_2O_3 has been described as a fully ordered monoclinic lattice with 50% of Al atoms on tetrahedral sites [59, 60]. They also argued

that the structure labeled δ-Al_2O_3 is actually a mixture of γ- and θ-Al_2O_3. η-Al_2O_3 has been described as having a similar structure to γ-Al_2O_3, but with Al atoms placed in highly distorted 32e sites [55]. The uncertainty about the structure of all the metastable aluminas is due to the varying levels of disorder in each phase, with γ-Al_2O_3 being the most disordered and accordingly, the most misunderstood.

1.4.2 Gamma-Alumina Atomic Structure: The Debate Thus Far

The crystal structure of γ-Al_2O_3 has been investigated using many different approaches including x-ray diffraction (XRD) [55, 57, 61], neutron diffraction [62], nuclear magnetic resonance (NMR) [59, 61, 63], infrared spectroscopy X-ray photoelectron spectroscopy (XPS) [64], as well as various computational techniques [65-72]. The structure of γ-Al_2O_3 was described shortly after being discovered by Verwey in 1935 as having a spinel-like ($Fm\bar{3}m$) structure similar to the traditional AB_2O_4 spinels with lattice parameter a equal to 7.9 Å [55, 73]. Recent studies have shown the ($Fd\bar{3}m$) space group to be more accurate [74]. In a spinel structure such as magnesium aluminate ($MgAl_2O_4$), the oxygen atoms are arranged in a face-centered cubic lattice whereas the A(Mg) and B(Al) cations occupy the 8a (tetrahedral) and 16d (octahedral) interstitial sites of the lattice respectively (Figure 4) [73, 75]. The 8a and 16d sites are thus called the spinel sites. Adding up the number of sites for the Wyckoff positions gives the stoichiometry $Al_{24}O_{32}$, which simplifies to Al_3O_4. To achieve the correct stoichiometry of Al_2O_3, 8/3 cation vacancies must be introduced into the unit cell [55], giving a simplified stoichiometry of $Al_{8/3}\square_{1/3}O_4$, where □ is an Al vacancy. Due to the addition of Al vacancies, this structure is sometimes called a defective spinel structure.

The distribution of vacancies between tetrahedral and octahedral sites has been the subject of ongoing debate and is one of the major unresolved questions. While some studies have suggested vacancies only in octahedral sites [76], others have suggested vacancies only in tetrahedral sites [57, 77], and more recent studies have suggested a ratio of about 63% tetrahedral : 37% octahedral [63, 74]. Experimental studies based on refinement of diffraction data or NMR experiments have suggested either vacancies on tetrahedral sites or a mix of tetrahedral and octahedral sites, whereas the placement of vacancies on octahedral sites has been primarily supported by computational studies. Additionally, the vacancies are typically assumed to be randomly distributed on the cation sites, such that tetrahedral vacancies for example are found on different 8a tetrahedral sites in different unit cells within a given γ-Al_2O_3 sample. Thus, the actual cation sublattice is effectively disordered.

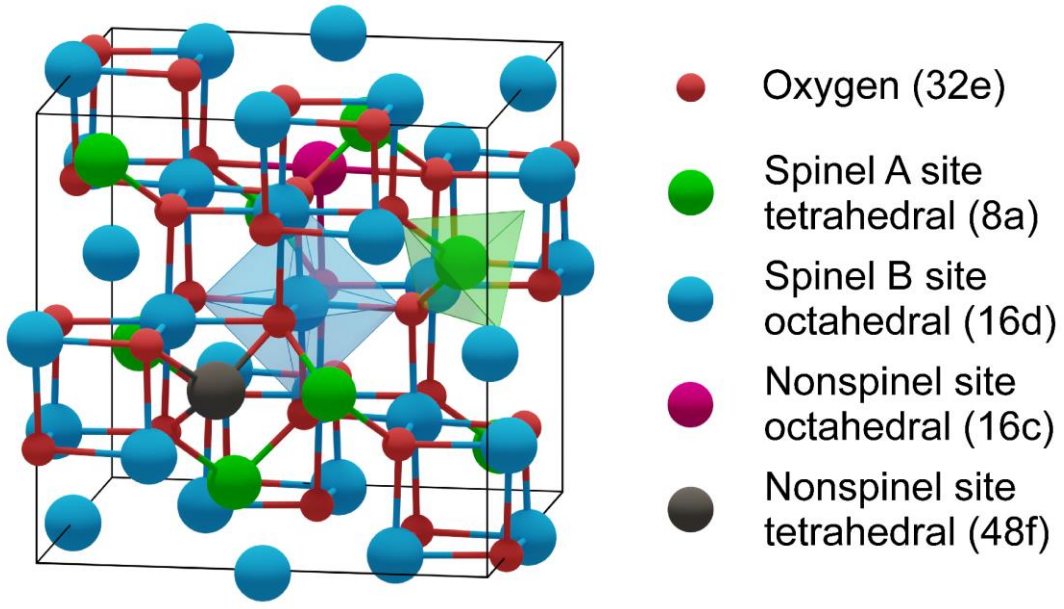

Figure 4. Schematic of the cubic spinel structure with examples of nonspinel sites.

More recently, structures challenging the traditional cubic spinel-like structure of γ-Al_2O_3 have been proposed [62, 65, 68, 78, 79]. These include nonspinel structures in which Al atoms are not restricted to occupying only spinel sites in the crystal lattice. Some possible nonspinel sites that are occupied in common nonspinel models are shown in Figure 4.

The possibility of Al atoms existing in nonspinel sites in the γ-Al_2O_3 structure was first suggested by Zhou and Snyder, who refined a structure with Al atoms in 32e sites with unusual five-coordinated symmetry [55]. However, the suggestion of five-coordinated Al sites could also be explained by an abundance of undercoordinated surface Al atoms in a high surface-area γ-Al_2O_3. Since then, more nonspinel models have been proposed including tetragonal models by Paglia with $I4_1/amd$ symmetry [62] and the monoclinic model described by Digne et al. [78]. It was also suggested that γ-Al_2O_3 contained hydrogen in its bulk structure as a consequence of the boehmite dehydration synthesis [80], but this was generally considered unlikely given the possibility of γ-Al_2O_3 synthesis from anhydrous precursors. The presence of bulk hydrogen in the γ-Al_2O_3 structure has since been refuted [81].

1.4.3 γ-Al_2O_3 Structure Models

Due to the difficulty in resolving the structure of γ-Al_2O_3, many different structures have been proposed in the literature. These structures are broadly divided into two categories:

- Spinel-based models: These are models that are based on the traditional spinel structure. In these models, O atoms are arranged in an FCC lattice and Al atoms are specifically limited to spinel A and B sites (see Figure 4). Depending on the selection of the unit cell size and the arrangement of Al vacancies (fixed/nonrandom vs. random), the symmetry of the model could be as high as cubic (random vacancy arrangement) or

have a lower symmetry space group. When the vacancy arrangement is random, the unit cell of the model must be described using some degree of fractional occupancy.

- Nonspinel models: While the O atoms in these models are also arranged in an FCC lattice, Al atoms are not restricted to spinel A and B sites and can occupy any interstitial site (see Figure 4 for example nonspinel Al sites). Since Al atoms can exist in more sites, the potential number of finite configurations of a nonspinel model with random vacancy arrangement is many times more than the spinel-based models. Some have argued that in this way, the search space for models is increased leading to better fitting structure models than the spinel-only structures .

The most commonly cited alternative models to the cubic spinel-based model considered in this project are the monoclinic spinel-based model described by Pinto et al. [79], the tetragonal nonspinel model proposed by Paglia et al. [62], and the monoclinic nonspinel model described by Digne et al. [78]. The unit cells of the published models considered in this project are shown in Figure 5, with their relevant structural aspects summarized in Table 1. All the models contain a nearly identical fully occupied face-centered cubic (FCC) O sublattice. The Al sublattice, on the other hand, is different for each model, differing by symmetry, occupied sites, and type of occupied sites (tetrahedral vs. octahedral, spinel vs. nonspinel). All these aspects contribute to the differences in their respective diffraction patterns. For the traditional cubic spinel, the spinel sites are 8a (tetrahedral) and 16d (octahedral) by Wyckoff notation. The equivalent sites for a tetragonal unit cell are 4a (tetrahedral) and 8d (octahedral).

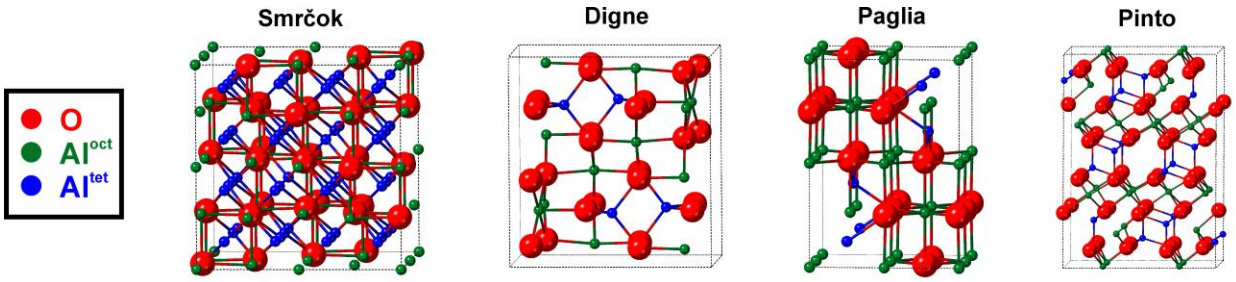

Figure 5. Schematic representations of the unit cells of the considered bulk γ-Al_2O_3 models: Smrčok cubic spinel model, Digne monoclinic nonspinel model, Paglia tetragonal nonspinel model, and Pinto monoclinic spinel-based model [62, 74, 78, 79].

Table 1. Relevant structural details and Al atom distributions of the considered bulk γ-Al_2O_3 models.

Model	Symmetry (Space Group)	Dimensions	Number of sites per unit cell	Partially occupied Al sites?	Al site positions	Al ratio in Tetrahedral vs. Octahedral	Al ratio in Spinel vs. nonspinel sites	Refs
Smrčok	Cubic ($Fd\bar{3}m$)	a = 7.9382 Å	120	Yes	8a, 16d, 16c, 48f	37:63	94:6	[74]
Paglia	Tetragonal ($I4_1/amd$)	a = 5.652 Å c = 7.871 Å	36	Yes	4a, 8d, 8c	29:71	73:27	[62]
Pinto	Monoclinic (C2/m)	a = b = 5.663 Å c = 13.71 Å α = β = 90.6° γ = 60.401°	80	No	n/a	38:62	100:0	[79]
Digne	Monoclinic ($P2_1/m$)	a = 5.587 Å b = 8.413 Å c = 8.068 Å α = γ = 90° β = 90.59°	40	No	n/a	25:75	32:68	[78]

The specific γ-Al_2O_3 models focused on in the remainder of this study are described in the following subsections.

1.4.3.1 Monoclinic Spinel-Based Model

The monoclinic model proposed by Pinto et al. was computationally derived based on a spinel structure. Starting with the $MgAl_2O_4$ spinel structure, three $MgAl_2O_4$ primitive cells were stacked on top of each other. The Mg atoms were then replaced with Al. Then two Al atoms were removed to give Al vacancies. The most energetically favorable sites for the Al vacancies in the model were found to be on octahedral sites with the farthest possible spacing, based on DFT calculations. The final optimized structure was a fully specified monoclinic spinel-based model with all Al vacancies located on octahedral sites [79]. As a model without fractionally occupied sites, it has been significantly used for γ-Al_2O_3 electronic and surface property calculations. The experimental verification given was the close match of the lattice parameter *a* for the model (transformed to have cubic symmetry) to experimental reported values.

This model has been viewed as a way to overcome the fractional occupancy of Al sites by ordering the vacancies in a reduced symmetry model; however, it is unclear if the vacancy ordering is in fact descriptive of the true structure of γ-Al_2O_3.

1.4.3.2 Tetragonal Nonspinel Model

The tetragonal model proposed by Paglia *et al.* [62] was obtained from an empirical fitting of neutron diffraction data, in addition to SAED and magic angle spinning NMR. Paglia et al. found that simulated neutron diffraction from a cubic spinel-based model exhibited a good fit to their experimental neutron diffraction data, but the fit could be improved by moving some of the Al atoms to octahedral nonspinel sites. The ratio of tetrahedral to octahedral Al atoms in their

nonspinel model was found to agree with experimental NMR data. Additionally, they showed that the diffraction pattern from γ-Al_2O_3 powder could be indexed in either cubic or tetragonal space groups. The final model was tetragonal with ~ 27% of Al atoms on octahedral nonspinel sites and fractionally occupied Al sites in the unit cell.

1.4.3.3 Monoclinic Nonspinel Model

The monoclinic nonspinel model described by Digne et al. [78] was based on simulations of boehmite dehydration described in Ref [66]. Molecular dynamics (MD) simulation of the dehydration process revealed that first the structure of boehmite collapsed as hydrogen and water molecules were removed. This resulted in a close-packed O lattice with all Al atoms in octahedral sites. The boehmite to γ-Al_2O_3 transition made it difficult to track if Al atoms were in spinel or nonspinel sites, but at least some of the Al atoms must be in nonspinel sites since there are fewer spinel octahedral sites than Al atoms in the unit cell. Thereafter, Al atoms were allowed to migrate to nearby vacant interstitial sites in the model. The most energetically favorable model was found to have 25% of Al atoms in tetrahedral sites.

This model has found widespread application particularly in DFT simulations [51, 82-86]. The major benefits of this model for *ab initio* simulations are the smaller unit cell compared to other models, in addition to the fully occupied lattice sites, which enable the creation of supercell models for surface studies more easily than models with fractionally occupied lattice sites [87]. Experimental verification of the Digne monoclinic nonspinel model was based on γ-Al_2O_3 powder XRD [66], as well as a calculated bulk modulus close to the experimental value [78].

1.4.3.4 Differences between γ-Al_2O_3 Models

While the O lattice is nearly identical for all these models, the distribution of Al cations both between spinel and nonspinel sites as well as between tetrahedral and octahedral sites is a major difference and defining factor for each model. Additionally, the unit cells of both the cubic spinel model and tetragonal nonspinel model contain fractionally occupied Al cation positions, unlike the monoclinic nonspinel and monoclinic spinel-based models. However, the fractional occupancy of Al positions in the cubic spinel and tetragonal nonspinel models could represent disorder intrinsic in the γ-Al_2O_3 structure that is in effect missed in the fully specified models such as the monoclinic nonspinel and monoclinic spinel-based model [88].

Some of the proposed γ-Al_2O structures have been previously compared by different groups. Sun *et al.* compared multiple spinel models and the Digne monoclinic nonspinel model [78] using synchrotron XRD on commercial γ-Al_2O_3, finding that the spinel models better reproduced the structural features of γ-Al_2O_3 [89]. This conclusion was challenged by Paglia *et al.* [90] and Digne *et al.* [91], both suggesting that the material studied by Sun *et al.* was actually δ-Al_2O_3. However, Smrčok *et al.* [74] determined, by XRD Rietveld refinement from single-crystal γ-Al_2O_3 produced by reaction of β-sialon and steel, a cubic spinel-based structure of γ-Al_2O_3 with only 6% of Al atoms in nonspinel sites. Ferreira *et al.* later found using DFT simulations that spinel-like γ-Al_2O_3 was more thermodynamically stable than the Digne monoclinic nonspinel model [71], with simulated infrared (IR) spectra also better agreeing with the spinel-like structure [71, 92]. These previous studies demonstrate the ongoing debate over the γ-Al_2O_3 structure.

1.4.4 Reasons for Difficulty in γ-Al_2O_3 Structure Determination

The uncertainty about the γ-Al_2O_3 structure is in large part due to the nature of commercially available γ-Al_2O_3, which has typically been used for structure studies. Commercially available γ-Al_2O_3 produced by boehmite dehydration is not ideal for a model catalyst due to its poorly defined crystallinity and presence of impurities [66, 93]. It has been observed that poorly crystalline γ-Al_2O_3 has a higher surface area than γ-Al_2O_3 produced from highly crystalline precursors [43], which explains why it is preferred for catalyst applications. Large, clean, γ-Al_2O_3 single-crystals, which would be ideal for structural analysis, are not normally produced commercially [94-96].

The inherent disorder in the γ-Al_2O_3 is also a major contributing factor to the difficulty in unambiguously resolving its structure. The disorder directly affects the resolution of powder diffraction experiments, with higher background and broadened peaks as a result. Other characterization techniques are affected as well. This problem combined with the relative similarity of the alumina phases has complicated characterization, particularly in commercial γ-Al_2O_3 where multiple alumina phases are often present due to the nature of the synthesis [92].

The experimental techniques so far used to characterize the γ-Al_2O_3 structure have also contributed to the uncertainty. Powder XRD and other ensemble techniques average over thousands of crystals, and in the case of a highly porous, impure sample, the structure of averaged material may vary widely from sample to sample. NMR is highly sensitive to atomic coordination; however, the spectroscopic contribution of the bulk cannot be easily distinguished from that of the surface [97], which is especially problematic for high surface-area materials such as γ-Al_2O_3. These factors must be overcome or at least accounted for to improve the accuracy of γ-Al_2O_3 structure characterization.

The synthesis of single-crystalline γ-Al_2O_3 for structural studies is therefore a major step in accurate structural characterization. γ-Al_2O_3 has been observed forming on the surface of aluminum containing intermetallics including NiAl, which are used as high-temperature refractory alloys [98-101]. The passivating alumina layer that forms on these alloys evolves into γ-Al_2O_3 at specific temperatures. Surface scientists have taken advantage of this discovery to grow ultrathin layers of Al_2O_3 on NiAl (110) which are about 0.5 nm in thickness [102-104]. However, those films cannot be precisely described as γ-Al_2O_3 because the film thickness does not constitute up to one complete unit cell of γ-Al_2O_3. Furthermore, such a thin layer of Al_2O_3 support introduces the possibility of the NiAl substrate influencing the chemistry of the nanoparticles deposited on the Al_2O_3 surface. Single crystal γ-Al_2O_3 (111) with bulk-like crystalline properties has been produced by oxidizing single crystal NiAl (110) under controlled conditions [105]. This approach has been used to prepare model γ-Al_2O_3 catalyst supports. γ-Al_2O_3 produced through this method is better suited for the intended structural analysis, as it is highly crystalline and should not include hydrogen or water in the bulk structure, unlike boehmite-derived γ-Al_2O_3 [66, 93]. The synthesis and characterization of model highly crystalline γ-Al_2O_3 for this project is discussed in detail in sections 3.2.1 and 4.1, respectively.

1.4.5 Importance of Ascertaining the Correct Structure of γ-Al_2O_3

Ambiguity in the structure models has led to many different models being used for theoretical simulations—including models that are now known to be less accurate than others [88]—resulting in sometimes contradictory findings, e.g., the prediction of the relative surface energies of low index γ-Al_2O_3 surfaces, which are important for modeling catalysis. Early work by Blonski et al. [70] using a cubic spinel model with all vacancies in tetrahedral sites found that

the γ-Al_2O_3 surface energies followed the trend of (100) < (111) < (110). Work by Pinto et al. [79] using a spinel-based model with all vacancies in octahedral sites showed a slightly different surface energy trend of (100) ≈ (111) < (110). On the other hand, Digne et al. [78] using a nonspinel model found that the surface energies follow the trend of (100) < (110) < (111). These contradictory results highlight the impact of the choice of model on theoretical calculation results of a property that is relevant to catalysis. Similar problems exist with calculations of the band gap (important for predicting electronic behavior), and the bulk modulus (important for predicting mechanical behavior) [78, 79, 94]. A more accurate description of the γ-Al_2O_3 structure is therefore vitally important to ensure the reliability of theoretical predictions of γ-Al_2O_3 properties, with determining the distribution of Al vacancies being a key step. Ultimately the effectiveness of a rational design approach using γ-Al_2O_3-based catalysts is inextricably dependent on the accuracy of the γ-Al_2O_3 models used.

With atomistic simulations becoming more prevalent and γ-Al_2O_3 continuing to be a material of interest especially in heterogeneous catalysis, accurate determination of the atomic structure of γ-Al_2O_3 is essential for realistic and predictive simulations of its performance. Predicted catalytic properties will depend on the arrangement of atoms at surfaces and in the subsurface, which in turn is dependent on the atomic arrangement specified by the bulk model used.

1.5 Platinum/Gamma-Alumina Catalyst

Platinum is possibly the most ubiquitously used transition metal catalyst, as it is one of the most efficient catalysts for many industrially relevant reactions including the oxygen reduction

reaction (ORR), naphtha reforming, gas sensing, CO oxidation and methane oxidation to methanol [106-108]. In many of these applications, Pt is supported on gamma-alumina (γ-Al_2O_3) [45, 109]. The Pt/γ-Al_2O_3 catalyst system has found widespread use in industrial applications, including in fuel cells, petroleum reformers and catalytic converters [110, 111]. Pt is used in nanoparticle form for a wide variety of important reactions [47, 112-114]. As such it is a highly relevant catalyst, both for present day and future applications.

γ-Al_2O_3 is commonly described as a non-reducible or slightly reducible support, which means that it does not interact with catalyst NPs significantly [31]. However, the previously commonplace notion that γ-Al_2O_3 is an inert support because it is technically nonreducible is continuously being challenged [115], with the surface properties in particular of γ-Al_2O_3 having been known to play an important role in the dispersion, physical properties, and electronic structure of supported Pt NPs [116-118]. Through high resolution electron microscopy and ultra-high magnetic field nuclear magnetic resonance (NMR) studies of Pt NPs on the γ-Al_2O_3 (100) surface, Kwak et al. pointed out that unsaturated pentacoordinate Al^{3+} sites serve to anchor Pt atoms at low surface loading [118]. Nellist and Pennycook observed using high-angle annular dark-field (HAADF) STEM that mono-atomically dispersed Pt were anchored at oxygen vacancies on the γ-Al_2O_3 surface, and that Pt appeared to be partially dissolved into the top layers of γ-Al_2O_3 [119]. And theoretical work by Sanchez et al. has shown that interaction between Pt NPs and a γ-Al_2O_3 support led to the unusual effect of negative thermal expansion (NTE) of the Pt NPs and creation of disorder in the Pt NPs [120]. Furthermore, simulations of Pt_{10} nanoclusters on the γ-Al_2O_3 (110) surface have shown that the clusters can be stabilized by surface O atoms [27].

These previous studies show that the interaction between γ-Al_2O_3 support and Pt NPs is more significant and more complex than previously anticipated, warranting further study.

Determining the specific atomic bonding between Pt atoms and the γ-Al_2O_3 support surface is important to understand both the structural and the electronic properties that result from the interaction between a Pt NP and γ-Al_2O_3 support. This understanding is also ultimately necessary to model the entire Pt/γ-Al_2O_3 catalyst more accurately in theoretical simulations. While this aspect was not the main thrust of this project, the results found here can potentially contribute to the heterogeneous catalysis field, rather than solely be an academic exercise.

1.6 Overview

An overview of the breakdown of this dissertation by chapter is provided here. In **Chapter Two**, the specific objectives of this research are described.

Chapter Three provides the description of the experimental and computational approaches used in this work in sufficient detail to enable interpretation of the results. General synthesis and characterization conditions as well as simulation parameters used are also described in this chapter. It is explicitly mentioned in the subsequent chapters where any alternative conditions or parameters were used. **Chapter Four** describes the characterization of the model γ-Al_2O_3 to ensure that not only was aluminum oxide formed by the synthesis procedure, it was indeed single-crystalline and pure.

Chapter Five details the effects of electron beam damage on γ-Al_2O_3 structure and the artifacts induced by beam damage in EELS spectra. It was found that damage caused by the radiolysis mechanism produced sharp artifacts in the O-K edge EELS spectra even at short acquisition times, and this type of damage could be suppressed by operating at cryo temperature (cryo-STEM/EELS). In **Chapter Six**, several of the most commonly cited γ-Al_2O_3 models from

literature were investigated using simulated SAED with reference to experimental SAED from the model γ-Al_2O_3. The cubic spinel-based model ($Fd\bar{3}m$) was found to best describe the γ-Al_2O_3 structure based on both the presence and relative intensities of diffracted reflections in the SAED pattern. **Chapter Seven** describes the investigation of the vacancy distribution in the cubic spinel-based γ-Al_2O_3 model. The majority (50–90%) of Al vacancies were shown to exist on tetrahedral sites, contrary to several common spinel-based models where vacancies are placed primarily or entirely on octahedral sites. In **Chapter Eight**, the ability to model the electronic structure of γ-Al_2O_3 using existing models was investigated. It was found that all the models produce similarly accurate representations of the electronic structure, but discrepancies were found in models with significantly different vacancy distributions (monoclinic spinel-based model) and with highly distorted tetrahedra/octahedra and inaccurately long bond lengths (monoclinic nonspinel model). Also, the use of a simple, tractable interfacial model Pt/γ-Al_2O_3 interface is presented in this chapter.

2.0 Objectives

The overall goal of this research project is to advance the understanding of the structure of γ-Al_2O_3. The studies described herein are designed primarily to elucidate details of the atomic structure of γ-Al_2O_3, to contribute towards resolving the debate about the γ-Al_2O_3 structure.

The primary tools used to pursue this goal are:

- Thin film synthesis
- Selected-area electron diffraction (SAED)
- Kinematical electron diffraction simulation
- High-resolution electron energy-loss spectroscopy (EELS)
- Real space multiple scattering (MS) EELS simulation

The project is broken down into these individual objectives:

- Synthesis of model, well-crystallized polycrystalline and single-crystalline γ-Al_2O_3 (111) thin films for reliable structure characterization. This is achieved by controlled thermal annealing of a single-crystal NiAl (110) precursor.
- Since high-resolution EELS will be acquired from the beam-sensitive γ-Al_2O_3, an approach that minimizes electron beam damage-induced artifacts is developed and validated. Understanding of electron beam damage mechanisms in γ-Al_2O_3 is also advanced.
- Clarification of the most accurate space group and unit cell to represent γ-Al_2O_3. Simulated polycrystalline and single-crystalline SAED data from four of the most commonly cited

structural models of γ-Al_2O_3 are compared to the experimental SAED to determine the most accurate model(s).

- Identification of the elusive vacancy distribution within the γ-Al_2O_3 structure. SAED and EELS experiments and simulations are employed on single-crystal γ-Al_2O_3 to investigate this question.
- Evaluation of the ability to accurately model γ-Al_2O_3 electronic structure using existing γ-Al_2O_3 models. High-resolution EELS and EELS simulation are the tools of choice for this study. Atomistic bonding at Pt/γ-Al_2O_3 (111) interface is studied to evaluate the balance of computational tractability against production of useful results for a simple Pt/γ-Al_2O_3 model.

3.0 Research Design and Methods

3.1 Research Design

The research methodology used to pursue the objectives outlined in Chapter 2 is detailed in this section. First, model catalyst systems of Pt on single-crystal γ-Al_2O_3 (111) thin films were prepared. The model systems were characterized using X-ray diffraction (XRD), scanning electron microscopy (SEM), atomic force microscopy (AFM), scanning/transmission electron microscopy (S/TEM) and electron energy-loss spectroscopy (EELS). Polycrystalline γ-Al_2O_3 thin film samples were also prepared and used to evaluate the crystal structure models for γ-Al_2O_3. Simulated EELS spectra and electron diffraction patterns were calculated to correlate with the corresponding experimental measurements to aid in analysis and interpretation. The general procedures described in this chapter were used for all the work reported hereafter, except where indicated.

The facilities used for this work include the Center for Functional Nanomaterials (CFN) at Brookhaven National Laboratory (BNL), the National Center for Electron Microscopy (NCEM) at Lawrence Berkeley National Laboratory (LBNL), the Advanced Materials Characterization and Testing Lab (AMCaT) at the University of California-Davis, the Center for Electron Microscopy and Analysis (CEMAS) at the Ohio State University, and the Materials Micro-Characterization Laboratory (MMCL) and the Nanoscale Fabrication and Characterization Facility (NFCF), both at the University of Pittsburgh.

3.2 Sample Preparation

3.2.1 Single-Crystal γ-Al_2O_3 (111) Synthesis

Single-crystal γ-Al_2O_3 (111) was prepared using the method developed by Zhang et al [105]. Equiatomic single-crystal NiAl oriented to its (110) surface and cut into 5 x 5 x 1.5 mm pieces was used (obtained from Ram Darolia, GE). The (110) surface orientation was confirmed by Bragg-Brentano (θ/2θ) XRD. The samples were then polished with SiC polishing papers through the sequence: 400 grit – 600 grit – 800 grit – 1200 grit. Afterwards, the samples were polished with alumina slurry through the sequence: 1 µm – 0.3 µm – 0.05 µm. The polishing ensured a largely flat and defect-free surface for the growth of the single crystal alumina. After polishing, the sample was ultrasonicated in deionized water to remove any leftover alumina slurry and then plasma cleaned in Ar plasma for 10 minutes to remove surface contaminants.

The polished samples were oxidized in a conventional tube furnace at 850°C for 1 hour. The tube was maintained under an Ar (Product grade, Matheson TriGas Inc.) atmosphere during the heating ramp to 850°C. Upon reaching the set point temperature, dry air (Air - Grade Dry, Matheson TriGas Inc.) was introduced into the tube at a flowrate of 0.1 L/min. After the oxidation was complete, Ar was reintroduced into the tube. The sample was left to gradually cool in the Ar atmosphere overnight, to minimize residual strain induced by coefficient of thermal expansion (CTE) mismatch between the Al_2O_3 thin film and the NiAl substrate.

3.2.2 Polycrystalline γ-Al_2O_3

Textured polycrystalline γ-Al_2O_3 films approximately 150 nm thick were grown by oxidation of single-crystal NiAl oriented a few degrees away from the (110) normal at 850 °C for 2 hours. The sample was then left to cool in an Ar atmosphere overnight akin to the single-crystal thin film synthesis discussed above. The polycrystalline film—with an average grain size of approximately 50 nm—was scraped off the NiAl substrate and onto a carbon-coated Cu TEM grid for characterization. The commercial γ-Al_2O_3 nano-powder used for comparison of diffraction data was acquired from Inframat Advanced Materials (γ-Al_2O_3 Nano Powder, 99.99% purity).

3.2.3 Deposition of Pt Nanoparticles on Model γ-Al_2O_3

The model γ-Al_2O_3 surface was first plasma cleaned in a mixed oxygen and argon plasma (1:4 O_2 to Ar ratio) for 5 minutes to remove carbon contaminants from the sample surface. The clean sample was then placed in a Pascal Technologies ultra-high vacuum (UHV) dual electron-beam evaporation system. Electron beam (e-beam) evaporation is a physical vapor deposition (PVD) technique where a focused electron beam is directed onto a target ingot in a chamber kept at high vacuum. The kinetic energy from the electrons is converted to thermal energy in the ingot, locally vaporizing the target material. The vapor then precipitates onto the surface of a substrate placed in the high vacuum chamber (Figure 6).

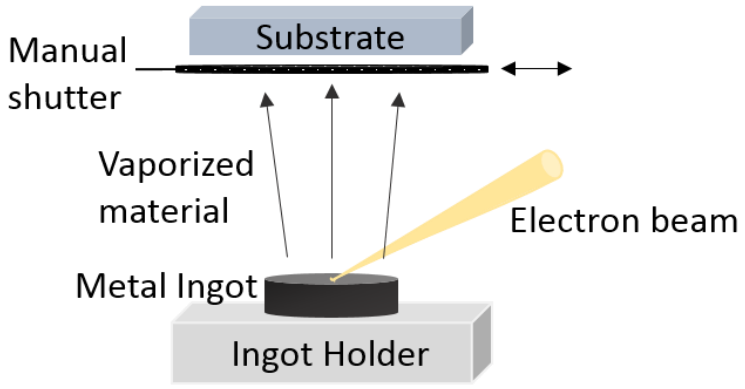

Figure 6. Schematic of e-beam evaporation setup.

The NiAl/γ-Al_2O_3 substrate was heated to 500°C and Pt was evaporated at a deposition rate of 2 Å/s for 3 seconds. The total deposition time was controlled via manual shutter. These deposition conditions resulted in 2–3 nm diameter Pt nanoparticles.

3.3 Experimental Characterization Tools

3.3.1 X-ray Diffraction (XRD)

X-ray diffraction is a technique commonly used to determine the crystal structure of a material. A crystal consists of a regular array of atoms with periodic long-range order. X-rays are electromagnetic waves within a certain range of wavelengths (10 pm to 10 nm). When X-rays are directed onto a crystal, the X-rays are scattered by the atoms in the crystal, specifically by the electrons around each atomic nucleus. This scattering interaction is elastic, meaning the X-rays do not lose energy but are simply redirected by the electrons. Since the crystal consists of many atoms, the X-rays are scattered in many directions. The X-rays cancel each other out (through destructive

interference) in most directions; however, in some specific directions, they constructively interfere. The condition for constructive interference is called the Bragg condition and is illustrated in Figure 7.

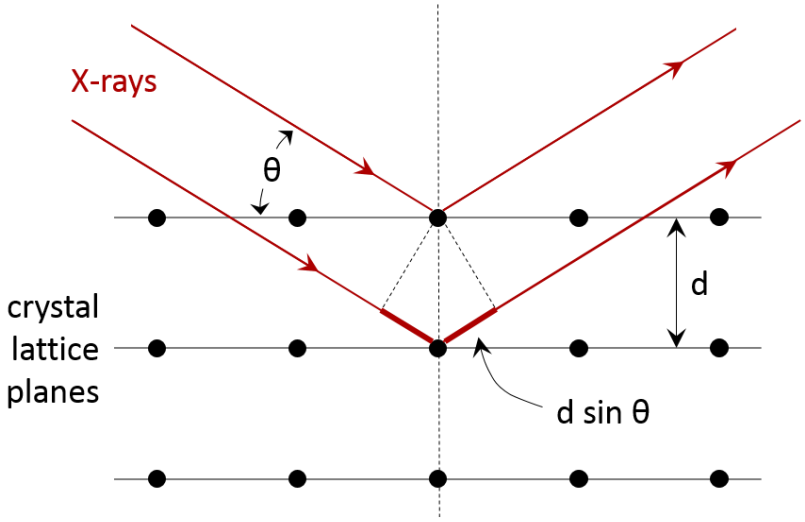

Figure 7. Bragg condition being satisfied in a crystal lattice leading to diffraction.

The black spheres represent atoms in the crystal lattice. d is the spacing between planes of atoms in a certain direction in the crystal and θ is the incidence angle of the incoming X-rays. The Bragg condition is described by an equation called Bragg's law:

$$2d \sin \theta = n\lambda \tag{3.1}$$

The Bragg condition implies that constructive interference of two X-rays striking a crystal will occur when the difference in path length between the X-rays (2d sin θ) is an integer multiple of the X-ray wavelength. By using X-rays of a controlled wavelength and measuring the angular position and intensities of diffracted X-rays that meet the Bragg condition, the spacing of atomic planes in the crystal can be determined.

The Bruker D8 Discover X-ray diffractometer at the NFCF was used with Cu Kα radiation, operated at 40 kV and 40 mA, to probe the crystal structures and planar orientations of the substrate and thin-film samples.

3.3.2 Surface Characterization Methods: Scanning Electron Microscopy (SEM) and Atomic Force Microscopy (AFM)

Scanning electron microscopy is one of a number of techniques that takes advantage of the interaction of fast electrons with matter. Fast electrons are electrons traveling at speeds much faster than the electrons in the material [121]. When fast electrons are directed onto a sample, a number of phenomena can occur. These phenomena are summarized in Figure 8.

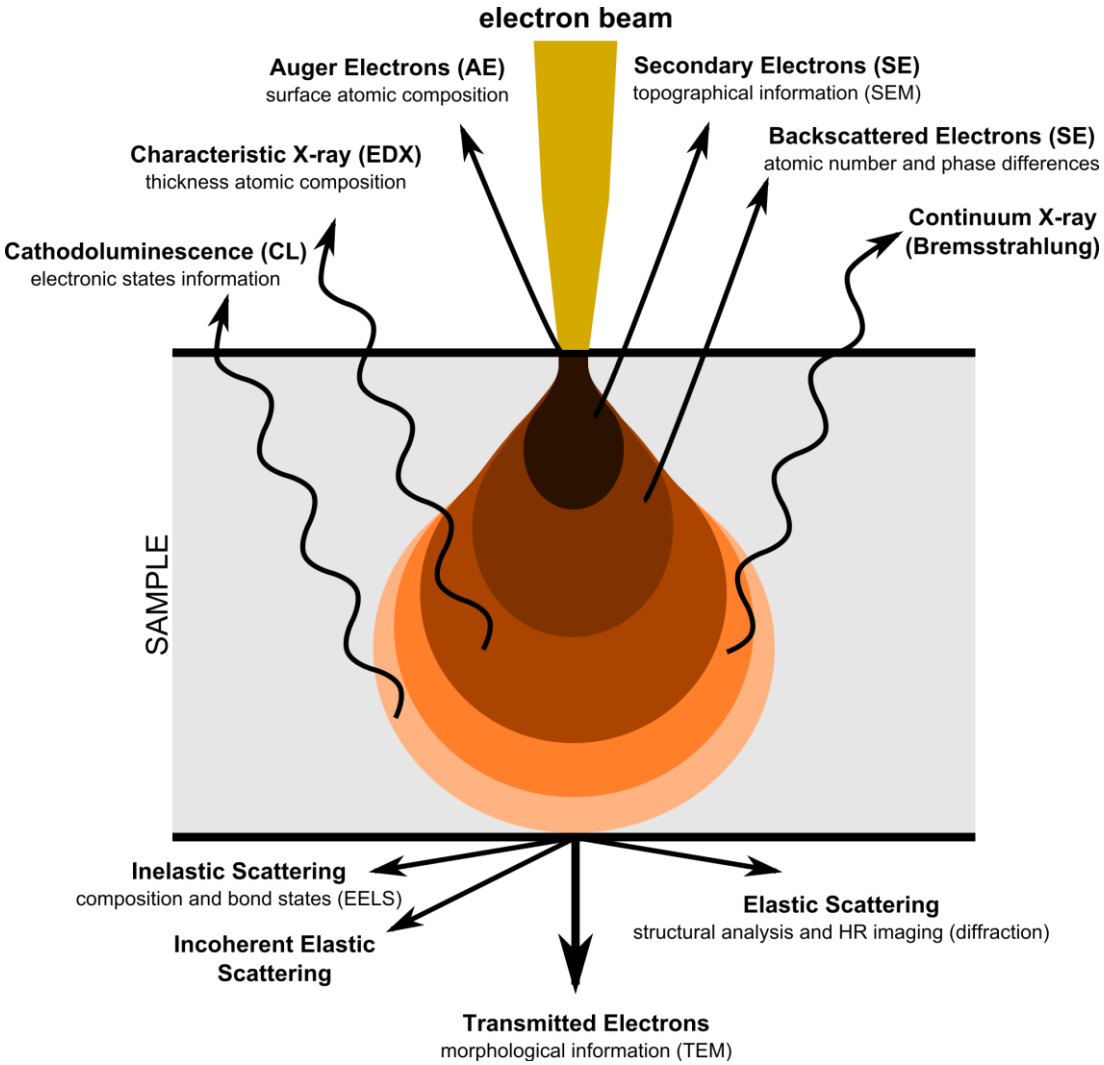

Figure 8. Phenomena produced by interaction of fast electron with matter.

In SEM, a focused electron beam is scanned over the sample surface and secondary or backscattered electrons are detected and used to form images. Secondary electrons (SE) are low energy electrons (<50 eV) produced by the beam-sample interaction. Because of their low energy, most SEs are reabsorbed in the sample, and only those produced near the surface of the sample are able to escape. Consequently, SE detection produces topographical images. Backscattered electrons (BSE) on the other hand are electrons that have been elastically scattered by the nuclei of atoms in the sample. They also originate from deeper in the sample. Since higher atomic number atoms have larger nuclei, they backscatter electrons more strongly. Hence the image formed by BSEs includes phase and composition information. The JEOL JSM6510, Zeiss Sigma500 VP, and FEI Scios at the NFCF were used, operated between 2kV and 10kV, to image sample surfaces after preparation steps.

In atomic force microscopy, a physical probe is used in the form of a very fine-tipped (~20 nm width at tip) cantilever to image material surfaces. The fine-tipped cantilever is scanned over the surface of the material with nanometer step size using piezoelectric controllers. The deflection of the cantilever in the Z direction (corresponding to changes in surface height) as it is scanned across the surface is determined by shining a laser onto the back of the cantilever and measuring the change in reflected laser signal using a photodiode. The Veeco Dimension V Scanning Probe Microscope at the NFCF was used in tapping mode—where the probe does not contact the surface but instead oscillates just above the surface at its resonance frequency—to acquire topographical images and surface roughness measurements.

3.3.3 Focused Ion Beam (FIB)

Focused ion beam operates similarly to SEM, but instead of electrons, a focused beam of ions is used. Ions of liquid metals are normally used, with gallium (Ga^+) ions being the most common. When the focused ion beam strikes the sample, kinetic energy is transferred to the atoms in the sample and material is removed (sputtered away) at the point of the impact. The sputtered material leaves the surface in the form of secondary ions or neutral atoms. By varying the current and position of the focused ion beam, the sputtering can be precisely controlled to produce desired shapes, a process called milling or patterning. Additionally, secondary electrons are produced by the ion beam-surface interaction. As in SEM, the SEs can be collected and used to form topographical images of the surface. FIB is often combined with SEM in the same equipment, such that SEM is used for surface imaging while FIB is simultaneously used for milling and patterning. The FEI Helios at BNL and the FEI Scios at the NFCF, both dual-beam FIB-SEMs, were used to prepare cross-sectional TEM samples of the model Pt/γ-Al_2O_3 through milling.

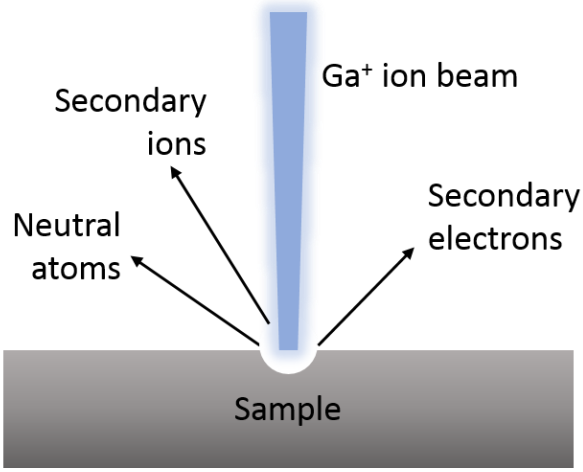

Figure 9. Interaction of focused ion beam with a sample.

3.3.3.1 Cross-Sectional TEM Sample Preparation

Cross-sectional TEM samples were prepared using a dual-beam FIB-SEM (FEI Helios and FEI Scios) according to the following general procedure. An area of the sample was selected from which to prepare a cross-sectional TEM sample (Figure 10a). A 10 µm x 2 µm area of the sample surface was coated with a 200 nm thick layer of amorphous carbon and then a 1 µm thick layer of platinum *in situ* in the FIB-SEM using the built-in gas injection systems (GIS) (Figure 10b). The carbon and platinum coatings are sacrificial layers used to protect the sample surface from the high-energy Ga^+ ion beam during the rest of the procedure. Using the Ga ion beam, trenches are milled on either side of the desired area, leaving a cross-sectional lamella 10 µm wide and ~2 µm thick (Figure 10c). An Omniprobe micromanipulator tip was used to transfer the lamella to an Omniprobe TEM half-grid, to which it was then welded (Figure 10 d-e). Finally, the lamella was thinned with the 30kV ion beam with progressively lower currents down to <100 nm thickness and then polished with the ion beam at 5 kV and finally 2 kV (Figure 10f). The sample was then further thinned in an E. A. Fischione 1040 NanoMill with a 500 eV Ar^+ ion beam, which also removed the implanted Ga^+ ions and the amorphized layers of surface damage caused by the higher-energy FIB ion beam. Final sample thickness was < 60 nm as observed in SEM.

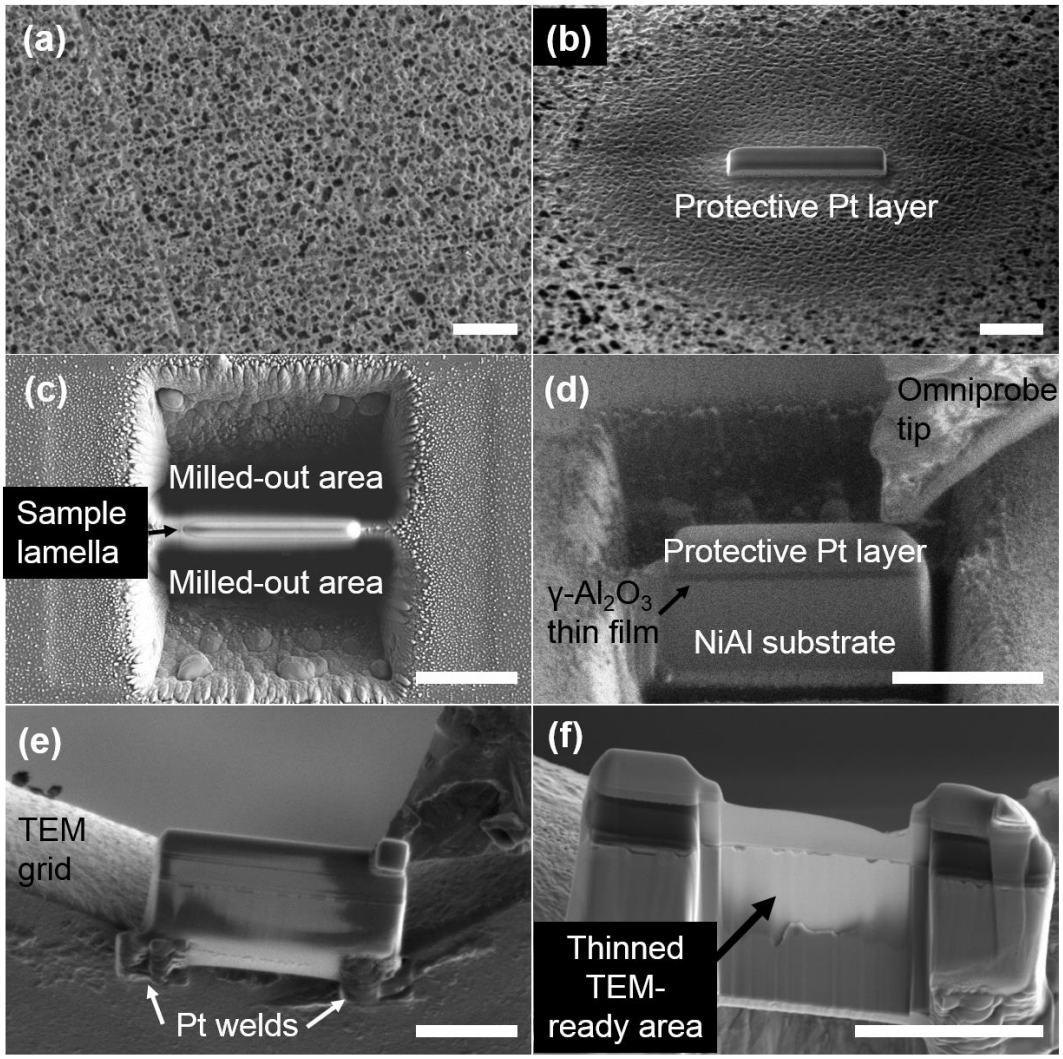

Figure 10. Dual-beam FIB-SEM cross-sectional TEM sample preparation procedure. Scale bar = 5 µm.

3.3.4 Transmission Electron Microscopy (TEM) and Scanning TEM (STEM)

In transmission electron microscopy, high-energy electrons are used to image thin samples at the nanoscale and below. The samples must be thin enough (usually < 100 nm thick) for electrons to transmit through. The electrons interact with the sample as they are transmitted through and the transmitted electrons are detected and use to form an image.

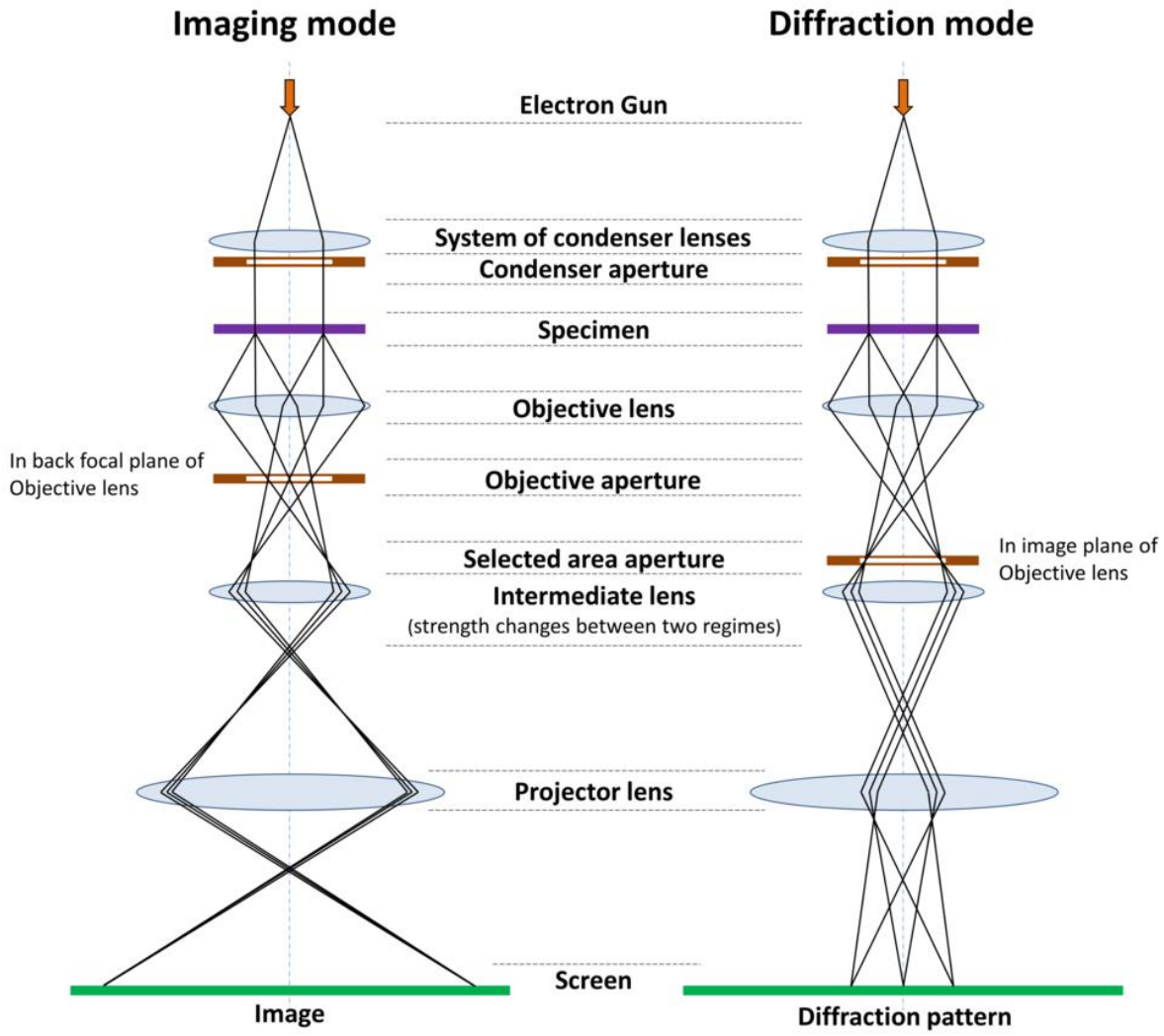

Figure 11. Schematic of conventional TEM in imaging and diffraction modes.

Conventional TEM is usually performed in either imaging mode or diffraction mode. In both cases, images are formed using a parallel electron beam. Contrast arises in an image when some portion of the electrons, upon interacting with the sample, are scattered at an angle from the optic axis (the "center" of the microscope column) and/or have the phase of their wavelength shifted. In imaging mode, the presence of contrast in images can be either due to the mass-thickness effect or due to diffraction. Both contrast-forming phenomena can also occur simultaneously. Heavier atoms scatter electrons more strongly than lighter atoms, hence regions of the sample with higher mass atoms will appear darker. Similarly, thicker regions of the sample will scatter electrons more than thinner regions, thereby making thicker regions appear darker. In a crystalline sample, electrons will also be diffracted by the crystal lattice, producing contrast depending on the orientations of grains in the sample. In diffraction mode, diffraction of the electron beam by a crystalline sample can be used in a similar way to XRD to probe the crystal structure of a material (see Section 3.3.5 about electron diffraction).

To form a typical bright-field (BF) image, an aperture (the objective aperture) is placed around the optic axis, allowing only electrons that remain along the optic axis after transmission to pass through. Regions of the sample where electrons transmit through unaffected (such as holes) produce the brightest intensity in such an image. Regions containing heavier elements or thicker parts of the sample scatter more electrons away from the optic axis and thus appear darker. A dark field (DF) image can also be formed by placing the objective aperture around a diffracted beam rather than the optic axis. In this case, the regions of the sample that diffract electrons into the diffracted beam appear bright while the rest of the sample appears dark.

Scanning TEM (STEM) works by a similar mechanism to SEM, in that the electron beam is focused and scanned over the sample area, but rather than using SEs to form an image,

transmitted electrons are used. Like in conventional TEM, a BF image can be formed by detecting electrons that transmit along or are scattered close (<10 mrad) to the optic axis. Annular detectors are used to detect electrons scattered away from the optic axis at a larger angle. These electrons are used to form annular dark field (ADF) images. High-angle annular dark field (HAADF) images are formed when electrons scattered >50 mrad away from the optic axis are used. At these angles, the electrons reaching the detector are predominantly Rutherford scattered—incoherent, elastic scattering from atomic nuclei—rather than from (coherent) diffraction scattering. The electron scattering cross-section for this kind of interaction is, in practice, proportional to $\sim Z^{1.7\text{-}1.8}$, where Z is the atomic number. Thus, contrast in HAADF images is primarily a function of the atomic number of the elements present in the sample (higher Z leads to higher image intensity), which is why it is often called Z-contrast imaging.

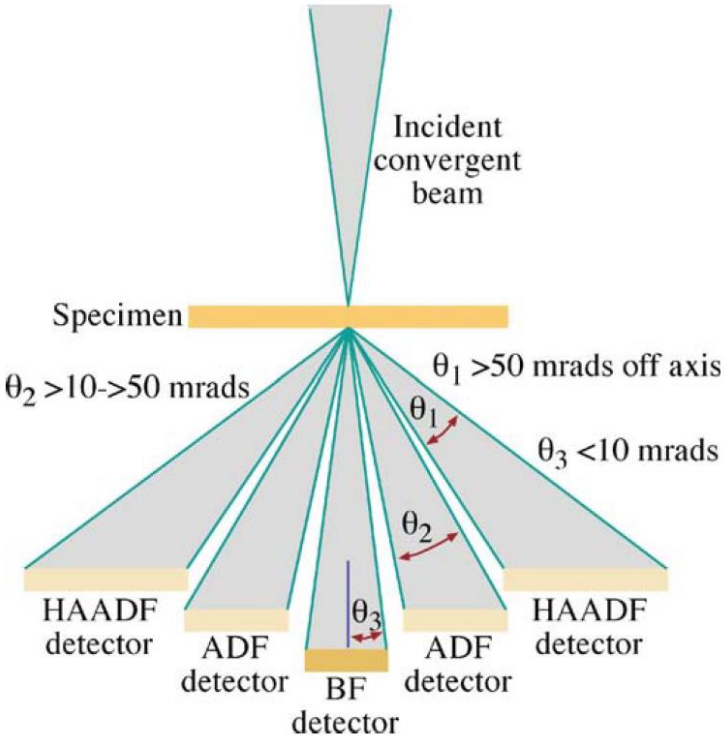

Figure 12. Detector setup for STEM differentiated by scattering angles [122].

A summary of the different S/TEMs used in this work is shown in Table 2.

Table 2. S/TEMs used, relevant parameters, and applications.

Microscope	Location	Specs	Usage
Hitachi H9500 TEM	NFCF, U. Pitt	▪ 100 – 300 kV	▪ 200 – 300 kV ▪ Conventional TEM imaging ▪ SAED
JEOL JEM 2100F S/TEM	NFCF, U. Pitt	▪ 80 – 200 kV ▪ Gatan Image Filter (GIF)	▪ 200 kV ▪ HAADF-STEM ▪ EELS
TEAM 0.5 S/TEM	NCEM, LBNL	▪ 50 – 300 kV ▪ Electron gun monochromator ▪ Probe and image aberration correction (Double-corrected)	▪ 200 kV ▪ HAADF-STEM ▪ EELS
FEI Tecnai F20 S/TEM	NCEM, LBNL	▪ 120 – 200 kV ▪ Electron gun monochromator ▪ GIF	▪ 200 kV ▪ HAADF-STEM ▪ EELS
JEOL JEM 2100F-AC S/TEM	AMCaT Lab, UC Davis	▪ 80 – 200 kV ▪ Probe aberration corrector ▪ GIF	▪ 200 kV ▪ HAADF-STEM ▪ EELS
Hitachi HD2700C STEM	CFN, BNL	▪ 80 – 200 kV ▪ Probe aberration corrector ▪ Gatan Enfina EELS detector	▪ 80 – 200 kV ▪ HAADF-STEM ▪ EELS
FEI Titan3 G2 S/TEM	CEMAS, OSU	▪ 60 – 300 kV ▪ Electron gun monochromator ▪ Image corrector ▪ K2 direct electron detector ▪ GIF	▪ 200 – 300 kV ▪ Monochromated ▪ STEM ▪ EELS

Analogously to light optics, the problem of lens aberrations also exists in electron optics. While the impact of lens aberrations on the image resolution in S/TEM can be reduced by careful microscope operation, they nonetheless create a lower resolution limit in conventional uncorrected microscopes. Aberration-corrected microscopes improve the lower resolution limit by correcting lens aberrations. The most problematic aberration for imaging resolution—and that which is primarily controlled for with aberration correctors—is spherical aberration (C_s). Spherical aberration occurs when the electrons passing through a lens are not all focused to the same focal point because of the spherical nature of the lens, resulting in blurring of fine features. When the C_s-correcting device is placed in the condenser system of lenses (see Figure 11), it is called a probe-corrector. This approach forms a finer electron beam probe and is ideal for STEM. When the C_s-correcting device is placed below the objective lens (Figure 11), it is called an image-corrector. This setup results in better image resolution. An electron gun monochromator uses a Wien filter to reduce the energy spread of the electron emitted by the gun. Using a monochromated beam increases the energy resolution of spectroscopy collected in the TEM such as EELS.

3.3.5 Selected-Area Electron Diffraction (SAED)

Selected-area electron diffraction is a technique performed in TEM that probes the crystal structure of a sample. Like X-ray diffraction, electrons that meet the Bragg condition (Figure 7) in a crystal lattice are diffracted. When electrons pass through a single crystal, the electrons are diffracted to specific angles based on the atomic arrangement (or lattice) in the crystal, forming a regular pattern of spots called a diffraction pattern (DP) (Figure 13a). The pattern of spots formed by diffracted beams is a slice through the reciprocal lattice; i.e. the Fourier transform of the real space crystal lattice. The section of the reciprocal lattice shown in the DP depends on the

orientation of the single crystal. Since the reciprocal lattice is directly related to the real lattice, the symmetry of the real lattice is observed in the DP.

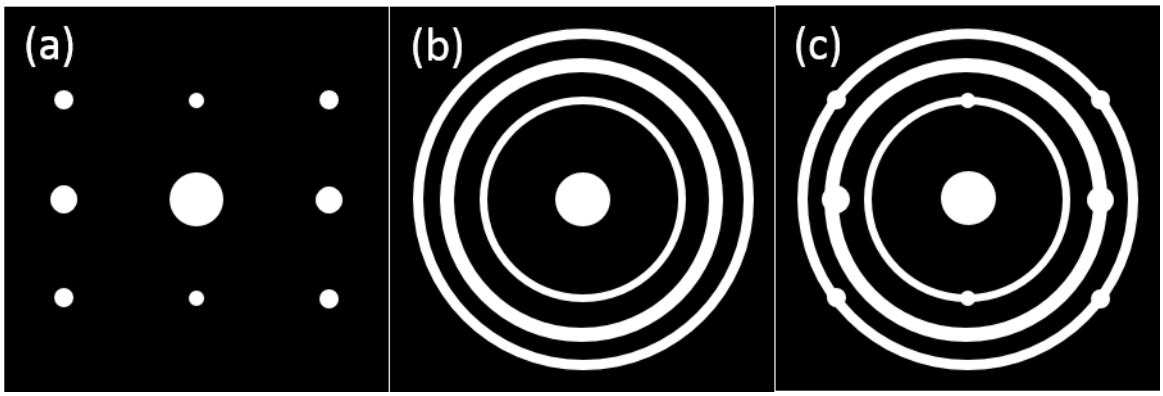

Figure 13. Types of SAED patterns by sample crystallinity. (a) Single-crystal, (b) polycrystalline, and (c) textured polycrystalline.

The central spot in the pattern is called the direct beam and is composed of the electrons that pass through or close to the optic axis, which is usually the majority of electrons. The diffracted spots – all others in the pattern – each correspond to a specific set of lattice planes. For each spot, its distance from the central spot corresponds to the spacing of its corresponding planes, and the relative angles correspond to their orientation. The relative intensity of the spots in the diffraction pattern is a function of the structure factor F of the crystal, described as:

$$F = \sum_{n=1}^{N} f_n \exp\{2\pi \mathrm{i}\,(hx_n + ky_n + lz_n)\} \tag{3.2}$$

Here f_n is the atomic scattering factor for the n'th atom in the unit cell, hkl are the Miller indices of the diffracted reflection (peak), and $x_n y_n z_n$ are the coordinates of the n'th atom in the unit cell. The structure factor is thus dependent on the arrangement (coordinates) of atoms in the unit cell. By indexing the diffraction spots, the symmetry and orientation of the crystal can be determined. When there are many crystals present in the sample with a random distribution of orientations, the

spot pattern becomes a ring pattern (Figure 13b). This is akin to rotating the single crystal about the optic axis, consequently the reciprocal lattice (single crystal DP) is rotated about the direct beam. If the distribution of crystal orientations is non-random, i.e. there is texture present, some spots will be present in the ring pattern (Figure 13c). These spots correspond to crystal orientations that are more heavily represented in the sample.

The technique is called selected-area diffraction because the region of the sample from which the diffraction pattern is formed can be selected using a selected-area aperture (Figure 11). SAED has the advantage over XRD that samples as small as a few hundred nanometers in size can be examined, whereas XRD can only study samples down to the micrometer scale.

Azimuthally averaged line profiles of experimental diffraction patterns were made using the DiffTools [123] plugin for Gatan Digital Micrograph™. The azimuthal averaging procedure is useful to convert a 2D pattern into a 1D line profile that can be easily compared to other SAED profiles. Details of the conversion of experimental polycrystalline SAED patterns to a line profile, in particular the background subtraction, can be found in Appendix B.

3.3.6 Electron Energy-Loss Spectroscopy (EELS) and Energy-Loss Near-Edge Structure (ELNES)

Electron energy-loss spectroscopy is a technique commonly carried out in TEM/STEM where the amount of energy lost by transmitted electrons is detected and used to probe the sample chemistry. When fast electrons interact with a TEM sample, they can transfer energy to the sample through a variety of scattering interactions. While most of the transmitted electrons will be elastically scattered and lose very little energy to the sample, a small fraction of transmitted electrons will lose >50 eV of energy and are considered inelastically scattered. These are called

energy-loss electrons. The electron-sample interaction generates various types of excitation events which are quantized, such as plasmons, phonons, interband transitions and core-electron excitations [124]. During collection, the energy-loss electrons are dispersed according to the amount of energy lost, resulting in a spectrum such as the example in Figure 14. The zero-loss peak (ZLP) is the most intense since this contains the elastically scattered electrons. Peak intensity decreases with energy loss since more energetic interactions are exponentially less likely to occur. "Low-loss peaks" are those that occur within the first 50 eV of the ZLP.

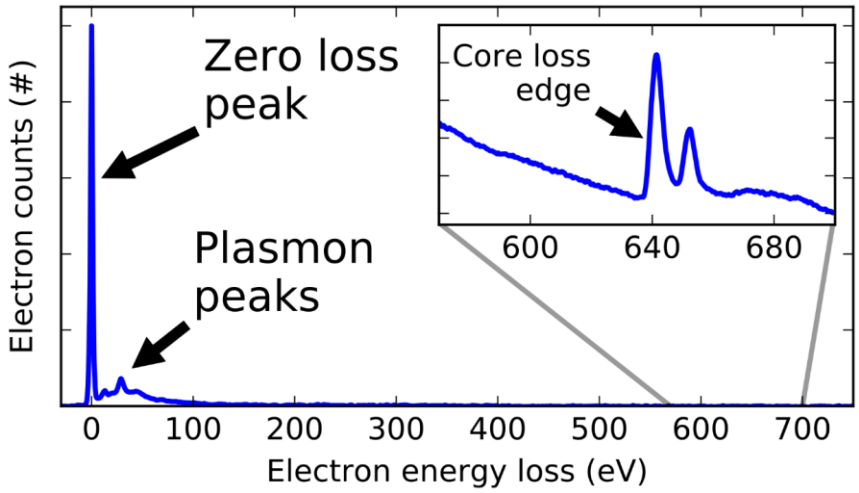

Figure 14. Schematic of energy-loss spectrum.

A core-electron excitation occurs when a fast electron transfers enough energy to an inner-shell electron of an atom in the sample to excite that electron into a normally unoccupied orbital above the valence orbitals. When core-electron excitations occur, the EELS spectra show an edge (core-loss edge) at a characteristic energy loss for a specific element. The characteristic energy loss is determined by the binding energy of the core-electron in an atom of the given element.

Core-loss spectra are referred to by the element and the orbital from which the core-electron is excited. For example, the oxygen-K (O-K) edge occurs at ~520 eV.

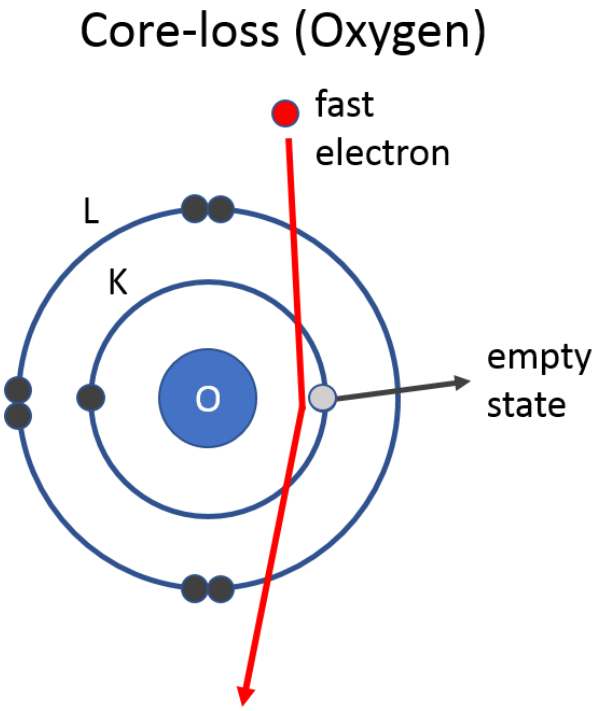

Figure 15. Atomic-level schematic of core-loss event resulting in O-K edge EELS signal.

Provided the sample is thin enough that only one excitation event occurs per transmitted electron (single scattering), the core-loss edge provides information about the chemistry of the materials in the sample, including atomic coordination, bonding, charge transfer and oxidation states. The energy-loss near-edge structure (ELNES) features—those that occur within 50eV of the edge onset—are of particular interest because the fine structure in ELNES reflects the unoccupied local site- and symmetry-projected density of states (LDOS) above the Fermi level. Hence ELNES gives information on the atomic coordination and local electronic structure.

EELS on an aberration-corrected STEM is one of the most effective analytical techniques for characterizing local chemical and electronic properties at the nanoscale due to its exceptionally high spatial resolution. Aberration-corrected STEM-EELS enables the acquisition of EELS at specific features such as interfaces and defects, which provide important atomistic insight about their chemistry.

For the work discussed herein, O-K edge, Al-$L_{2,3}$, Al-K, and Ni-L edge core-loss EELS spectra were collected. A Gatan Ultra-Low-Temperature Double-Tilt (ULTDT) cryo holder was used when performing STEM-EELS to minimize electron beam damage to the sample, since γ-Al_2O_3 is highly beam sensitive and is thus rapidly damaged by the focused high-energy electron beam in STEM (See Chapter 5.0 for an in-depth discussion). The cryo holder uses liquid nitrogen to cool the sample to cryogenic (~77 K) temperatures. EELS spectra were generally acquired as spectral images (a spectrum acquired at each pixel of the STEM image). The core-loss edges were background subtracted using a power law fit in Digital Micrograph™. Absolute edge onsets were calibrated using the position of the ZLP. Since the samples were very thin, such that plasmon scattering was almost nonexistent, no additional deconvolution was performed on the core-loss spectra before analysis.

3.4 Computational Tools

3.4.1 Density Functional Theory (DFT)

Density functional theory (DFT) is a computational modelling method used to investigate the electronic and nuclear structure of systems of interacting particles such as atoms and molecules.

Functionals (i.e. a function of a function) of electron density, which is spatially dependent, are used to determine the properties of a system containing many electrons. DFT calculations enable the prediction of material properties and behavior from quantum mechanical first principles (*ab initio*).

Planewave DFT calculations were carried out using the Vienna Ab Initio Simulation Package (VASP). The generalized gradient approximation was employed with the exchange-correlation function of Perdew, Burke and Ernzerhof (PBE). The electron-nuclear interactions were represented in terms of projected augmented waves (PAW). A 400 eV planewave cutoff was used. Validation of the computational framework was done by checking that the energy cutoff, k-grid, and energy tolerances were sufficient to converge energy differences to less than 1 meV. Specific parameters used for individual studies can be found in the respective appendices.

3.4.2 EELS Simulation

Under the single scattering approximation, fine structure in ELNES reflects the unoccupied local site- and symmetry-projected density of states (LDOS), which can be calculated. The local coordination of atoms, bonding, charge transfer, and oxidation state can then be inferred from the reflection of the LDOS [125-127].

There are two main *ab initio* approaches for calculating EELS spectra [126, 128]. The traditional method is the band-structure (BS) method, which is based on calculating the electronic band structure of periodic crystalline materials in reciprocal space. The other is the real-space multiple scattering (MS) method, which does not require periodicity and is calculated in real space with a finite cluster of atoms.

In the MS formalism, core-level EELS spectra are calculated using Fermi's golden rule for the initial and final states of the electron transition. The sum over final states is carried out using the real space Green's function. The electron transitions are also governed by dipole-dipole transition rules, which are included in the Green's function formalism. The final state rule is used to treat the presence of a core-hole in the final state but not the initial state, meaning that the initial states should be the ground state while the final state should be calculated including a screened core-hole. Finally, the calculated DOS is converted to a simulated EELS spectrum using the given microscope parameters. In FEFF9, atomic potentials can be calculated self consistently, full multiple scattering with the given atomic cluster is used, and the core-hole screening can be treated directly.

Near-edge EELS simulations were carried out using the FEFF9 program. FEFF9 is an *ab initio* MS code used to calculate various excitation spectra including EELS [28, 129]. The inputs needed for the program to calculate EELS spectra are the structure (in the form of a structure file) and the calculation parameters, which include the microscope parameters. The input file used for the calculations includes the description of the cluster and control cards (capitalized in the input file) that describe the parameters to be used. An annotated example input file is included in Appendix A for reference. FEFF calculations are performed in real-space and do not require any symmetry, thus it is particularly suited for calculations of aperiodic systems such as interface models and highly disordered bulk models. A concise yet practical description of the EELS simulation procedure using FEFF is given by Moreno et al. [128].

Candidate structures used for EELS calculations were generally first optimized using DFT. FEFF simulates the EELS spectrum for a single atom at a time, so simulated EELS for the bulk structural models were calculated by performing a weighted average of the simulated EELS from

each nonequivalent scattering atom. The specifics of the EELS simulations for each part of the project are discussed in the respective chapters.

3.4.3 Electron Diffraction Simulation

Kinematical diffraction simulation was used to create the simulated diffraction profiles and patterns. Assuming only a single elastic scattering event occurs for each electron that interacts with the sample (kinematic assumption), the relative intensity of diffracted reflections can be calculated using the structure factor equation shown in Equation 3.2. The reflection intensity is directly proportional to the structure factor, but to convert the structure factor to the reflection intensity, several constants such as reflection multiplicity and Lorentz factor must be included in the calculations, all of which are done automatically in the simulation program.

The kinematical assumption was confirmed by the observation of blank discs in the convergent beam electron diffraction (CBED) patterns obtained from the cross-sectional γ-Al_2O_3 TEM samples. In CBED, a convergent beam is used rather than the parallel beam used in SAED. This results in a pattern of bright discs rather than spots. The presence of fine structure in the discs is due to dynamical scattering, therefore the absence of fine structure indicates minimal dynamical scattering.

Simulated electron diffraction patterns and data were generated using the CrystalMaker®, CrystalDiffract®, and SingleCrystal® software suite (CrystalMaker Software Ltd, Oxford, UK, http://crystalmaker.com). CrystalDiffract® was used to simulate polycrystalline diffraction line profiles for the considered models. SingleCrystal® was used to calculate reflection intensities and simulate the spot patterns for the considered models. In both programs, the structure model and diffraction parameters including microscope parameters are the required inputs.

4.0 Characterization of the Model γ-Al_2O_3

4.1 Single-Crystal γ-Al_2O_3 Thin Film Properties: Surface Orientation, Surface Roughness, Thickness, and Composition

The (111) orientation of the single-crystal γ-Al_2O_3 thin film was confirmed by the presence of only the γ-Al_2O_3 (222) peak in addition to the NiAl (110) substrate peak in θ/2θ XRD, as shown in Figure 16. The shoulder on the NiAl (110) peak is due to Cu $K_{\alpha 2}$ radiation from the Cu source. The root mean square (RMS) surface roughness of the γ-Al_2O_3 was determined using AFM with a 2 nm coated-Al cantilever tip and a 20 x 20 μm scan area. The RMS roughness differed from sample to sample but was generally within the range of 2 – 10 nm. It is important to keep the surface roughness the same or less than the size of the deposited Pt nanoparticles to ensure enough flat support surfaces for analysis.

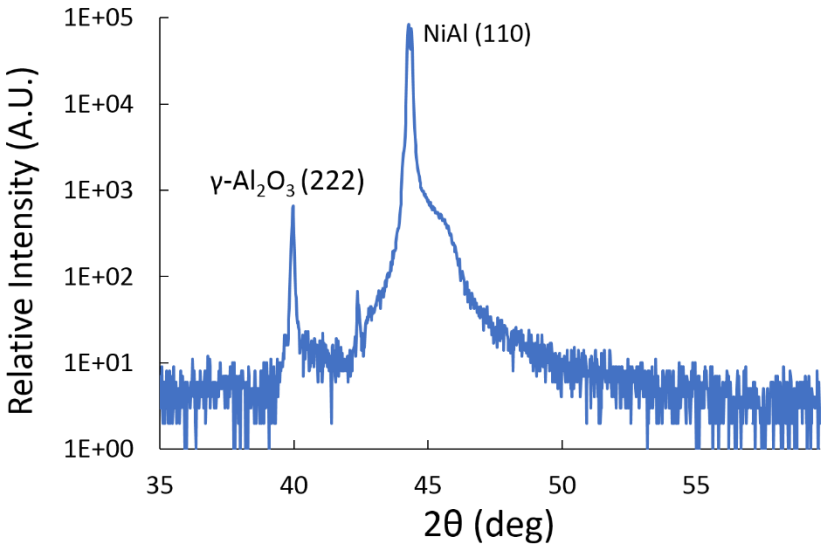

Figure 16. θ/2θ XRD of the γ-Al_2O_3/NiAl (110) showing the γ-Al_2O_3 (222) peak.

FIB was used to mill a cross-section and check the thickness of the γ-Al_2O_3 (111) layer (Figure 17). The γ-Al_2O_3 (111) layer was about 80-130 nm thick for NiAl oxidation conditions of 850°C and 1 hr.

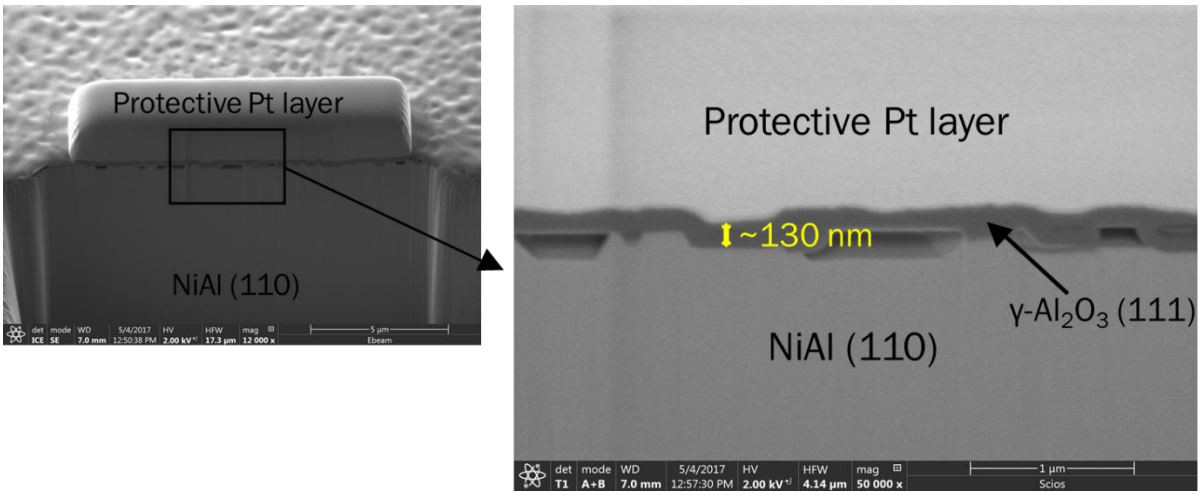

Figure 17. SEM image of cross-section of γ-Al_2O_3 (111)/NiAl (110) made using FIB.

A cross-sectional TEM sample of the NiAl (110)/γ-Al_2O_3 (111) was then made using FIB. To confirm that the oxide layer was not a Ni-spinel or other Ni oxide, an EELS line scan was acquired across the NiAl/γ-Al_2O_3 interface as indicated on the high-angle annular dark-field (HAADF)-STEM image of the sample in Figure 18a. The EELS line scan was acquired on a JEOL 2100F TEM/STEM operated at 200kV with a Gatan Image Filter. The O-K and Ni-L edges of the EELS spectra from the numbered positions were extracted and plotted in Figure 18b and Figure 18c, respectively. The spectra are offset vertically for clarity. The positions of the edges are indicated with dashed vertical lines. At points 1 and 2 on the NiAl layer, no O-K edge signal was observed but there was a strong Ni-L edge signal. The Ni-L signal remained visible until point 3, at the NiAl/Al_2O_3 interface, which is where the O K edge signal began to appear. Upon crossing

the interface into the Al_2O_3 (at points 4 and 5), the Ni-L edge signal disappeared while a strong O-K edge was observed. These results confirm the formation of aluminum oxide only with no nickel detected.

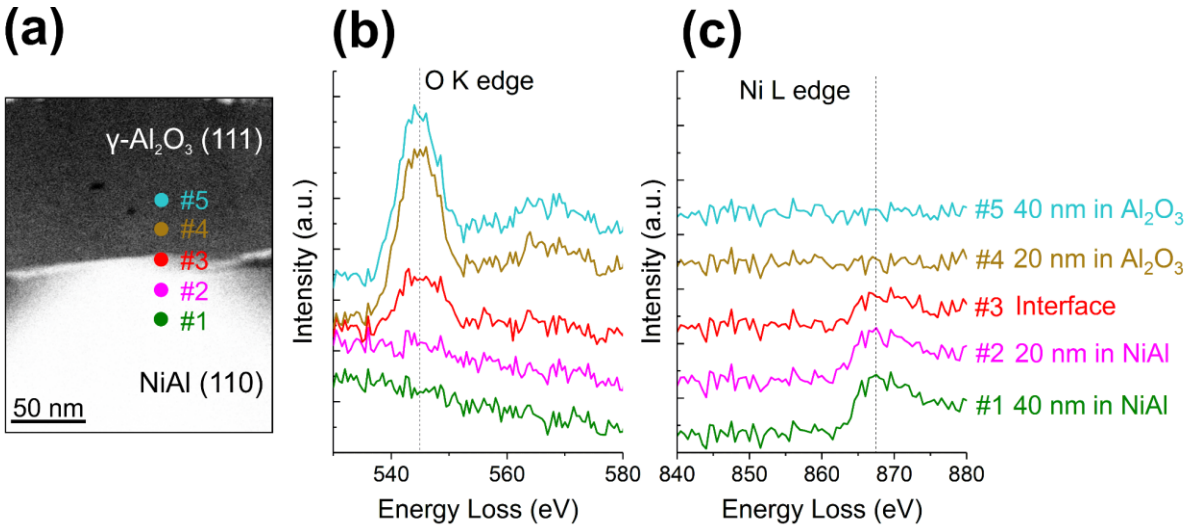

Figure 18. (a) HAADF-STEM image of the NiAl/γ-Al_2O_3 cross-section sample showing where the EELS line scan was acquired. EELS spectra from each of the positions numbered 1 through 5 along the line scan are shown in (b) and (c).

4.2 Polycrystalline γ-Al_2O_3

A powder XRD pattern of a commercial γ-Al_2O_3 nano-powder (Inframat Advanced Materials, γ-Al_2O_3 Nano Powder, 99.99% purity) is shown for reference in Figure 19. The peaks are notably broad, which is normal for γ-Al_2O_3, with some additional broadening caused by the small crystallite sizes of the nano-powder (less than 20 nm).

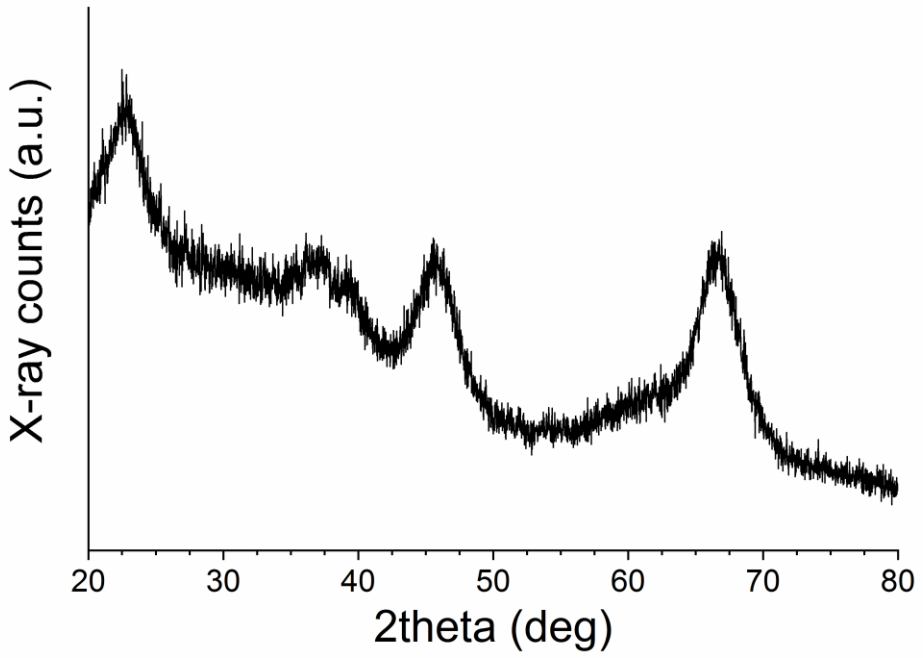

Figure 19. Powder XRD pattern acquired from commercial γ-Al_2O_3 nano-powder.

SAED from the textured polycrystalline γ-Al_2O_3 thin film was compared to SAED from the commercial γ-Al_2O_3 nano-powder (Figure 20). The diffraction patterns were compared using the ring ratio method for cubic crystal structures and shown in Table 3. The ring ratio method compares the ratios of the radius (R) of one ring to the previous ring. This approach negates the effect of potentially different calibrations of the diffraction pattern absolute scale due to the diffraction patterns being acquired at different times or on different machines. The comparison shows an excellent match between the two, confirming that the sample prepared by NiAl oxidation is in fact γ-Al_2O_3. Furthermore, the azimuthally averaged line profiles of the diffraction patterns shown in Figure 20 (b) and (d) are shown in Figure 21, corrected for differing camera calibrations. The peak intensities are nearly identical, further confirming the sample as polycrystalline γ-Al_2O_3.

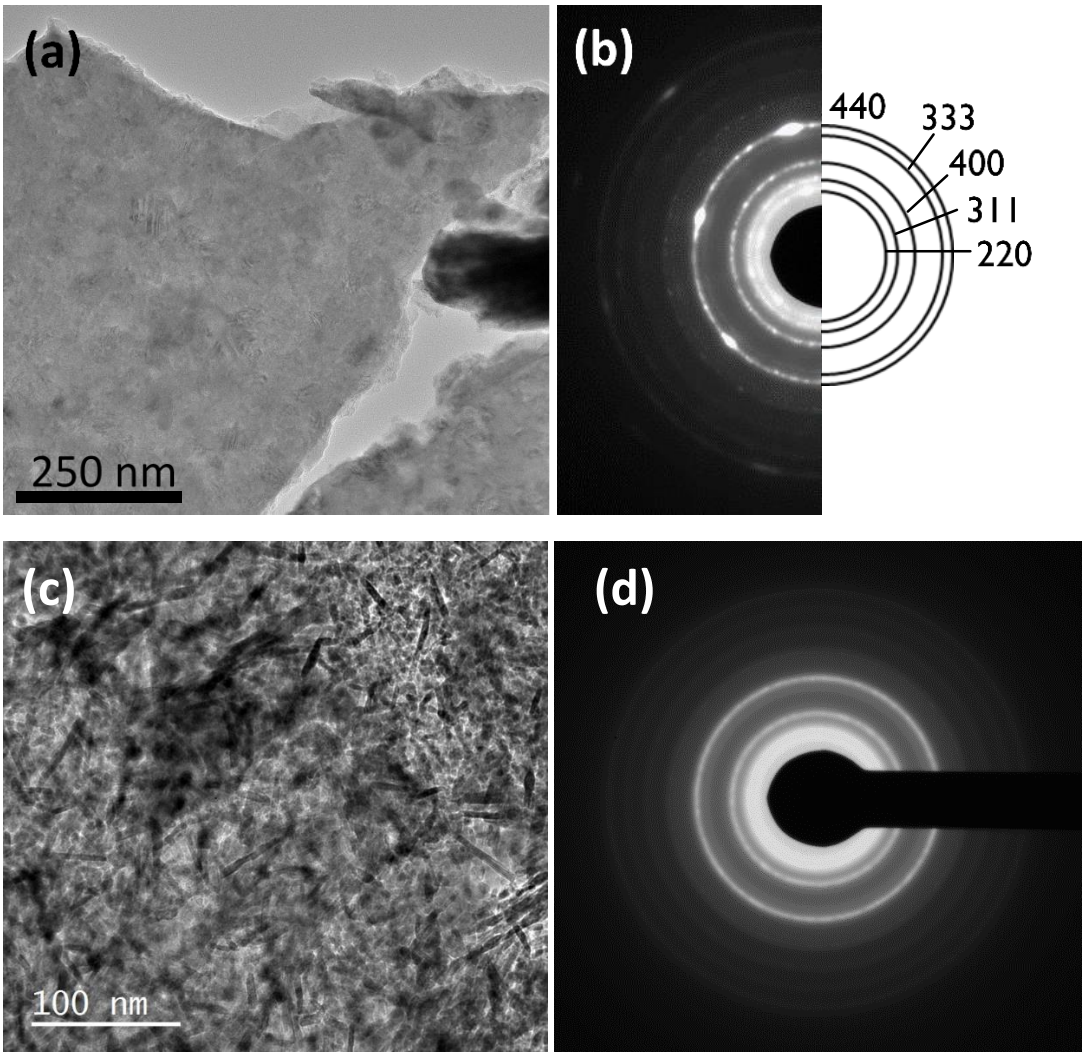

Figure 20. (a) Textured polycrystalline γ-Al_2O_3 film prepared by NiAl oxidation and (b) corresponding SAED pattern indexed based on the cubic spinel. (c) Commercial γ-Al_2O_3 nano-powder and (d) corresponding SAED pattern.

Table 3. Comparison of SAED patterns of (111) textured polycrystalline γ-Al_2O_3 film and the commercial γ-Al_2O_3 nano-powder.

FCC hkl	Film R (nm^{-1})	Powder R (nm^{-1})	Film ring ratios	Powder ring ratios	% difference (%)
400	4.962	5.037	1.239	1.243	0.283
333	6.463	6.586	1.302	1.307	0.384
440	6.991	7.148	1.081	1.085	0.335
622	8.161	8.358	1.167	1.169	0.164

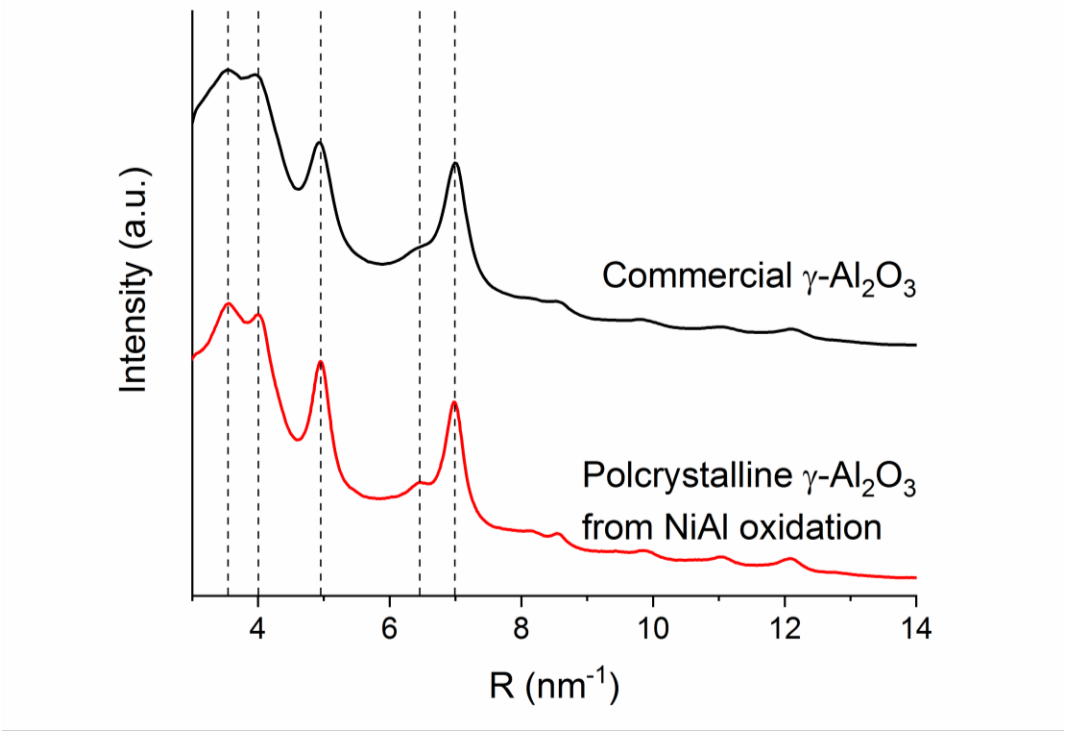

Figure 21. Comparison of azimuthally averaged profiles from the polycrystalline γ-Al_2O_3 film prepared by NiAl oxidation and the commercial γ-Al_2O_3 nano-powder.

A cross-sectional TEM sample was made using FIB. Bright-field TEM was used to determine the film thickness (Figure 22a) of about 150 nm. The corresponding dark-field TEM image of the cross-sectional sample revealed columnar grains (Figure 22b). Dark-field TEM from the top-down view (Figure 22c) was used to estimate the average and maximum grain sizes of 50 nm and 150 nm respectively.

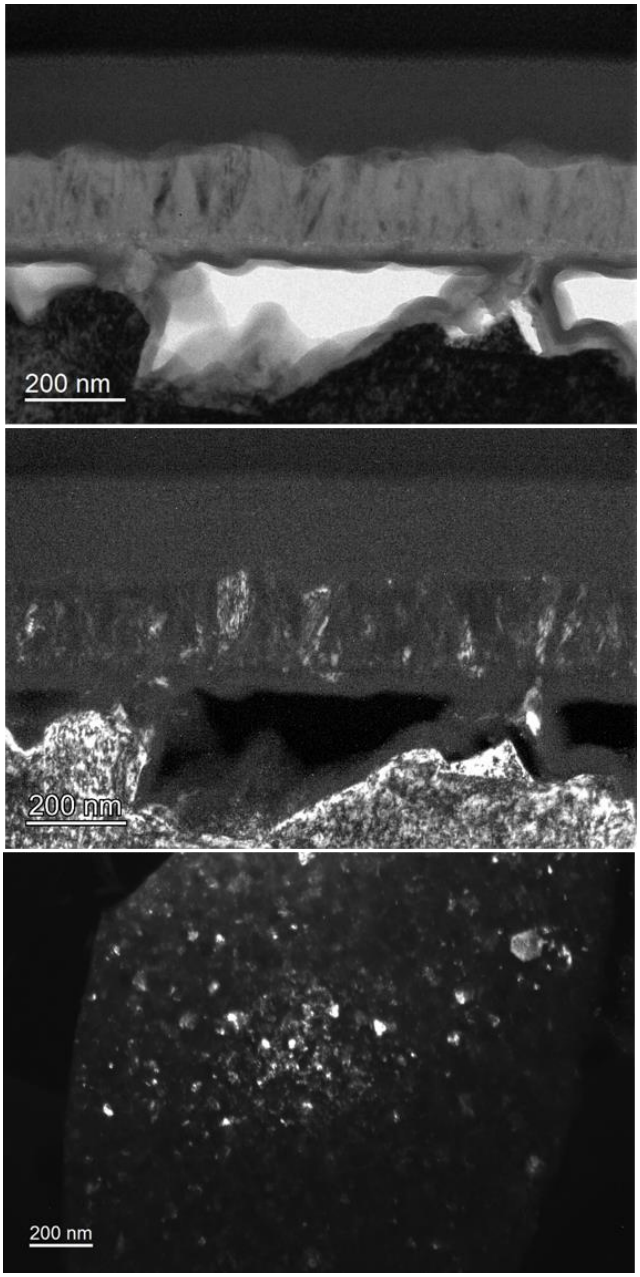

Figure 22. (a) Cross-sectional bright-field TEM image of polycrystalline γ-Al_2O_3 thin film on NiAl, with characteristic voids seen at the interface. The top two layers are amorphous Pt used to protect the sample surface during FIB milling. (b) Corresponding dark-field TEM image of the polycrystalline γ-Al_2O_3 film cross-section formed using a section of the (111) ring. (c) Dark-field TEM image of the scraped polycrystalline γ-Al_2O_3 thin film formed using a (111) texture spot.

4.3 Model γ-Al_2O_3 Cross-Sectional TEM/STEM Samples

Cross-sectional TEM samples were then made using a FIB as previously described. The cross-sectional TEM samples were characterized using TEM and STEM. Example S/TEM images are shown in Figure 23 and Figure 24. The platinum nanoparticles deposited for the interface structure case study can be observed on the single-crystalline γ-Al_2O_3 surface.

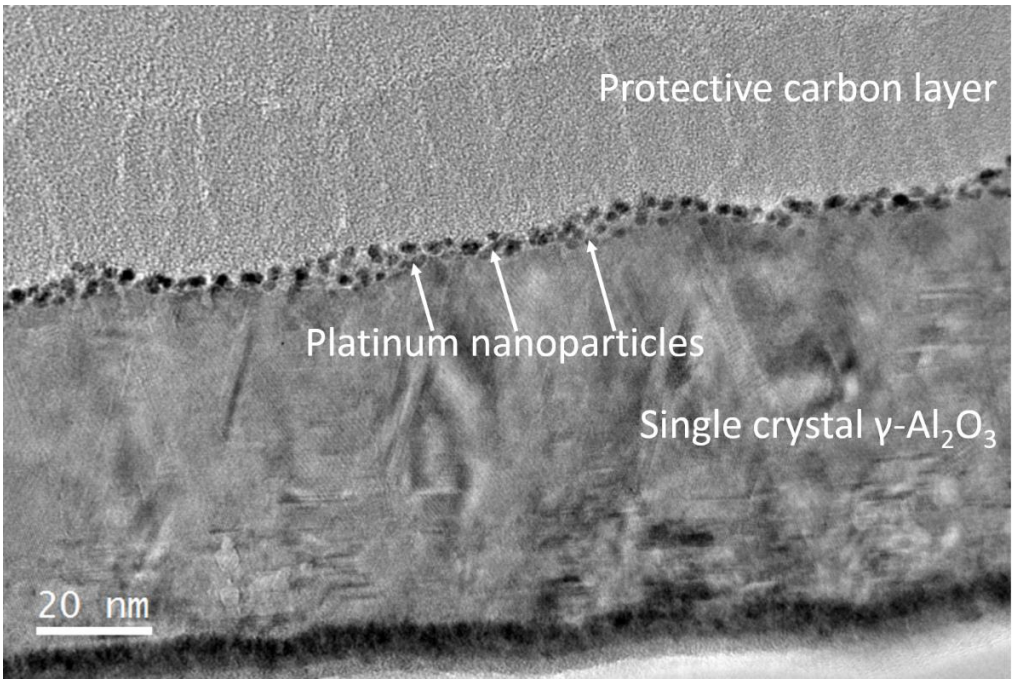

Figure 23. TEM image of cross-sectional Pt/γ-Al_2O_3 sample.

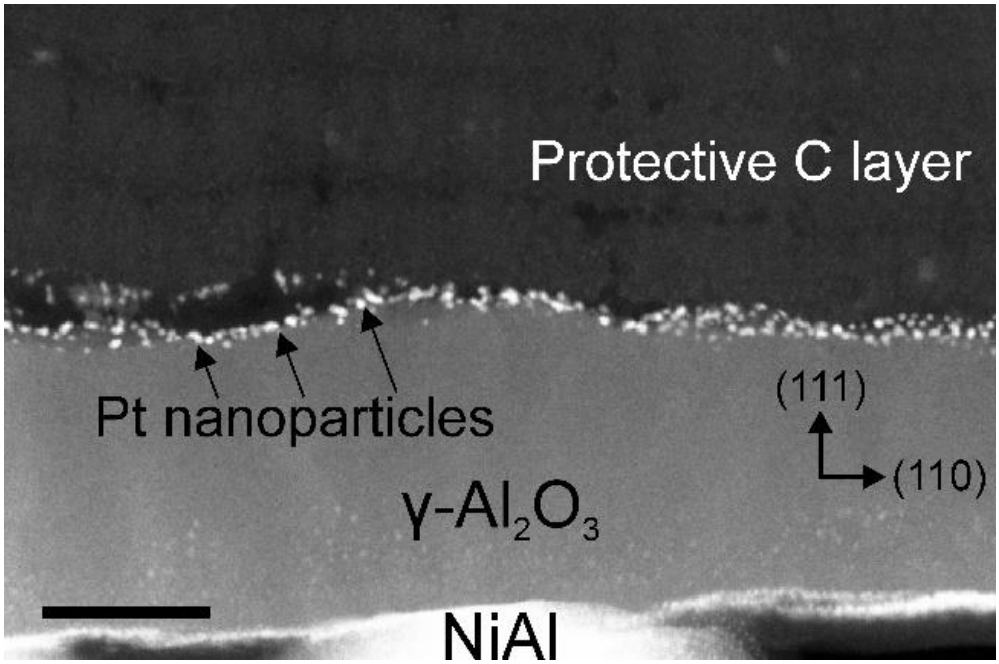

Figure 24. Medium-angle annular dark-field (MAADF) STEM image of the cross-sectional Pt/γ-Al_2O_3(111) model catalyst. Scale bar = 50 nm.

5.0 Electron Beam Damage in γ-Al_2O_3 and Suppression using Cryo-STEM/EELS

The contents of this chapter will be published in:

H.O. Ayoola, C.-H. Li, S.D. House, C.S. Bonifacio, K. Kisslinger, J. Jinschek, W.A. Saidi, J.C. Yang, Origin and Suppression of Beam Damage-Induced Oxygen-K Edge Artifact from γ-Al_2O_3 using Cryo-EELS, Ultramicroscopy, Accepted.

5.1 Preamble

In the preceding chapters, high-resolution EELS has been established as a major tool for several of the key objectives of this research project. However, γ-Al_2O_3 is highly susceptible to beam damage by the focused electron probe [130], and this issue must be addressed before reliable high-resolution EELS can be acquired. Beam damage occurs in inorganic materials primarily by radiolysis, knock-on damage (sputtering), and electrostatic charging mechanisms [131-134]. These mechanisms can potentially alter the structure and chemistry of the material locally [133], which in turn can create artifacts in the EELS spectra that complicate or mislead data interpretation [135]. The presence of damage-induced artifacts has been noted to obscure other intrinsic EELS features of oxides, thus hindering analysis [136, 137].

Ordinarily, spectrum acquisition time or electron dose could be reduced to minimize the beam damage; however, this also has the unintended consequence of reducing the amount of signal collected and reducing spectrum quality, which limits accurate analysis of fine spectral features. Cryo-STEM—STEM experiments performed using specialized holders or microscopes that keep

the sample at cryogenic temperature—is a promising solution, with beam damage suppression having been demonstrated in some oxides using cryo-EELS [138, 139].

The oxygen-K edge EELS of beam-sensitive oxides including γ-Al_2O_3 is affected by electron beam damage in a well-recognized way, often through formation of a pre-edge peak. A pre-edge peak observed ~9 eV below the main O-K edge peak in magnesium aluminate ($MgAl_2O_4$) spinel was attributed to the formation of free O_2 by beam damage [127, 140]. Similarly, an O-K pre-edge peak at 531 eV was also seen in EELS spectra acquired from beam-damaged α-alumina [136] and attributed to O_2 gas bubbling under the focused electron beam.

Although these previous studies point to the likely origin of the damage-induced pre-edge peak in beam-sensitive oxides, the exact source in γ-Al_2O_3 has not been explored. The aim of this chapter is to elucidate the beam damage mechanisms in γ-Al_2O_3 as well as evaluate the potential of using cryo-EELS to suppress electron beam damage in γ-Al_2O_3. Single-crystal γ-Al_2O_3 and both room-temperature and cryo-temperature high-resolution STEM-EELS are used to systematically study beam damage-induced artifacts in the Al-$L_{2,3}$ and O-K edge ELNES of γ-Al_2O_3. Subsequent correlative analysis of the experimental data with multiple scattering EELS simulations is employed to determine the likely atomistic source of the O-K pre-edge peak seen in beam damaged γ-Al_2O_3.

5.2 Study-Specific Methods

5.2.1 Sample Preparation and Characterization

Monochromated EELS data were acquired from the cross-sectional single-crystalline γ-Al_2O_3 samples on an FEI Titan3^{TM} G2 60-300 S/TEM operated at 300 kV in parallel EELS mode, with collection and convergence angles of 18 and 10 mrad respectively. A Gatan Cryo-Holder cooled using liquid nitrogen to a working temperature of -186°C was used for the cryo experiments. EELS spectra were collected either as time series during the hole drilling, or as spectrum images after the hole drilling. EELS time series at cryo temperature were collected with an exposure time of 1s, while all other spectra were acquired with exposure times of 0.5 s. Energy resolution calculated from the full-width half-maximum (FWHM) of the ZLP was about 0.3 eV in all acquired spectra.

5.2.2 Computational Details

EELS spectra simulations were carried out using FEFF9 [28, 128]. Self-consistent field (SCF) potentials were calculated with a 6 Å cluster while full multiple scattering (FMS) was employed with an 8 Å cluster. The final state rule approximation was used to treat core-hole effects. The DFT calculations were carried out using VASP [141, 142] in conjunction with the PBE [143] exchange-correlation functional and Tkatchenko-Scheffler [144, 145] van der Waals corrections. Other computational parameters are described in Appendix B.1.

The γ-Al_2O_3 models containing surface O-O dimers were derived from the spinel-based models developed by Acikgoz et al [146]. Each model was the result of removing hydrogen from

a different surface site before optimizing the structure. The bulk γ-Al_2O_3 model described by Digne et al. [78] was used to generate the drilled hole model.

5.3 Results and Discussion

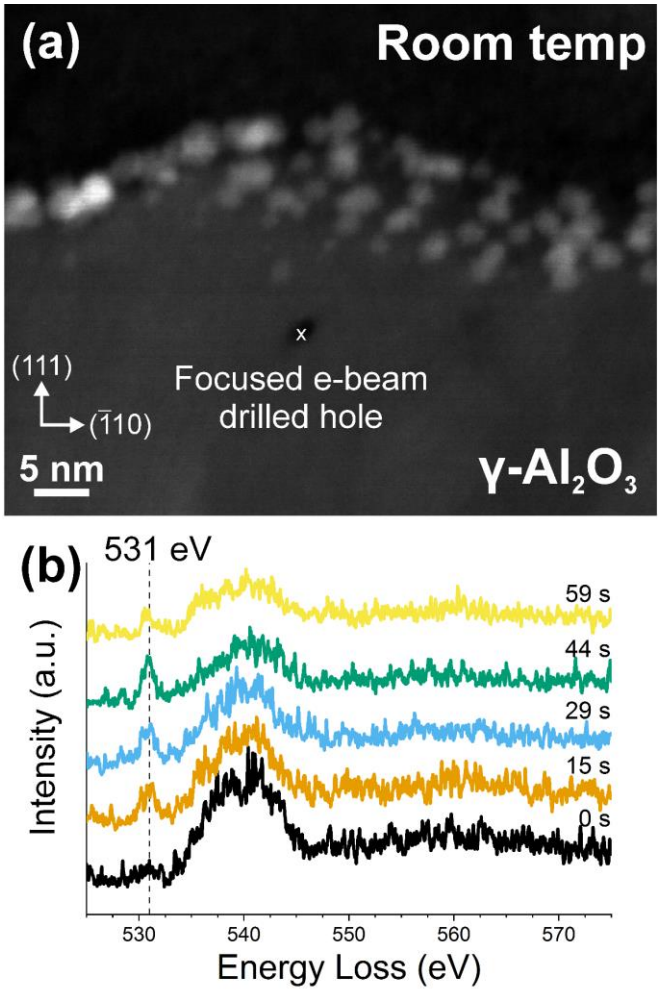

Figure 25. (a) Dark-field STEM image of γ-Al_2O_3 sample with the position of the hole drilled by the focused electron beam marked with an x. (b) Time-resolved O-K edge EELS spectra acquired at room temperature during e-beam hole drilling. The characteristic e-beam damage-associated pre-edge peak at 531 eV was marked with a dotted line.

A dark-field STEM image of the cross-sectional sample is shown in Figure 25a. The Pt nanoparticles seen in Figure 25 and Figure 26 were deposited on the sample for the study in Chapter 8.4 and play no role in the experiments reported in this chapter. All EELS data were collected within the γ-Al_2O_3 only, sufficiently far away that the Pt could have no effect on the data. The TEM cross-section is covered by a carbon layer deposited during the FIB lift-out process. A hole has been drilled in the γ-Al_2O_3 at the position marked with an "x" using the focused electron beam at room temperature (RT). During the hole drilling, an O-K edge EELS time series was acquired and is shown in Figure 25b. The characteristic O-K edge peak is seen, with a pre-edge peak also manifesting at the marked and labeled 531 eV position. The pre-edge peak intensity increases, reaches a maximum intensity, and then decreases with time during the hole drilling.

As can be seen in the O-K edge EELS time series displayed in Figure 25b, the intensity of the O-K pre-edge peak changes during the hole drilling. At the beginning of the focused beam experiment, the pre-edge peak is barely visible, since the damage has only just begun and is still minimal. 15 seconds later, the pre-edge peak intensity has increased to almost its maximum, highlighting the rapid damage that occurs in such a beam-sensitive material at RT. By 44 seconds, the pre-edge peak appears to be at its maximum intensity, almost at the level of the main O-K edge peak, which has itself begun to decrease in intensity due to loss of material at the point of the focused e-beam consistent with hole drilling. By 59 seconds, the intensity of the pre-edge peak has begun to diminish. The transient nature of the beam damage associated pre-edge peak has been observed in previous EELS experiments in other oxides [140, 147] and is consistent with the formation of O-related phenomena that then escape the sample environment such as O_2 gas or bubbles, as has been proposed for complex oxides [136, 140].

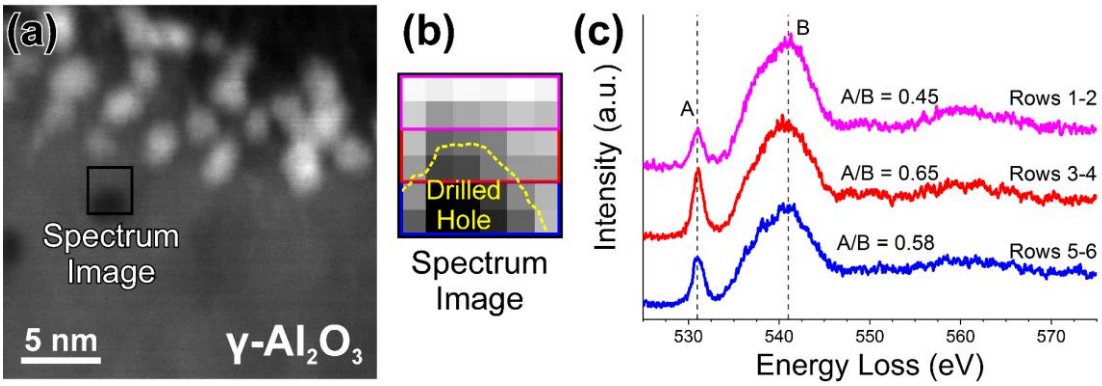

Figure 26. (a) Dark-field STEM image of γ-Al_2O_3 sample after hole drilling at room temperature. An EELS spectrum image, marked by the box, was acquired around the hole edge. (b) Close-up of spectrum image showing individual pixels, each containing an EELS spectrum. The rough edge of the drilled hole is marked with the dotted line. The O-K edge EELS spectra in the pixels within each colored box were summed and displayed in (c). The relative intensity of the pre-edge peak was calculated for each summed spectrum.

After the RT hole drilling, an EELS spectrum image was acquired also at RT from the region around the hole edge. A dark-field STEM image of the cross-sectional sample with a drilled hole in the γ-Al_2O_3 is shown in Figure 26a, with the area of spectrum image acquisition marked with the box and labeled. The close-up of the EELS spectrum image is shown in Figure 26b. Each pixel contains an EELS spectrum corresponding to that position. The edge of the hole is marked using the dotted line. The EELS spectra from the pixels in each box were summed and are plotted in Figure 26c. The pre-edge peak at the same 531 eV energy as seen in Figure 25 is also present. The ratio of the intensity of the pre-edge peak in each summed spectrum relative to the main peak (A/B) is shown. The intensity of the pre-edge peak is higher in the summed spectrum from rows 3-4, which corresponds mostly to the edge of the hole, as shown by the calculated intensity ratio. The intensity of the summed spectrum from rows 5-6 is second highest; this area of the spectrum

image encompasses a small section of the hole edge. The summed spectrum from rows 1-2 (that do not overlap with the hole) shows the lowest intensity pre-edge peak.

The summed spectra from regions around the edge of the drilled hole shown in Figure 26c all show the pre-edge peak caused by beam damage. However, the spectrum from rows 3-4, which contains mostly the area around the hole perimeter, shows the highest pre-edge peak intensity as confirmed by the intensity ratio. It is important to note that the spectra in each pixel in Figure 26b were collected with a 0.5 s acquisition time, during which the liberation of O_2 gas would not be expected to generate as intense a pre-peak—particularly considering the pre-peak has a similar intensity to that in Figure 25b after 15 s of continuous exposure. This suggests that a significant contribution to the O-K pre-edge peak is an O-related structure that is more abundant on the perimeter of the surfaces formed by the beam damage, in addition to the liberation of free O_2 gas.

Additional evidence of the damage-induced surface O species has been previously reported. EFTEM was used to show that the damage-induced pre-edge peak signal around a hole drilled in amorphous alumina was primarily localized to the hole edge [148]. Prior study of ionization damage by Cazaux has suggested that radiolysis damage occurs on the sample surface first and progresses toward the bulk since electrons associated with surface atoms are less strongly bound [149]. These prior studies support the explanation that O species causing the pre-edge peak are found primarily on the beam-damaged surfaces. The transient nature of the pre-edge peak in Figure 25b can therefore be explained thusly; with the pre-peak intensity correlated to the perimeter of the drilled hole, the pre-peak intensity increases as the size of the hole increases, eventually reaching a maximum and diminishing thereafter as the O_2 species on the surface are removed by the electron beam, perhaps as O_2 gas or bubbles.

It is important to consider the potential effect of scattering delocalization on the spatial resolution of the EELS spectrum images. Under the single scattering assumption, the delocalization due to inelastic scattering which is relevant for core-loss EELS was calculated using the formula provided by Egerton [150]:

$$(d_{50})^2 \approx \left(0.44\lambda/\theta_E^{3/4}\right)^2 + (0.52\lambda/\beta)^2 \quad (5.1)$$

where d_{50} is the diameter containing 50% of the inelastically scattered electrons, $\theta_E \approx E/2E_0$ with E being the core-loss energy and E_0 the primary beam energy, and β is the EELS collection angle. The calculation gives an inelastic scattering delocalization diameter of 0.18 nm, which is significantly smaller than the pixel size. Based on these calculations, it is safe to conclude that delocalization does not significantly affect the EELS analyses in this study.

The spectrum image in Figure 26b also shows that the damage is detected not only in the area directly impinged upon by the beam, but also radiates outward from the point of the focused beam. The STEM image shows reduced intensity just outside the hole perimeter relative to the pristine γ-Al_2O_3, indicating material loss. Summed spectra from rows 1-2 which do not include the drilled hole still show the pre-edge peak caused by beam damage, albeit at a lower intensity. This indicates that significant radiation damage that modifies the structure of the material can occur in the vicinity of the electron beam just outside the volume of material being directly probed by the beam. While all the main damage mechanisms can have long-range effects, radiolysis is expected to be the primary long-range mechanism since secondary electrons released by the initial beam interaction carry much of the transferred energy to then interact with further atoms in the sample [131, 151]. Also note that reducing the accelerating voltage to 80 kV did not prevent the formation of the pre-edge peak (Appendix Figure 26).

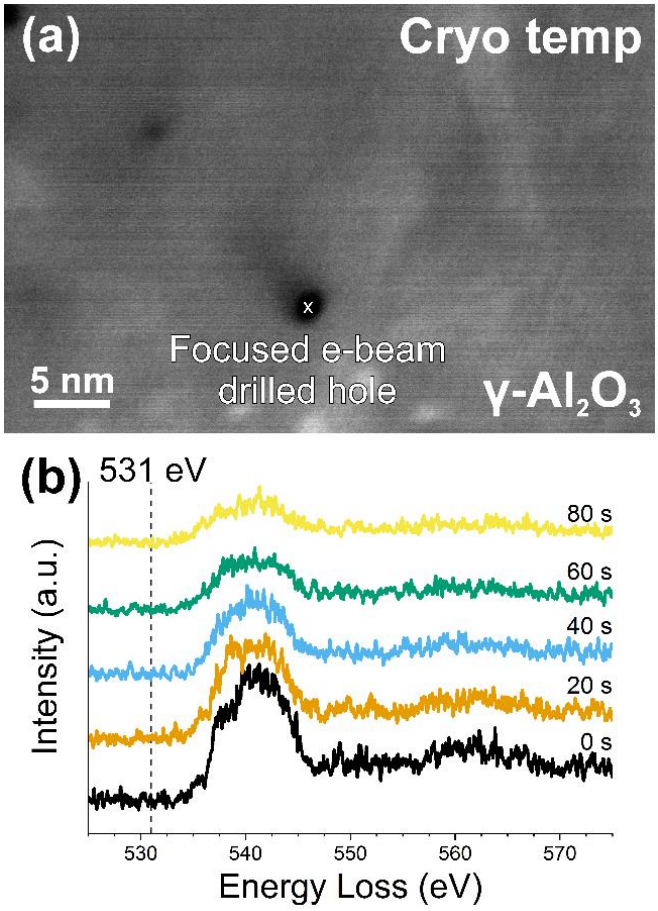

Figure 27. (a) Dark-field STEM image of γ-Al_2O_3 sample with the position of the hole drilled by the focused electron beam marked with an x. (b) Time-resolved O-K edge EELS spectra acquired at cryo temperature during e-beam hole drilling. The position of the characteristic damage-associated pre-edge peak at 531 eV is marked with the dotted line.

The hole drilling experiment was repeated in a new area of the cross-sectional sample, this time at cryo temperature (CT). The dark-field STEM image showing the drilled hole marked with an "x" in the γ-Al_2O_3 is shown in Figure 27a. An O-K edge EELS time series was also acquired during the hole drilling and is displayed in Figure 27b. No pre-edge peak was observed at any point during the CT hole drilling.

Figure 27 depicts a similar hole drilling experiment as the previously discussed, but at CT. The CT experiment proceeded in the same way as the RT experiment; after about 60 seconds of focusing the electron beam at a point, a hole was drilled in the γ-Al_2O_3. In this case however, there was no pre-edge peak seen in the O-K edge EELS timeseries acquired during the hole formation. The spectrum image acquired around the hole edge in Figure 28 also confirms the lack of an O-K pre-edge peak. This finding confirms that operating at CT suppressed the formation of the surface feature that produces the pre-edge peak.

Since no pre-edge peak is seen at CT despite visible hole drilling, it is proposed that the source of the pre-edge peak is primarily a consequence of radiolytic processes, as has been previously suggested [130, 152]. Interestingly, the beam damage induced O-K pre-edge peak in a similar oxide was shown to have a dose-rate dependent threshold [147]. Here however, the dose rate is the same for both the RT experiment where the pre-edge peak is seen and the cryo experiment where no pre-edge peak is seen, suggesting an independent temperature effect in addition to the dose-rate effect. Operating at CT appears to suppress radiolytic beam damage as expected [131], while both knock-on damage and electrostatic charging which would be dose-dependent [132, 148] still occur. This would explain why a hole is still drilled by the beam at CT, confirming the observations of Humphreys et al [148, 153].

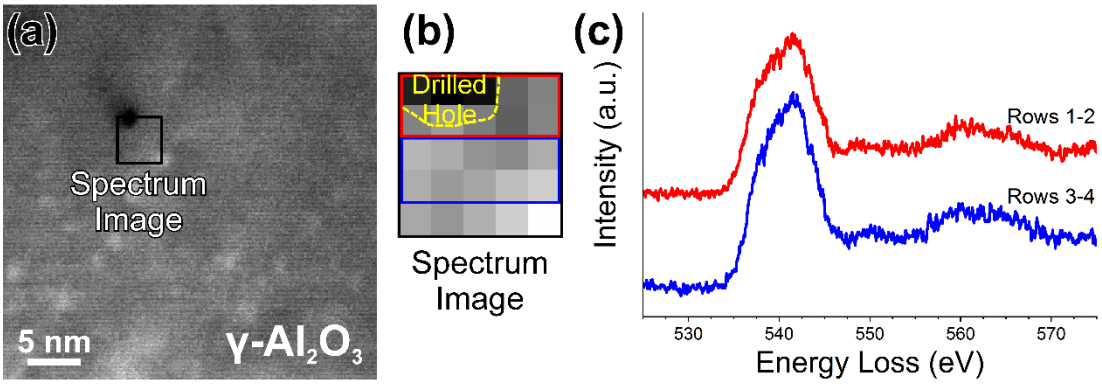

Figure 28. (a) Dark-field STEM image of γ-Al_2O_3 sample after hole drilling at cryo temperature. An EELS spectrum image, marked by the box, was acquired around the hole edge. (b) Close-up of spectrum image showing individual pixels, each containing an EELS spectrum. The rough edge of the drilled hole is marked with the dotted line. The O-K edge EELS spectra in the pixels within each colored box were summed and displayed in (c).

Mirroring the RT experiments, an EELS spectrum image was acquired after the CT hole drilling from the region around the hole edge. A dark-field STEM image of the drilled hole with the area of spectrum image acquisition marked with a box is shown in Figure 28a. The close-up of the spectrum image, with the edge of the hole marked, is shown in Figure 28b. The summed spectra from the enclosed pixels in the boxes in Figure 4b are shown in Figure 28c. No pre-edge peak was seen in the O-K edge EELS spectra around the edge of the CT drilled hole.

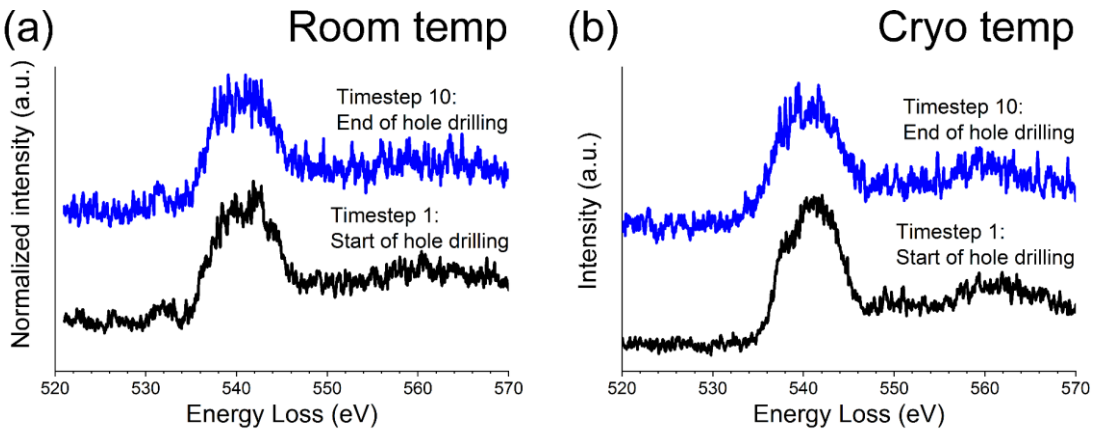

Figure 29. Comparison of the first and last O-K edge EELS spectra from the timeseries acquired during hole drilling at (a) room temperature and (b) cryo temperature.

The first and last O-K edge EELS spectra from the beam damage time series acquired at RT (Figure 25) and CT (Figure 27) are shown in Figure 29. No discernible difference was observed between the first and last spectra at either RT or CT, save for a slight increase in the intensity of the main peak at the edge onset at cryo temp. However, there is an apparent decrease in the signal-to-noise of the final timestamp spectra compared to the initial timestamp spectra.

A comparison of the first and last spectra of the O-K edge timeseries from both the RT and CT experiments (Figure 29) shows no significant difference, suggesting no major difference in O coordination once pre-peak inducing O species have been formed and removed in the RT experiments. This also suggests Al must be simultaneously removed at a similar rate during beam damage, otherwise changes in O coordination would be expected. A slight increase in the intensity of the main peak at the edge onset in the CT spectra can be observed. This could be due to the increased presence of undercoordinated (3-fold) O, as seen in EELS simulations reported by Ching et al [94]. However, it is difficult to compare the fine structure due to the decreased signal-to-noise in the later timeseries spectra. The comparison of the early O-K edge spectra from the hole drilling

time series between the RT experiment and CT experiments shown in Figure 30 shows a slight difference of the fine structure in the main peak at 541 eV. The shape of the O-K edge acquired at CT (as shown with best signal-to-noise in Figure 28) closely resembles previously reported O-K edge EELS from γ-Al_2O_3 [154], suggesting the change is in the RT O-K edge. Small variations in fine structure can be seen at different timepoints in the RT O-K EELS timeseries, but the CT O-K edge EELS shape remains fairly consistent during the timeseries acquisition. Similar damage-induced fine structure fluctuations have been observed in damaged α-Al_2O_3 [136], suggesting small continuous changes in O coordination during hole drilling. That this damage is apparent in the first collected EELS spectrum highlights the difficulty of acquiring damage-free EELS spectra at RT from γ-Al_2O_3.

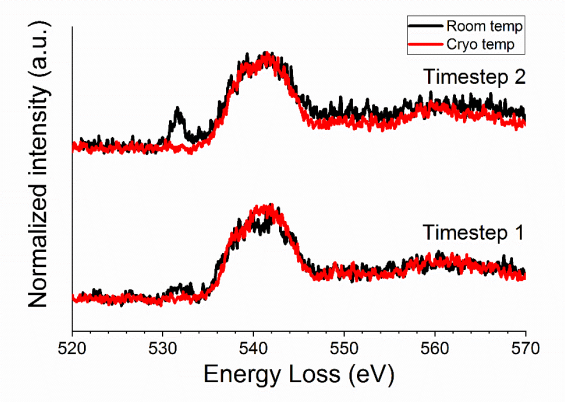

Figure 30. Comparison of the early O-K edge spectra from the hole drilling time series between the room temperature experiment and cryo temperature experiments.

The first two spectra of the timeseries acquired at RT and CT are plotted in Figure 30. No significant difference in the spectra shapes were observed, but the spectra were consistently noisier in the RT experiments than in the CT experiments. The difference in intensity of the region 545 –

570 eV at timestamp 2 is due to slightly different background levels from the background subtraction procedure. The beam damage O-K edge EELS experiments are summarized in Table 4.

Table 4. Summary of EELS experiments evaluating effects of beam damage on O-K edge EELS spectra at different temperatures.

Hole drilling O-K edge EELS observations	**200kV, RT**	**200kV, -186°C**
Hole formation with growing pre-edge peak	Yes	No
Hole formation with no pre-edge peak	No	Yes

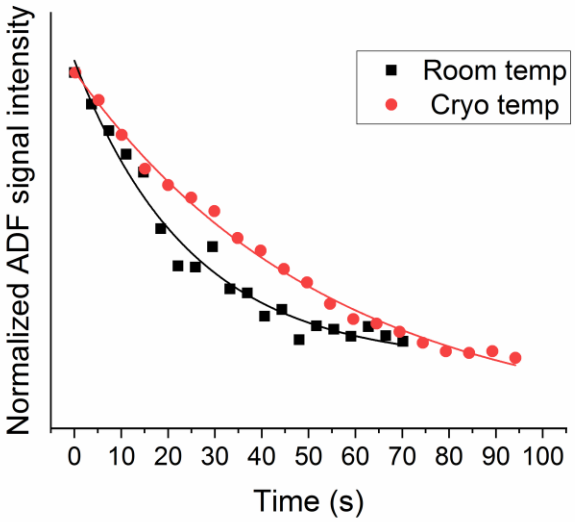

Figure 31. Hole drilling rates at room temperature and at cryo temperature determined by the normalized intensity of the annular dark field (ADF) detector signal during hole drilling.

The rates of hole drilling during the beam damage experiments at RT and CT were estimated using the normalized intensity picked up by the annular dark field (ADF) detector during focused e-beam hole drilling (Figure 31). The hole drilling rates fit well to an exponential decay behavior (with R^2>0.97); faster at the start of the hole drilling and continuously decreasing with time. The equations for the hole drilling rate exponential decay fits are:

i. $$\text{RT: y} = 1.5\text{E6} * \exp\text{^}(-x/24.7) + 8.1\text{E6} \quad (5.2)$$

ii. $$\text{CT: y} = 1.7\text{E6} * \exp\text{^}(-x/53.9) + 7.8\text{E6} \quad (5.3)$$

The form of the exponential decay equation used is:

$$y = A_1 * exp(-x/t_1) + y_0 \quad (5.4)$$

where A_1 is the initial value, t_1 is the time constant, and y_0 is the final value.

Hole drilling occurs more rapidly during pre-edge peak formation in the RT experiment as a result. Hole drilling also occurred faster at RT than at CT. This is consistent with the reduction of beam damage by operating at CT that was observed in the EELS timeseries. Since radiolysis appears to be associated with the pre-edge peak formation, the suppression of radiolysis by operating at CT may correlate with the reduction of the hole drilling rate in the early stages of the CT hole drilling experiment. Interestingly, radiolysis is expected to be a more significant damage mechanism than knock-on for insulating materials [131, 155]. The suppression of radiolysis by cryo-STEM only slightly lowers the damage rate, suggesting that electrostatic charging may be the most significant damage mechanism in γ-Al_2O_3, as has been proposed for some other oxides [134].

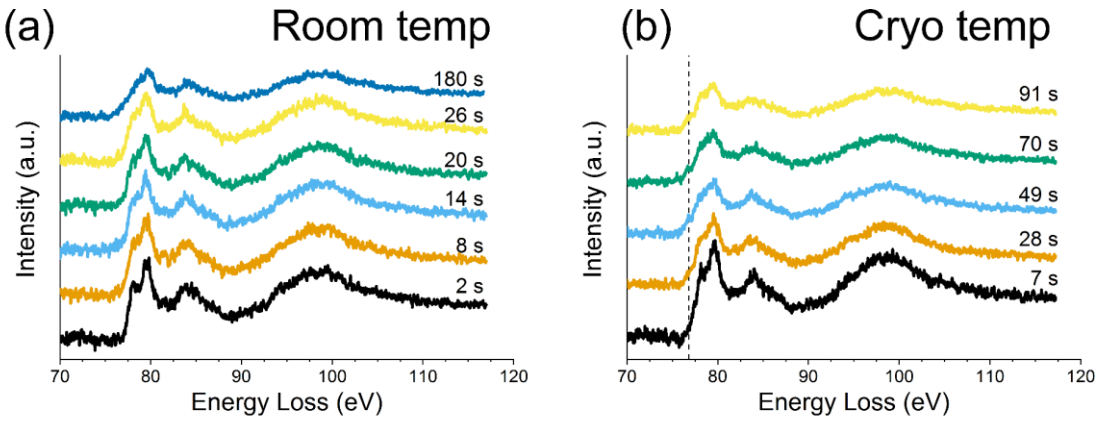

Figure 32. Time-resolved Al-$L_{2,3}$ edge EELS spectra acquired at (a) room temperature and at (b) cryo temperature during e-beam hole drilling. The position of the increased pre-edge intensity at 77 eV is marked with the dotted line.

To gain deeper insight into the beam damage mechanisms occurring in γ-Al_2O_3, additional hole drilling experiments were conducted at both RT and CT, with Al-$L_{2,3}$ edge EELS timeseries acquired during the experiments and shown in Figure 32. At RT, the main observation is a gradual decay of the shoulder on the main peak at 79 eV with time. This peak has been assigned to the tetrahedral Al sites [94, 136] in γ-Al_2O_3, suggesting Al atoms on tetrahedral Al sites are preferentially removed, similarly to the beam damage observations in $MgAl_2O_4$ [156]. However, complete decay of the tetrahedral Al peak only occurs after long-time exposure to the beam (>3 minutes). At CT, the Al-$L_{2,3}$ edge changes in a consistent manner to the RT experiment, however there is an increase in pre-edge intensity at about 77 eV seen more prominently in the CT experiment. The spectra containing the increased pre-edge intensity are strikingly similar to the Al-$L_{2,3}$ EELS of amorphous Al_2O_3 and of $Al_2Ge_2O_7$ [136], which contains 5-coordinated Al atoms only. This suggests the presence of 5-coordinated Al and possibly other Al coordination types besides 4 and 6 in the beam damaged area, which is explained by the suppression of radiolysis by

operating at CT. With knock-on and electrostatic charging being the main damage mechanisms, undercoordinated Al atoms that have lost O neighbors due to these damage mechanisms do not form new bonds before being sputtered away, and the increased number of 5-coordinated Al atoms can be detected. The increased pre-edge intensity is not observed at RT, where radiolytic energy transfer enables the undercoordinated Al atoms to form new bonds and the structure to rearrange during damage.

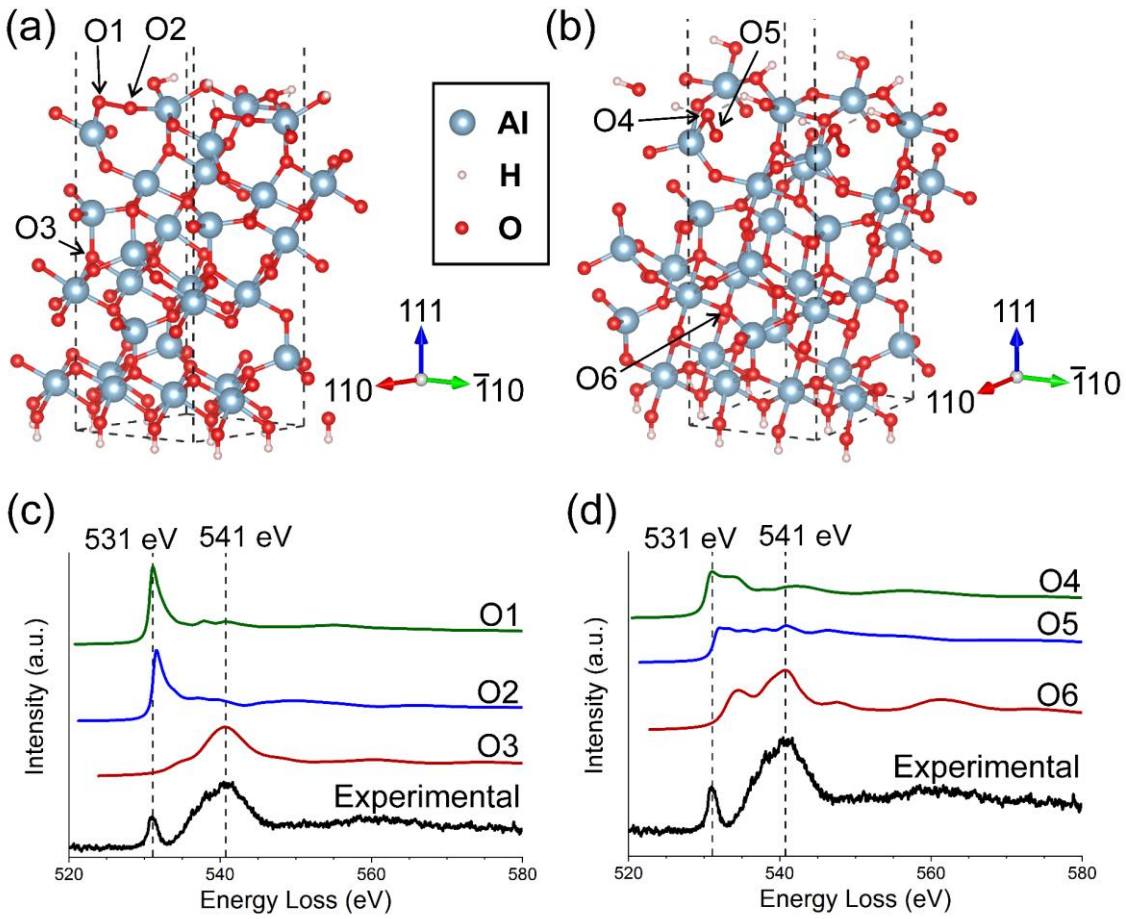

Figure 33. (a,b) Partially hydroxylated γ-Al_2O_3 (111) surface slab models with O atoms in the surface O dimers labeled O1 and O2 in (a) and O4 and O5 in (b). Bulk O atoms used for comparison are labeled O3 in (a) and O6 in (b). (c,d) Simulated O-K edge EELS spectra from the labeled O atoms in the models compared to the experimental O-K edge with damage-induced pre-edge peak.

Partially hydroxylated γ-Al_2O_3 (111) surface slab models containing a surface O dimer were used to perform MS EELS simulations to explain the origin of the O-K edge EELS pre-edge peak. The first surface model is shown in Figure 33a, with the O atoms of the O dimer labeled O1 and O2. A bulk O atom labeled O3 was used for comparison. The simulated O-K edge ELNES from O1-O3 are plotted in Figure 33c and compared to the experimental O-K edge EELS acquired from the edge of the RT drilled hole. The positions of the peaks from the simulated O-K edge ELNES of the dimer O atoms align with that of the pre-edge peak seen in the experiment, while the simulated EELS from O3 aligns with the normal EELS O-K edge spectrum. ELNES simulations were performed on a second γ-Al_2O_3 (111) surface model containing a surface O dimer to confirm the results from the first model. The model is shown in Figure 33b, with the O atoms of the O-O dimer labeled O4 and O5, and a bulk O atom that was used for comparison labeled O6. The simulated O-K edge ELNES from the O atoms labeled O4-O6 are plotted in Figure 33d compared to the experimental O-K edge EELS. The peak positions from the simulated O-K edge ELNES of the dimer O atoms again align with the experimentally observed pre-edge peak.

Previous reports on other oxide materials suggested that the source of the pre-edge peak is the presence of O-O species [130, 140, 147]. A prior theoretical study of the (111) surface of γ-Al_2O_3 indicated some possible scenarios resulting in surface O-O bond formation, one such model finding that surface O-O dimers were formed after partial dehydration of a hydroxylated (111) γ-Al_2O_3 surface and subsequent relaxation [146]. Additionally, the cubic spinel-based model has been demonstrated to be the most accurate bulk model for γ-Al_2O_3 [88]. Thus, the partially hydroxylated spinel-based (111) surface model from the work by Acikgoz et al [146] was used for the subsequent EELS simulations. It is important to note that while the surface of the model is

(111), the electron beam direction in the EELS simulations is the [110] direction of the model, to match the experimental setup.

The (110) and (111) surface of γ-Al_2O_3 is expected to be at least partially hydroxylated at RT [157]. Surface hydrogen removal or dehydration could potentially occur during electron beam irradiation and damage, through a form of electron-stimulated desorption [158]. Additionally, Al has a 4 times lower displacement energy (E_d) than O in the alumina framework [159], and it can be expected that Al atoms will be more rapidly displaced by knock-on damage than O atoms. Electrostatic charging would also induce the migration of O anions into the irradiated area and the simultaneous migration of cations away [160]. These phenomena would have the effect of accumulating excess O atoms in the beam damaged area that could potentially then form peroxy O-O bonds more readily through radiolytic processes. Beam damage has also been observed to cause atomic restructuring in the probed material [161, 162] that could potentially in this case result in O-O bond formation. Further work however is required to determine the exact mechanism of O-O formation due to beam damage and is not further explored here. Instead, the focus here is on whether the presence of surface O-O dimers does in fact reproduce the O-K pre-edge peak.

The multiple scattering approach to simulating EELS spectra calculates the ELNES from a single absorbing atom at a time. Hence, the O-K ELNES from the O atoms in the O dimer (O1 and O2) in Figure 33a were simulated individually. The simulated ELNES shown in Figure 33c from both O dimer atoms consist of a sharp peak at the same position as the pre-edge peak from experiment. The simulated ELNES from a bulk O is plotted to check that the bulk O atoms indeed match the experimental peak position, thus confirming the results of the surface O dimer atom simulated O-K ELNES. For comparison, a model of the beam damage was created by simply removing atoms to form a hole from a bulk alumina model and simulated the EELS from the

surface O atoms after relaxing the atomic positions to the equilibrium structure (Appendix Figure 1). These simulations did not produce the pre-edge peak at 531 eV seen in the experiments. Based on these results, the presence of strong O-O bonds formed on the surface of the beam damaged γ-Al_2O_3 is proposed to be the likely source of the O-K pre-edge peak.

The O-O bond origin of the pre-edge peak was further confirmed by ELNES simulations from a second O dimer-containing surface model (Figure 33b). The simulated ELNES from the O dimer atoms show the edge onset at ~531 eV matching the experimentally observed pre-edge peak. However, these simulated ELNES also show additional fine structure after the sharp edge onset whereas those from the first surface model only show a sharp peak at ~531 eV (Figure 33c). This difference is likely because the O dimer atoms in Figure 33b are slightly below the surface and the O2 atom is bonded to two other Al atoms in addition to the O1 atom. This was confirmed by a third set of ELNES simulations from an O dimer-containing surface model (Appendix Figure 2). Both O atoms of the dimer in that model are bonded to two other Al atoms. Consequently, the simulated ELNES from the O-O dimer atoms in Appendix Figure 2 consisted of the sharp edge onset at ~531 eV and additional fine structure. These simulations suggest that for the sharp peak to be produced at 531 eV, the O-O dimer atom should be bonded to only one other Al atom and should not be partially surrounded by other atoms.

5.4 Outcomes

In this chapter, it has been demonstrated that the use of cryo temperatures suppresses the formation of O dimers during the beam damage process, thereby suppressing the O-K pre-edge peak. Operating at cryogenic temperature appears to slow down the indirect atomic displacement

processes associated with radiolysis [133], which appears to contribute to the formation of surface O-O bonds. Knock-on damage, sputtering, and electrostatic charging however appear largely unaffected by temperature reduction. Despite showing that surface O-O species produce the pre-edge peak, the contribution of O_2 gas released by the electron beam on the formation of the pre-edge peak cannot be completely ruled out. This is because the simulated O-K edge ELNES of the O dimer atoms appears similar to the O-K edge EELS reported for O_2 gas [137].

6.0 Evaluating the Accuracy of Common γ-Al_2O_3 Structure Models by Selected Area Electron Diffraction

The contents of this chapter have been published in:

H.O. Ayoola, S.D. House, C.S. Bonifacio, K. Kisslinger, W.A. Saidi, J.C. Yang, Evaluating the accuracy of common γ-Al_2O_3 structure models by selected area electron diffraction from high-quality crystalline γ-Al_2O_3, Acta Materialia, 182 (2020) 257-266.

6.1 Preamble

The aim of this chapter is to determine the most accurate structure model for γ-Al_2O_3 from existing models. Many structure models have been proposed, therefore the refinement of an entirely new structure from scratch is obviated. Up to this point, there has not been a direct comparative study of the various γ-Al_2O_3 structure models using data from a pure, highly crystalline γ-Al_2O_3. To acquire diffraction from the thin γ-Al_2O_3 films while avoiding the larger NiAl substrate, the high spatial resolution of SAED using a TEM is ideal. Being two-dimensional, SAED patterns can also clearly distinguish structures that differ by symmetry unlike powder XRD. Previously reported SAED-based studies of γ-Al_2O_3 [75, 76, 99, 100, 163, 164] were completed before any of the now widely used models were proposed. In this chapter, the commonly cited spinel and nonspinel γ-Al_2O_3 models described in Section XX are compared with each other against experimental data from highly crystalline γ-Al_2O_3 by means of SAED. Both the polycrystalline and single-crystalline γ-Al_2O_3 thin films are studied. Simulated electron diffraction

data for the γ-Al_2O_3 models are compared to the electron diffraction data acquired from the γ-Al_2O_3 thin films to gauge the accuracy of the proposed crystal structures.

The models considered in this study were selected based on their frequency of occurrence in the recent literature. The Smrčok model was chosen as the cubic spinel model for this study because it is the most recently proposed cubic spinel model and it was determined based on single-crystal data [74]. It is similar to the cubic spinel model proposed by Gutierrez et al.[68], but with 6% of Al atoms placed in nonspinel sites, amounting to less than 1 Al atom per unit cell. In practice, this was found to be indistinguishable from a 100% spinel structure based on SAED analysis, and therefore the Smrčok model is effectively considered a cubic spinel model.

6.2 Study-Specific Methods

High-resolution (HR)TEM images and SAED patterns from the single-crystalline and polycrystalline γ-Al_2O_3 thin films were acquired with a Hitachi H9500 TEM operated at 200 and 300 kV. Details of the electron diffraction simulations and the conversion of polycrystalline SAED patterns to a line profile, in particular the background subtraction, are discussed in Appendix A.

The simulated polycrystalline diffraction profiles were compared to the experimental diffraction profile using standard crystallographic figures of merit, namely the Bragg factor (R_B) and the profile factor (R_p). These figures of merit have been previously used to determine the best-fitting γ-Al_2O_3 models in comparison to neutron diffraction data [62, 90]. The Bragg factor compares the intensities of individual reflections (peaks) in the simulated diffraction profile to the corresponding reflections in the experimental profile and is a measure of the fit of the model to the experimental diffraction data. The profile factor is a measure of the fit of the overall shape of the

diffraction profile, which implicitly includes the accuracy of the modeling of the structure, experimental parameters, and peak shapes. The values R_B and R_p are calculated as shown:

$$R_B = \frac{\sum|I_{ko} - I_{kc}|}{\sum I_{ko}} \tag{6.1}$$

$$R_p = \frac{\sum|y_{io} - y_{ic}|}{\sum y_{io}} \tag{6.2}$$

where I_{ko} is the observed and I_{kc} is the calculated intensity of the for Bragg reflection k, y_{io} is the observed and y_{ic} is the calculated intensity at step i. The Bragg factor was calculated using only the major peaks in the experimental spectrum (< 8 nm^{-1}). For both figures of merit, a perfect fit would have a value of 0. It is important to note that these figures of merit are derived from Rietveld refinement, which is more commonly performed using X-ray and neutron diffraction data. The experimental uncertainties such as background and detector response associated with electron diffraction are generally more difficult to account for and model than X-ray or neutron diffraction, therefore the values of these figures of merit calculated herein are expected to be further from 0 than would be typically seen.

Beyond visual comparison of spot positions, the Bragg factor (R_{Bs}) and the ratio of intensities of major reflections (peaks) were used to compare the simulated single-crystal SAED patterns to the experimental SAED patterns. The Bragg factor (R_{Bs}) was calculated using equation (1). All the visible reflections (peaks) in the line profiles from the experimental single-crystal SAED pattern and the corresponding peaks in the simulated SAED patterns were used to calculate R_{Bs}. The peaks labeled in Figure 39d-f were those used to determine the ratios of reflection intensities. The simulated spot patterns in Figure 40 were made by inputting relative spot intensity data from the simulation in SingleCrystal into a self-written code in MATLAB.

6.3 Results and Discussion

6.3.1 Polycrystalline Diffraction and Analysis

The SAED pattern from the textured polycrystalline γ-Al_2O_3 thin film is shown in Figure 34. The presence of complete rings confirms that this γ-Al_2O_3 film is polycrystalline, however, the six-fold symmetric spots appearing on some rings indicate the presence of a (111) texture, assuming the cubic model. The azimuthal average of the rings, avoiding the texture spots, is overlaid and aligned to the SAED pattern. The inset shows the TEM image of the region of the film from which the pattern was acquired. The ring pattern is identical to that from a commercial γ-Al_2O_3 powder (Figure 20) as determined by the ratios of the corresponding diffraction ring radii (Table 3). The peak intensities from the azimuthal averages of the diffraction patterns of both samples are also nearly identical (Figure 21), confirming the γ-Al_2O_3 identity of the film. Bright- and dark-field cross-sectional TEM images of the polycrystalline γ-Al_2O_3 film and a dark-field TEM image of the scraped polycrystalline γ-Al_2O_3 film formed using a (111) texture spot are shown in Figure 22. The TEM images in Figure 22 were used to confirm the film thickness and average grain size.

For the SAED analysis and electron diffraction simulations, an important consideration is the background subtraction. Due to the stronger interaction of electrons with atoms compared to X-rays, the background scattering is more intense, as seen in the azimuthal average shown in Figure 34. The amorphous carbon support film on the TEM grid contributes some diffuse intensity to the SAED pattern. Since both the carbon support film and γ-Al_2O_3 film are thin, their diffraction was treated as kinematic (*i.e.*, involving a single scattering event) [165], and the contribution of the carbon film was removed by subtracting the amorphous SAED pattern from a region with only

the carbon film from the combined SAED pattern (Figure 34), as detailed in Appendix Figure 3 [166]. Thereafter, the remaining diffuse background was accounted for using both a lognormal-based spline fit and direct measurement of the background intensity between the diffraction rings (Appendix Figure 4–Appendix Figure 7) [167]. For a more detailed discussion of the background subtraction process, see Appendix C.2.

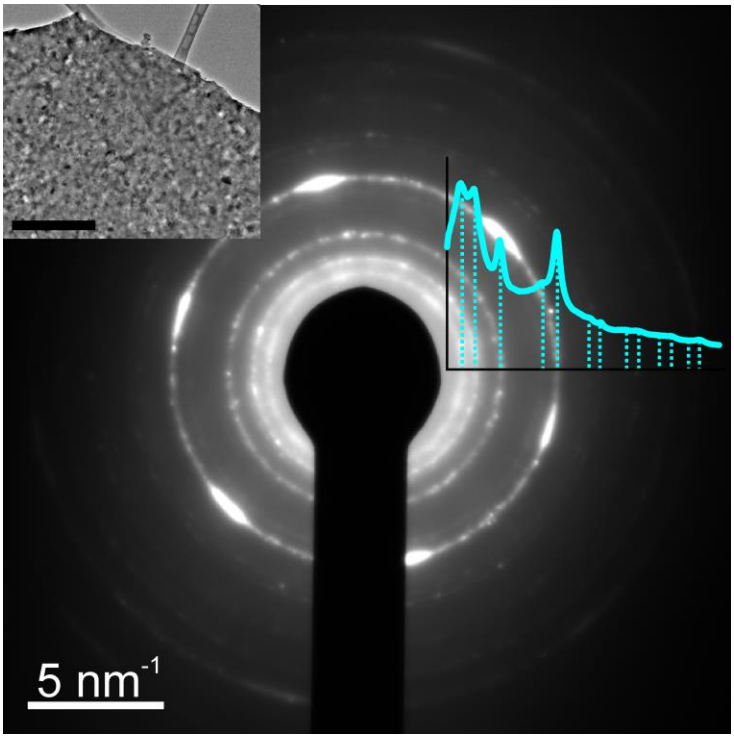

Figure 34. SAED pattern from the 850 °C, 2 hr oxidized polycrystalline γ-Al_2O_3 film scraped from the NiAl surface and deposited onto a carbon-coated TEM grid. The inset shows a TEM image of the polycrystalline γ-Al_2O_3 film (scalebar = 500 nm). The overlaid plot is the corresponding azimuthally averaged profile of the SAED pattern.

The azimuthally averaged line profile of the diffraction pattern in Figure 34 is plotted together with the simulated diffraction profiles for each γ-Al_2O_3 model in Figure 35. The

diffraction profiles in Figure 35 have been offset vertically for ease of visibility. The dashed lines indicate the peak positions in the experimental diffraction profile. The main peaks for each model are indexed. Visual inspection of peak positions and shapes were used as the first basis of comparison. Quantitative figures of merit were then used as a secondary basis of comparison. Because the methods used to account for background correction, dynamical (*e.g.*, plural scattering) diffraction effects, and CCD camera response are approximate, focus is placed on the comparison of the main peaks present below $8nm^{-1}$ using the Bragg factor R_B. This is because low intensity peaks are expected to suffer from the most uncertainty in intensity as a result of nonlinear CCD camera response.

Overall, the diffraction profiles of all the models show good agreement with the experimental profile based on peak shapes and positions (Figure 35a). The diffraction profiles of the Smrčok cubic spinel and Pinto monoclinic spinel-based models are nearly identical, which is unsurprising given that the Pinto model is based on a cubic spinel, as previously discussed. Of the models considered, the Digne monoclinic nonspinel model exhibits the worst fit to the experimental results based on peak shapes and positions due to the complete mismatch of the first two experimental peaks (~3.6 nm^{-1} and ~4.2 nm^{-1}): the Digne model produces one broad peak between 3.5 nm^{-1} and 4.5 nm^{-1}. Figure 35b shows a close-up on the region between 3 nm^{-1} and 6 nm^{-1} for each profile in Figure 35a. The Digne model diffraction profile has multiple peaks of similar intensity within the range of 3.5 – 4.5 nm^{-1}, which is completely different from the experiment and the other models.

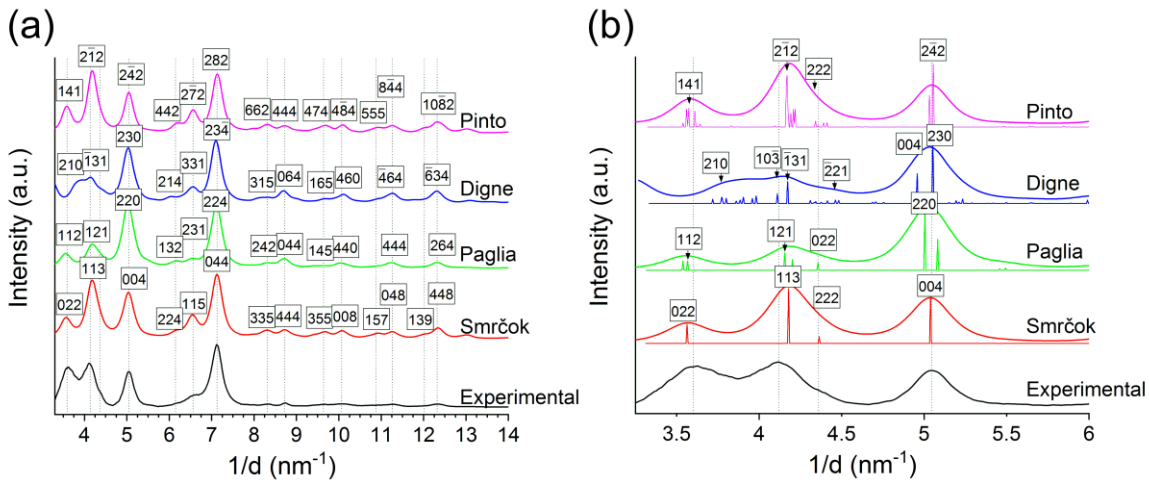

Figure 35. (a) Azimuthally averaged line profile of the experimental SAED pattern shown in Figure 34, plotted with the simulated diffraction data for each of the models considered. The dashed lines indicate the peaks in the experimental diffraction profile. The main peaks for each model are indexed, with overlapping labels omitted for clarity. (b) The region from 3 – 6 nm^{-1} from (a) showing the contributing peaks to the profile.

The fits of the models compared to the experimental profile were quantified using the previously described figures of merit, the results of which are summarized in Table 5. Uncertainties in the R_B and R_p are from the standard deviation of the values calculated for different background subtraction techniques, which is the most significant source of uncertainty. Uncertainties in the R_{Bs} are propagated from the averaging of symmetrically equivalent spots in the experimental SAED. The Bragg factor R_B confirms that the spinel-based models fit the peak intensities of the main peaks better than the nonspinel models. The profile factor R_p then shows that the cubic spinel model gives the best fit to the overall profile, with the Digne monoclinic nonspinel model exhibiting the worst fit. The tetragonal nonspinel model fits the profile factor nearly as well as the Pinto monoclinic nonspinel model, but the large deviations in the peak

intensities of the first three major peaks compared to the experimental profile (< 6 nm^{-1}) ultimately render its Bragg factor significantly worse. Visual inspection of the simulated profiles combined with the figures of merit confirm the Digne monoclinic nonspinel model as the worst fitting model.

Table 5. Figures of merit used to compare the fits of the simulated polycrystalline diffraction profiles to the experimental (Figure 35a) and the fits of the simulated single-crystal SAED patterns to the corresponding experimental single-crystal pattern (Figure 38a). The single-crystal Bragg factor (R_{Bs}) compares the intensities of the individual peaks in the line profiles in Figure 39.

Model	Polycrystalline SAED		Single-crystal SAED
	Bragg factor (R_B)	Profile factor (R_P)	Bragg factor (R_{Bs})
Cubic spinel (Smrčok)	0.27±0.03	0.39±0.02	0.24±0.03
Tetragonal nonspinel (Paglia)	0.42±0.08	0.48±0.05	0.49±0.06
Monoclinic nonspinel (Digne)	0.38±0.06	0.56±0.03	*
Monoclinic spinel-based (Pinto)	0.26±0.04	0.50±0.02	*

The relative peak intensities are a function of both the arrangement of atoms in the unit cell and the crystal lattice or space group. The relative peak intensities as quantified by the R_B value in the diffraction profiles of the Smrčok cubic spinel and Pinto monoclinic spinel-based models are both closer to the experimental profiles than the Paglia tetragonal nonspinel model. Considering that the spinel-based models have different space groups but similar atomic arrangements, the spinel atomic arrangement appears closer to the atomic arrangement in the γ-Al_2O_3 film than the nonspinel models. Interestingly, despite the spinel models being a better match to the experimental profile, there is a slight mismatch of the position of the first two peaks compared to the

experimental profile, with the first peak being slightly lower and the second slightly higher than the experimental. The mismatch could be due to the presence of a tetragonal distortion in the unit cell of the γ-Al_2O_3, which has been previously seen in boehmite-derived γ-Al_2O_3 [55, 65]. This would be surprising, however, because the tetragonal distortion is believed to result from the transformation of boehmite to γ-Al_2O_3. Therefore, the presence of the peak position mismatch suggests the possibility that the tetragonal distortion could be an intrinsic property of γ-Al_2O_3 regardless of the preparation method.

6.3.2 Single-Crystal Diffraction and Analysis

Since a single best fitting model could not be determined conclusively through the polycrystalline diffraction analysis, analysis of electron diffraction from γ-Al_2O_3 single crystals was performed. The near single-crystal oxide film was confirmed as pure aluminum oxide using electron energy-loss spectroscopy (Figure 18), then confirmed as γ-Al_2O_3 by comparison to other previously reported single-crystal γ-Al_2O_3 SAED patterns [60, 75, 76, 101, 168]. The TEM images in Figure 36 are cross-sectional views of the crystalline γ-Al_2O_3 film grown by oxidation of single-crystal NiAl (110). Twins can be seen throughout the film, which were indexed as (111) twins assuming the cubic model. The corresponding SAED pattern (Figure 36b) likewise exhibits the expected twin spots (and orientation) from these lattice planes. The determination of which spots are from which twin was confirmed by fast Fourier transforms (FFT) generated from portions of the image on opposite sides of a twin boundary (Figure 37). Additionally, FFT from certain areas of the film along a twin boundary, such as (c), showed extra spots with 3x the (111) plane spacing, likely due to a layered ordering along the twin boundaries. This effect is also seen in the diffraction pattern, albeit with low intensity spots due to the sparseness of these regions. Figure 36c shows

the indexed [001] SAED pattern from the NiAl substrate. The interplanar spacings for both materials are labeled in the HRTEM image in Figure 36d: (222) in the γ-Al_2O_3 and (110) in the NiAl. The HRTEM micrograph was Wiener filtered to remove amorphous contributions [169]. All planes and directions labeled in Figure 36a and Figure 36d are assuming the cubic spinel model. Continuing on with the cubic spinel assumption, the epitaxy between the γ-Al_2O_3 film and the NiAl substrate displays the Nishiyama-Wasserman orientation relationship, NiAl (110)[001] || γ-Al_2O_3 (111)[011], as expected for this NiAl oxidation condition [100, 105].

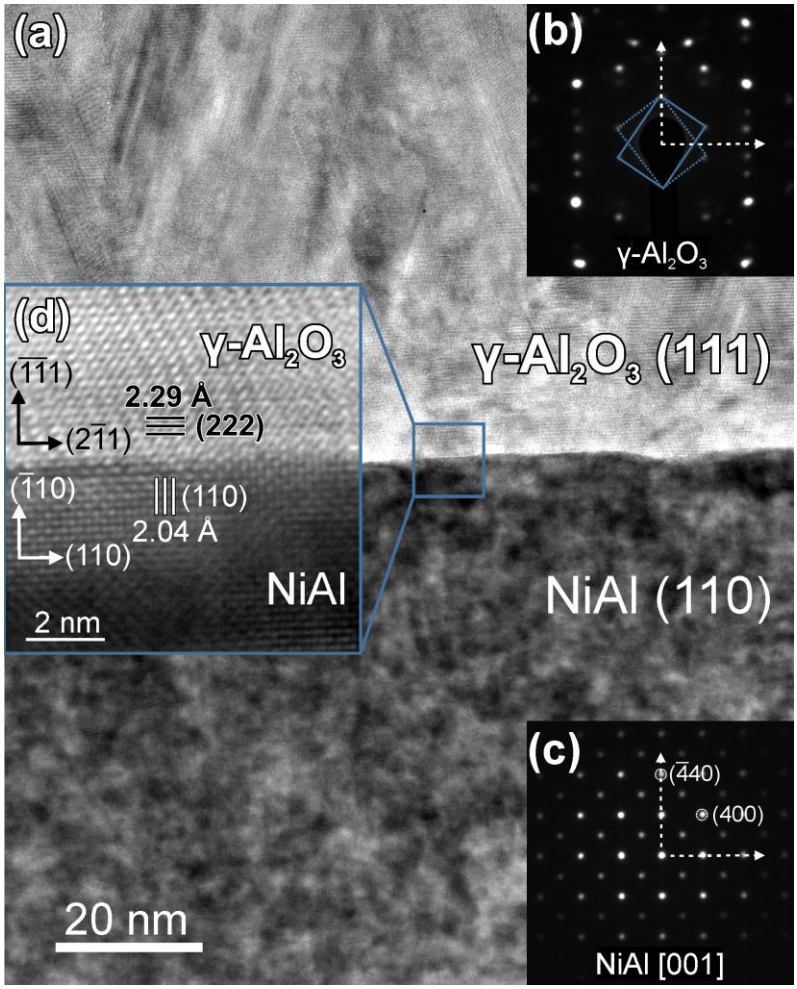

Figure 36. (a) Cross-sectional TEM image of the γ-Al_2O_3 film formed by NiAl (110) oxidation. (b) SAED pattern from the γ-Al_2O_3 film. Twin patterns are marked with solid and dotted rectangles. (c) SAED pattern from the NiAl indexed in the simple cubic system. (d) HRTEM image of the NiAl/γ-Al_2O_3 interface taken from the depicted region in (a), showing the FCC lattice stacking and the measured lattice spacing of the γ-Al_2O_3.

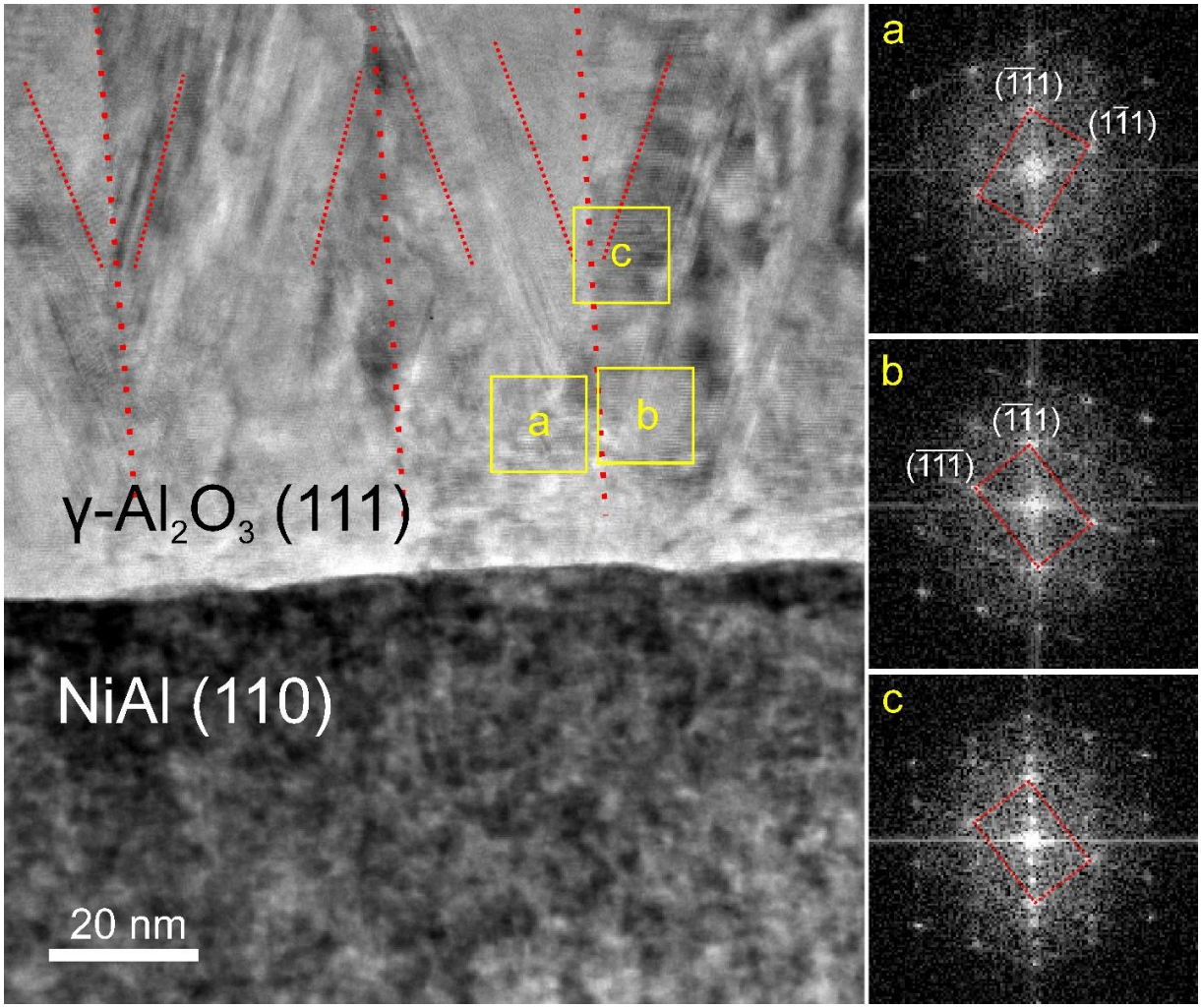

Figure 37. Cross-sectional TEM image of the γ-Al_2O_3 film formed by NiAl oxidation. The twinning and twin boundaries found in the film are indicated with red dotted lines. The yellow boxes labeled a and b are areas on opposite sides of a twin boundary where FFTs were produced. The corresponding FFTs are shown in a and b.

The SAED spot pattern from the single-crystal film (Figure 36) was compared with the simulated single-crystal SAED patterns for the models under consideration (Figure 38a). Additional SAED spot patterns from other zone axes were acquired for comparison and are also shown in Figure 38b and Figure 38c. The experimental SAED pattern shown in Figure 36 and Figure 38a is twinned and so the corresponding simulated SAED patterns were also twinned to match. The simulated SAED patterns from the Digne model are easily distinguished by visual inspection from the rest of the patterns, further confirming it as the least accurate model. The Digne model patterns exhibit spots where there are none in the experimental pattern and is absent spots where there should be spots. The line profiles shown in the supplemental information from the Digne [010] (Appendix Figure 9) and [-101] (Appendix Figure 10) SAED patterns highlight the additional and missing spots compared to the experimental pattern. The simulated SAED patterns from the Pinto monoclinic spinel-based model contain the same spots as the other patterns, but also contain several additional spots not observed in the experimental pattern. The additional spots are highlighted in the line profiles taken from the Pinto [001] (Appendix Figure 9) and [100] (Appendix Figure 10) SAED patterns. The presence of extra spots from both of these models suggests that the lowered symmetry of the monoclinic lattice is inaccurate. These additional spots do not show corresponding rings in the simulated polycrystalline diffraction line profiles because they are either too low in intensity and are subsumed into nearby larger peaks (as in Figure 35b), or they are outside the angular range plotted.

The SAED patterns from the Smrčok cubic spinel and Paglia tetragonal nonspinel models are nearly identical to each other. Comparison of the SAED patterns from both models to the experimental shows that both the cubic spinel and tetragonal nonspinel models describe the arrangement of spots well. This is not surprising, as both models contain the same FCC O sublattice

and similar unit cell symmetries, with the differences between the models being the lattice/spacegroup and the distribution of Al atoms in the unit cell. To distinguish between the two remaining models, relative spot positions and intensities in their simulated SAED patterns were compared to those of the experimental SAED patterns.

Figure 39 compares the spot positions and intensities of the Smrčok and Paglia models alongside the experimental pattern. The green, red, and blue boxes indicate the regions where line profiles (Figure 39d-f) were taken. The simulated patterns are indexed, with yellow labels representing the twin spots. For the line profiles from the experimental SAED pattern (Figure 39a), the intensities of all symmetrically equivalent spots in the pattern were averaged. This served to minimize the effect on the spot intensities of slight misalignment of the specimen relative to the zone axis. By visual inspection, the green line profile (Figure 39d) shows a better match to the Smrčok cubic spinel model than the Paglia tetragonal nonspinel model. It is more difficult to determine visually which model better fits the red and blue line profiles. Interestingly, there is a clear shift in the positions of the peaks (spots) in the Paglia tetragonal nonspinel model SAED compared to the experimental in the blue line profiles (Figure 39f), while the peaks in the Smrčok cubic spinel model line up more closely with the experimental. There is also a shift in the peaks for both models in the red line profiles (Figure 39e), with the peaks from the Smrčok cubic spinel model again being closer to the experimental. The shift in the peaks suggests that the unit cell dimensions and the tetragonal lattice of the Paglia model are less accurate.

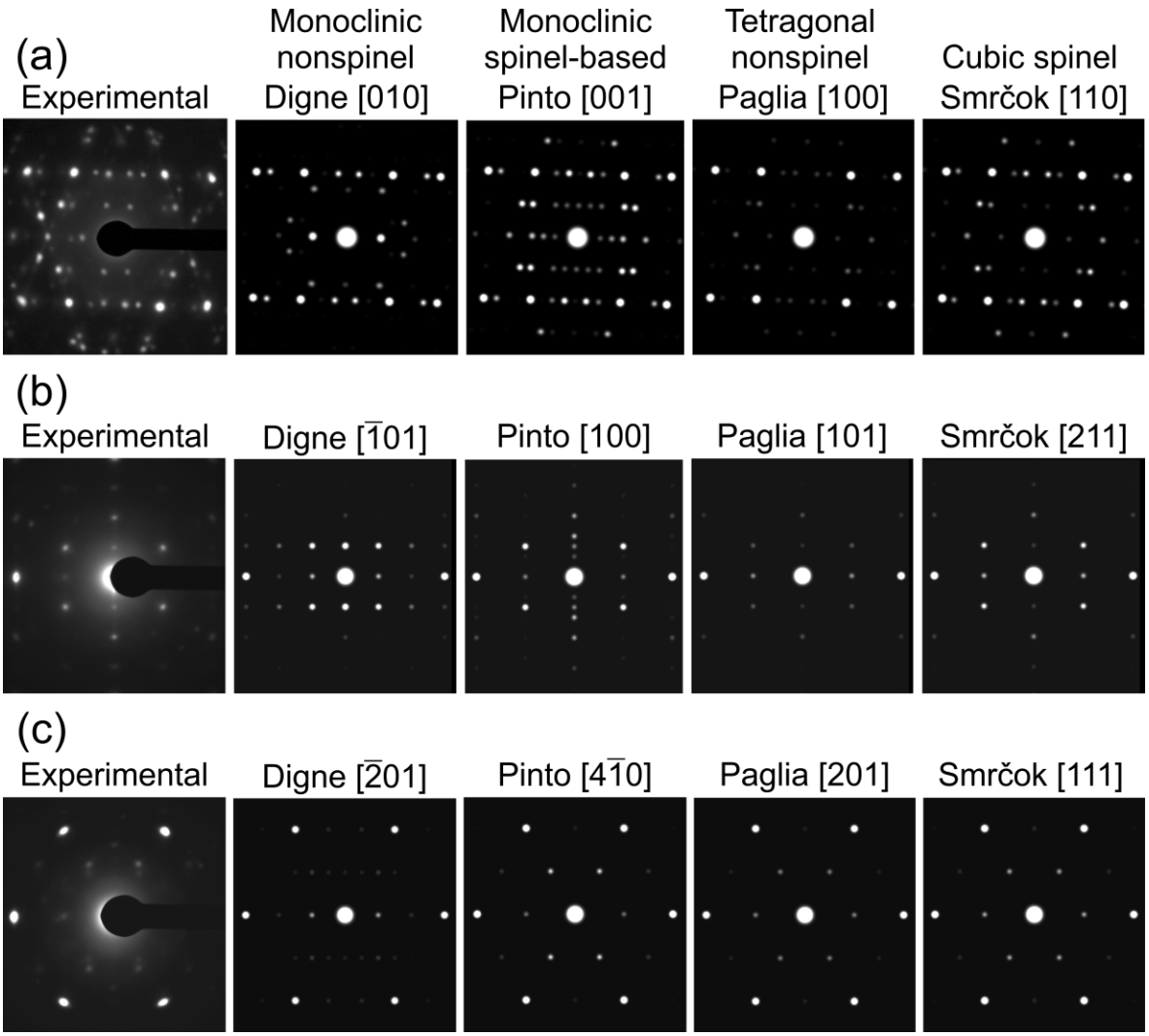

Figure 38. Comparison of experimental SAED spot patterns from three different zone axes to simulated diffraction patterns for the corresponding zone axes for each model.

The Bragg factors (R_{Bs}) shown in Table 5 were then used to compare the models. R_{Bs} is not considered for the Digne and Pinto models as they were already eliminated by analysis of single-crystal SAED line profiles (Appendix Figure 9 and Appendix Figure 10). The Bragg factors for both models are identical to those obtained from the polycrystalline diffraction analysis, which validates the quantitative comparison method. The ratios of intensity for the labeled peaks in each line profile were calculated and are tabulated in the supplemental information (Appendix Table 3). A useful consideration is whether the ratio of the peak intensities is greater or less than 1, because this is insensitive to the uncertainty added from nonlinearity in the CCD detector response. Considering both the green and blue line profiles (Figure 39d and f), the Smrčok model shows peak intensities A>B and E>F which is consistent with the experimental, while the Paglia model shows the opposite. From the red line profile (Figure 39e), the Paglia model has the ratio of peak intensities consistent with experiment with D>C while the Smrčok model is reversed, however the difference is smaller than the other two line profiles. Overall, this metric also favors the Smrčok model over the Paglia model (Appendix Table 3). The better match of the Smrčok cubic spinel model is further confirmed by line profile analysis of the SAED spot pattern acquired from a second zone axis (Appendix Figure 11), where the ratio of peak maximums for peaks A and B is closer to the experimental for the Smrčok model than the Paglia model.

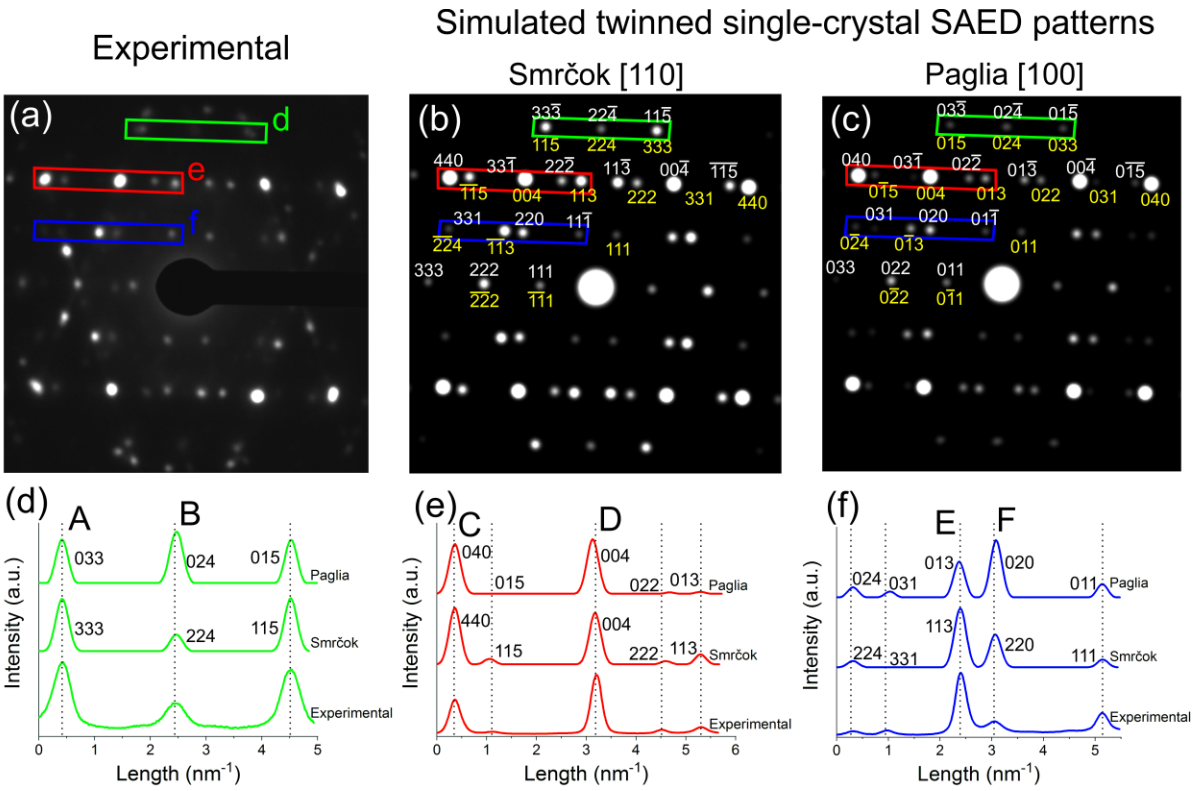

Figure 39. Comparison of SAED spot pattern from single-crystal γ-Al_2O_3 film (a) and simulated spot patterns from Smrčok cubic spinel (b) and Paglia tetragonal nonspinel (c) models. Below the diffraction patterns are the line profiles of intensity taken from the areas outlined by the correspondingly colored and labeled rectangles. For the line profiles from the experimental SAED pattern (a), the intensities of all symmetrically equivalent rows of spots were averaged. The peaks used to calculate intensity ratios are labeled.

In the Smrčok model SAED pattern (Figure 39c), the 113 spot is brighter than the 220 spot, which matches the experimental pattern. However, for the Paglia model, the corresponding 013 spot is less intense than the 020 spot. This is a key difference, as previously reported diffraction patterns also show the 113 spot brighter than the 220 spot [43, 76, 100], supporting the validity of the collected data. It is important to note that the 331 spot in the Smrčok model diffraction and the 031 spot in the Paglia model diffraction are both present, but are of such low relative intensity that peaks do not appear in the line profiles. Since both models reproduce the same arrangement of diffraction spots, whether a cubic or tetragonal lattice is more accurate could not be definitively determined. However, the spot intensities reveal which model has the more accurate arrangement of atoms in the unit cell. In single-crystal electron diffraction, the relative spot intensities are indicative of only the atomic arrangement in the unit cell. Since the O lattice is identical in both models, the better fit of the spot intensities from the Smrčok cubic spinel model to the experiment suggests that the Al atom distribution is more accurate in the Smrčok cubic spinel model than the Paglia tetragonal nonspinel. This is interesting, as the Paglia tetragonal model has been considered by some to be the most accurate model available [94].

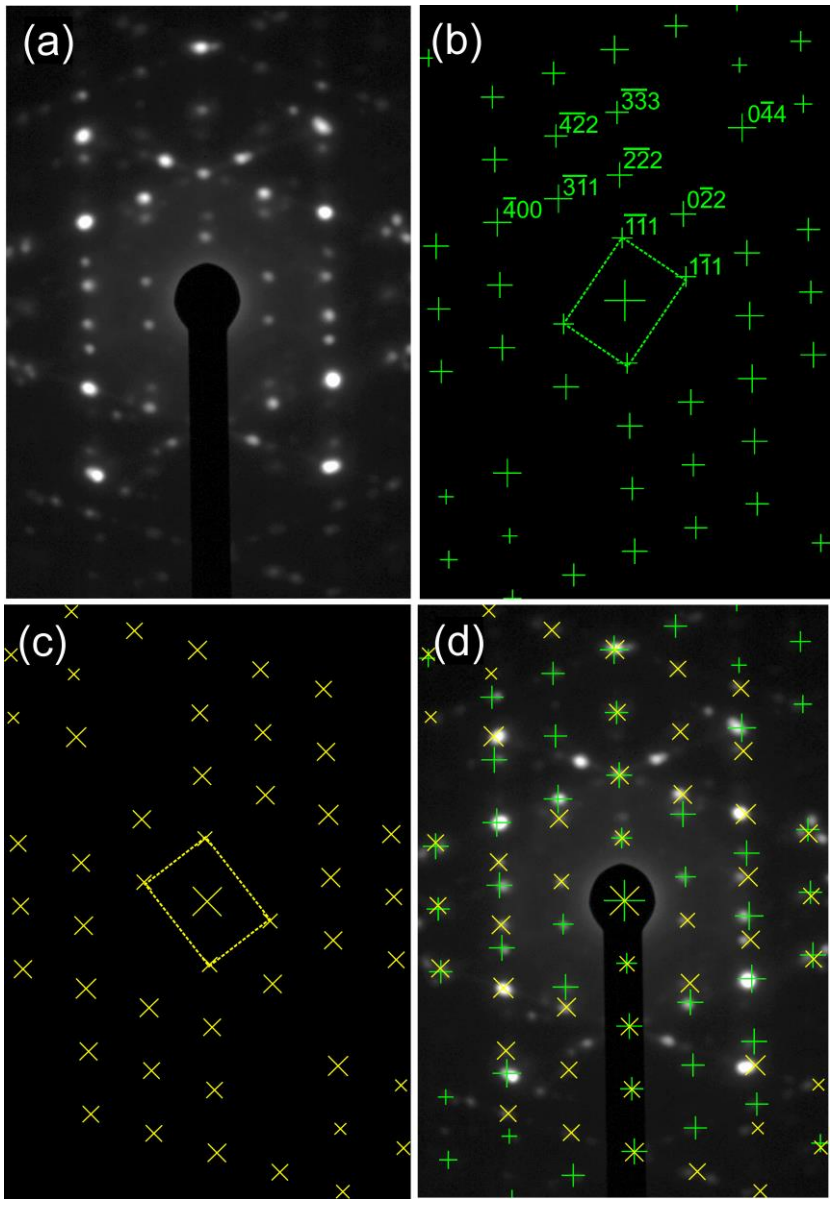

Figure 40. (a) SAED of the single-crystal γ-Al_2O_3 film. (b) Simulated diffraction patterns of one (111) twin pattern of [011] oriented cubic spinel γ-Al_2O_3 in green and the (c) 2nd twin pattern of [011] oriented cubic spinel γ-Al_2O_3 in yellow. (d) Both simulated (111) twin patterns overlaid on the SAED pattern from the as-prepared single-crystal γ-Al_2O_3 film.

A thorough indexing of the SAED spot pattern using the Smrčok cubic spinel model is shown in Figure 40: (a) the experimental diffraction pattern from the crystalline γ-Al_2O_3 next to (b) the simulated [110] oriented cubic spinel pattern in green from one (111) twin and (c) in yellow from the other (111) twin. The simulated [110] spinel pattern with (111) twinning matches the experimental spectra almost exactly, except for a few spots. The additional spots (such as the extra 400 and 440 spots) that do not show up in the simulated patterns are from (111) twinned crystals rotated differently from the two main twins shown by the rectangles. The additional spots seen between the (111) multiples of spots which are unexplained by the cubic spinel model are likely due to a layered ordering caused by the presence of multiple twin boundaries throughout the sample. HRTEM images and FFTs of the twinned single crystal confirm the presence of these small regions along twin boundaries where the layered ordering originates (Figure 37). Interestingly, the simulated single-crystal SAED pattern of the Pinto monoclinic spinel-based model in Figure 38a contains some of the spots attributed to the twin ordering, which suggests that the Al lattice in the Pinto monoclinic spinel-based model is more ordered than in the actual γ-Al_2O_3 structure. In contrast to the polycrystalline γ-Al_2O_3 film, there is no indication in the SAED of a tetragonal distortion in the thinner, twinned single-crystal γ-Al_2O_3 film, suggesting a possible size or thickness dependence of the tetragonal distortion.

6.3.3 Differences between Structures and Implications

A review of the literature to date, combined with the results of the current study, suggests the possibility that some of the materials previously used to refine the γ-Al_2O_3 structure are not pure γ-Al_2O_3, but rather contain undetermined amounts of incompletely crystallized γ-Al_2O_3. The Al sublattice of Al_2O_3 becomes increasingly ordered during the dehydration of boehmite to α-

Al_2O_3, with γ-Al_2O_3 being the first phase along that transition and, as such, the least ordered phase [43, 54]. In the same vein, during the dehydration of boehmite to γ-Al_2O_3, there is a continuous migration of Al atoms from the boehmite configuration until the characteristic Al distribution of γ-Al_2O_3 is reached [66]. It is possible that a batch of γ-Al_2O_3 produced from a less homogeneous precursor, such as boehmite, consists of varying fractions of incompletely formed γ-Al_2O_3 with slightly differing degrees of Al ordering, depending on the precursor characteristics and heterogeneity in the synthesis procedure and/or equipment. This would explain why the reported empirically refined structure models of γ-Al_2O_3 seem to be slightly different depending on the precursor and synthesis procedure, and why different average structures and Al atom distribtutions have been calculated from nominally "the same" material γ-Al_2O_3. This would also explain why the studies of single-crystal γ-Al_2O_3 (*i.e.*, Smrčok *et al.* [74] and the data reported herein) yielded more similar structures. The influence of the surface also cannot be neglected. The surface of γ-Al_2O_3 normally consists of many coordinatively unsaturated Al sites [118, 170]. These sites influence the analysis of the Al cation distribution, therefore rendering high surface-area γ-Al_2O_3 non-ideal for refining the Al distribution in the bulk model. This complication likely contributes to the difficulty in firmly establishing the Al cation distribution in γ-Al_2O_3 in research efforts to date. Interestingly, some studies have suggested that γ-Al_2O_3 also contains a nm-scale local structure [61, 171]. The formation of a longer-range order in specific regions of the sample is linked to the presence of twin defects (Figure 37) and does not appear to be an inherent property of the γ-Al_2O_3 structure itself.

An interesting prior study determined that the Pinto model was more accurate than the Digne model based on the prediction of surface energies [172]. The results of that investigation are consistent with the findings of this study that the Digne model is less accurate than the Pinto

model. However, the diffraction-based analyses in this work do not provide any additional insight into surface energy predictions. The presence of primarily (111) and (111) textured surfaces in the synthesized γ-Al_2O_3 samples are due to the epitaxial relationship of the γ-Al_2O_3 with the NiAl (100) substrate, not necessarily the inherent surface energies of the material.

6.4 Outcomes

The objective of this study was to determine of the most commonly cited γ-Al_2O_3 models which is most accurate. The cubic spinel-based model has been demonstrated to be the most accurate of the commonly used γ-Al_2O_3 models. However as the results demonstrate, none of the models considered here provide a full satisfactory match to the experimental diffraction, indicating a need to futher refine existing models or develop more accurate ones. The simulated polycrystalline diffraction profiles show how similar the models are, illuminating why conclusive structure determination has proven difficult for γ-Al_2O_3.

The disorder in γ-Al_2O_3 is represented in the cubic spinel-based and tetragonal nonspinel models by fractionally occupied Al sites. Thus, models that set Al atoms in specific sites in the unit cell can introduce a degree of ordering that is not characteristic of γ-Al_2O_3. However, models used in simulations generally require that all atomic sites be fully occupied, and compromise must be made in the creation of supercells or in the choice of model. Therefore, it is prudent to justify the use of and carefully examine results obtained from the fully specified models.

Indexing of the single-crystal SAED pattern confirms that the Smrčok cubic spinel model shows excellent agreement with the γ-Al_2O_3 structure. Overall, the results suggest that the Digne

monoclinic and Paglia tetragonal nonspinel models (and potentially other nonspinel models) may not be as accurate as previously thought.

The next step to improve the accuracy of the γ-Al_2O_3 structure is to further refine the cubic spinel-based model, i.e. the vacancy distribution within that structure. This is accomplished in Chapter 7.0.

7.0 Determination of the Vacancy Distribution over Al Cation Sites in γ-Al_2O_3

The contents of this chapter are included in a manuscript in preparation:

H.O. Ayoola, C.-H. Li, M.P. McCann, S.D. House, J.J. Kas, J. R. Jinschek, J.J. Rehr, W.A. Saidi, J.C. Yang, Determination of the vacancy distribution over Al cation sites in γ-Al_2O_3, Chemistry of Materials.

7.1 Preamble

The results of the study described in Chapter 6.0 established that the average structure of γ-Al_2O_3 is best described by a cubic spinel-like structure, confirming previous studies [71, 74, 88, 89]. The distribution of cation vacancies between tetrahedral and octahedral sites in such a model has not been conclusively determined, however.

In this chapter, a synergistic combination of SAED and EELS experiments and simulations are used to investigate the distribution of Al vacancies in the cubic spinel-based γ-Al_2O_3 structure. SAED patterns are acquired from single-crystal γ-Al_2O_3. The relative intensities of reflections from the SAED patterns are compared to those of simulated diffraction from cubic spinel-based γ-Al_2O_3 models with varied Al vacancy distributions. Simulated EELS spectra for several cubic spinel-based γ-Al_2O_3 models with varied Al vacancy distributions are compared to each other and to experimental high-resolution EELS spectra from single-crystal γ-Al_2O_3 to characterize the coordination and cation arrangement in γ-Al_2O_3. These SAED and EELS results are used in correlation to determine the Al vacancy distribution in the γ-Al_2O_3 structure.

7.2 Study-Specific Methods

7.2.1 Experimental Methods

SAED patterns were acquired using a Hitachi H9500 TEM operated at 200 kV. SAED patterns were acquired from two cross-sectional samples cut at a 90° angle to each other to record diffraction patterns from several different zone axes. Care was taken to avoid saturation of the camera's dynamic range in all diffraction images. The intensity of each spot was determined by fitting a Gaussian to the 2d profile of the spot and calculating the area underneath the Gaussian. Only reflections with intensities above the 2:1 signal-to-noise (SNR) threshold were used to calculate ratios. The spot with the maximum intensity for each set of symmetrically equivalent reflections was used to calculate the intensity ratio.

Al-$L_{2,3}$, O-K, and Al-K EELS spectra were recorded on a monochromated FEI Titan3™ G2 equipped with a high-resolution Gatan Image Filter Quantum® ERS (996) and operated at 300 kV. High-resolution spectra reported in this work were acquired in parallel EELS mode with a collection angle of 18 mrad and convergence angle of 10 mrad. The energy resolution was determined from the full-width half-maximum (FWHM) of the zero-loss peak (ZLP) to be about 0.25 eV. A Gatan cryo-holder was used to minimize electron beam damage by cooling the samples to liquid nitrogen temperature (~77 K), as demonstrated in Chapter 5.0 [173]. EELS spectra were collected as spectrum images, with an acquisition time for each pixel of 0.5 s for the Al-$L_{2,3}$ and O-K edges and 5 s for the Al-K edge. The spectra from all pixels were aligned using the ZLP and summed to increase SNR while avoiding damage. Summed EELS spectra were then background subtracted using either a power law fit for the Al-$L_{2,3}$ and O-K edges or a linear background for the Al-K edge. Deconvolution was found to be unnecessary since the samples were very thin and

little plural scattering was detected in the low-loss spectra collected. Additional smoothing was performed on the Al-K edge using FFT filtering.

7.2.2 Computational Methods

Simulated diffraction data from the cubic spinel models were calculated using SingleCrystal® in the CrystalMaker® suite. The lattice dimensions of the cubic spinel-based model described by Gutierrez et al. [68] were used and the fractional occupancy was systematically changed as necessary before the diffraction data was calculated. The intensity ratios of the same pairs of reflections calculated from the SAED experiments were then calculated. The absolute deviation with respect to the experimental value was calculated for each ratio and all the errors were averaged to obtain the mean absolute deviation (MAD). The vacancy distribution models were then compared; the model(s) with the lowest MAD value indicating the best fit.

Calculations of O-K, Al-$L_{2,3}$ and Al-K edge ELNES for the various γ-Al_2O_3 models were carried out using FEFF9. 12 Å clusters were made from each model for the EELS simulations. Self-consistent field potentials (SCF) [174] and full multiple scattering (FMS) were both calculated with a radius of 6 Å (85–110 atoms) about the absorbing atom. This radius was sufficient to provide converged calculations of the ELNES spectra (Appendix Figure 12). Final state effects were included via the final-state rule core-hole, and the many-pole model self-energy [175]. An instrumental broadening factor of 0.25 eV was added to each calculated spectrum to match the experimental energy resolution.

The FEFF code calculates the ELNES spectrum for an individual selected atom, so the spectra for nonequivalent atom positions were calculated and averaged to generate the simulated spectra for a model. For the cubic spinel structures with varied Al cation distributions, the lattice

dimensions of the cubic spinel-based model described by Gutierrez et al. [68] were used. For each vacancy configuration, a large supercell was made with no vacancies, then Al vacancies were generated randomly to produce the correct stoichiometry and ratio of tetrahedral to octahedral Al. This procedure was carried out multiple times to produce 10 configurations, to account for possible configurational variations. The EELS simulations were then averaged over all configurations. Although γ-Al_2O_3 is likely under some tensile strain due to the substrate, unstrained models were used for simulations as strain is expected to have only a slight effect on the EELS spectra [176-178], see Appendix Figure 13. Furthermore, comparison of the EELS spectra shown here to previously reported EELS spectra from commercial γ-Al_2O_3 [136, 154] show very close similarity confirming that strain has very little effect on the EELS.

Calculated spectra are automatically aligned by FEFF, which gives an approximate chemical shift, as it is an all electron code. A single overall shift of the final averaged spectrum was used to align with experiment. Calculated ELNES spectra are aligned using a main peak in the experimental spectra, after the absolute energies of the experimental spectra have been aligned using the zero-loss peak.

7.3 Results and Discussion

7.3.1 SAED Results and Analysis

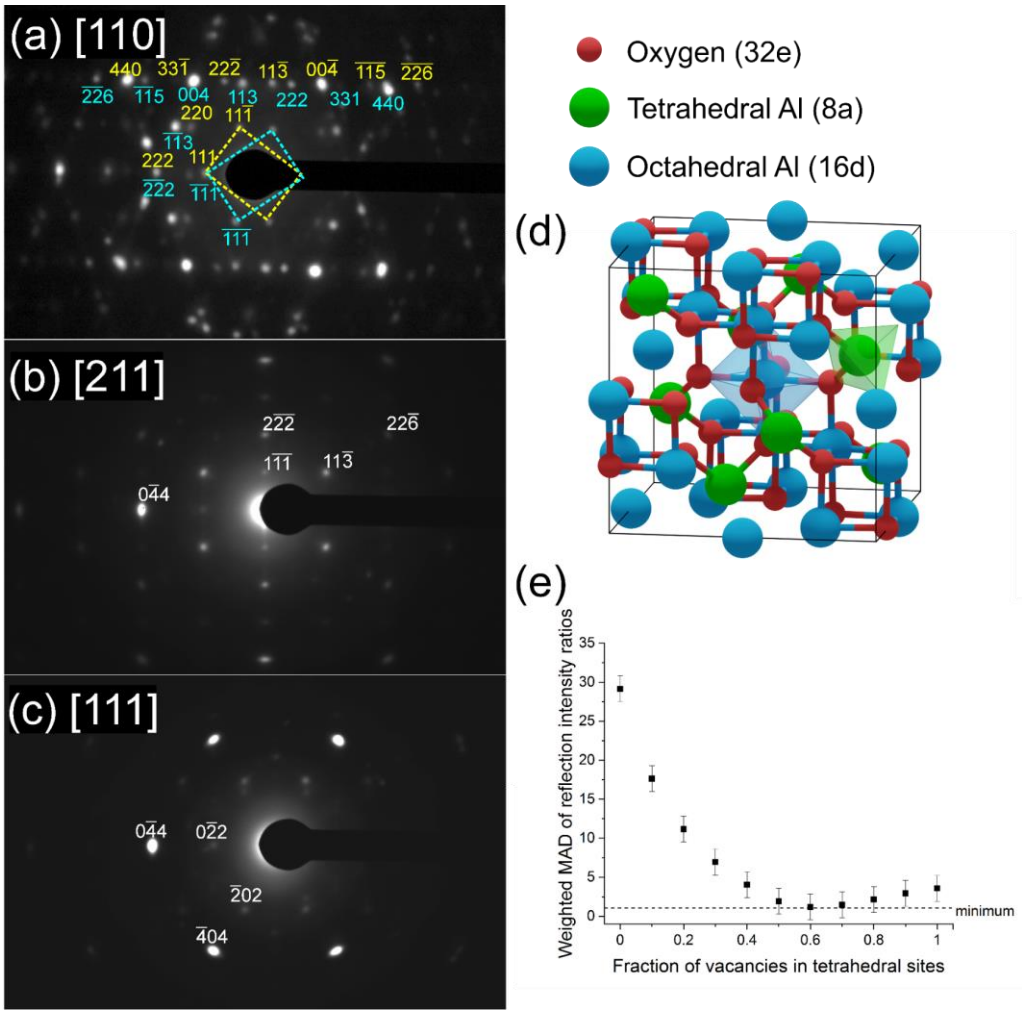

Figure 41. Single-crystal SAED patterns acquired from the (a) [110], (b) [211], and (c) [111] zone axes of γ-Al_2O_3. Reflections used for the intensity ratio analysis are indexed. The [110] pattern exhibits mirrored reflections due to twinning; the reflections from either twin are labeled in either blue or yellow. (d) Schematic of a generic cubic spinel model. (e) Mean absolute deviation (MAD) of reflection intensity ratios relative to the experimental values for each cubic spinel model vs fraction of Al vacancies in tetrahedral sites in the model.

SAED patterns acquired from the single-crystal γ-Al_2O_3 thin films are shown in Figure 41a-c. Three different zone axis (ZA) patterns were imaged. Each ZA pattern was indexed using the cubic spinel model space group ($Fd\bar{3}m$, no. 227). The [110] ZA pattern (Figure 41a) exhibited two mirrored sets of spots, indicating widespread growth twinning about the (111) planes, as previously described in γ-Al_2O_3 produced by thermal annealing of NiAl [54, 88, 105]. Reflections from either of the twin patterns are indexed in cyan below the spot for twin 1 or yellow above the spot for twin 2. In the [211] ZA pattern, the twin patterns overlap since the pattern is mirrored across the (111) planes, hence only one pattern is observed. Anisotropic broadening of reflections can be seen in the SAED patterns, which can be attributed to both the disordered nature of the cation sublattice [179] and to the presence strain in the γ-Al_2O_3 thin film due to the substrate.

Ratios of the reflection intensities were calculated from the SAED patterns shown in Figure 41 since the absolute intensities would not be directly comparable to the simulated SAED reflections. Intensity ratios were calculated from each diffraction pattern for each pair of reflections shown in Table 6. The intensity for each reflection was normalized by the {111} reflection intensity. The twin patterns in Figure 41a were treated as two separate patterns to calculate the intensity ratios. The intensity ratios from each pattern were then averaged to give the values shown in Table 6. Overlapping reflections due to twinning in the [110] ZA pattern (Figure 1a), such as the {333} reflections, were not used. The uncertainty in the averaged intensity ratios was then calculated using the standard error of the mean (SEM):

$$SEM = {}^{\sigma}/_{\sqrt{n}} \tag{7.1}$$

where σ = standard deviation and n = number of values averaged. A weight was given to each pair of reflections based on the intensities of the reflections, such that brighter spots with higher SNR were weighted more heavily. The weight for each reflection was calculated by dividing by the sum

of all the reflection intensities. The weighting values were used to calculate the weighted mean absolute deviation (MAD) for the models.

Table 6. Ratios of intensity of given pairs of reflections from Figure 41a-c.

Reflections	Intensity ratios	Weighting
220/111	0.88 ± 0.12	0.052
113/111	3.34 ± 0.31	0.123
222/111	1.80 ± 0.29	0.067
400/111	14.32 ± 2.19	0.407
440/111	9.49 ± 1.80	0.241
115/111	1.01 ± 0.02	0.053
622/111	1.14 ± 0.05	0.056

For the comparison between the calculated relative intensities and the experimental to be meaningful, the experimental sample must be thin enough to assume kinematical diffraction, i.e. each electron only undergoes a single elastic Bragg scattering event as it passes through the sample. Convergent beam electron diffraction (CBED) patterns revealed no visible fine structure, supporting the assumption of primarily kinematical diffraction.

A schematic of the cubic spinel model with cation sites identified is shown in Figure 41d. The 32 oxygen atoms are set in a face-centered cubic arrangement. The spinel cation sites are highlighted in green and blue; the 8 spinel tetrahedral sites are colored green while the 16 spinel octahedral sites are colored blue. Since the number of Al vacancies required for stoichiometry is fractional and Al vacancies are normally thought to be randomly distributed in the lattice, the unit cell description of the cubic spinel model normally includes some partial occupancy of the Al sites.

Several cubic spinel-based models were generated with systematically varied Al vacancy distributions between tetrahedral and octahedral sites, starting with a model with 0% of vacancies

on tetrahedral sites and increasing in increments of 10% up to a model with 100% of vacancies on octahedral sites. The site occupancy for each model is shown in Appendix Table 4. For each model, the relative intensities of single-crystal diffraction reflections were calculated. The intensity ratios for the reflections given in Table 6 were then calculated. The absolute deviation for each intensity ratio with respect to the experimental value was calculated, and then the weighted MAD was calculated by averaging the deviations for all the intensity ratios using the weights given in Table 1. The unweighted MAD was also calculated for comparison and is shown in Appendix Figure 17. The choice of weighted versus unweighted MAD produced no significant differences in the relative deviations between models, the scaling in absolute deviation being effectively identical for each point.

The weighted MAD for each model is plotted in Figure 41e. The error in each MAD was propagated from the error in the experimental data. To use SAED in such a quantitative way, the sources of error in the experimental intensity ratios must be considered. There are several possible sources of measurement error stemming from the acquisition of the SAED patterns. Dynamic range, nonlinearity, and gain uniformity of the TEM camera contribute to this error. To prevent dynamic range oversaturation, SAED patterns were taken with appropriate beam illumination and exposure time such that there was no intensity saturation observed in the acquired patterns. A factor of 2.5% was added to the error to account for nonlinearity and gain uniformity, based on reported specifications of the TEM camera. No gamma correction was done on the images since gamma correction skews the relative intensities of spots. The spot with the maximum intensity out of a set of symmetrically equivalent spots was used to reduce the error associated with slight misalignment of the zone axis. The cubic spinel model chosen as a basis (lattice parameters and atomic sites) is expected to have an effect, since some models are more or less distorted from the

ideal spinel lattice, such as the cubic spinel-based model described by Smrčok et al [74]. Additionally, a second set of intensity ratios was calculated using different pairs of reflections, to ensure that the choice of reflection pairs did not influence the results. The weighted MAD plot using the second set of intensity ratios (Appendix Figure 18) was nearly identical to that in Figure 41e.

Comparison of the MAD values suggests that the models with 50% – 80% of vacancies placed in tetrahedral sites provide the best fit to the experimental data. The model with 100% of vacancies on octahedral sites exhibits the worst fit to the experimental data. This is contrary to several commonly cited models including those proposed by Gutierrez et al. [68] and Pinto et al. [79] in which placing Al vacancies on octahedral sites is found to be the most stable arrangement. A previous experimental SAED study found that disorder in the Al sublattice is primarily in the tetrahedral positions [75]. This is consistent with the results found here; since in the best fitting γ-Al_2O_3 unit cell structures the octahedral sites are almost fully occupied (because majority of the vacancies are on tetrahedral sites), those sites will be generally more ordered than the tetrahedral sites.

7.3.2 ELNES Results and Analysis

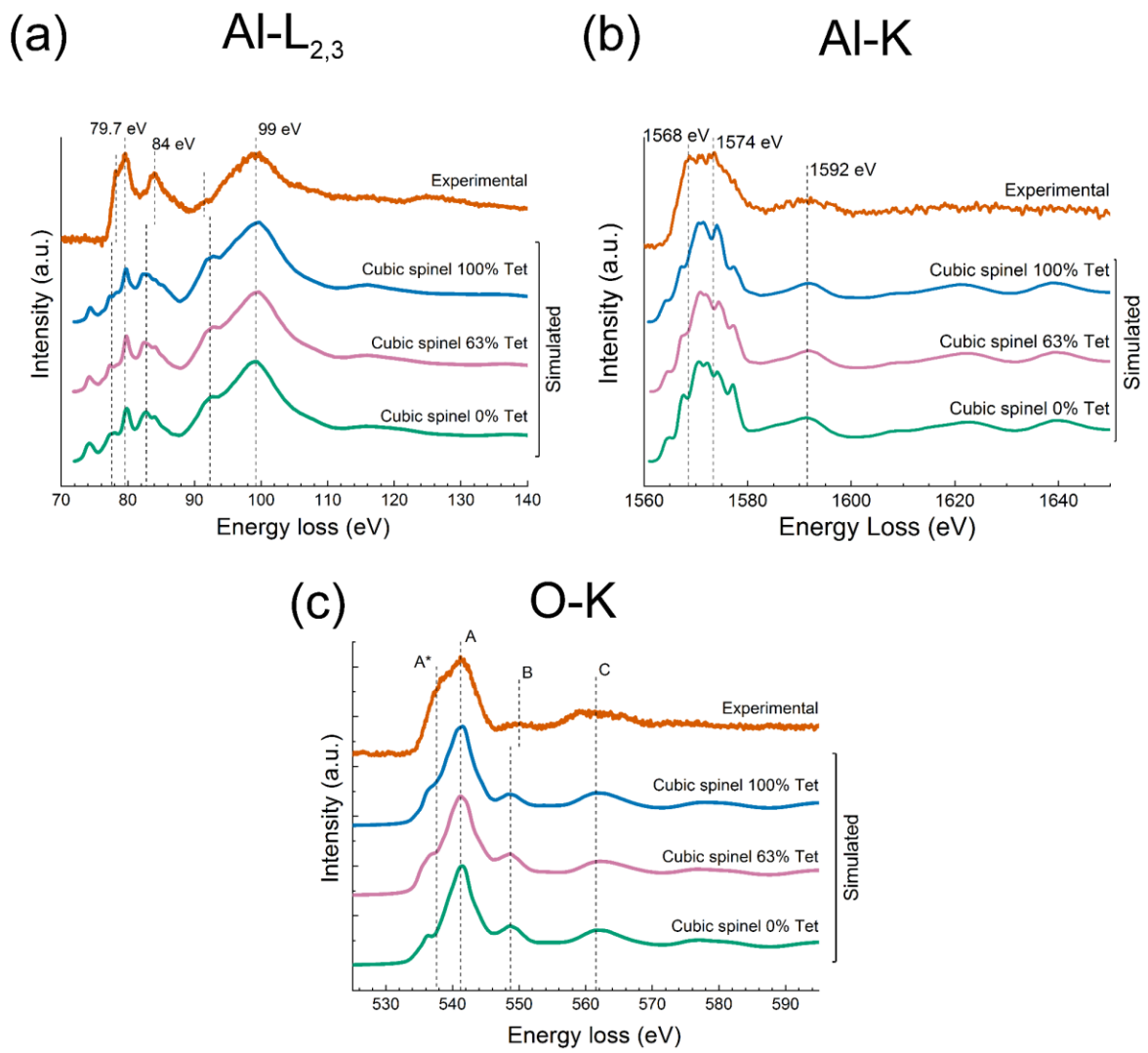

Figure 42. Simulated (a) Al-$L_{2,3}$, (b) O-K, and (c) Al-K edge ELNES from cubic spinel γ-Al_2O_3 models with varied vacancy distributions compared to the experimental γ-Al_2O_3 EELS spectra.

To further probe the Al cation distribution in γ-Al_2O_3, high-resolution EELS spectra were collected. The experimental EELS spectra acquired from the single-crystal γ-Al_2O_3 sample as well as those calculated using FEFF for the spinel-based γ-Al_2O_3 structural models are shown in Figure 42. Considering the experimental EELS spectra, the line shape of the Al-$L_{2,3}$ edge spectrum is nearly identical to that reported by Bouchet and Colliex for γ-Al_2O_3 [136]. The line shape of the experimental O-K edge spectrum is characteristic of the O-K edge EELS spectra of spinels [125, 127, 180, 181], further confirming the spinel-like structure of γ-Al_2O_3. As far as could be determined, no EELS experiment showing the Al-K edge of γ-Al_2O_3 has been reported before. The identifiable features in the experimental EELS spectra are highlighted with dashed lines for comparison with the simulated EELS spectra. The high-resolution experimental EELS spectra without the simulated EELS are shown in Appendix Figure 19.

The Al-$L_{2,3}$ and Al-K EELS edges were first analyzed because of their known sensitivity to Al coordination [94, 136, 182, 183]. Focus was first placed on the Al-$L_{2,3}$ edge due to its inherently higher SNR. Four major features were identified in the experimental Al-$L_{2,3}$ edge spectrum shown in Figure 42a, namely: a sharp peak at 79.7 eV with a prominent shoulder at about 78 eV, a second sharp peak at 84 eV, and a broad peak at 99 eV. To investigate the impact of the vacancy distribution on the EELS, simulated EELS from three cubic spinel-based models with 100%, 63%, and 0% of cation vacancies in tetrahedral sites were compared to the experimental EELS. Qualitative agreement is achieved between all the simulated spectra and the experimental, with all the highlighted peaks present in the simulated spectra, albeit with some shift of relative positions. The peaks at 78 eV and 84 eV are consistently shifted to lower energy-loss in all the calculated spectra, while the bump at 92 eV is shifted slightly higher. There is a small pre-edge peak present in the Al-$L_{2,3}$ ELNES simulations that is not present in the experimental.

To clarify the contributions of tetrahedral vs octahedral Al sites to the EELS, simulated EELS spectra from a single tetrahedral Al and a single octahedral Al are shown in Figure 43 compared to the experimental Al-$L_{2,3}$ edge. The main broad peak is present in both spectra. The other two labeled main peaks at 79.7 eV and 84 eV only clearly align with the octahedral Al spectrum, but their relative intensities are significantly lower in the simulation than in the experimental EELS. Previously reported EELS simulation results of the Al-$L_{2,3}$ edge using the OLCAO method have shown similarly reduced peak intensities [94], suggesting this limitation may not be specific to MS-based calculations. The pre-edge peak at 78 eV is also attributed to a tetrahedral Al contribution. The octahedral Al spectrum closely resembles the experimental spectrum, suggesting the site-averaged spectrum should be dominated by the octahedral Al contribution. This would suggest maximizing the occupancy of Al on octahedral sites (placing vacancies on tetrahedral sites) would increase the fit of the simulated EELS to the experimental EELS.

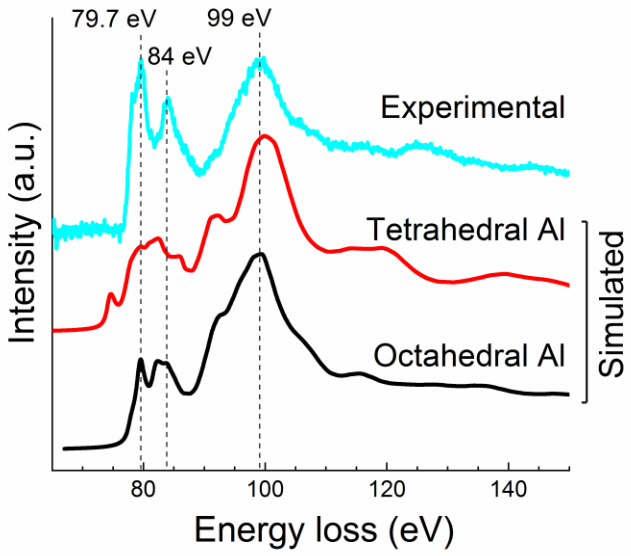

Figure 43. Simulated Al-$L_{2,3}$ edge ELNES for both a single tetrahedral Al atom and a single octahedral Al atom in the cubic-spinel based model compared to the experimental Al-$L_{2,3}$ edge spectrum.

Full- potential effects are the likely cause for disparities between the simulated Al-$L_{2,3}$ edge spectra and the experimental, in particular for the simulated EELS of tetrahedral Al sites. To investigate the accuracy of the EELS simulations for differently coordinated Al atoms, EELS simulations were performed of α-Al_2O_3 (octahedral Al sites only) and $AlPO_4$ (tetrahedral Al sites only). Simulated Al-$L_{2,3}$ spectra of α-Al_2O_3 showed good agreement with experimental data while the simulated Al-$L_{2,3}$ spectra of $AlPO_4$ was less accurate, highlighting the deficiency in modeling EELS for Al occupying tetrahedral sites (Appendix Figure 21). However, it is important to note that $AlPO_4$ has large pores in its structure, which may exacerbate the full-potential effects and render the EELS simulations from tetrahedral Al atoms in that structure even less accurate. FEFF uses the muffin-tin approximation, which approximates the potential field around atoms in a crystal lattice as spheres within which the potential experienced by electrons is symmetric about

the nucleus of the atom, and the potential between the spheres as constant. This approximation can have a significant effect on d-state level splitting [127]. Full-potential based ELNES simulations may remedy some of the undesirable consequences of the muffin-tin potential approach.

For the Al-K edge (Figure 42c), three major peaks are labeled, two overlapping peaks at 1568 eV and 1574 eV, and a broad peak at 1592 eV. The presence of the first two peaks are not clearly identified in the simulations, but the shape of the overlapped peak is present. There is also a small pre-edge peak seen in the Al-K ELNES similar to the Al-$L_{2,3}$ ELNES. Again, there is little difference between the simulated EELS with respect to Al vacancy distribution. The simulated Al-K edge spectra for the models seem to show better agreement with the experiment, likely because the K edge transition is less complex than that of the $L_{2,3}$ edge [184]. Similarly to the Al-$L_{2,3}$ edge, the octahedral Al site seems to match the experimental spectrum closely (Appendix Figure 22), which would be consistent with the Al-K signal being dominated by the octahedral Al contribution.

The calculated Al-$L_{2,3}$ edge EELS spectra shown in Figure 42a show little variation in terms of peak positions or intensities with respect to changes in the Al vacancy distribution. This can be explained because the O lattices of the models are identical, the difference between the models being the fraction of Al occupying tetrahedral vs octahedral sites. However, the range of possible ratios in the spinel model is small, such that with 100% of vacancies on tetrahedral sites the Al fraction in tetrahedral sites is 25%, while if 100% of vacancies are placed on octahedral sites, the Al fraction is 38%. The O-K edge should be more sensitive to changes in the Al vacancy distribution since O coordination is directly affected.

Due to the relative insensitivity of the Al edges to variation of the vacancy distribution, focus was turned to the information provided by the O-K edge EELS. The O-K edge should be more sensitive to changes in the Al vacancy distribution since average O coordination is directly

affected. Three major peak positions are identified in the O K edge spectra (Figure 42c) and labeled A-C. Peak A exhibits a left shoulder, labeled A*. Assuming there are two peaks within the broad A peak and A* shoulder, the position of the shoulder A* in the experimental was determined by fitting two Gaussians to the broad peak (Appendix Figure 23). The positions of peaks A*, A, and C are all consistent between the experimental and calculated spectra. In the simulated O-K edge spectra, the position and intensity of the shoulder A* notably changes as the percentage of vacancies in tetrahedral sites increases. This dependence of the shoulder A* position and intensity on the cation site distribution has been noted in prior studies using EELS when investigating other spinels [125, 181]. This behavior is analogous to the difference seen between O K edge EELS spectra of normal and inverse spinels [127, 181]. Overall, the peak positions in all simulated spectra agree with the experimental spectra to within 1 eV, which is within acceptable error for this method.

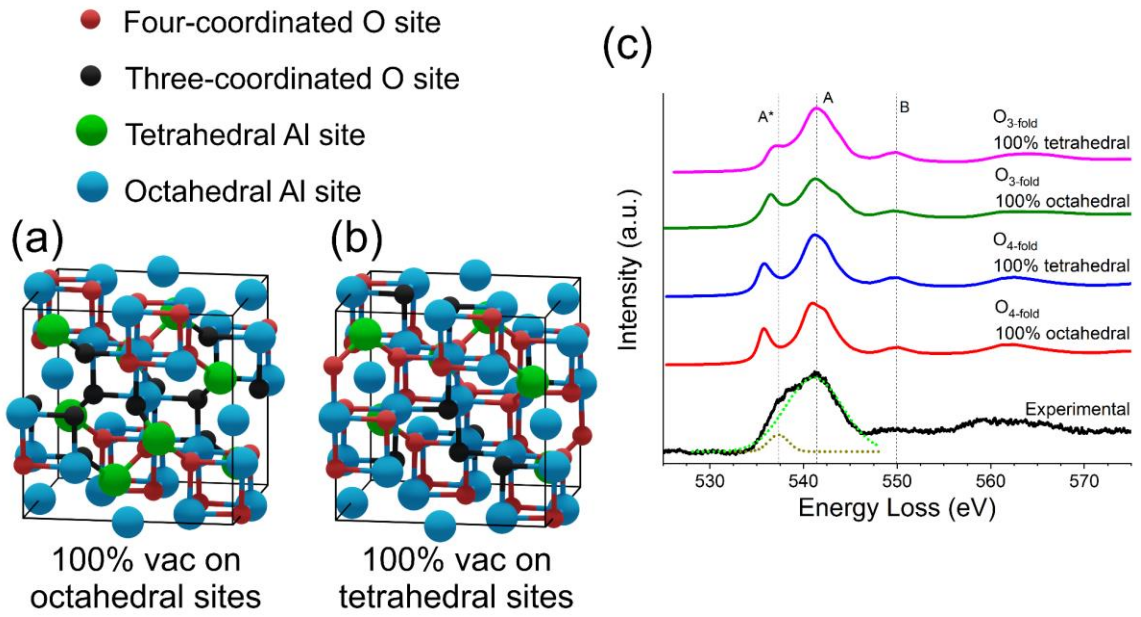

Figure 44. (a) Cubic spinel-based γ-Al_2O_3 model with 100% of vacancies placed on octahedral sites (Gutierrez model [68]). (b) Cubic spinel-based model with 100% of vacancies placed on tetrahedral sites. The two types of O sites, four-coordinated ($O_{4\text{-fold}}$) and three-coordinated ($O_{3\text{-fold}}$), are differentiated by color in both models. (c) Simulated O-K edge EELS spectra for nonequivalent O sites in both models compared to experimental EELS. The components of the experimental broad peak were fit with Gaussians as shown with the dashed fit lines.

The O-K edge EELS spectra of the spinel-based models show systematic differences when varying the Al vacancy placement. This is due to changes in the O coordination caused by the specific arrangement of Al atoms in the structure. In a normal spinel structure with all the spinel sites occupied (e.g. $MgAl_2O_4$), all O sites are four-coordinated, with each O atom having one tetrahedral Al and three octahedral Al nearest neighbors. Since vacancies must be introduced into Al sites to get the right stoichiometry of Al_2O_3, the coordination of some O atoms must necessarily

be reduced from four. Assuming vacancies are not placed in neighboring Al sites in the structure (typically assumed, to maintain the highest charge distribution), then O atoms next to vacant Al sites will have one fewer neighbor and become three-coordinated. Thus, there are two classes of O sites present in the cubic spinel-based γ-Al_2O_3 model regardless of vacancy distribution: four-coordinated O ($O_{4\text{-fold}}$) and three-coordinated O ($O_{3\text{-fold}}$). Schematics of the two extremes of vacancy distribution—100% vacancies on octahedral sites and 100% vacancies on tetrahedral sites—are shown in Figure 44a-b, with the two classes of O sites highlighted in each model. Table 7 summarizes the coordination of the nonequivalent O sites from both models. Regardless of the arrangement of Al vacancies, the $O_{4\text{-fold}}$ sites always have the same nearest neighbor coordination because of the spinel symmetry. The $O_{3\text{-fold}}$ sites however have different nearest neighbor coordination depending on the placement of Al vacancies.

Table 7. Coordination of nonequivalent O sites in the cubic spinel model and number of bonds to each nonequivalent Al site.

O site, spinel model	Tetrahedral Al	Octahedral Al
$O_{4\text{-fold}}$, 100% octahedral vacancies (Type 1)	1	3
$O_{4\text{-fold}}$, 100% tetrahedral vacancies (Type 2)	1	3
$O_{3\text{-fold}}$, 100% octahedral vacancies (Type 3)	1	2
$O_{3\text{-fold}}$, 100% tetrahedral vacancies (Type 4)	0	3

The simulated EELS spectra of each of the four different O sites described in Table 7 are shown in Figure 44b compared to the experimental O-K edge spectrum. In the experimental O-K

edge, the components of the main peak at ~ 541 eV were fit with two Gaussians as shown. The simulated EELS for the $O_{4\text{-fold}}$ sites in both models are unsurprisingly identical. The $O_{3\text{-fold}}$ sites however show some key differences in the A* peak shoulder. The peak shoulder A* is shifted closer to its position in the experimental spectrum for the type 3 O site, and even closer for the type 4 O site. This further confirms that when assuming that the Al vacancies exist primarily on tetrahedral sites, the simulated EELS is in better agreement with the observed experimental data. Thus, the EELS simulations further support the conclusion from the SAED analysis that Al vacancies exist primarily on tetrahedral sites. However, the EELS data does not show enough sensitivity to further refine the results from the SAED analysis.

It is important to note a potential impact of the source of the γ-Al_2O_3 used in this study. γ-Al_2O_3 derived from boehmite has been described as frequently displaying a tetragonal distortion [54, 185]. It is not unreasonable to surmise that the vacancy distribution may differ somewhat based on the synthesis of the investigated γ-Al_2O_3. However, comparison of both the experimental SAED patterns and EELS spectra reported here to previously published data [54, 75, 76, 136] from boehmite-derived γ-Al_2O_3 confirm that the γ-Al_2O_3 synthesized for this study is likely representative of γ-Al_2O_3 in a broad sense, such that the conclusions drawn here could apply to γ-Al_2O_3 produced through either synthesis route.

7.4 Outcomes

The objective of this chapter was to determine the Al vacancy distribution in the spinel-based γ-Al_2O_3 structure. Comparison of the intensity ratios of reflections in the SAED patterns of the models to the experimental SAED patterns revealed that the majority (50% – 80%) of Al

vacancies exist on tetrahedral sites, corresponding to 27% – 31% of Al atoms occupying tetrahedral sites. This result was corroborated by comparison of high-resolution EELS experiments with simulated EELS spectra from systematically altered γ-Al_2O_3 models. However, the relative lack of sensitivity of the EELS to vacancy distribution rendered it unable to further refine the conclusion from the SAED analysis.

8.0 EELS-Based Studies of Common γ-Al_2O_3 Bulk Structure Models and Subsequent Description of the Local Bonding at the Pt/γ-Al_2O_3 (111) Interface Using a Tractable Interfacial Model

The contents of this chapter are included in a manuscript in preparation (1) and in a published manuscript (2):

(1) H.O. Ayoola, C.-H. Li, M. McCann, S.D. House, J. Jinschek, W.A. Saidi, J.C. Yang, Assessing the structure of γ-Al_2O_3 through EELS experiments and simulations, The Journal of Physical Chemistry C.

(2) H.O. Ayoola, C.S. Bonifacio, Q. Zhu, C.-H. Li, S.D. House, J.J. Kas, J. Jinschek, J.J. Rehr, W.A. Saidi, J.C. Yang, Probing the Local Bonding at the Pt/γ-Al_2O_3 Interface, The Journal of Physical Chemistry C, (2020).

8.1 Preamble

The results discussed in Chapters 6.0 and 7.0 have clearly demonstrated that the most accurate structure model of γ-Al_2O_3 is the cubic spinel-based model with 27% - 31% of Al atoms in tetrahedral sites (the balance in octahedral sites). However, this knowledge does not necessarily render the other less accurate models immediately useless. The cubic spinel-based model contains fractionally occupied Al sites, but for most calculations, a model with all sites fully occupied must be used. To use the cubic spinel-based model for such calculations, a large supercell must first be made with the right stoichiometry. Many such supercells must then be generated to account for all

the possible configurations of the fully occupied Al lattice since the Al vacancies are not necessarily ordered. The sought-after calculations must then be run for each configuration and then intelligently averaged. This procedure can quickly become intractable depending on the properties being calculated. As such, it is worthwhile to continue to consider other models for simulations, especially since these additional models are still widely used.

Since it also provides local electronic information, EELS provides complementary information to the electron diffraction-based investigation described earlier in Chapter 6.0. Thus, EELS provides an avenue to evaluate the accuracy of the electronic structure predicted by the commonly cited γ-Al_2O_3 models. EELS has also been used to probe the structure and bonding of interfaces, primarily in studying composite materials [186, 187].

Few EELS spectra of γ-Al_2O_3 have been reported, and of those that have been published, the best energy resolution achieved is only about 0.6 eV [136, 154]. The high-resolution EELS used in this project achieved an energy resolution of 0.25 eV. The presence of both tetrahedral and octahedral Al in the γ-Al_2O_3 structure means that existing EELS spectra of octahedral Al such as those from α-Al_2O_3 or tetrahedral Al such as $AlPO_4$ do not provide perfect reference fingerprints. It is therefore necessary to be able to simulate the EELS spectra to study the electronic and chemical properties of γ-Al_2O_3 using EELS.

This chapter is divided into two parts. In the first part, simulated EELS for the commonly cited γ-Al_2O_3 models described in Section 1.4.3 were compared to each other and to high-resolution experimental EELS spectra from single-crystal γ-Al_2O_3 thin films. In the second part, the interfacial bonding between Pt and γ-Al_2O_3 was investigated using experimental and simulated EELS with relatively simple interfacial models based on the monoclinic nonspinel model of γ-Al_2O_3.

8.2 Study-Specific Methods

8.2.1 Experimental Methods

The experimental bulk EELS spectra displayed in this chapter are the same as those from Chapter 7.0. Aberration-corrected STEMs used to acquire STEM and EELS data for the interface study included a TEAM 0.5 S/TEM (operated at 80 and 200kV), a Hitachi STEM (operated at 200 kV) and a JEM JEOL 2100F-AC S/TEM (operated at 200 kV). On those microscopes, EELS spectra and spectral images were acquired with a dispersion of 0.3 eV/channel, energy resolution of about 0.5 eV, and collection and convergence semi-angles of 16 mrad. Electron beam damage to the sample was prevented by cooling the sample to a working temperature of -145°C (-186°C in the monochromated EELS experiments) using a Gatan cryo-holder, as demonstrated in Chapter 5.0 and Appendix E.3. The spectra from all pixels were aligned using the ZLP or the C-K edge from the protective carbon layer (from FIB) and summed to increase SNR while avoiding damage. Summed EELS spectra were then background subtracted using a power law fit. Deconvolution was found to be unnecessary since the samples were very thin and little plural scattering was detected in the low-loss spectra collected.

8.2.2 Computational Methods

Calculations of O-K, Al-$L_{2,3}$ and Al-K edge ELNES for the various γ-Al_2O_3 models were carried out using FEFF9. 12 Å clusters were made from each model for the EELS simulations. Self-consistent field potentials (SCF) [174] and full multiple scattering (FMS) were both calculated with a radius of 6 Å (85–110 atoms) about the absorbing atom. For the interface study,

a full multiple scattering (FMS) radius of 8 Å was used. Final state effects were included via the final-state rule core-hole, and the many-pole model self-energy [175]. An instrumental broadening factor of 0.25 eV was added to each calculated spectrum to match the experimental energy resolution.

The interface models were optimized using first principles DFT calculations carried out within the PBE [143] exchange-correlation functional and PAW pseudopotentials [188, 189] as implemented in VASP. The (111) surface of γ-Al_2O_3 was modeled using the monoclinic non-spinel model proposed by Digne et al. [78], to correlate with the surface orientation obtained from the oxidation of NiAl (110). Details of the DFT calculations can be found in Appendix E.

Since FEFF simulates the EELS spectra from a single chosen central atom, all atoms of the same type (i.e. O vs. Al) in non-equivalent positions in the model were averaged for the bulk spectra. For the cubic spinel-like and the tetragonal nonspinel models with partially occupied Al sites, a large supercell was first made with no vacancies, then Al vacancies were generated randomly to produce the correct stoichiometry and ratio of tetrahedral to octahedral Al. This procedure was carried out multiple times to produce 10 configurations, to account for possible configurational variations. The EELS simulations were then averaged over all configurations.

Calculated spectra are automatically aligned by FEFF, which gives an approximate chemical shift, as it is an all electron code. A single overall shift of the final averaged spectrum was used to align with experiment. Calculated ELNES spectra are aligned using a main peak in the experimental spectra, after the absolute energies of the experimental spectra have been aligned using the zero-loss peak. The simulated spectra for the interface models were aligned to each other using the main Al-L_2 or O-K edge peak. The simulated bulk EELS signal was aligned to the

experimental EELS signal, and thereafter all simulated spectra were aligned to the simulated bulk EELS signal.

8.3 Assessment of Bulk Models Using EELS

Table 8. γ-Al_2O_3 models considered for EELS simulations and relevant properties.

Unit cells	Cubic spinel-like model [74]	Monoclinic spinel-based model [79]	Tetragonal nonspinel model [62]	Monoclinic nonspinel model [78]	α-Al_2O_3 [190]
Space group	$Fd\bar{3}m$ (No. 227)	B112/m (No.12)	$I4_1/amd$ (No. 141)	$P2_1/m$ (No. 11)	$R\bar{3}c$ (No. 167)
Lattice parameters: a, b, c (Å)	a=b=c=7.9382	a=9.7887, b=13.7120, c=5.6973	a=b=5.652 c=7.871	a=5.587, b=8.413, c=8.068	a=b=4.754 c=12.99
α, β, γ	$\alpha=\beta=\gamma=90°$	$\alpha=\beta=90°$ $\gamma=89.3062°$	$\alpha=\beta=\gamma=90°$	$\alpha=\gamma=90°$ $\beta=90.59°$	$\alpha=\beta=90°$ $\gamma=120°$
Al distribution (%)	Al_{tet}: 36.7, Al_{oct}: 63.3	Al_{tet}: 37.5, Al_{oct}: 62.5	Al_{tet}: 29.3, Al_{oct}: 70.7	Al_{tet}: 25, Al_{oct}: 75	Al_{oct}: 100
O distribution (%)	N/A	$O_{3\text{-fold}}$: 50, $O_{4\text{-fold}}$: 50	N/A	$O_{3\text{-fold}}$: 33.3, $O_{4\text{-fold}}$: 66.7	$O_{4\text{-fold}}$: 100
Average Al-O bond length (Å)	1.898	1.893	1.932	1.899	1.912

The structural information of the models used for the EELS simulations are shown in Table 8. α-Al_2O_3 is included for comparison. Supercells were made for the cubic spinel-like and tetragonal nonspinel models since the reported unit cells contain partially occupied sites and such models cannot be used for multiple scattering EELS simulations; this is also why no O distribution is reported for those models. The cubic spinel-like model is named as such because although the structure is cubic and Al atoms are placed in spinel sites, a small fraction (6%, ~1 Al atom per unit

cell) of Al atoms are placed in nonspinel sites. In the nonspinel models on the other hand, a large fraction of Al atoms is found in nonspinel sites; 27% in the tetragonal model and 68% in the monoclinic model.

The simulated EELS for the nonspinel models are shown in Figure 45 in comparison to the experimental EELS spectra. The major features in the Al-$L_{2,3}$ edge spectrum are all present in the simulated spectra. Specifically, the cubic spinel-like model exhibits all the peaks seen in the experimental spectrum, with some small shifts in peak position. The pre-edge peak seen in the spinel-based models is also seen, suggesting it may be caused by tetrahedral Al specifically in the spinel arrangement. The tetragonal nonspinel model also exhibits all the peaks from the experimental, but the relative intensity of the shoulder peak at 78 eV is too high. This is because this model has a relatively high fraction of Al atoms in the 16c nonspinel octahedral site (8c in the tetrahedral space group) shown in Figure 4. The contribution to that peak comes primarily from that nonspinel octahedral Al atom (Figure S8). There is also splitting of the 99 eV peak, due to the distortion of the Al octahedra in the model, similarly to crystal field splitting due to Jahn-Teller distortion [191]. The monoclinic nonspinel model shows the least agreement. Both the shoulder at 78 eV and the peak at 84 eV are shifted by 2+ eV. This is because the signal is dominated by the octahedral Al contribution, with 75% of Al atoms in octahedral sites. Slightly changing the lattice parameter of the model can also cause a relative peak shift, due to changes of bond strengths and overlapping of orbitals [191].

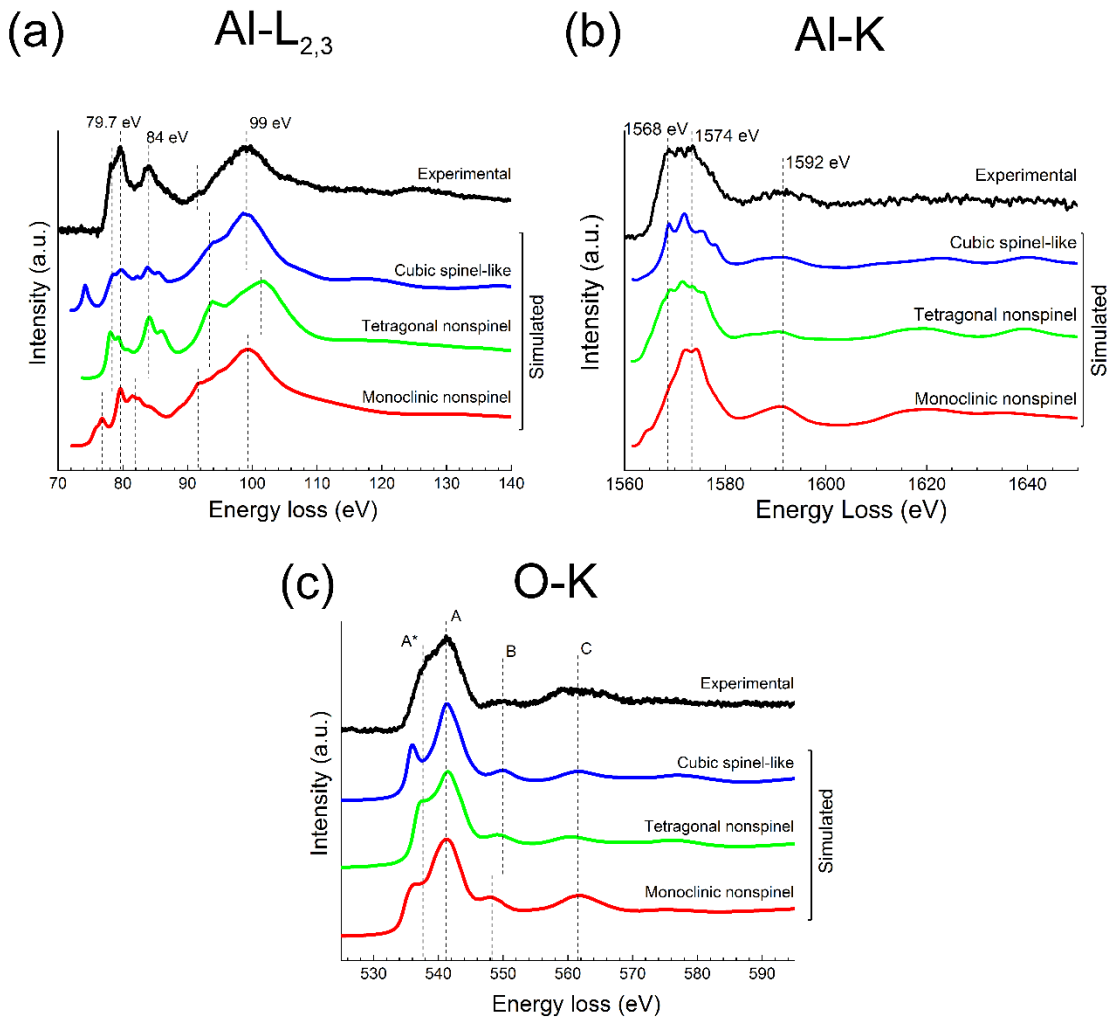

Figure 45. Simulated (a) Al-$L_{2,3}$, (b) O-K, and (c) Al-K edge ELNES from nonspinel γ-Al_2O_3 models compared to the experimental γ-Al_2O_3 EELS spectra.

The simulated Al-K spectra also exhibit good agreement with the experimental spectra. The Al-K edge highlights the importance of the tetrahedral Al contribution; in the monoclinic nonspinel model which has the lowest amount of tetrahedral Al, the main peak is not as broad as it is for the other models or in the experimental EELS. This is because the contribution of the tetrahedral Al atoms serves to broaden the peak, as shown in the site-specific simulations from the cubic spinel models (Figure S6).

With respect to the O-K edge simulations, the cubic spinel-like and tetragonal nonspinel models show better agreement to the experimental EELS than the spinel-based models, since all the peaks are present at the correct positions, including peak B. As with the spinel-based models, the shoulder A* is further away from peak A in the simulated EELS, than in the experimental, except for the tetragonal nonspinel model. This is because of the distribution of O coordination types present in those models. The placement of some Al atoms in nonspinel sites creates a larger range of FNN O coordination types than in the spinel-based models. However, in the cubic spinel-like model and the monoclinic nonspinel model, the O-K edge signal is dominated by the contribution of type 1 and type 3 O sites, which explain why the shoulder A* is further away from the main peak A, similarly to the monoclinic spinel-based model. The tetragonal nonspinel model exhibits a near-perfect match of all peak positions and relative intensities to the experimental EELS, including the shoulder A*. This model has the highest number and widest distribution of different O FNN coordination types (Table 3), suggesting that the disorder induced by this arrangement is representative of the γ-Al_2O_3 structure. Previous molecular dynamics study of the γ-Al_2O_3 structure suggested the presence of varying O coordinations [69], which is supported by these results.

Table 9. Relevant properties nonspinel supercell models.

Nonspinel Models	Al ratio in spinel vs nonspinel sites	O distribution (%)
Cubic spinel-like model	94:6	$O_{2\text{-fold}}$: 3.1 $O_{3\text{-fold}}$: 50 $O_{4\text{-fold}}$: 37.5 $O_{5\text{-fold}}$: 9.4
Tetragonal nonspinel model	73:27	$O_{2\text{-fold}}$: 10.9 $O_{3\text{-fold}}$: 40.6 $O_{4\text{-fold}}$: 32.8 $O_{5\text{-fold}}$: 9.4 $O_{6\text{-fold}}$: 6.3

It is important to mention that for the supercell models, the relative presence of different types of oxygen coordination is dependent on how the supercell is made. Even with a given percentage of Al atoms in tetrahedral vs octahedral and spinel vs nonspinel sites, the exact placement of Al vacancies in the supercell directly affects the distribution of O coordination types. However, this is not expected to have a significant effect on the simulated EELS from the cubic spinel-like model, since the number of Al atoms in nonspinel sites is so small that the Al arrangement still primarily follows spinel symmetry.

The necessity of disorder to more accurately describe the local γ-Al_2O_3 structure as demonstrated here explains why similarities have been found with amorphous Al_2O_3 [94, 192]. The fractional occupancy of Al sites in the cubic spinel-like and tetragonal nonspinel models implicitly describe a level of disorder that is not present in the other models. However, the average structure of γ-Al_2O_3 is well-described by cubic spinel-based models. The presence of Al atoms in nonspinel sites cannot be summarily ruled out, as it is found to improve the agreement of simulated

EELS to the experiment, but the results also show that placing too many Al atoms in nonspinel sites also reduces the model accuracy. The cubic spinel-like model with a small fraction of Al atoms in nonspinel sites to increase the O site distribution appears to be the best compromise to create a local γ-Al_2O_3 model.

8.4 Pt/γ-Al_2O_3 (111) Interface Bonding Investigation

An overview dark-field image of the cross-sectional Pt/γ-Al_2O_3 FIB lift-out sample is shown in Figure 24. 2-3 nm diameter Pt NPs deposited by e-beam evaporation, which appear bright in intensity, can be seen covering the γ-Al_2O_3 surface. Above the NPs, there is a protective carbon layer, which was deposited to protect the sample surface during FIB sample preparation. Below the γ-Al_2O_3, part of the NiAl substrate is visible. Large voids formed at the NiAl/γ-Al_2O_3 interface during thermal oxidation are also visible. Further in-depth characterization details of the structure and composition of the Pt/γ-Al_2O_3 samples can be found in previous reports [88, 193].

The edges used for the ELNES analysis were the Al-$L_{2,3}$ and O-K edges. The other major Al edge, the Al-K edge at ~1560 eV, did not provide significant enough signal-to-noise to distinguish interfacial contributions from the bulk. While Pt edges would be ideal to reveal the interfacial Pt bonding, the major Pt edges occur at very high energy losses (>2 keV). The signal-to-noise ratio for EELS edges above 2 keV is very low and fine structure analysis is impractical, therefore the major Pt edges could not be used.

8.4.1 Al-$L_{2,3}$ Edge ELNES

High-angle annular dark-field (HAADF) STEM images and Al-$L_{2,3}$ edge EELS spectra of the Pt/γ-Al_2O_3 interface are included in Figure 46. Figure 46a shows the Pt/γ-Al_2O_3 interface prior to EELS acquisition. Al-$L_{2,3}$ EELS spectra at the Pt/γ-Al_2O_3 interface were acquired as an 8 x 8 pixel spectrum image (SI), which is demarcated with a box (cf. Figure 46c). An EELS spectrum was acquired at each pixel. Figure 46b shows the dark-field (DF) image of the region within the box in Figure 46a. . The specific pixels where EELS spectra were extracted from and displayed in Figure 46d are highlighted with the colored squares in Figure 46b and Figure 46c. Four pixels were summed for both the representative interface and bulk EELS spectra to increase the signal-to-noise ratio and show the near-edge fine structure more clearly. The representative Al-$L_{2,3}$ edge EELS spectra from the bulk γ-Al_2O_3 has the expected line shape when compared to previously reported Al-$L_{2,3}$ edge EELS spectra of γ-Al_2O_3 [136]. The major difference in the interface spectra is an increase in intensity of the peak labeled a* (in Figure 46d). This peak has been previously attributed to the presence of tetrahedrally-coordinated Al atoms in the alumina structure [136, 182, 184, 186, 194]. Since γ-Al_2O_3 contains both tetrahedrally- and octahedrally-coordinated Al atoms, the increase in intensity of the tetrahedral Al fingerprint at the interface suggests that the fraction of tetrahedral Al at the interface is greater than that in the bulk γ-Al_2O_3.

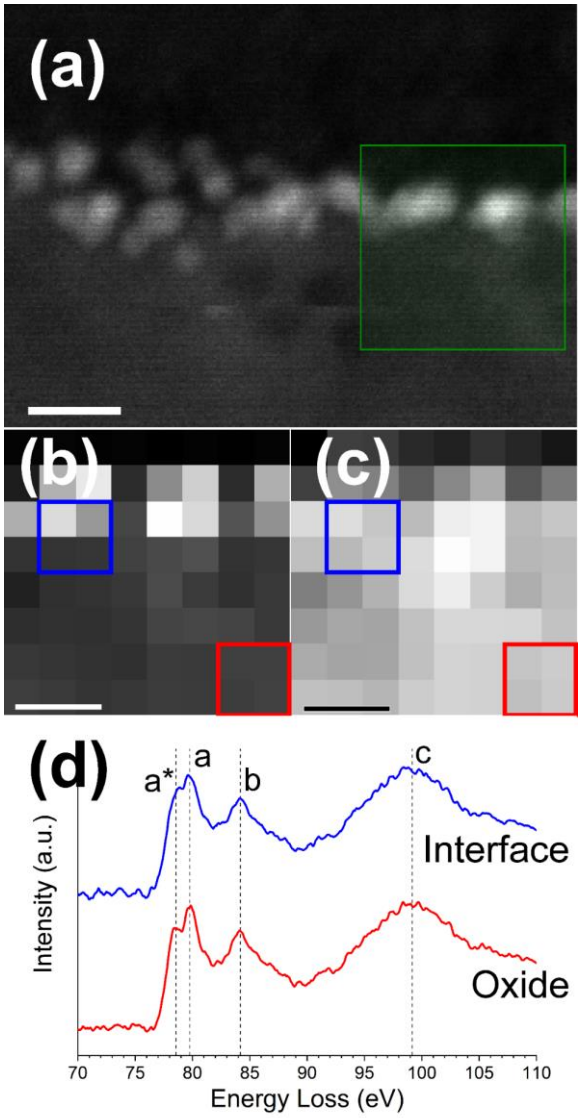

Figure 46. (a) High-angle annular dark-field (HAADF) image of the Pt/γ-Al_2O_3(111) sample with the area of EELS spectrum image acquisition shown with the box. Scale bar = 5 nm. (b) DF image of the area within the box marked in (a), with each pixel having an associated EELS spectrum. Scale bar = 2 nm. (c) Spectrum image of the area within the box marked in (a), where each pixel contains an Al-$L_{2,3}$ edge EELS spectrum. Scale bar = 2 nm. (d) Al-$L_{2,3}$ edge EELS spectra extracted from the pixels marked by boxes in the DF(b) and SI (c) image. The plotted EELS spectra from each box consists of the summed EELS spectra from the enclosed pixels.

8.4.2 O-K Edge ELNES

The analogous HAADF STEM images and O-K edge EELS spectra of the Pt/γ-Al_2O_3 interface are included in Figure 47. The Pt/γ-Al_2O_3 interface prior to EELS acquisition is shown in Figure 47a. In this case, EELS spectra at the Pt/γ-Al_2O_3 interface were acquired as a 7 x 7 pixel spectrum image, again demarcated with a box. Figure 47b shows the DF image of the region within the box in Figure 47a. Figure 47c shows the corresponding spectrum image. EELS spectra were extracted from the pixels enclosed in the colored squares and displayed in Figure 47d. Two pixels were summed for both the representative interface and bulk EELS spectra. The representative O-K edge EELS spectra from both the bulk γ-Al_2O_3 and the Pt/γ-Al_2O_3 interface have the expected line shape when compared to previously reported O-K edge EELS spectra of γ-Al_2O_3 [136]. However, an O-K edge pre-peak was observed at ~ 534 eV in spectrum imaging pixels acquired at the Pt/γ-Al_2O_3 interface. This pre-peak was only observed at the interface and nowhere else in the sample; however, it was observed at about 50% of Pt/γ-Al_2O_3 interfaces that were examined. Due to the low relative intensity of this peak, the experiment was replicated with different microscopes with different noise profiles, and the pre-peak was still observed only at the interface (Appendix Figure 24). This pre-peak appeared without observable beam damage, as confirmed by the HAADF image of the region after EELS SI acquisition (Appendix Figure 25).

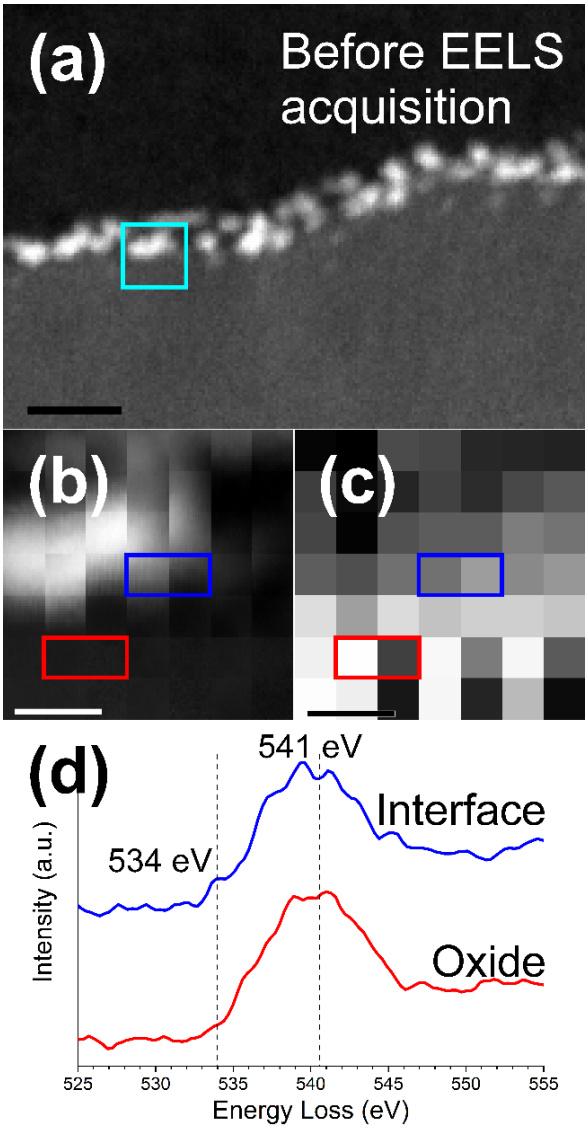

Figure 47. (a) High-angle annular dark-field (HAADF) image of the Pt/γ-Al_2O_3(111) sample with the area of EELS spectrum image acquisition shown with the box. Scale bar = 10 nm. (b) DF image of the area within the box marked in (a), with each pixel having an associated EELS spectrum. Scale bar = 2 nm. (c) Spectrum image of the area within the box marked in (a), where each pixel contains an O-K edge EELS spectrum. Scale bar = 2 nm. (d) O-K edge EELS spectra extracted from the pixels marked by boxes in the DF (b) and SI (c) image. The plotted EELS spectra from each box consists of the summed EELS spectra from both enclosed pixels.

8.4.3 Confirmation of Electron Beam Damage Suppression

At room temperature and both 200 kV and 80 kV, the γ-Al_2O_3 support was rapidly damaged by the electron beam (Appendix Figure 26), as evidenced by the formation of holes drilled by the electron beam (Figure 48a). At 80 kV, the beam damage was slowed, however the sample was still rapidly damaged, particularly during EELS spectra acquisition. O-K edge EELS spectra acquired around the area of beam damage showed an O-K edge pre-peak, as seen in Figure 48b. The intensity of this O-K edge pre-peak varied as a function of exposure time and field of view during EELS acquisition (Figure 25). This is a distinctive attribute of the damage-induced pre-peak that has been noted in O-K edge EELS of other oxides [140]. In contrast, the interface pre-peak did not appear to vary in intensity due to beam exposure, similarly to previously noted O-K edge pre-peaks seen in EELS spectra from other spinel materials [180]. In addition, the main peak in the beam-damaged O-K edge EELS spectrum appears to be shifted higher in energy by 1.6 eV compared to the interface O-K edge EELS. The shift of peak energies due to beam damage has also been previously noted for other oxides [140, 195].

The presence of a pre-peak at 534 eV that differs from the beam damage pre-peak has been noted previously [130, 136]. Jiang et al. suggested that the pre-peak at 534 eV is due to dangling or undercoordinated O atoms [147]. Colliex et al. proposed from the perspective of molecular orbital theory that the 531 eV pre-peak is from the t_{2g} orbital while the 534 eV pre-peak is from the e_g orbital [136]. Refer to Chapter 5.0 for a more in-depth exploration of beam damage in this system.

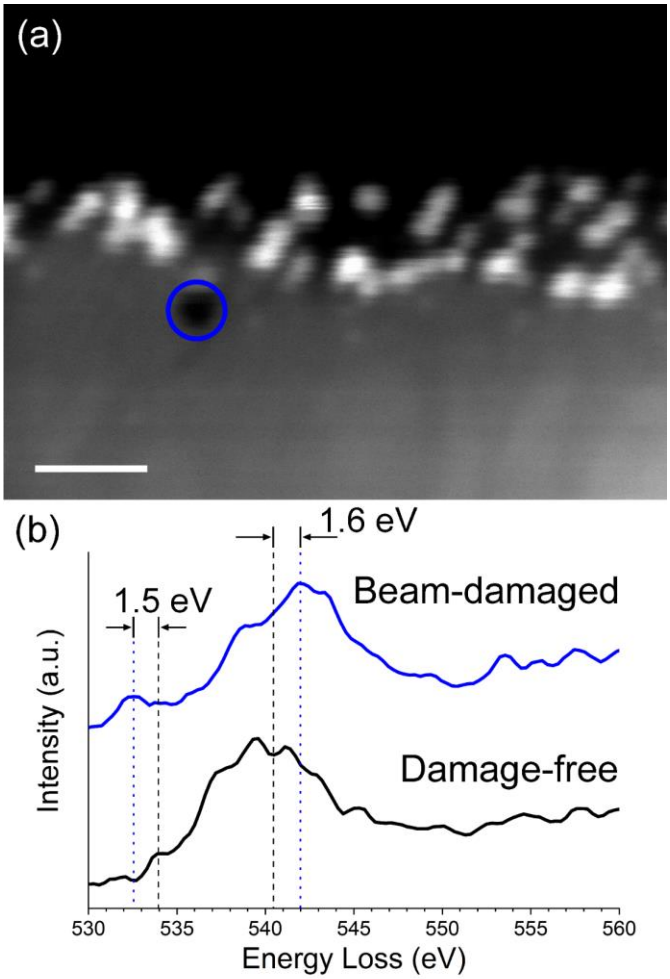

Figure 48. (a) HAADF image of a region of the Pt/γ-Al_2O_3 cross-sectional sample where the electron beam has drilled a hole creating visible beam damage. Scale bar = 10 nm. (b) O-K edge EELS spectrum acquired from the area around the drilled hole compared to the EELS spectrum from the Pt/γ-Al_2O_3 interface shown in Figure 47d.

The energy resolution of the experiment allows me to confidently suggest that the 1.5 eV difference in peak position between the beam damaged O-K edge EELS and the interface O-K edge EELS (Figure 48) are due to different phenomena occurring. Energy stability of the electron beam was not expected to be an issue as energy instability should shift the entire spectrum, rather than a single peak. This suggests that the presence of this O-K edge pre-peak is related to a characteristic O bonding state or environment present at the Pt/γ-Al_2O_3 interface, rather than a result of beam damage.

To confirm the fingerprint-based interpretations of the EELS spectra and develop a corresponding model of the Pt/γ-Al_2O_3 interfacial bonding, DFT was used to generate different possible interface structures and calculate their respective O-K edge near-edge EELS spectra. It is important to note that despite the endeavor to collect EELS spectra in the flattest possible areas of the interface, the alumina surfaces in the probed areas were not atomically flat. However, the surface need not be atomically flat since the goal is not to model the entire NP and support surface, but rather the bonding interaction between the abundant (111) terraces and the Pt atoms at the interface.

8.4.4 Pt on γ-Al_2O_3 (111) Surface Bonding Motif Models

8.4.4.1 γ-Al_2O_3 Model Selection

While the cubic spinel-based model of γ-Al_2O_3 has been confirmed to be the most accurate model in these single-crystal γ-Al_2O_3 samples [88, 196, 197]—the nonspinel model proposed by Digne et al [78] has been widely used to create surface models for theoretical simulations [82, 118, 198-202]. The monoclinic nonspinel model has the benefit over the cubic spinel model of fully occupied lattice sites and the benefit over the remaining models of the smallest unit cell. This

means a large supercell is not needed for calculations and computational expense is significantly lowered. The simulated O-K edge EELS also exhibits a good fit to the experimental O-K edge EELS (Figure 45). Comparison of the simulated O-K edge EELS from the monoclinic nonspinel to that from a cubic spinel model [68] (with varying Al site distributions based on reported literature values) is shown in Figure 49 compared to experimental EELS from the γ-Al_2O_3 support. The monoclinic nonspinel model reproduces the O-K edge EELS as accurately as the cubic spinel-based models. Based on these criteria, the monoclinic nonspinel model was used for further EELS simulations.

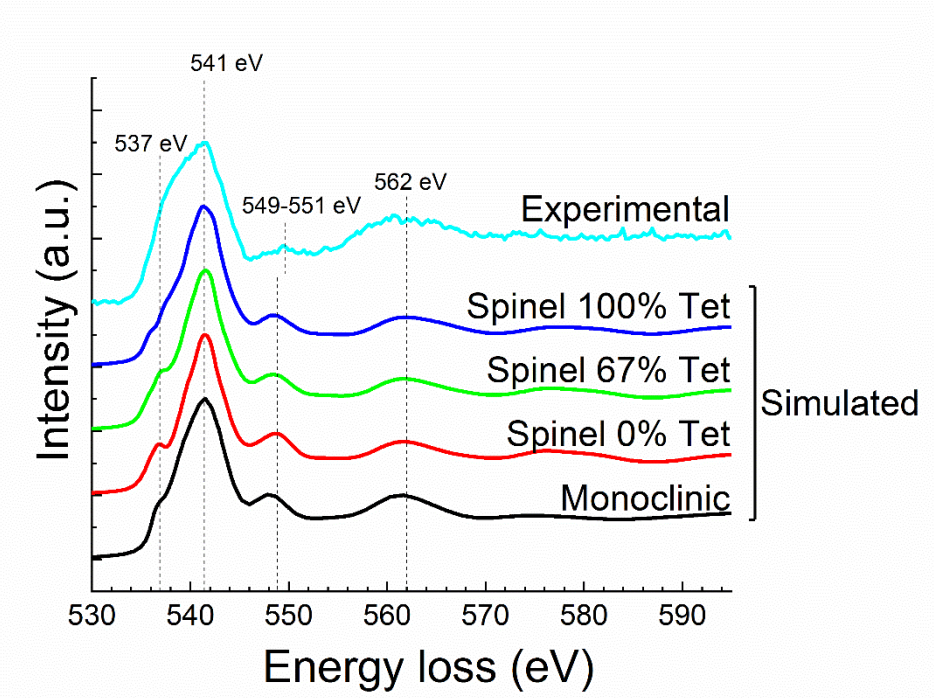

Figure 49. Experimental and simulated O-K edge EELS spectra of γ-Al_2O_3. The distributions of cation vacancies in tetrahedral (Tet) sites vs. octahedral (Oct) sites in the cubic spinel models were varied and compared with the Digne monoclinic nonspinel model.

8.4.4.2 Pt Adsorption and O Vacancies on γ-Al_2O_3 (111) Surface

The adsorption site for a Pt atom and nanocluster on the γ-Al_2O_3 (100) and (110) surfaces has been studied previously using DFT calculations [118, 203], but limited work has been done on the γ-Al_2O_3 (111) surface. Figure 50a shows the γ-Al_2O_3 (111) surface model used. The unit cell is marked by the dashed lines, with the wavy lines showing where the cell was truncated for the figure. On the top surface layer, there are four Al atoms, two of which are in 3-fold planar sites and are labeled as Al^p atoms, and two of which are in 3-fold truncated tetrahedral sites and are labeled as Al^t atoms. This surface model is supported by previous work using a defective spinel-based model [204] and a nonspinel model [205], both confirming the presence of 3-coordinated Al atoms on the optimized (111) surface. Therefore, the conclusions of this investigation are expected to be independent of the choice of a spinel-based or nonspinel model, and the use of the simpler monoclinic nonspinel model is justified. It has been proposed that on the γ-Al_2O_3 surface, the presence of oxygen vacancies could play a crucial role in modifying the electrical properties of γ-Al_2O_3 [120]. Therefore, the formation energy of an oxygen vacancy on the γ-Al_2O_3 (111) surface was investigated in this study. As expected for non-reducible oxides such as γ-Al_2O_3, the energy penalty for vacancy formation is high, ranging from 3.77 – 6.02 eV, on any of the 12 γ-Al_2O_3 (111) surface oxygen sites labeled in Figure 50 (Appendix Table 7).

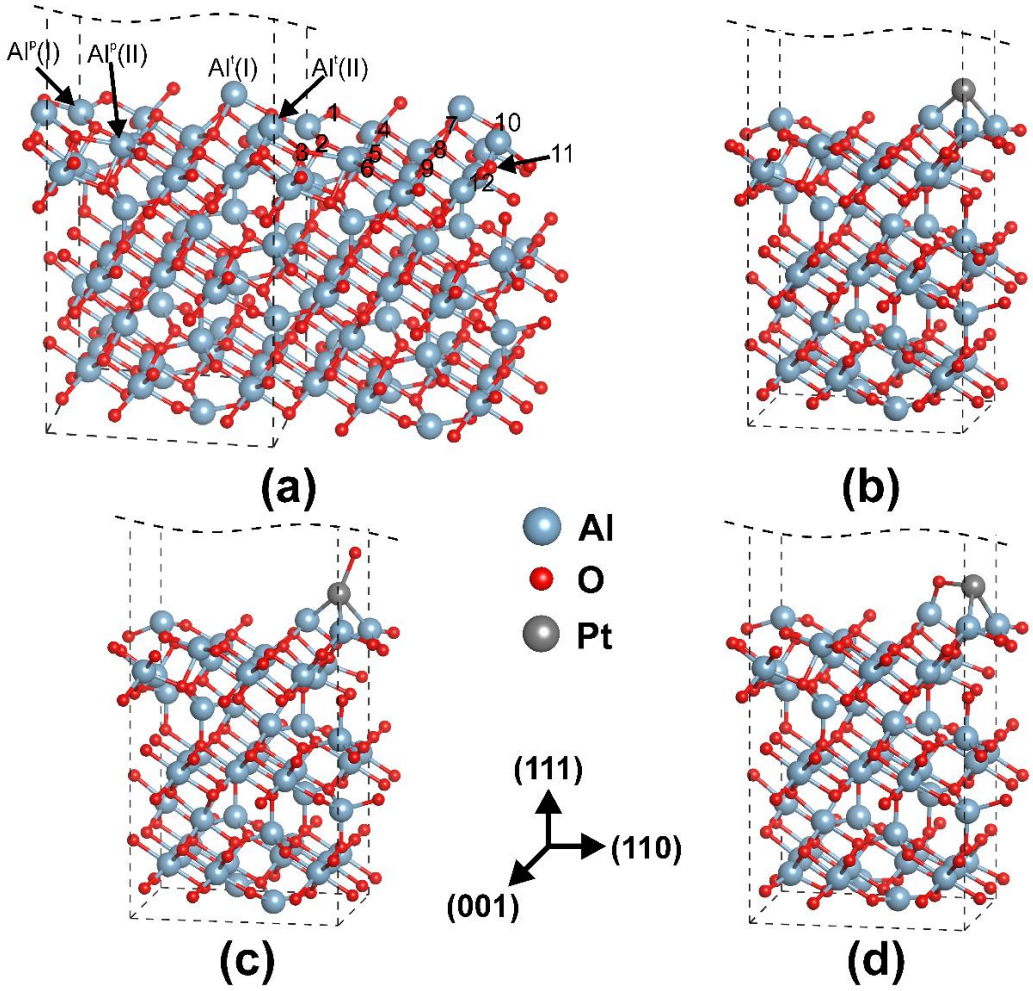

Figure 50. (a) Extended model of the γ-Al_2O_3 (111) surface used for calculations. The four types of surface Al atoms are labeled: two 3-fold planar configurations (Al^p) and two 3-fold truncated tetrahedral configurations (Al^t). The 12 possible locations of surface O vacancies are also numbered. (b) Model of the most stable Pt atom adsorption configuration on the γ-Al_2O_3 (111) surface. (c) Metastable configuration of Pt adsorbed on the γ-Al_2O_3 (111) surface and bonded to an oxygen adatom extracted from a neighboring O site. (d) Bonding model consisting of Pt adsorbed on the γ-Al_2O_3 (111) surface and bonded to an oxygen adatom, forming a bidentate -Al-Pt-O-Al- bridge.

All possible adsorption sites for a Pt atom on the γ-Al_2O_3 (111) surface were then investigated. The adsorption configurations and energies are reported in Appendix Figure 28 and Appendix Table 8. The results show that the Pt atom prefers to bind to the surface Al atoms, and the presence of a Pt atom can influence the γ-Al_2O_3 (111) surface morphology significantly by altering the positions of surface Al and O atoms. This adsorption-related surface effect has previously been seen on the (100) and (110) surfaces, as well [116]. The most stable configuration (Figure 50b) has Pt binding to both Al^t (I) and Al^t (II), and to Al^p (I). Pt also strongly alters the coordination of the Al^p (I) atom, turning it into an Al^t atom, resulting in a tri-coordinated bridging configuration. This binding preference can be attributed to the strong Lewis-acid nature of the electron-deficient Al atom at the 3-fold coordination site [118].

While the investigation of O vacancy formation on the γ-Al_2O_3 (111) surface suggested that uninfluenced O vacancy formation is unlikely, O vacancy formation on the γ-Al_2O_3 (111) surface can be influenced by the presence of surface Pt adatoms. For example, when introducing a Pt adatom at the vicinity of the V_O^7 configuration, the energy penalty for the formation of an oxygen vacancy drops by 1.30 eV, which suggests that the existence of a Pt adatom can promote the formation of oxygen vacancy on γ-Al_2O_3 (111) surface. One may expect the possibility of Pt adatom-induced oxygen vacancy formation on the γ-Al_2O_3 (111) surface, in which case the oxygen atom extracted from the γ-Al_2O_3 (111) surface vacancy site subsequently adsorbs on the Pt adatom. The Pt-O adsorption energy may then compensate the energy penalty of oxygen vacancy formation on γ-Al_2O_3 (111) surface, resulting in a thermodynamically favorable configuration as depicted in Figure 50c. However, computational investigation shows that such attempt to introduce an oxygen vacancy, then place the oxygen atom from the vacancy site on the Pt adatom (Figure 50c) reduces the system stability thermodynamically by 0.43 eV compared to the normal Pt adsorption

configuration (Figure 50b). In the case of a new instance of Pt adsorption on the γ-Al_2O_3 (111) surface during mass transport of a Pt atom, the Pt adsorption energy is sufficient to fuel the formation of oxygen vacancy at the cost of 0.43 eV thermodynamically, which can lead to the formation of the configuration in Figure 50c as a metastable state.

In a more general case, when an external oxygen atom is supplied, -Al-Pt-O- like surface configurations on the γ-Al_2O_3 (111) surface can be formed thermodynamically with a -3.21eV gain in system stability (Figure 50d). Such means of external oxygen atom supply may include: oxygen adatoms released from other surfaces, or micro-facets from surface defects such as step-edges that can be expected with γ-Al_2O_3 [172], etc. Another possibility is that with adsorption of a Pt NP with more than one Pt atom on the γ-Al_2O_3 (111) surface, oxygen vacancy formation may be facilitated and could produce oxygen adatoms that can be adsorbed on the Pt NP surface. The detailed possible sources for oxygen adatom supply is beyond the scope of this study.

8.4.5 EELS Simulations of Pt/γ-Al_2O_3 (111) Model(s)

MS EELS simulations were used to determine if the DFT-optimized interface bonding model was descriptive of the interfacial bonding as revealed in the experimental ELNES features. Simulations of the ELNES of O atoms from the most stable Pt adsorption configuration model (Figure 50b) were carried out and are shown in Figure 51a compared to the experimental interface O-K edge EELS spectrum. 2NN O refers to 2nd nearest neighbor O atoms to the adsorbed Pt atom which is bonded only to surface Al atoms. The results show that neither the 2NN O atoms nor the surface O atoms produce the pre-peak seen in the interface O-K edge EELS spectrum. This confirms that the pre-peak is not merely a surface feature, which might be expected if the pre-peak

is caused solely by dangling O bonds as has been suggested for the beam-damage induced pre-peak [147].

Finding that the most stable Pt adsorption model (Figure 50b) does not accurately describe the O bonding at the interface, the O-K edge EELS from the Pt adsorption + O adatom models (Figure 50c-d) was then simulated. The simulated O-K edge EELS for the O adatoms in both models in Figure 50c-d are shown in Figure 51b compared to the experimental interface O-K edge EELS spectrum. For the O adatom bonding model in Figure 50c, the corresponding simulated O-K edge EELS shows a peak at a slightly lower energy than that of the pre-peak seen in the experimental interface O-K edge EELS spectrum. The simulated EELS of the O adatom in the bidentate -Al-Pt-O bridge configuration shown in Figure 50d gives a peak at the same energy as the pre-peak seen experimentally. This result suggests that the existence of a surface Pt atom can stabilize and host single O adatom(s) on the γ-Al_2O_3 (111) surface.

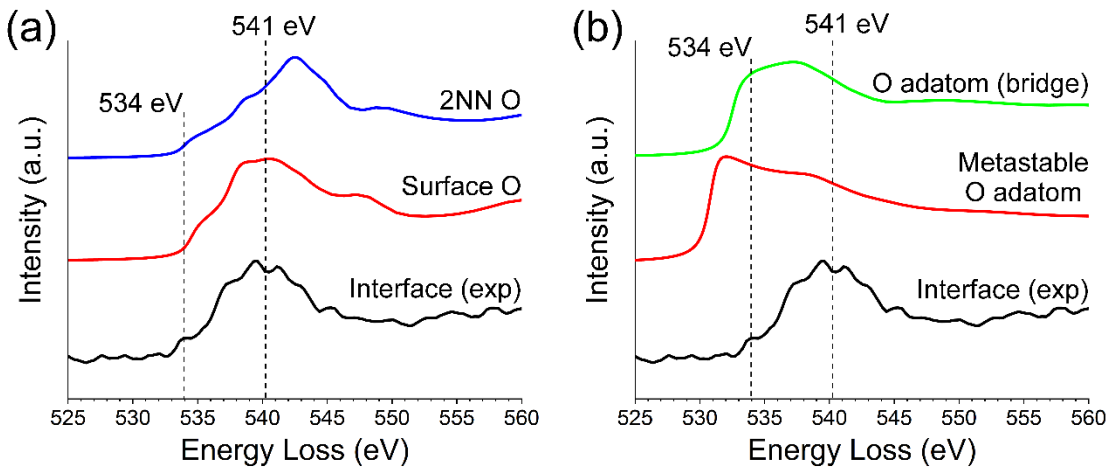

Figure 51. FEFF simulated O-K edge EELS spectra of (a) surface and neighboring O atoms in the model shown in Figure 50b and (b) O adatoms from the models shown in Figure 50c-d compared to the O-K edge EELS spectrum acquired at the Pt/γ-Al_2O_3 (111) interface.

Table 10 provides a summary of the features of the bonding motif that produce the pre-peak in the O-K edge EELS spectrum seen experimentally. Results show that the -Al-Pt-O surface configuration is the key motif to explain the ELNES features produced experimentally at the Pt/γ-Al_2O_3 (111) interface. A similar Ag-O-Al surface structure has been observed with Ag on γ-Al_2O_3 suggesting this may be a general interfacial structure for similar systems [206]. The bonding of Pt atoms to tri-coordinated Al atoms on the γ-Al_2O_3 (111) surface forming Al tetrahedra explains the increased intensity of the a* peak seen in the experimental Al $L_{2,3}$-edge spectra (Figure 46d). This was also confirmed by Al-$L_{2,3}$ ELNES simulations. The presence of an undercoordinated O atom(s) relative to the bulk O atoms appear to play a key part in the formation of the pre-peak, however the specific symmetry of the bonded O is likely also required to form the pre-peak seen in the experimental EELS spectrum. Previous EELS experiments have shown that the formation of an O-K edge pre-peak is influenced by the symmetry of the bonded atom(s) [207, 208]. Also, an analogous peak seen in transition metal spinels but not in $MgAl_2O_4$ was interpreted as being from hybridization of O-p with metal p and d states [209], which further buttresses the emergence of this pre-peak due to O bonded to Pt and Al at the interface.

Table 10. Summary of EELS simulations for different interface bonding configurations.

Pt/ γ-Al_2O_3 (111) interface models	**Surface O**	**Neighboring O to adsorbed Pt**	**O adatom, no O vacancy**	**O adatom + neighboring O vacancy**
Pre-peak at 534 eV	No	No	Yes	Yes

The interface-localized Al $L_{2,3}$ ELNES feature was observed in all acquired interface spectra, suggesting that the Pt consistently bonds to tri-coordinated Al atoms on the γ-Al_2O_3 (111) surface. On the other hand, the O-K edge pre-peak was observed in only about 50% of Pt/γ-Al_2O_3

(111) interfaces, suggesting that the Al-Pt-O bridge bonding configuration is not always present at the interface. This would be consistent with the potential O adatom sources proposed including proximal step-edges and possible O vacancy formation during Pt NP adsorption, since those sources may not always occur at the NP adsorption site. However, resolving the specific conditions that result in the pre-peak forming O bonding beyond the proposed mechanisms for O adatom provision was not further explored here.

This study shows that a single Pt atom adsorption can modify the γ-Al_2O_3 surface, contributing to the observed experimental EELS spectrum. While this model is certainly too simplistic to completely describe the modified alumina surface structure, it is nontrivial to completely determine the surface modifications using a large Pt cluster. This is because the cluster can attain many different configurations on the surface that are close in energy, which requires extensive calculations on many potential structures that must be screened to find the lowest energy structure. For example, a similar approach was applied to find the optimum Pt clusters on MoS_2 where the initial potential structures were selected from an ab initio molecular trajectory [210] or obtained using an adaptive genetic approach in conjunction with classical atomistic potentials and first-principles calculations [211]. Additionally, γ-Al_2O_3 surfaces pose more challenges compared to that of MoS_2 given its more complex chemical composition and topology.

Overall, the value of ELNES to understand the structure and bonding at specific metal-oxide interfaces is demonstrated, building upon previous similar studies. The reduced Al atom coordination at the interface has been observed in previous studies of metal-alumina interfaces [186]. On the other hand, while there has been much debate about the significance of O-K edge pre-peaks, these results demonstrate a clear distinction between the damage-induced pre-peak and the interfacial pre-peak that has thereafter been explained using a simple interfacial bonding

model. Such bonding models as those used in this work have been previously employed to gain fundamental understanding of interfaces [184, 186, 187].

8.5 Outcomes

The objectives of this chapter were to first determine the relative accuracy of established models in simulating the electronic structure of γ-Al_2O_3 as observed in ELNES and then to describe the Pt/γ-Al_2O_3 (111) interface bonding using a simple interface model. High-resolution EELS spectra were acquired from single crystal γ-Al_2O_3 and compared to simulated EELS from the γ-Al_2O_3 structure models. The peak shoulder A* in the O-K edge spectrum was identified as a signature of the cation distribution in the models. By resolving the O-K edge EELS signals from each type of O site present in the spinel-based models, it was revealed that the models with Al vacancies on tetrahedral sites provided the best agreement to the EELS experiments. The placement of Al atoms in nonspinel sites generally improved the agreement of the EELS simulations to the experiments. A wide distribution of O coordination types, as in the tetragonal nonspinel model, provided the best description of the oxygen coordination in γ-Al_2O_3. The presence of disorder was revealed as a key descriptor of the γ-Al_2O_3 atomic arrangement, which inherently reduces the accuracy of any fully specified models. This provides a framework to evaluate γ-Al_2O_3 models and supercells intended for use in theoretical calculations.

The relatively simple interfacial model used in this work enabled the understanding of metal-support oxide interfacial bonding phenomena. Specifically, analysis of the Al $L_{2,3}$-edge ELNES showed a reduction in the average coordination of Al atoms at the interface compared to

the bulk, which was consistent with the presence of tetrahedrally coordinated atoms bonded to Pt. While the pristine γ-Al_2O_3 (111) surface is unlikely to form O vacancies to provide a source of O adatoms, the O adatom can potentially be extracted from a surface O site during the migration of Pt atoms on the surface or can come from an external O source. In both cases, the O-K edge EELS showed a pre-peak at the same energy. The Al-Pt-O bonding at the interface resulted in a different electronic state local to the interface that could play a role in catalytic behavior. These results further challenge the notion that γ-Al_2O_3, as a non-reducible oxide support, only interacts minimally with supported catalyst NPs. The results also show that despite the cubic spinel-based model being the most accurate model, less accurate models such as the monoclinic nonspinel model can still be useful for certain applications, where validation for their use is provided. From the basic understanding of the bonding configurations present at the metal-oxide interface, the bonding of nanoclusters to oxide support surfaces can then be understood and developed.

9.0 Conclusions, Outlook, and Recommendations

9.1 Conclusions

The primary objective of this research project was to develop a more accurate understanding of the atomic structure of γ-Al_2O_3. This was undertaken through synergistic experimental and theoretical SAED and EELS, all employed on carefully synthesized high-quality polycrystalline and single-crystal γ-Al_2O_3 thin films. In summary, the structure of γ-Al_2O_3 was found to be best described by a cubic spinel-based model with all Al atoms placed only on spinel sites and 50% - 80% of Al vacancies placed on tetrahedral sites. The distribution of Al atoms between octahedral and tetrahedral sites in the spinel-based model only exhibited a minor effect on the bulk electronic structure as observed in high-resolution EELS, suggesting that a more tractable spinel-based model such as the Pinto monoclinic spinel-based model may be sufficient to model bulk electronic properties. This hypothesis should be further tested, however. It would be expected that surface properties, particularly local properties, would be more significantly affected by the Al distribution in the model, since the arrangement of Al terminated surfaces will vary. That being noted, a scenario was demonstrated using the Digne nonspinel model that indicates that such a less accurate but more tractable model could be useful to model certain surface properties provided adequate justification and validation is given. The findings from each chapter are summarized as follows:

Chapter 5: Electron Beam Damage in γ-Al_2O_3 and Suppression using Cryo-STEM/EELS

Cryo-EELS experiments on γ-Al_2O_3 were shown to be effective in reducing electron beam damage and suppressing the formation of EELS artifacts in the O-K edge resulting from structural

modification primarily by radiolysis damage. The source of the beam damage associated O-K pre-edge peak was proposed to be due to surface O-O dimers on the altered surfaces in the beam damaged area. EELS simulations have provided support for this hypothesis. This study showed that specific artifacts in EELS spectra can be suppressed in a straightforward and repeatable way using cryo-EELS. As a result, high quality EELS can be collected while retaining sufficient SNR.

Chapter 6: Evaluating the Accuracy of Common γ-Al_2O_3 Structure Models by Selected Area Electron Diffraction

SAED experiments and simulations revealed that the cubic spinel-based model with space group $Fd\bar{3}m$ and lattice parameter *a* equal to 7.9 Å is the most accurate average model for γ-Al_2O_3. The models can be ranked in order of decreasing accuracy of the bulk structure: cubic spinel-based > tetragonal nonspinel > monoclinic spinel-based > monoclinic nonspinel. Overall, the results suggest that the Digne monoclinic and Paglia tetragonal nonspinel models (and potentially other nonspinel models) may not be as accurate as previously thought.

Chapter 7: Determination of the Vacancy Distribution over Al Cation Sites in γ-Al_2O_3

Experimental and simulated SAED and high-resolution EELS revealed that 50% – 90% of Al vacancies exist on tetrahedral sites in the cubic spinel-based model, corresponding to 26% - 31% of Al atoms occupying tetrahedral sites. Additionally, it was observed that the simulated EELS spectra were not as sensitive to the Al vacancy distribution as the SAED pattern, suggesting that the electronic structure is not drastically affected by the shift of a small number of Al atoms between tetrahedral and octahedral sites in the cubic spinel model.

Chapter 8: EELS-Based Studies of Common γ-Al_2O_3 Bulk Structure Models and Subsequent Description of the Local Bonding at the Pt/γ-Al_2O_3 (111) Interface Using a Tractable Interfacial Model

The EELS simulations from the commonly used γ-Al_2O_3 models all exhibited good agreement with the experimental EELS, unsurprisingly confirming that none of the models radically misrepresent the electronic structure of γ-Al_2O_3. Small discrepancies in the simulated EELS of the nonspinel models suggests that placement of several Al atoms in nonspinel sites reduces the accuracy of the model, but the exact cutoff could not be clearly determined within the accuracy of the MS EELS simulations. The disordered (fractionally occupied) models also showed better agreement of EELS simulation to experiment, highlighting the importance of disorder in accurately representing the γ-Al_2O_3 structure.

The correlative experimental and theoretical approach taken in this work combined with the simple interface model has enabled the understanding of metal-support oxide interfacial bonding phenomena. High-resolution cryo-EELS and EELS simulations from the simple interface model revealed the presence of tetrahedrally coordinated surface atoms bonded to Pt and an Al-Pt-O bonding configuration at the interface that could play a role in catalytic behavior. These results also highlight that less accurate γ-Al_2O_3 models such as the monoclinic nonspinel model can still be useful for certain applications, where validation for their use is provided.

The findings reported in this project represent important contributions to the scientific community that advance understanding of the structure of γ-Al_2O_3, as well as its electron beam sensitivity and interfacial bonding with Pt. Understanding of the relative accuracy and utility of commonly used models has also been obtained. These findings will contribute to improving the approach to modeling γ-Al_2O_3 in theoretical calculations, which will ultimately lead to accelerated discovery and design of γ-Al_2O_3-based catalysts through improved predictive simulations within the rational catalyst design paradigm.

9.2 Outlook

While significant contributions and progress were made in this project, there remain avenues to build upon this work and expand understanding of the γ-Al_2O_3 structure. Firstly, this work shows that none of the current most commonly used structural models of γ-Al_2O_3 match the experimental data exactly. This of course suggests that there is room for improvement in developing a still more accurate structural understanding of γ-Al_2O_3. The presence of Al cations in nonspinel sites has yet to be conclusively demonstrated or disproven. The exact ratio of Al cations in tetrahedral vs octahedral sites has also been difficult to establish. The methods employed in this work have not shown sufficient sensitivity to narrow the cation distribution beyond the range established in the study Chapter 7.0. Some experimental electron microscopy techniques have been demonstrated to reveal vacancy distribution, including high-resolution electron tomography, 3-D electron diffraction, atomic resolution EDS, and quantitative HAADF-STEM [212-215]. However, these techniques are subject to beam effects since γ-Al_2O_3 is such a beam-sensitive material. Furthermore, the presence of slight distortions from perfect cubic symmetry, as have been reported in γ-Al_2O_3 from certain sources, cannot be ruled out either based on the current work. Despite these limitations, ELNES analysis based on MS simulations using different types of bulk γ-Al_2O_3 models shows that there are indeed effects of slight structural modification present in ELNES that could potentially be observed with ultrahigh-resolution EELS systems.

With respect to beam damage suppression in γ-Al_2O_3, a combination of cryo-EELS and low-dose STEM could potentially completely eliminate beam damage when examining γ-Al_2O_3. Also, the complete mechanism of beam-induced damage that results in surface O-O bonds in γ-Al_2O_3 has not been fully determined here, leaving room for further exploration. Beam damage

suppression will be absolutely key to enable the use of more advanced electron microscopy techniques to characterize the structure of γ-Al_2O_3.

The peculiar O bonding seen at the interface of some Pt NPs with the γ-Al_2O_3 (111) surface could be of relevance to catalysis, particularly with respect to NP stability, in light of the reported Pt NP stabilizing effect of the (111) surface of magnesium aluminate spinel ($MgAl_2O_4$) [216]. This could possibly explain why NPs are stabilized by the (111) surface, assuming the same behavior applies to γ-Al_2O_3, which also possesses a spinel structure, as shown [88]. Furthermore, the exact explanation for the occurrence of the O adatom bonding at only ~50% of observed Pt/γ-Al_2O_3 (111) has yet to be conclusively determined. Surface steps or other surface defects could possibly provide the O adatom, but this has not yet been demonstrated to be the case. This would, however, be consistent with the perspective of defect stabilization of Pt NPs on the γ-Al_2O_3 surface, as has been proposed for certain other oxide systems [37].

The stability of Pt clusters on the γ-Al_2O_3 surface could be studied *in situ* in a manner similar to the experiments reported by Li et al. [216] where certain surface orientations of $MgAl_2O_4$ (spinel) were demonstrated to stabilize Pt under reaction conditions. Key to such a study, however, would be synthesis of other surface orientations of γ-Al_2O_3 with comparable control as the (111) surface-oriented γ-Al_2O_3 synthesized in this work. Alternatively, the relative stability of different metal clusters on the γ-Al_2O_3 (111) surface as model catalyst systems could be investigated. The usefulness of such planar model catalysts to understand fundamental aspects of heterogeneous catalysis has been abundantly demonstrated in the study of the Au/TiO_2 catalysts [36].

9.3 Recommendations

Suggested future work is summarized as follows:

1. Synthesis
   a. Development of methods to synthesize model γ-Al_2O_3 supports with surface orientations other than (111):

      Using the NiAl (110) thermal oxidation method of model γ-Al_2O_3 synthesis, only the (111) surface orientation can be grown. It has been suggested that uniform alumina thin films can also be grown on Ni_3Al (111) [17] and on $MgAl_2O_4$ (110) [96]. This could be a possible avenue to synthesize other surface orientations of γ-Al_2O_3.

   b. Simultaneous size- and shape-control of Pt NPs:

      This would enable more in-depth modeling of the model catalyst since the interacting surface of the Pt NP and the γ-Al_2O_3 support would be known. Synthesis of shape-controlled Pt NPs was attempted in the course of this project through the inverse-micelle method established by Roldan-Cuenya et al [217-222]. This was successful in producing shape-controlled NPs as small as 1 nm in diameter; however, the NPs were ligand-encapsulated to control the size and shape during synthesis. Upon complete removal of the ligands using an annealing technique similar to that of Cargnello et al. [223], the NP shape was lost on almost every occasion. Therefore, if the inverse-micelle method of shape control is to be used, an effective method of removing the ligands without modifying the NP sizes and shapes must be developed. Otherwise, alternative methods of shape control must be explored.

   c. Synthesis and study of other relevant metal NPs combined with the model γ-Al_2O_3 support.

2. Characterization

a. Ultrahigh-resolution EELS acquisition:

   The monochromated EELS used in this work achieved a minimum energy resolution of ~0.25 eV. Some EELS setups, however, have been shown to achieve even finer energy resolution, as low as 4.2 meV [224]. Such ultrahigh-resolution EELS may be capable of observing some of the ELNES changes seen in EELS simulations from different bulk γ-Al_2O_3 models or of resolving subtler signatures of metal-support bonding that have so far been missed.

b. *In situ* TEM/STEM studies of the evolution of the structure and interfacial chemistry of the model Pt/γ-Al_2O_3 catalysts:

   These cutting-edge experimental setups would be the next step toward fully understanding the catalytic behavior of Pt/γ-Al_2O_3 by enabling direct observation of the structural and chemical dynamics occurring during catalytic reaction.

3. Modeling

a. Multiscale modeling of the catalyst to develop a more complete atomistic picture of Pt/γ-Al_2O_3 interface structure and chemistry:

   Current interface models only consist of single Pt atoms and limited accuracy of γ-Al_2O_3 surface structure, both of which can be improved upon. To incorporate realistic NP sizes in simulations, a multiscale approach must be employed since DFT alone cannot handle such large systems. Appropriate force fields must be developed so molecular dynamics approaches such as ReaxFF [225] can be used to model the system.

b. Full potential-based simulation of EELS spectra:

   The FEFF9 code for EELS simulation is limited to using muffin-tin potentials, which can lead to some inaccuracies in the simulated EELS. Full potential codes that can also handle

aperiodic systems would represent an overall improvement, possibly enabling the discovery and interpretation of more EELS bonding and structure signatures.

c. *Ab initio* molecular dynamics (MD) modeling of beam damage mechanism:

While the presence of O-O dimers caused by electron beam irradiation of γ-Al_2O_3 was demonstrated, the mechanisms resulting in O-O formation have not been fully described. Furthermore, the mechanism by which going to cryo temperatures removes or prevents the formation of O-O dimers is currently unknown.

Appendix A Sample FEFF Input File

See Section 3.4.2 for description of EELS simulation using FEFF.

```
 * This feff file was generated by Demeter 0.9.24
 * Demeter written by and copyright (c) Bruce Ravel, 2006-2015

 * --*--*--*--*--*--*--*--*--*--*--*--*--*--*--*--*--*--*--*--*--*--*--*--*--*--*--*--*--*--*--*--*--*--*--*--*--
 * title = Corundum
 * title = Ishizawa, N.
 * title =  A structural investigation of alpha-Al2O3 at 2170 K
 * title =  T = 300 K
 * space = R -3 c :H
 * a     =   4.75400    b    =   4.75400    c     =  12.99000
 * alpha =  90.00000    beta =  90.00000    gamma = 120.00000
 * rmax  =   8.33100    core  = Al
 * # polarization = 0.0  0.0  0.0
 * shift =     0.00000    0.00000    0.00000
 * atoms
 * # el.     x           y           z        tag
 *   Al     0.00000     0.00000     0.35228   Al
 *   O      0.30640     0.00000     0.25000   O
 * --*--*--*--*--*--*--*--*--*--*--*--*--*--*--*--*--*--*--*--*--*--*--*--*--*--*--*--*--*--*--*--*--*--*--*--*--

 * --*--*--*--*--*--*--*--*--*--*--*--*--*--*--*--*--*--*--*--*--*--*--*--*--*--*--*--*--*--*--*--*--*--*--*--*--
 *  total mu*x=1:  0.979 microns,  unit edge step:  1.537 microns
 *  specific gravity:  3.995
 * --*--*--*--*--*--*--*--*--*--*--*--*--*--*--*--*--*--*--*--*--*--*--*--*--*--*--*--*--*--*--*--*--*--*--*--*--
 *  normalization correction:    0.00219 ang^2
 * --*--*--*--*--*--*--*--*--*--*--*--*--*--*--*--*--*--*--*--*--*--*--*--*--*--*--*--*--*--*--*--*--*--*--*--*--

 *The first 26 lines are generated automatically by the ATOMS program
 *The ATOMS program was used to make the input file
 *from the CIF file of the alpha-Al2O3 structure

*The title of the calculation
TITLE name:     alpha Al2O3

*The core-loss EELS spectrum edge to be calculated
EDGE K

***The modules to be run, 1 = yes
***pot is potentials
***xsph is phase shifts
***fms is full multiple scattering
***genfmt is path expansion
***ff2chi is cross-section
*   pot    xsph  fms   paths genfmt ff2chi
CONTROL 1 1 1 1 1 1
```

```
PRINT 1 0 0 0 0 0

*** treatment of the self-energy
***(analogous to exchange-correlation in DFT)
*** ixc=0 means to use Hedin-Lundqvist model
*   ixc  [ Vr  Vi ]
EXCHANGE 0 0.0 0.0 0

*** Radius of small cluster for
*** self-consistency calculation (r_scf)
*** A sphere including 2 shells is
*** a good choice
*** l_scf = 0 for a solid, 1 for a molecule
*** n_scf is max number of iterations
*** ca is convergence criterion
*   r_scf  [ l_scf   n_scf   ca ]
SCF 6.0 0 100 0.2

*** Energy grid over which to calculate
*** DOS functions
*   emin  emax   eimag
EGRID
e_grid  -10  10.0  0.1
k_grid  last  6.0  0.07

***core-hole treatment
***default is final state rule (FSR)
***random phase approximation (RPA) can also be used
COREHOLE FSR

***Radius of full multiple scattering cluster in angstroms
*rfms
FMS 2

***parameters for conversion to ELNES spectrum
*E - beam energy in keV
*kx ky kz - beam direction in the crystal frame
*beta alpha - collection and convergence angles in mrad
*nr na - q-integration mesh
*dx dy - detector position in mrad
ELNES
200
1 2 0
10.0 18.0
5 3
0.0 0.0

***final energy shift correction (vrcorr)
***additional broadening (vicorr)
*vrcorr vicorr
CORRECTIONS 0.0 0.3

 POTENTIALS
  * ipot   Z      tag
     0     13     Al
```

```
    1     13     Al
    2     8      O


ATOMS                  * this list contains 170 atoms
*   x          y          z     ipot tag           distance
   0.00000    0.00000    0.00000  0  Al            0.00000
   1.48325    0.72831   -0.83638  2  O.1           1.85203
  -1.37236    0.92037   -0.83638  2  O.1           1.85203
  -0.11089   -1.64869   -0.83638  2  O.1           1.85203
   0.00000    1.45663    1.32862  2  O.2           1.97154
   1.26147   -0.72831    1.32862  2  O.2           1.97154
  -1.26147   -0.72831    1.32862  2  O.2           1.97154
   0.00000    0.00000    2.65723  1  Al.1          2.65723
   2.74472    0.00000    0.49223  1  Al.2          2.78851
  -1.37236    2.37700    0.49223  1  Al.2          2.78851
  -1.37236   -2.37700    0.49223  1  Al.2          2.78851
  -2.74472    0.00000   -1.67277  1  Al.3          3.21429
   1.37236    2.37700   -1.67277  1  Al.3          3.21429
   1.37236   -2.37700   -1.67277  1  Al.3          3.21429
  -0.11089    3.10531   -0.83638  2  O.3           3.21789
   2.74472   -1.45663   -0.83638  2  O.3           3.21789
  -2.63384   -1.64869   -0.83638  2  O.3           3.21789
   0.11089    1.64869   -3.00138  2  O.4           3.42619
  -1.48325   -0.72831   -3.00138  2  O.4           3.42619
   1.37236   -0.92037   -3.00138  2  O.4           3.42619
  -2.74472    0.00000    2.16500  1  Al.4          3.49582
   1.37236    2.37700    2.16500  1  Al.4          3.49582
   1.37236   -2.37700    2.16500  1  Al.4          3.49582
   2.74472    0.00000   -2.16500  1  Al.4          3.49582
  -1.37236    2.37700   -2.16500  1  Al.4          3.49582
  -1.37236   -2.37700   -2.16500  1  Al.4          3.49582
   2.85561    1.64869    1.32862  2  O.5           3.55498
  -2.85561    1.64869    1.32862  2  O.5           3.55498
   0.00000   -3.29737    1.32862  2  O.5           3.55498
   0.00000    0.00000   -3.83777  1  Al.5          3.83776
  -1.48325    0.72831    3.49362  2  O.6           3.86469
   1.37236    0.92037    3.49362  2  O.6           3.86469
   0.11089   -1.64869    3.49362  2  O.6           3.86469
   4.00620    0.72831   -0.83638  2  O.7           4.15687
  -2.63384    3.10531   -0.83638  2  O.7           4.15687
  -1.37236   -3.83363   -0.83638  2  O.7           4.15687
  -2.74472    1.45663   -3.00138  2  O.8           4.32013
   2.63384    1.64869   -3.00138  2  O.8           4.32013
   0.11089   -3.10531   -3.00138  2  O.8           4.32013
  -4.22797    0.72831   -0.83638  2  O.9           4.37101
   2.74472    3.29737   -0.83638  2  O.9           4.37101
   1.48325   -4.02569   -0.83638  2  O.9           4.37101
   1.26147    4.02569    1.32862  2  O.10          4.42297
  -1.26147    4.02569    1.32862  2  O.10          4.42297
   4.11708   -0.92037    1.32862  2  O.10          4.42297
  -4.11708   -0.92037    1.32862  2  O.10          4.42297
   2.85561   -3.10531    1.32862  2  O.10          4.42297
  -2.85561   -3.10531    1.32862  2  O.10          4.42297
   0.11089    3.10531    3.49362  2  O.11          4.67553
```

-2.74472	-1.45663	3.49362	2	O.11	4.67553
2.63384	-1.64869	3.49362	2	O.11	4.67553
4.11708	2.37700	0.00000	1	Al.6	4.75400
-4.11708	2.37700	0.00000	1	Al.6	4.75400
0.00000	4.75400	0.00000	1	Al.6	4.75400
4.11708	-2.37700	0.00000	1	Al.6	4.75400
-4.11708	-2.37700	0.00000	1	Al.6	4.75400
0.00000	-4.75400	0.00000	1	Al.6	4.75400
1.37236	3.83363	-3.00138	2	O.12	5.05849
-4.00620	-0.72831	-3.00138	2	O.12	5.05849
2.63384	-3.10531	-3.00138	2	O.12	5.05849
2.74472	0.00000	4.33000	1	Al.7	5.12664
-1.37236	2.37700	4.33000	1	Al.7	5.12664
-1.37236	-2.37700	4.33000	1	Al.7	5.12664
-2.74472	0.00000	-4.33000	1	Al.7	5.12664
1.37236	2.37700	-4.33000	1	Al.7	5.12664
1.37236	-2.37700	-4.33000	1	Al.7	5.12664
-1.48325	4.02569	-3.00138	2	O.13	5.23588
4.22797	-0.72831	-3.00138	2	O.13	5.23588
-2.74472	-3.29737	-3.00138	2	O.13	5.23588
-4.00620	0.72831	3.49362	2	O.14	5.36520
2.63384	3.10531	3.49362	2	O.14	5.36520
1.37236	-3.83363	3.49362	2	O.14	5.36520
1.26147	0.72831	-5.16638	2	O.15	5.36780
-1.26147	0.72831	-5.16638	2	O.15	5.36780
0.00000	-1.45663	-5.16638	2	O.15	5.36780
4.11708	2.37700	2.65723	1	Al.8	5.44623
-4.11708	2.37700	2.65723	1	Al.8	5.44623
0.00000	4.75400	2.65723	1	Al.8	5.44623
4.11708	-2.37700	2.65723	1	Al.8	5.44623
-4.11708	-2.37700	2.65723	1	Al.8	5.44623
0.00000	-4.75400	2.65723	1	Al.8	5.44623
-5.48945	0.00000	0.49223	1	Al.9	5.51147
2.74472	4.75400	0.49223	1	Al.9	5.51147
2.74472	-4.75400	0.49223	1	Al.9	5.51147
4.22797	0.72831	3.49362	2	O.16	5.53277
-2.74472	3.29737	3.49362	2	O.16	5.53277
-1.48325	-4.02569	3.49362	2	O.16	5.53277
-2.74472	0.00000	4.82223	1	Al.10	5.54864
1.37236	2.37700	4.82223	1	Al.10	5.54864
1.37236	-2.37700	4.82223	1	Al.10	5.54864
5.48945	0.00000	-1.67277	1	Al.11	5.73866
-2.74472	4.75400	-1.67277	1	Al.11	5.73866
-2.74472	-4.75400	-1.67277	1	Al.11	5.73866
1.48325	5.48231	-0.83638	2	O.17	5.74067
-5.48945	-1.45663	-0.83638	2	O.17	5.74067
4.00620	-4.02569	-0.83638	2	O.17	5.74067
5.37856	1.64869	1.32862	2	O.18	5.78034
-5.37856	1.64869	1.32862	2	O.18	5.78034
4.11708	3.83363	1.32862	2	O.18	5.78034
-4.11708	3.83363	1.32862	2	O.18	5.78034
1.26147	-5.48231	1.32862	2	O.18	5.78034
-1.26147	-5.48231	1.32862	2	O.18	5.78034
-0.11089	1.64869	5.65862	2	O.19	5.89495
1.48325	-0.72831	5.65862	2	O.19	5.89495

```
  -1.37236   -0.92037    5.65862  2  O.19          5.89495
  -1.37236    5.67437   -0.83638  2  O.20          5.89758
   5.60033   -1.64869   -0.83638  2  O.20          5.89758
  -4.22797   -4.02569   -0.83638  2  O.20          5.89758
   5.48945    0.00000    2.16500  1  Al.12         5.90095
  -2.74472    4.75400    2.16500  1  Al.12         5.90095
  -2.74472   -4.75400    2.16500  1  Al.12         5.90095
  -5.48945    0.00000   -2.16500  1  Al.12         5.90095
   2.74472    4.75400   -2.16500  1  Al.12         5.90095
   2.74472   -4.75400   -2.16500  1  Al.12         5.90095

END
```

Appendix B Additional Details for Electron Beam Damage in γ-Al_2O_3 and Suppression Using Cryo-EELS

Appendix B.1 Computational Details

The drilled hole model was made using the (110) surface of the non-spinel model proposed by Digne et al. [78], to correlate with the plan-view surface orientation of the γ-Al_2O_3 single-crystal sample. A supercell approach employing a (2×1) surface supercell and 4 layers in the non-periodic direction was used. A hole in the non-periodic direction with a diameter of 2 atoms was created in the center of the model by removing the atoms within that volume. The model was then optimized with DFT.

First principles DFT calculations were carried out within the Perdew-Burke-Ernzerhof (PBE) [143] exchange-correlation functional as implemented in the Vienna Ab initio Simulation Package (VASP) with Tkatchenko-Scheffler [144, 145] van der Waals corrections. Projected augmented wave (PAW) pseudopotentials were used to describe electron-nucleus interactions [189, 226-228]. The electronic self-consistent loops are terminated within energy-change tolerance of 1×10^{-6} eV. The electron wavefunction was expanded using planewaves with a 400 eV planewave cutoff. Validation of the computational framework was done by checking that the energy cutoff, k-grid, and energy tolerances were sufficient to converge energy differences to less than 1 meV.

Appendix B.1.1 MS (FEFF) ELNES Calculation Details

FEFF is a cluster-based program hence clusters of 10 A radius were used so that no edge effects occurred with a full multiple scattering (FMS) radius of 8 A. FEFF calculated O-K edge EELS spectra were aligned with the experimental EELS using “bulk” O atoms away from the surface of the model. The calculated spectrum for the bulk O atom was shifted to align the main O-K edge peak with the same peak in the experiment at ~541 eV. The FEFF calculated EELS spectra for the O-O dimer atoms were then shifted by the same value.

Appendix B.2 Drilled Hole Model Simulations

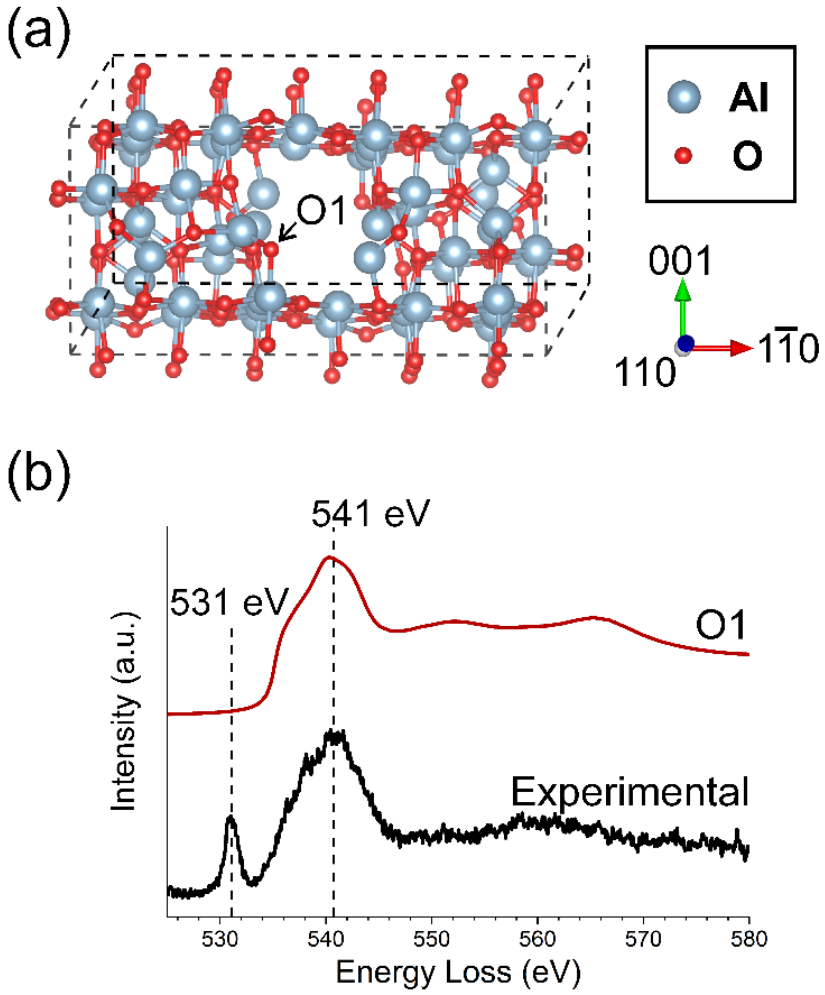

Appendix Figure 1. (a) γ-Al_2O_3 (110) surface slab model with simulated drilled hole and surface O atom at the edge of the hole labeled O1. (b) Simulated O-K edge EELS spectra from O1 compared to the experimental beam damaged O-K edge spectrum.

Appendix B.3 Additional O-O Surface Dimer Model Simulations

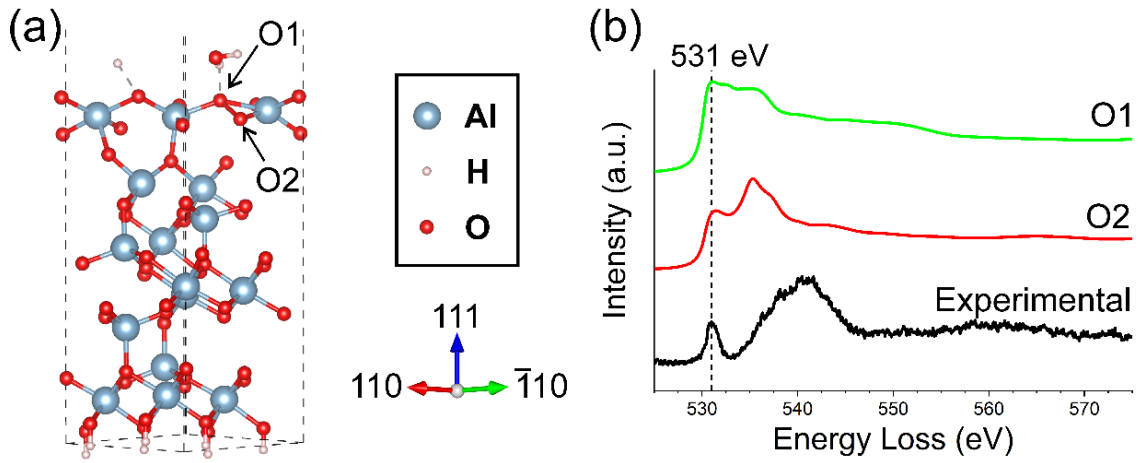

Appendix Figure 2. (a) Partially hydroxylated γ-Al_2O_3 (110) surface slab model with both O atoms in the surface O dimer labeled O1 and O2. (b) Simulated O-K edge EELS spectra from O1 and O2 compared to the experimental beam damaged O-K edge spectrum.

Appendix C Additional Details for Evaluation of γ-Al_2O_3 Models

Appendix C.1 Sample Preparation and Characterization Techniques

Single-crystalline γ-Al_2O_3 was grown by oxidation of single crystal equiatomic NiAl (110) after the method of Zhang et al. [105]. Cross-sectional TEM samples of the single-crystal γ-Al_2O_3 were prepared using a FEI Helios (dual-beam) FIB-SEM at 30 kV with a 5 kV ion beam used as the final polishing step. Cross-sectional TEM samples of the polycrystalline γ-Al_2O_3 were prepared using a FEI Scios FIB-SEM. For the polycrystalline oxide films, TEM-ready samples were made by scraping the oxide film and depositing onto a Cu TEM grid. TEM images and SAED patterns were acquired with a Hitachi H9500 TEM at 300 kV. Powder X-ray diffraction of the commercial γ-Al_2O_3 was collected using a Bruker D8 XRD diffractometer.

Appendix C.2 Conversion of Polycrystalline γ-Al_2O_3 SAED to Azimuthally Averaged Profile

First, the diffraction pattern was corrected for diffuse diffracted background not from the polycrystalline γ-Al_2O_3 thin film. Background subtraction must be done deliberately and carefully if peak intensities are to be considered as a basis of comparison for the simulated SAED profiles. The diffuse diffraction from the amorphous lacey carbon and ultrathin carbon film on the TEM grid was subtracted from the diffraction pattern. A diffraction pattern from just the backing carbon film was acquired in the same session as the polycrystalline γ-Al_2O_3 thin film (Appendix Figure

3b). This pattern was then simply subtracted from the SAED of the polycrystalline γ-Al_2O_3 thin film (Appendix Figure 3a), which consists of both the diffraction from the carbon film and the polycrystalline γ-Al_2O_3 film. This removed some of the diffuse diffracted background (Appendix Figure 3c).

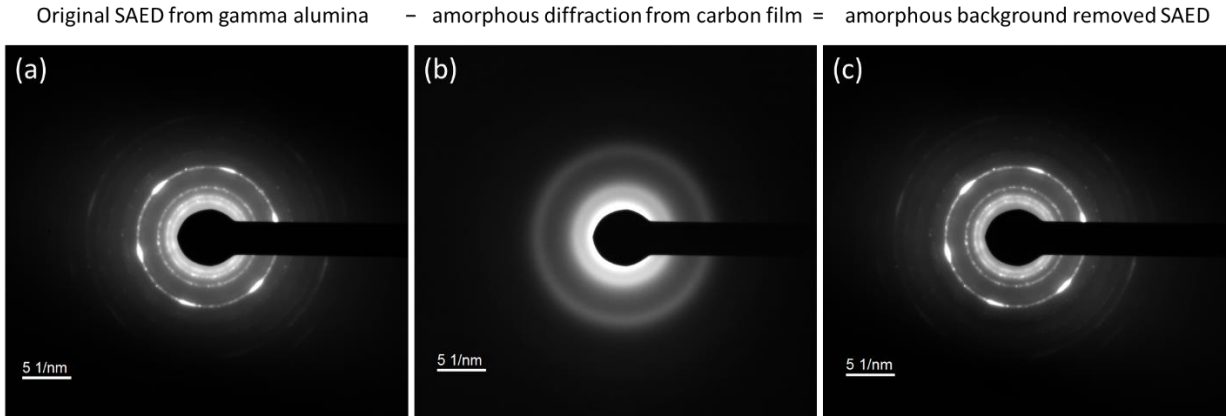

Appendix Figure 3. (a) SAED pattern from polycrystalline γ-Al_2O_3 thin film on carbon-backed TEM grid. (b) SAED pattern from carbon backing of TEM grid. (c) SAED pattern resulting from subtraction of (b) from (a).

The remaining background was fitted in two ways. First, a lognormal-based spline fit was used to fit the background (Appendix Figure 4). Visual inspection of the diffraction image suggested that this background fit was inadequate, as there remained some amorphous contribution to the diffraction pattern. The presence of this amorphous contribution suggests that the true background would be more intense than that predicted by this subtraction method. The statistical figures of merit were computed for the first background subtraction method and reported in Appendix Table 1. The background was then subtracted by a second method, where the intensity of the background was measured between each pair of rings in the diffraction pattern as shown in

Appendix Figure 5a. The background subtracted using this method and the resulting line profile are shown in Appendix Figure 5b. It can be expected that this method overpredicts the background, as there is diffuse scattering from the rings that bleeds into the background. This overprediction is especially problematic when measuring the background between two rings that are close to each other. The statistical figures of merit were computed for the second background subtraction method and reported in Appendix Table 2. It can be reasonably expected that the true background lies somewhere between these extremes. As such, the plotted backgrounds from both subtraction methods were averaged to give the background subtraction (Appendix Figure 6) and line profile used for the final comparison in the main document (Appendix Figure 7).

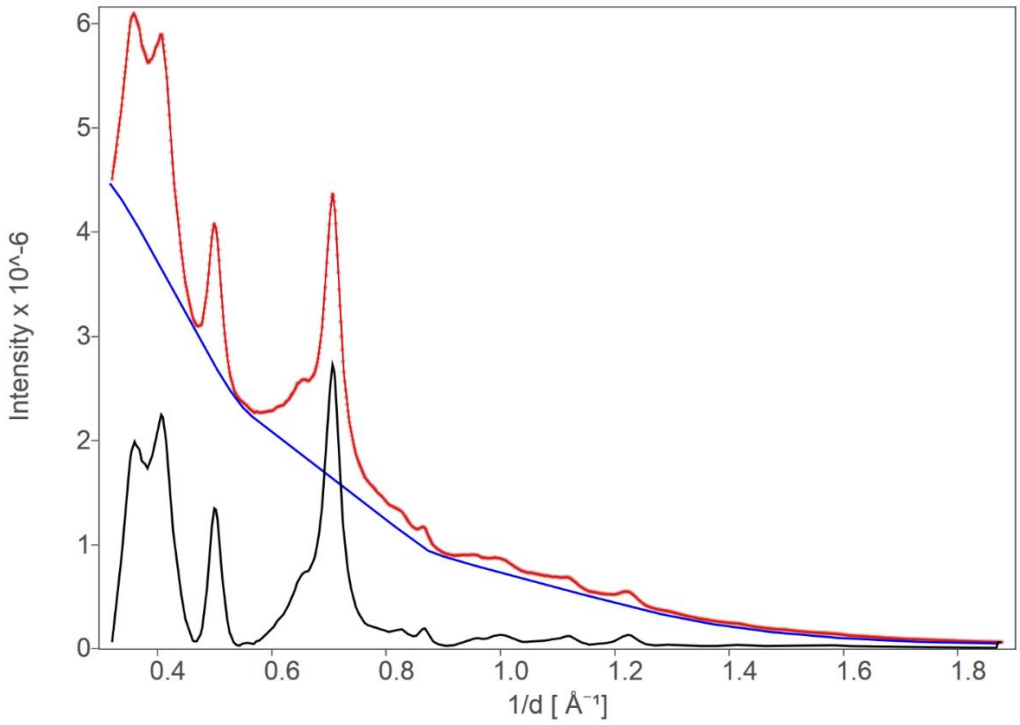

Appendix Figure 4. Background subtraction approach of azimuthally averaged profile of the polycrystalline γ-Al_2O_3 thin film SAED pattern using lognormal-based spline fit.

Appendix Table 1. Figures of merit used to compare the fits of the simulated diffraction profiles to the experimental polycrystalline diffraction profile with lognormal-based spline fit background subtraction method.

Model	Bragg factor (R_B)	Profile factor (R_p)
Cubic spinel-based (Smrčok)	0.26	0.43
Tetragonal nonspinel (Paglia)	0.50	0.56
Monoclinic nonspinel (Digne)	0.44	0.61
Monoclinic spinel-based (Pinto)	0.24	0.52

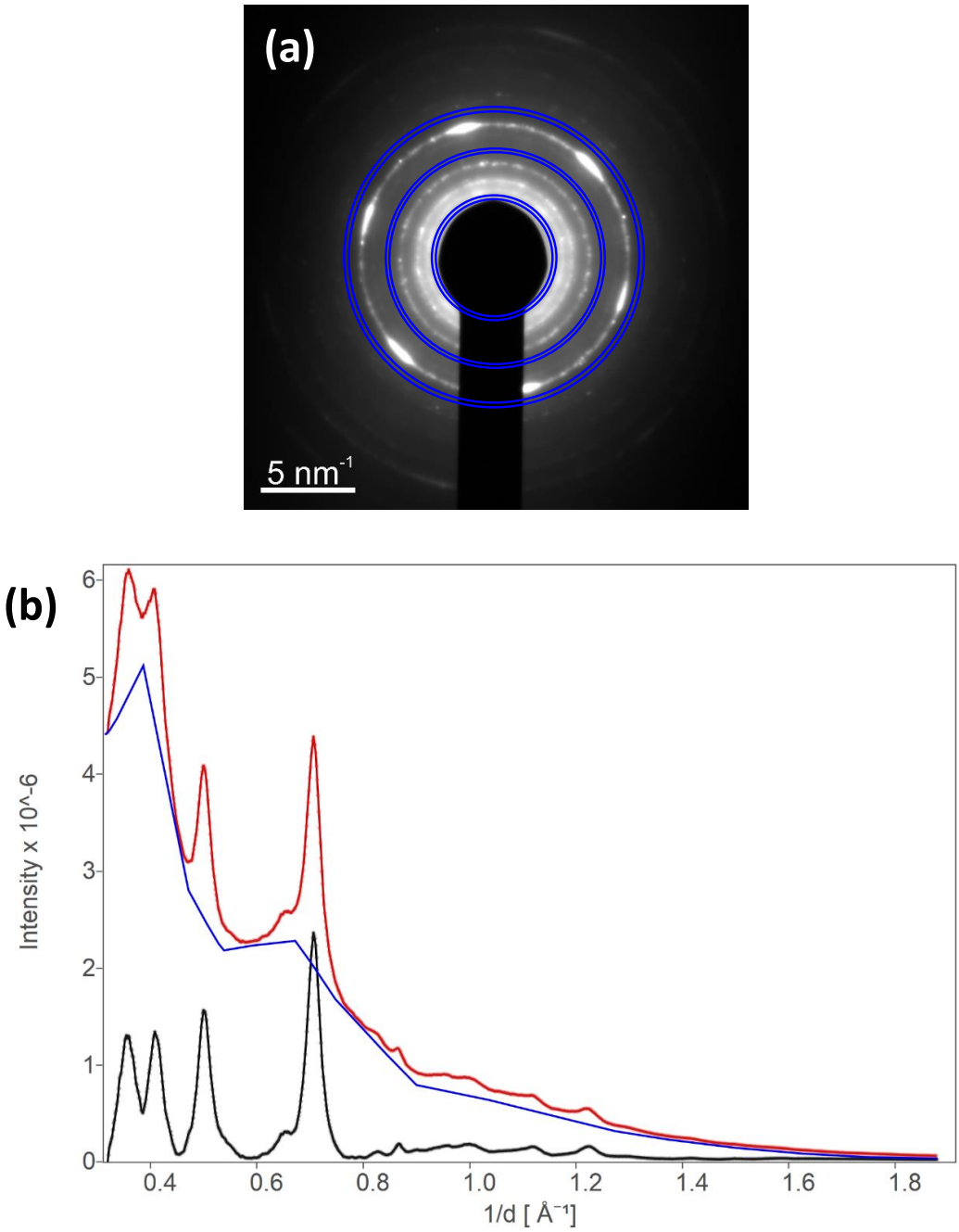

Appendix Figure 5. (a) Placement of rings on polycrystalline SAED pattern where background intensities were measured for background subtraction. (b) Background subtraction approach of azimuthally averaged profile of the polycrystalline γ-Al_2O_3 thin film SAED pattern by plotting measured background intensities and subtracting from the profile.

Appendix Table 2. Figures of merit used to compare the fits of the simulated diffraction profiles to the experimental polycrystalline diffraction profile with background subtraction method of measuring the background between diffracted rings.

Model	Bragg factor (R_B)	Profile factor (R_p)
Cubic spinel-based (Smrčok)	0.32	0.42
Tetragonal nonspinel (Paglia)	0.33	0.46
Monoclinic nonspinel (Digne)	0.31	0.58
Monoclinic spinel-based (Pinto)	0.31	0.54

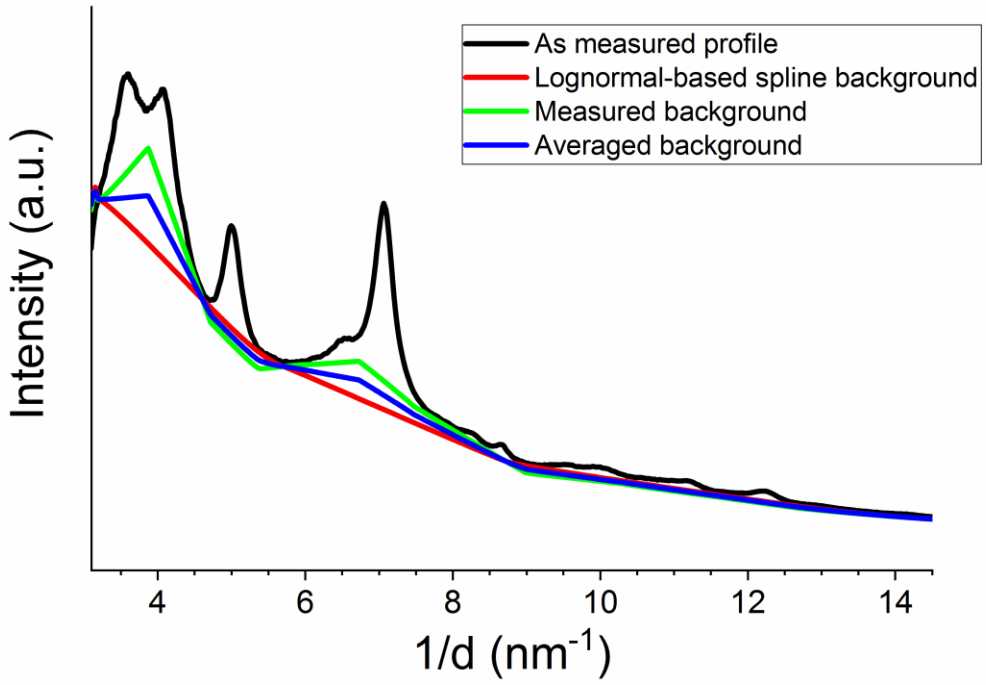

Appendix Figure 6. Averaging the two background subtraction techniques for the azimuthally averaged profile of the polycrystalline γ-Al_2O_3 thin film SAED pattern.

The polycrystalline diffraction profiles for the γ-Al_2O_3 models were generated using kinematical electron diffraction simulation implemented in the CrystalDiffract® software. The electron beam voltage (300 kV) and grain size (50 nm) were input into the program to replicate the experimental diffraction conditions. After testing Gaussian, Lorentzian and Pseudo-Voigt peak shapes, the Pseudo-Voigt shape with eta = 0.8 was found to fit best to the experimental line profile peak shapes. Peak width was selected to match the full-width half-maximum of the dominant peak (at ~7 nm^{-1}) in the experimental profile. The simulated line profiles were then normalized to the same scale as the experimental profile.

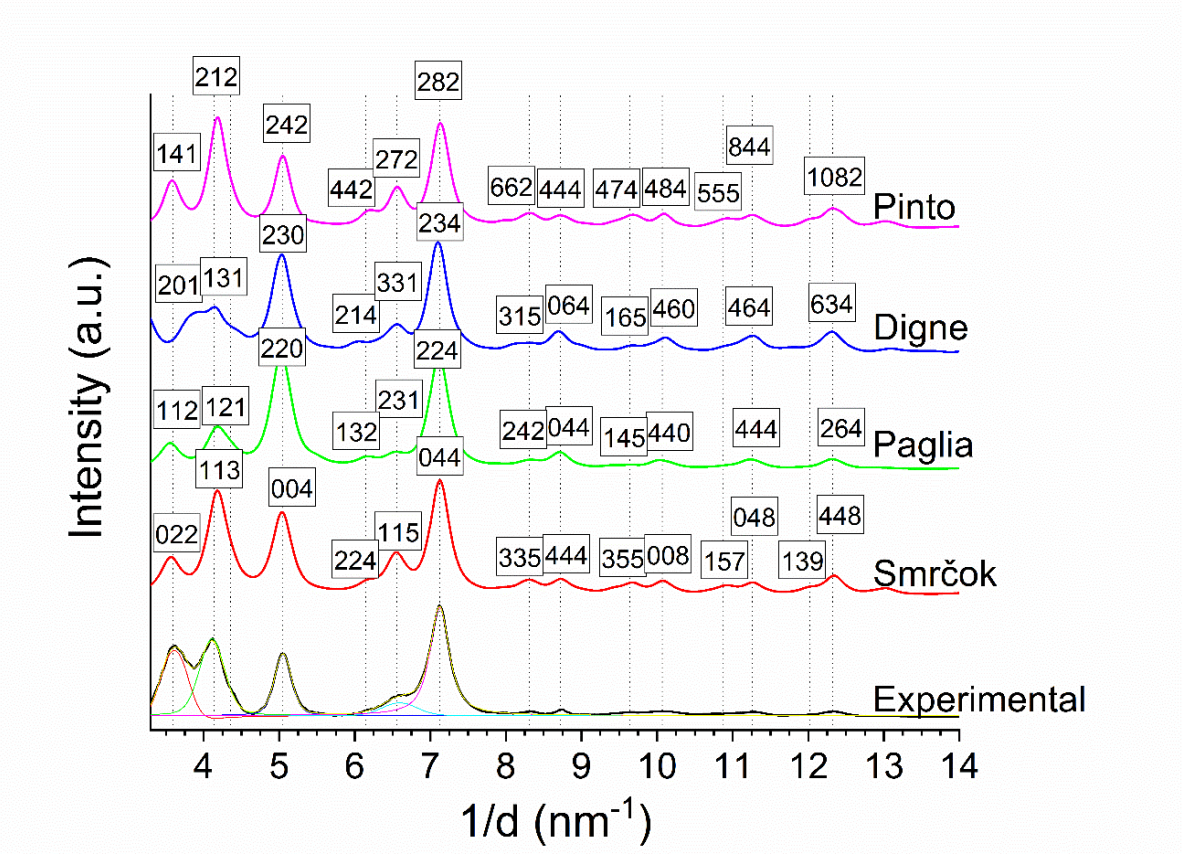

Appendix Figure 7. Azimuthally averaged line profile of the experimental polycrystalline SAED pattern, plotted with the simulated diffraction data for each of the models considered. The fitted peaks used to compute the Bragg factor are also shown plotted underneath the experimental profile.

Appendix C.3 Single-Crystal SAED Analysis

Appendix Figure 8 shows the diffraction pattern from the twinned single-crystal γ-Al_2O_3 film.

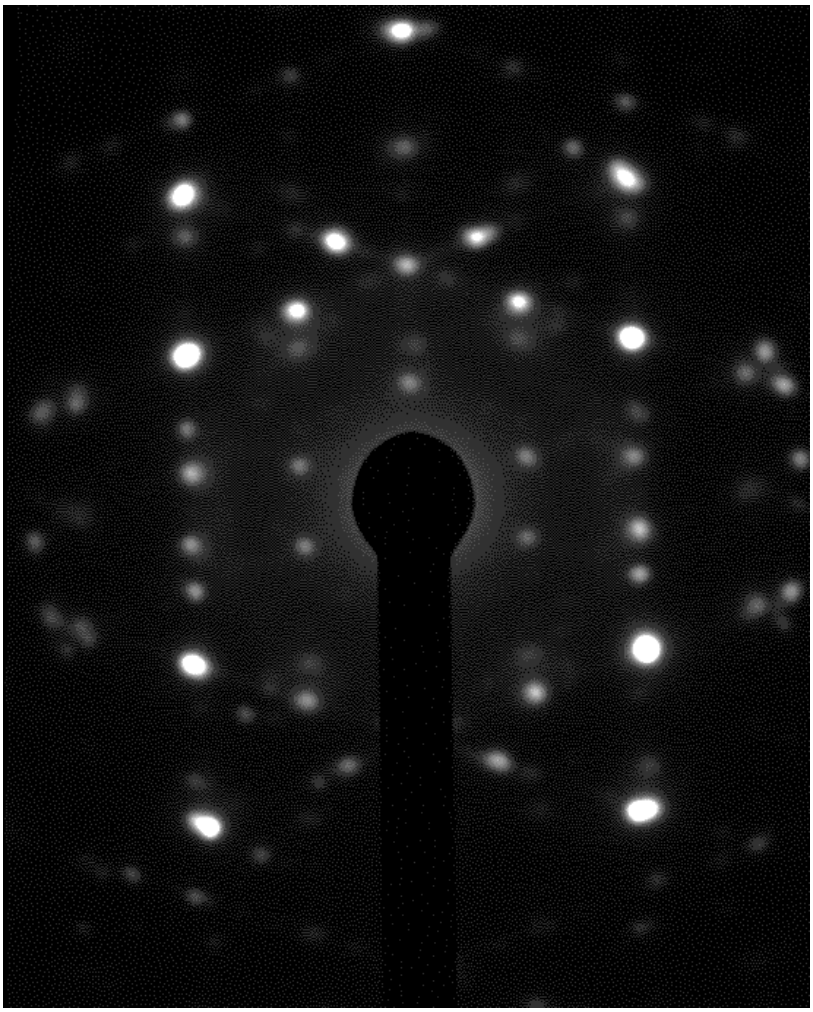

Appendix Figure 8. SAED of the as-prepared γ-Al_2O_3 film.

Appendix C.3.1 Single-Crystal SAED Simulations

The single-crystal diffraction spot patterns for the γ-Al_2O_3 models were generated using SingleCrystal. The electron beam voltage (200 kV), camera length (250 or 500 mm), and crystal thickness (50 nm) were input into the program to replicate the experimental diffraction conditions. The zone axis for each pattern was aligned to match the experimental as closely as possible. This was done by matching the crystal orientation in CrystalMaker for each of the models to that of the cubic spinel model which matched the experimental SAED pattern best. The diffraction patterns for twinned crystals were generated by simulating the diffraction pattern for each twin orientation separately and then combining the patterns into one. Line profiles of the single-crystal diffraction patterns were made in Gatan Digital Micrograph and used to compare the presence/absence of spots in the patterns.

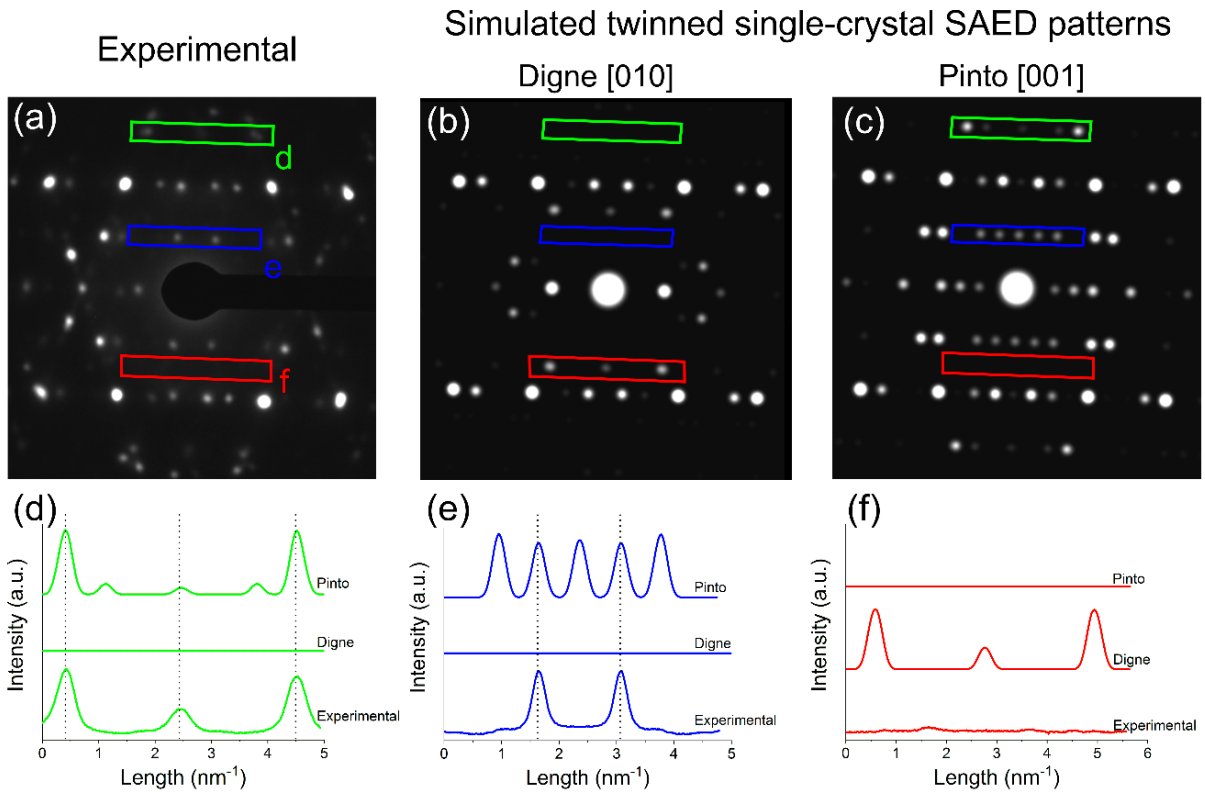

Appendix Figure 9. Line profile comparison of SAED spot patterns from Figure 38a and simulated spot patterns from the Digne monoclinic nonspinel (b) and Pinto monoclinic spinel-based (c) models. Underneath the diffraction patterns are the line profiles of intensity taken from the outlined area in each diffraction pattern. The dotted lines in (d), (e) and (f) highlight the peaks (spots) from the experimental SAED pattern.

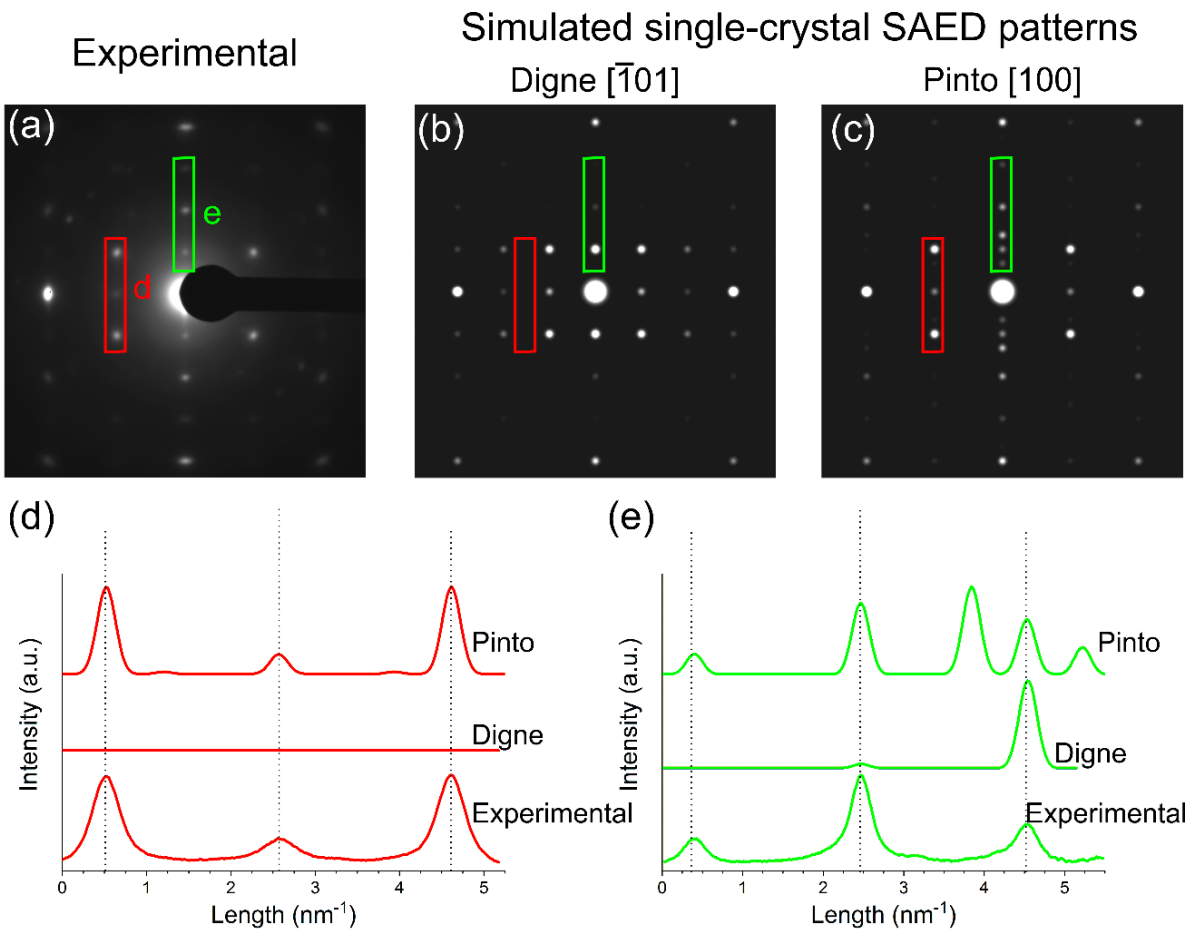

Appendix Figure 10. Line profile comparison of SAED spot patterns from Figure 38b and simulated spot patterns from the Digne monoclinic nonspinel (b) and Pinto monoclinic spinel-based (c) models. Underneath the diffraction patterns are the line profiles of intensity taken from the outlined area in each diffraction pattern. The dotted lines in (d) and (e) highlight the peaks (spots) from the experimental SAED pattern.

The simulated SAED patterns from the Digne model are visibly different from the rest of the patterns, further confirming it as the least accurate model. The line profiles in Appendix Figure 9 and Appendix Figure 10 highlight the mismatch of the Digne model. Where there are spots in the experimental SAED pattern (green and blue line profiles in Appendix Figure 9d and Appendix Figure 9e and red line profile in Appendix Figure 10d), there are none in the Digne model SAED patterns. Conversely, where there are no spots in the experimental (red line profile in Appendix Figure 9f), there are spots in the Digne [010] pattern. The simulated SAED patterns from the Pinto model contain the spots seen in the experimental patterns but also many additional spots. This is highlighted in Appendix Figure 9 and Appendix Figure 10, where additional spots are seen in both the green and blue line profiles in Appendix Figure 9d and Appendix Figure 9e, and in the red and green line profiles in Appendix Figure 10d and Appendix Figure 10e.

Appendix Table 3. Peak intensity ratios calculated using the line profiles taken from Figure 39. The intensity ratio mean absolute error (MAE) is the sum of the difference between model and experiment for each peak intensity ratio weighted by the sum of the peak intensity ratios for the experimental single-crystal SAED.

Single-crystal SAED	Green profile peak ratio (A/B)	Red profile peak ratio (C/D)	Blue profile peak ratio (E/F)	Intensity ratio MAE
Experimental	2.6	0.6	4.6	N/A
Cubic spinel-based (Smrčok) 110	3.2	1.1	1.8	0.5
Tetragonal nonspinel (Paglia) 100	0.8	0.9	0.6	0.8

Comparison of a line profile from the 2nd zone axis SAED pattern between the Smrčok and Paglia models (Appendix Figure 11) further confirms the Smrčok model as the most accurate model. The ratio of the labeled peaks A/B for the Smrčok cubic spinel model is closer to the experiment than the Paglia tetragonal nonspinel model. The intensity of the peaks A>B for the Smrčok model also, which is consistent with the experiment, whereas the opposite is true for the Paglia model.

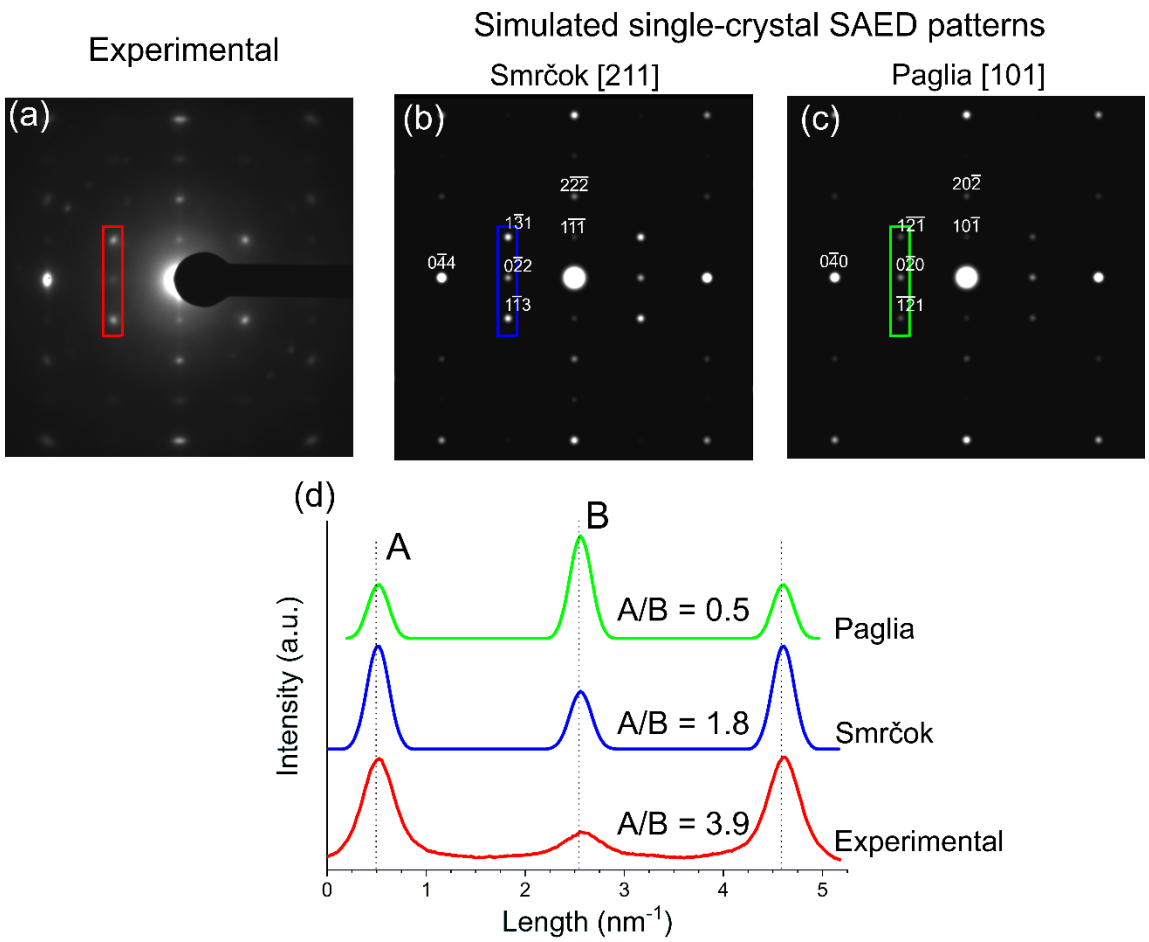

Appendix Figure 11. Line profile comparison of SAED spot patterns from Figure 38b and simulated spot patterns from the cubic spinel (b) and Paglia tetragonal nonspinel (c) models. Underneath the diffraction patterns are the line profiles of intensity taken from the outlined area in each diffraction pattern.

Appendix D Additional Details for γ-Al_2O_3 Vacancy Distribution Determination

Appendix D.1 Computational Details

Appendix D.1.1 Simulated Spectra Convergence with Cluster Size

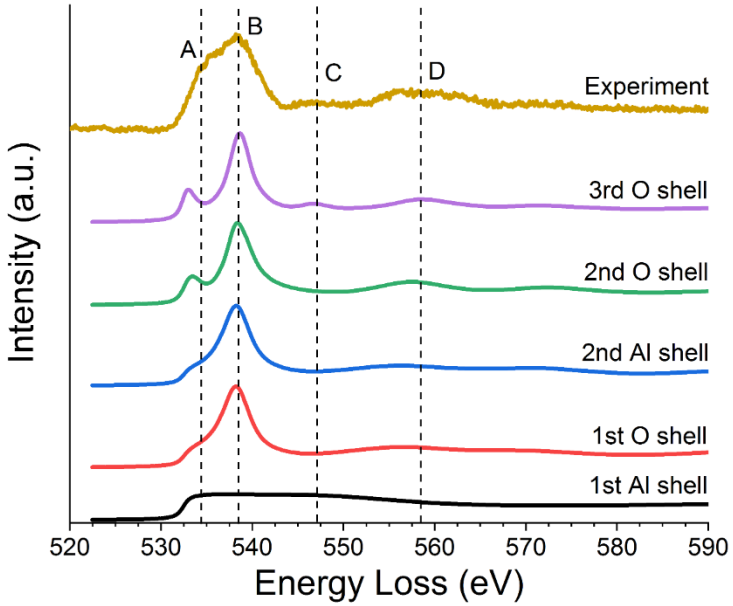

Appendix Figure 12. Calculations of O-K edge ELNES for different cluster sizes surrounding the excited atom using the cubic spinel γ-Al_2O_3 model.

Appendix Figure 12 shows the O-K edge ELNES simulations of varying cluster sizes of the cubic spinel γ-Al_2O_3 model. The first Al shell produces no fine structure, with only the hydrogenic edge being produced. Overall, the shell-by-shell simulations show that the spectral features arise primarily from scattering from oxygen shells. This makes sense since O is a much stronger electron scatterer than Al [182, 184, 229]. The scattering from the 1st O shell produces

the main peaks labeled B and D, scattering from the 2nd O shell produces the peak/shoulder A and scattering from the 3rd O shell produces the subtle peak C. Thus, a basic representation of the O-K edge could be reproduced using a four-oxygen-shell cluster (~6 Å cluster).

Appendix D.1.2 Limitations of the Simulation Procedure

FEFF uses the spherical muffin-tin approximation and does not perform calculations with full potentials. The spherical muffin-tin approximation for atomic potential fields approximates the potential field around atoms in a crystal lattice as non-overlapping spheres. The screened potential experienced by electrons within the sphere is approximated as spherically symmetric about the nucleus of the atom. This makes solutions to multiple-scattering equations more stable and easier to compute but may also alter relative peak size especially as full-potential effects can be large for d-states and can cause additional splitting of levels. The approximate nature of many-body effects such as quasiparticle self-energy corrections, core-hole, and disorder-induced broadening in the FEFF calculations contribute to the slight difference in peak positions between the simulated spectra and the experimental spectrum.

Appendix D.1.3 Influence of Strain on EELS Spectra

Strain in the crystal lattice can influence the EELS spectra acquired from a sample [176]. In the case of crystalline Al_2O_3 grown by oxidation of NiAl, it is known that there is residual strain in the Al_2O_3 due to lattice and coefficient of thermal expansion (CTE) mismatch [177]. However, for the epitaxial growth of these samples, the degree of lattice mismatch between NiAl (002) and γ-Al_2O_3 (044) is 2.6%, which is small. On the other hand, strain is detected in EELS spectra by

small peak shifts in low-loss EELS spectra (on the order of 0.16 eV per 1% volume change). Since the effect of strain is small, and this analysis is focused on near-edge features and not absolute peak positions of the EELS edges, the optimized structures with no strain were used in the reported calculations.

To further verify this assumption, single site O K edge EELS simulations were done for the pristine monoclinic model and for the monoclinic model with lattice parameter **a** modified to simulate the lattice mismatch induced strain from the NiAl substrate. Appendix Figure 13 show that the spectra are nearly identical, validating the assumption that the effect of strain on the EELS spectra is negligible for the purposes of this study. Note that these are single O atom simulations; the necessary site-averaging done in the full simulations will broaden the peak features that differ between the spectra.

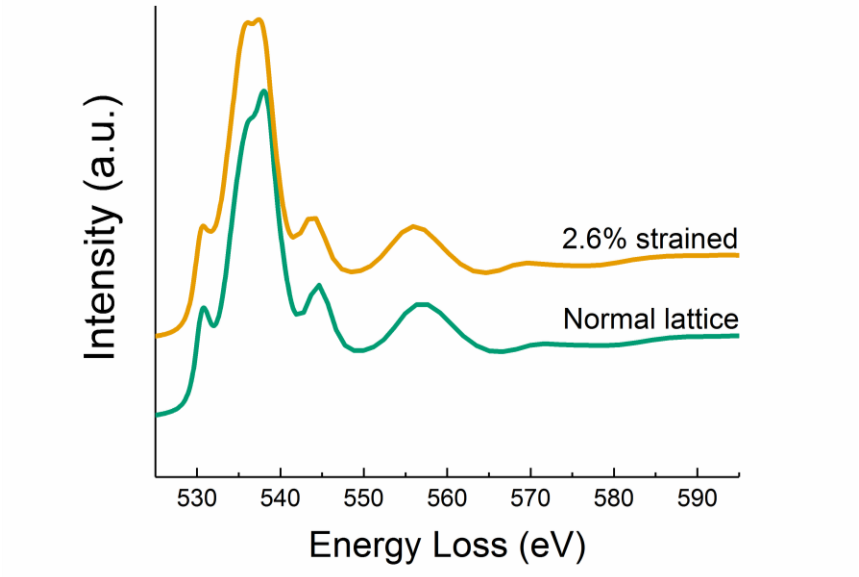

Appendix Figure 13. Simulated O-K edge EELS spectra for a single O atom in a cluster assembled using the normal monoclinic model lattice and a cluster simulating the lattice mismatch strain of the system.

Appendix D.2 Procedure to Calculate Mean Absolute Deviations for Each Vacancy Distribution Model

Appendix D.2.1 Calculation of Experimental Intensity Ratios

Integrated intensity was first calculated for each spot. First, a threshold mask was applied to the experimental diffraction pattern to exclude all pixels with intensity below 2x the background (Appendix Figure 14).

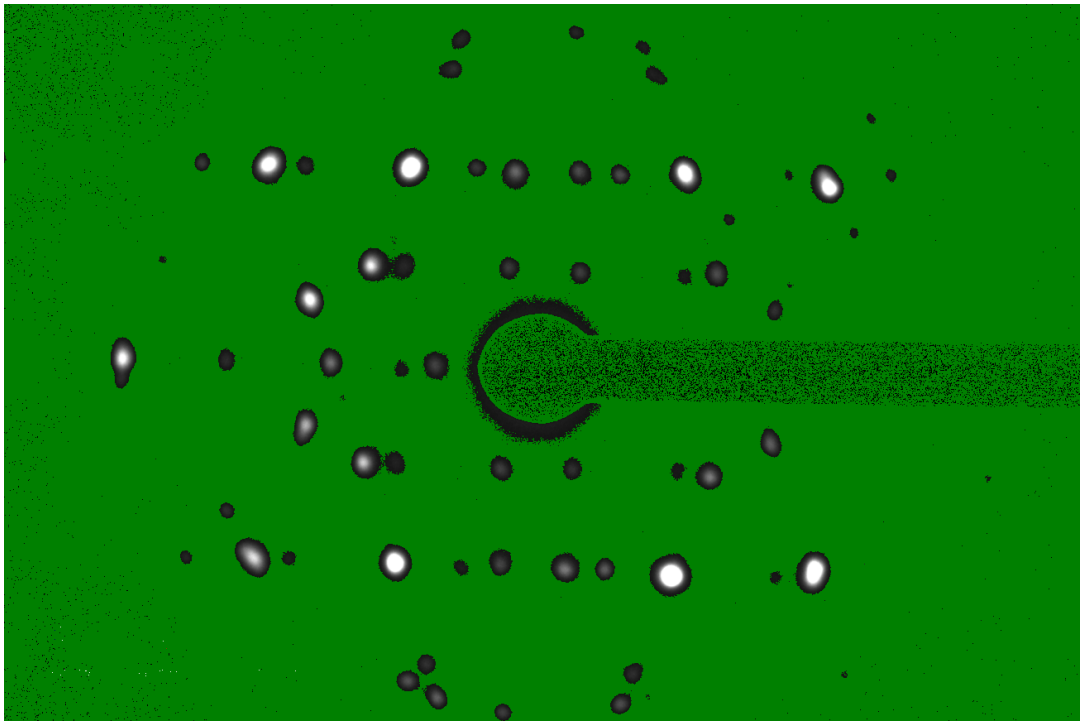

Appendix Figure 14. Experimental (110) zone axis SAED pattern with threshold mask applied. All pixels below the threshold are colored green.

Line profiles were placed on the diffraction spots to include the pixels above the threshold value. This produced a 2D Gaussian-like intensity profile for each spot. The profile for each spot

was fit with a Gaussian and the area under the Gaussian was calculated (Appendix Figure 15). This provided the value for integrated intensity for that spot. The spot with the maximum integrated intensity among all symmetrically equivalent spots (e.g. spot D among all {440} spots appearing on the SAED pattern) was used as the intensity value for the given reflection.

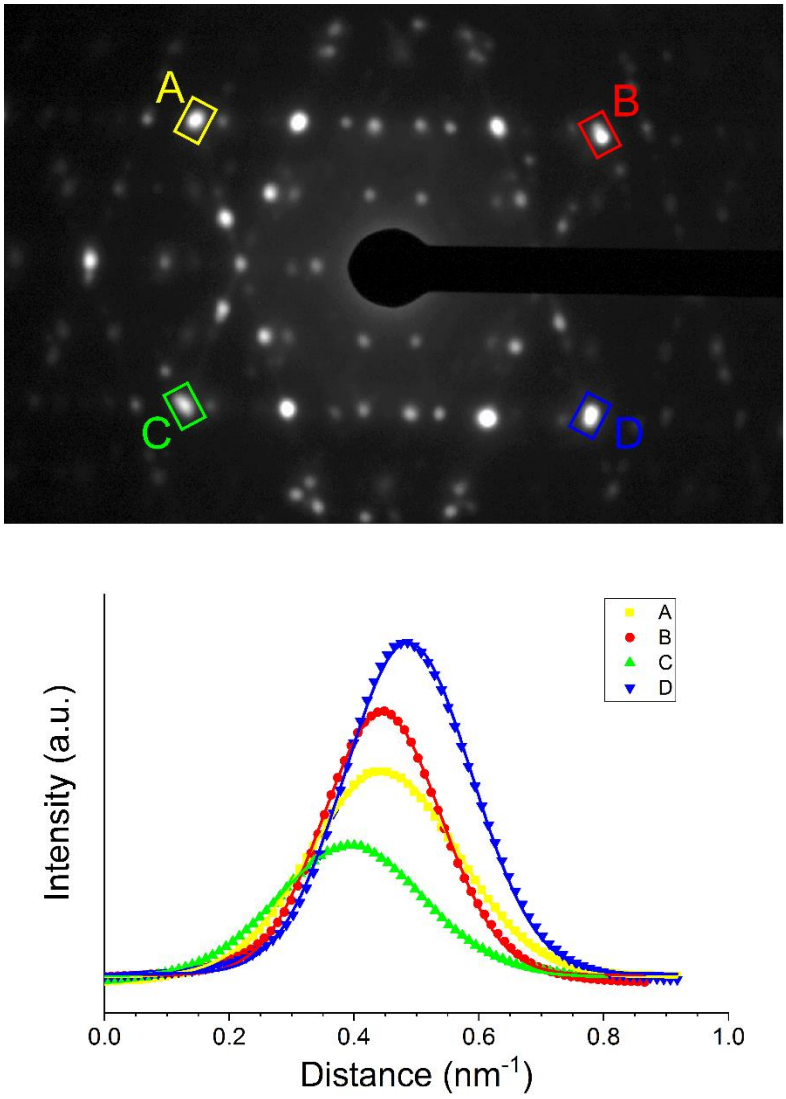

Appendix Figure 15. Example of line profiles taken of {440} spots from the [110] ZA SAED pattern. $R^2 > 0.95$ for all Gaussian fits.

The intensity ratios were then calculated for the given pairs of reflections in Table 6 in the main text using the intensity for each reflection calculated above. This was done for each of the diffraction patterns, with the twin patterns counting as two separate patterns. The intensity ratios for the same reflection pair but from different patterns were then averaged to get the values shown in Table 6. The weighting given to each reflection pair was calculated by giving the brightest reflection, the {400} reflection, a value of 1 and scaling all the reflections appropriately. The weighting for each reflection pair was then calculated by averaging the weights for the two reflections and scaling to the sum of all the weights.

Appendix D.2.2 Calculation of Simulated Intensity Ratios for Vacancy Distribution Models

Starting with the description of lattice parameters and atomic positions obtained from the Gutierrez cubic spinel-based model, models with varying Al vacancy distributions were made by altering the occupancy of tetrahedral (8a) and octahedral (16d) sites (Appendix Table 4). For each model, the diffraction data (i.e. list of reflections and their relative intensities) was calculated using SingleCrystal. The intensity ratios for the same pairs of reflections calculated for the experimental SAED patterns (as in Table 6 in the main text) were then calculated using the simulated diffraction data.

Appendix Table 4. Tetrahedral and octahedral site occupancy for all cubic spinel-based models used for SAED simulations.

Model	Fraction of vacancies in tetrahedral sites	Tetrahedral (8a) site occupancy	Octahedral (16d) site occupancy
1	0	1	0.8333
2	0.1	0.9667	0.8500
3	0.2	0.9333	0.8667
4	0.3	0.9000	0.8833
5	0.4	0.8667	0.9000
6	0.5	0.8333	0.9167
7	0.6	0.8000	0.9333
8	0.7	0.7667	0.9500
9	0.8	0.7333	0.9667
10	0.9	0.7000	0.9833
11	1	0.6667	1

Appendix Table 5. Example of intensity ratios calculated for a model with 50% (0.5) of Al vacancies placed on tetrahedral sites. The unweighted mean absolute deviation (MAD) for this model was calculated as 2.32. The weighted MAD was calculated as 2.55.

		50% of Al vacancies on tetrahedral sites		
Reflections	Experimental intensity ratio	Calculated intensity ratio	Absolute deviation ($\lvert I_{exp}-I_{calc}\rvert$)	Weighting
220/111	0.88	1.78	0.90	0.052
113/111	3.34	3.70	0.37	0.123
222/111	1.80	0.93	0.87	0.067
400/111	14.32	15.59	1.26	0.407
440/111	9.49	14.38	4.89	0.241
115/111	1.01	1.83	0.82	0.053
622/111	1.14	0.47	0.66	0.056

For each intensity ratio, the absolute deviation was calculated relative to the experimental value. An example of this process is shown in Appendix Table 5. The absolute deviations of the intensity ratios for all the considered models are shown in Appendix Figure 16. The absolute deviations for each reflection pair were then averaged to get the mean absolute deviation (MAD) which was used to compare the models to each other to determine the best fitting model.

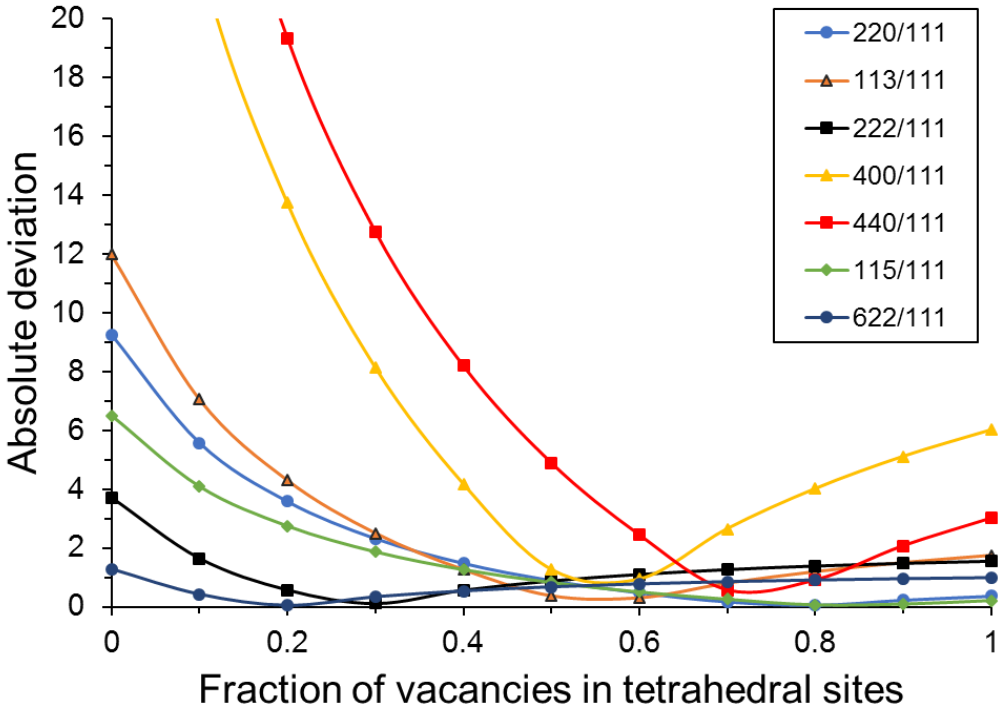

Appendix Figure 16. Absolute deviations of each intensity ratio relative to experimental value, plotted for each vacancy distribution model.

Appendix D.2.3 Mean Absolute Deviation Calculations (Unweighted vs Weighted)

The plot of mean absolute deviation shown in Figure 41 in the main text is the weighted mean. An unweighted mean absolute deviation was also calculated. The unweighted MADs are shown in Appendix Figure 17. No significant difference is observable.

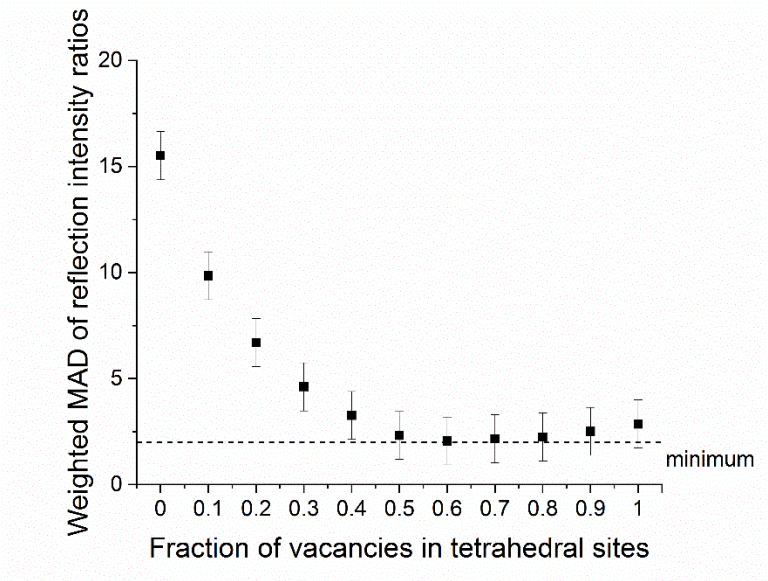

Appendix Figure 17. Unweighted mean absolute deviation (MAD) of reflection intensity ratios relative to the experimental values for each cubic spinel model vs fraction of Al vacancies in tetrahedral sites in the model.

Another set of calculations using another set of intensity ratios was performed to compare the effect of selecting different reflection pairs. The selected reflection pairs are shown in Appendix Table 6. The change in selection of reflection pairs had no significant effect on the calculated MAD values (Appendix Figure 18).

Appendix Table 6. Ratios of intensity of second set of reflection pairs.

Reflections	Intensity ratios	Weighting
113/111	3.64 ± 0.02	0.102
113/220	3.98 ± 0.70	0.101
222/111	1.52 ± 0.17	0.055
400/111	14.32 ± 2.19	0.336
440/111	8.08 ± 1.91	0.199
113/115	3.63 ± 0.09	0.102
113/622	3.34 ± 0.20	0.104

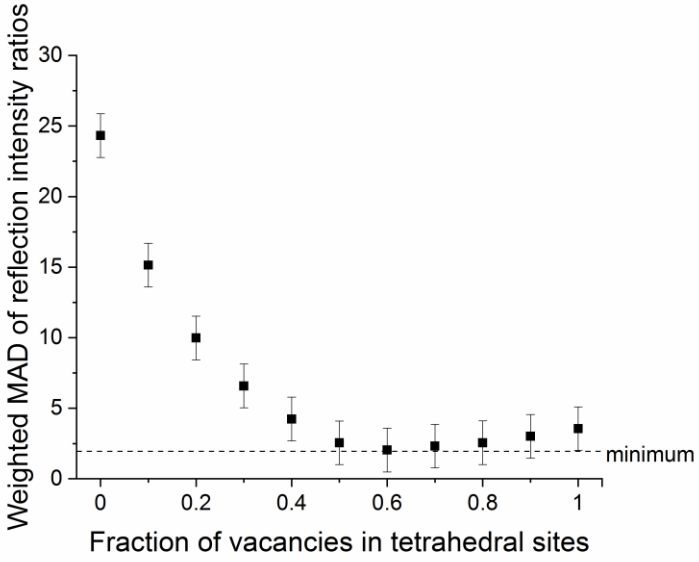

Appendix Figure 18. Weighted mean absolute deviation (MAD) values for each cubic spinel model calculated using the data in Appendix Table 6.

Appendix D.3 Experimental High-Resolution EELS Spectra

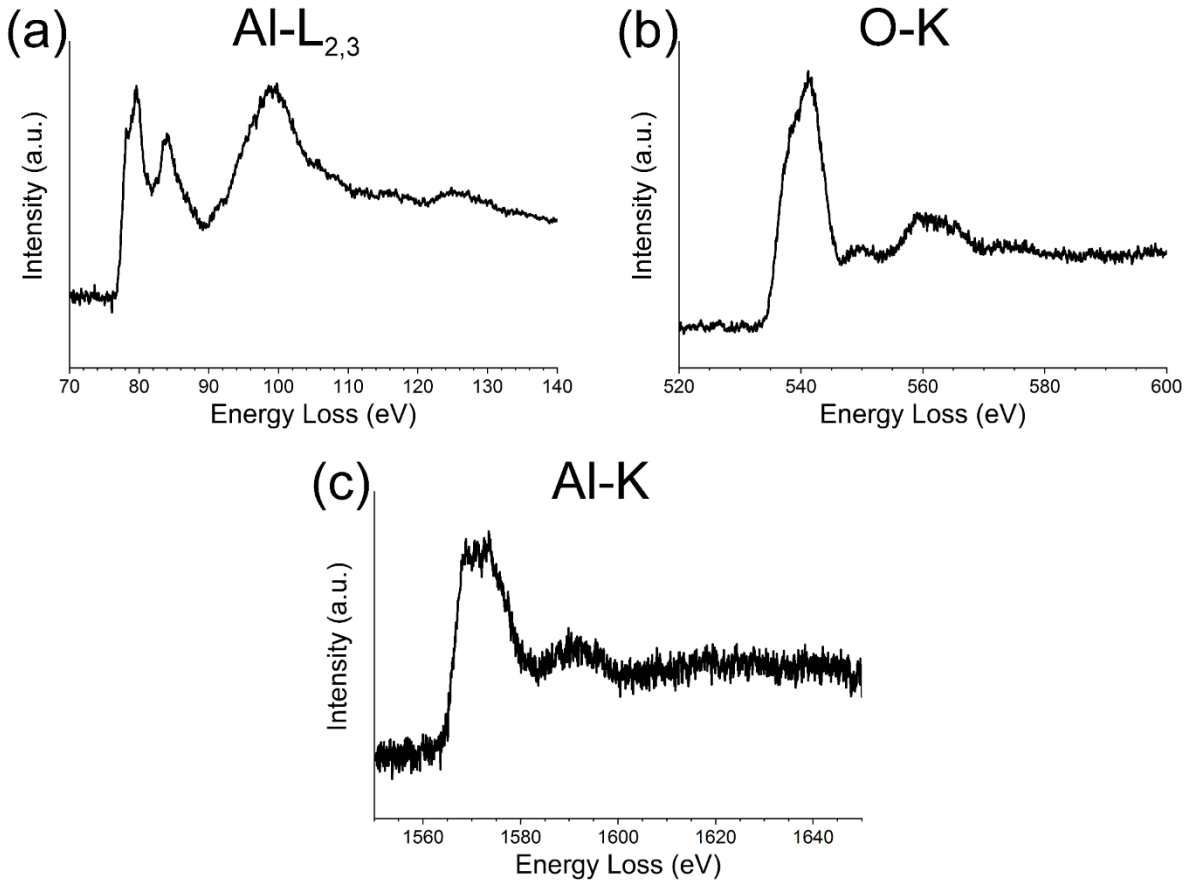

Appendix Figure 19. (a) Al-$L_{2,3}$ edge, (b) O-K edge, and (c) Al-K edge EELS spectra acquired from γ-Al_2O_3.

Appendix D.4 Tetrahedral Al vs Octahedral Al-$L_{2,3}$ edge ELNES Simulations

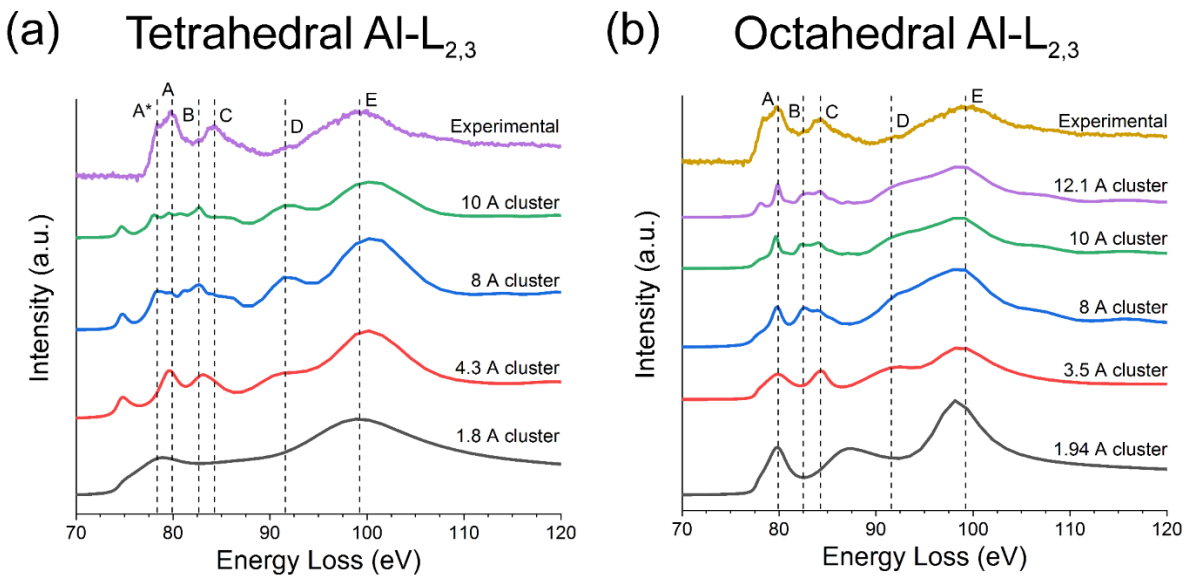

Appendix Figure 20. Calculations of Al-$L_{2,3}$ edge ELNES for different cluster sizes surrounding a (a) tetrahedral and (b) octahedral excited Al atom using the cubic spinel γ-Al_2O_3 model.

Al-$L_{2,3}$ edge ELNES simulations of varying cluster sizes of the cubic spinel γ-Al_2O_3 model are shown in Appendix Figure 20. Appendix Figure 20a shows the calculations with a tetrahedral Al atom as the absorbing atom, whereas Appendix Figure 20b shows the calculations with an octahedral Al atom as the absorbing atom. In both cases, the peak labeled E is present throughout, including in the first shell calculations, indicating that this feature is a consequence of the scattering from the first tetrahedron or octahedron.

For the tetrahedral Al atom (Appendix Figure 20a), a significant degree of fine structure emerges as the cluster size is increased. This indicates that the tetrahedral Al-$L_{2,3}$ ELNES is sensitive to medium-range order and calculations should be done using as large a cluster as

possible. Overall, the tetrahedral Al-$L_{2,3}$ edge ELNES does not appear to match the experimental EELS closely. This could either indicate a problem with the simulation of the tetrahedral Al-$L_{2,3}$ ELNES, or that the contribution of the tetrahedral Al to the overall γ-Al_2O_3 Al-$L_{2,3}$ edge EELS is minimal. To determine whether the former was the case, the Al-$L_{2,3}$ ELNES of berlinite ($AlPO_4$) was calculated and compared to the corresponding Al-$L_{2,3}$ edge EELS from literature [136] (Appendix Figure 21b) to gauge the accuracy of the FEFF simulation from tetrahedral Al atoms. $AlPO_4$ consists solely of tetrahedrally-coordinated Al atoms and should provide a baseline for scrutiny of the accuracy of the MS simulation. The Al-$L_{2,3}$ edge simulated from $AlPO_4$ did not exhibit a good match to the experimental spectrum. One potential explanation is that the relaxation of the dipole-selection rules governing the electronic transitions—required to accurately model the scattering from a non-centrosymmetric atom such as a tetrahedral Al atom—is not effectively accounted for in the FEFF calculations.

For the octahedral Al atom (Appendix Figure 20b), the main features (A,C-E) of the ELNES already appear with a 3.5 Å cluster, corresponding to the 3rd oxygen shell about the central Al atom. However, some fine structure does develop with further increasing cluster sizes. The octahedral Al-$L_{2,3}$ edge ELNES exhibits a better match to the experimental EELS. This suggests that there are significantly more octahedral Al atoms than tetrahedral in the γ-Al_2O_3 structure, which is expected. The accuracy of FEFF simulation of the Al-$L_{2,3}$ ELNES from an octahedral Al was also checked using alpha-alumina (α-Al_2O_3) which contains only octahedrally-coordinated Al atoms and displayed in Appendix Figure 21a. The simulation shows a much better match than the $AlPO_4$ Al-$L_{2,3}$ simulation. This further confirms the hypothesis that the non-centrosymmetric tetrahedral Al atom is the source of difficulty for the multiple scattering simulations using FEFF, since the octahedral Al—which is centrosymmetric—presents no significant issue.

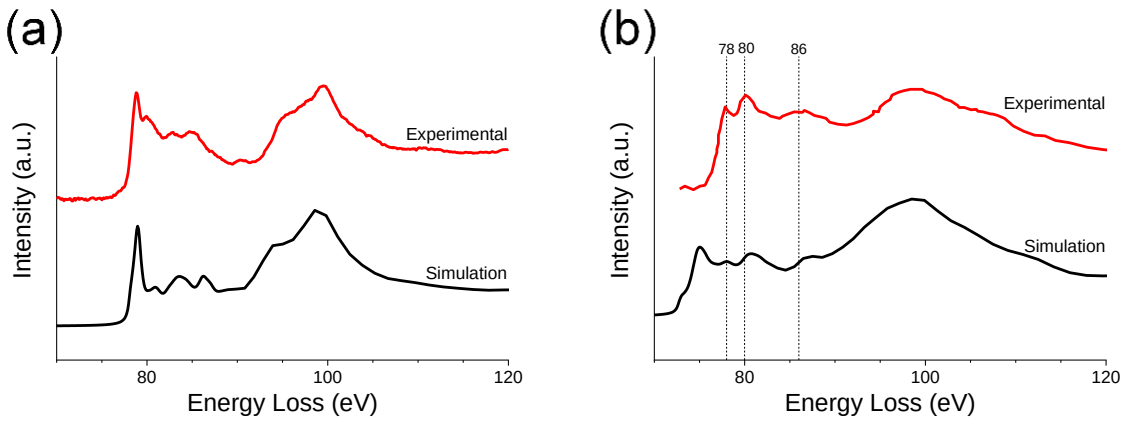

Appendix Figure 21. Al-$L_{2,3}$ EELS simulations from (a) alpha-alumina (α-Al_2O_3) and (b) berlinite ($AlPO_4$) compared to experimental EELS [136].

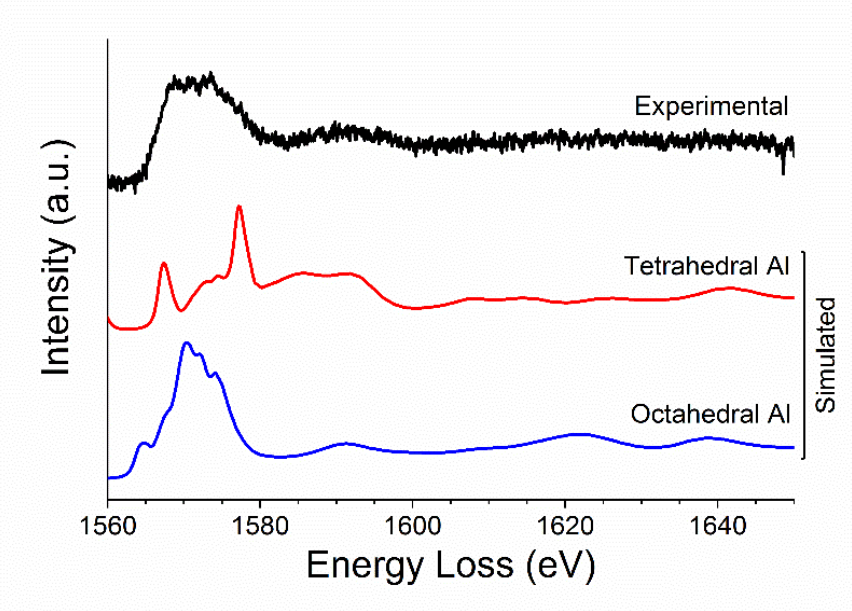

Appendix Figure 22. Simulated Al-K edge ELNES for both a single tetrahedral Al atom and a single octahedral Al atom in the cubic-spinel based model compared to the experimental Al-K edge spectrum.

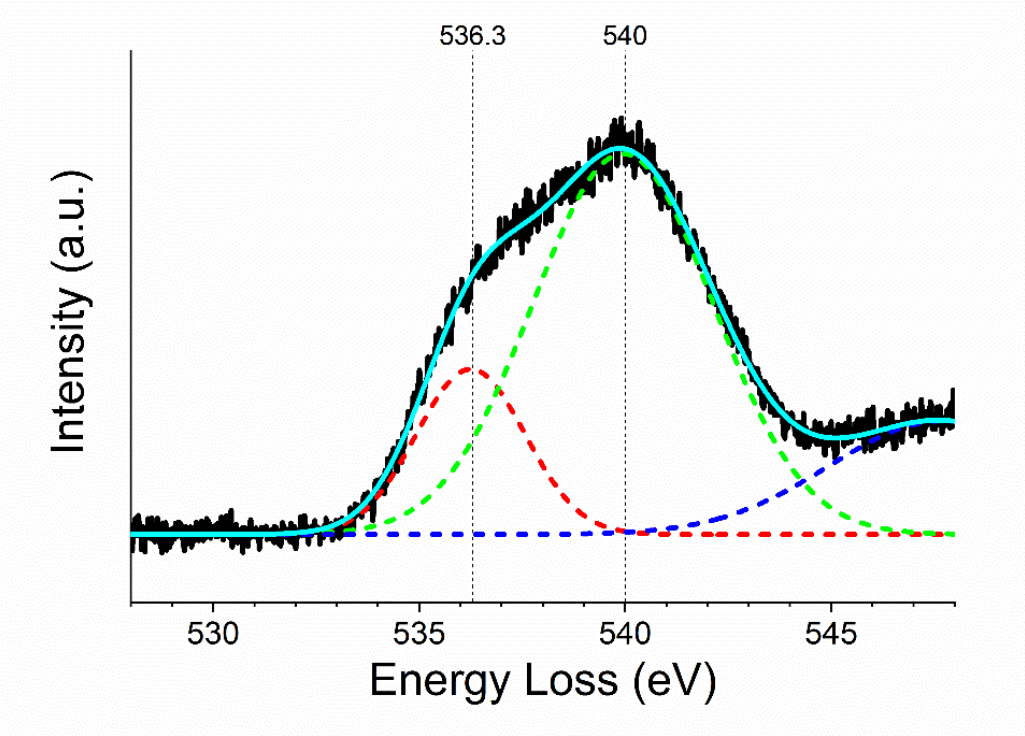

Appendix Figure 23. Fitting the O-K edge broad peak (labeled A in Section 7.3.2) with two Gaussian peaks. An excellent fit was achieved with $R^2 = 0.99$ with the peak positions and widths plotted in dashed lines.

Appendix E Additional Details for Pt/γ-Al_2O_3 (111) Interface Bonding Study

Appendix E.1 Computational Details

First principles DFT calculations were carried out within the Perdew-Burke-Ernzerhof (PBE)[143] exchange-correlation functional and projector augmented wave (PAW) pseudopotentials[188, 189] as implemented in the VASP. The electron wavefunction was expanded using planewaves with a 400 eV planewave cutoff. The (111) surface of gamma-alumina was modeled using the non-spinel model proposed by Digne et al.[78], to correlate with the surface orientation obtained from the oxidation of NiAl (110). A supercell approach employing a (1×1) surface supercell and 4 layers in the non-periodic direction was used. A vacuum of more than 15 Å was used to mitigate spurious interactions in the non-periodic direction. A 4 x 4 x 1 k-grid was used to sample the Brillouin zone. The energy relaxation was iterated until the forces acting on all the atoms were less than 1 meV/Å, with a convergence in the total energy at about 10^{-6} eV. The bottom 4 layers were held fixed during the relaxation. Validation of the computational framework was done by checking that the energy cutoff, k-grid, and energy tolerances were sufficient to converge energy differences to less than 1 meV.

Appendix E.2 Experimental Replication of Interfacial O-K Edge ELNES

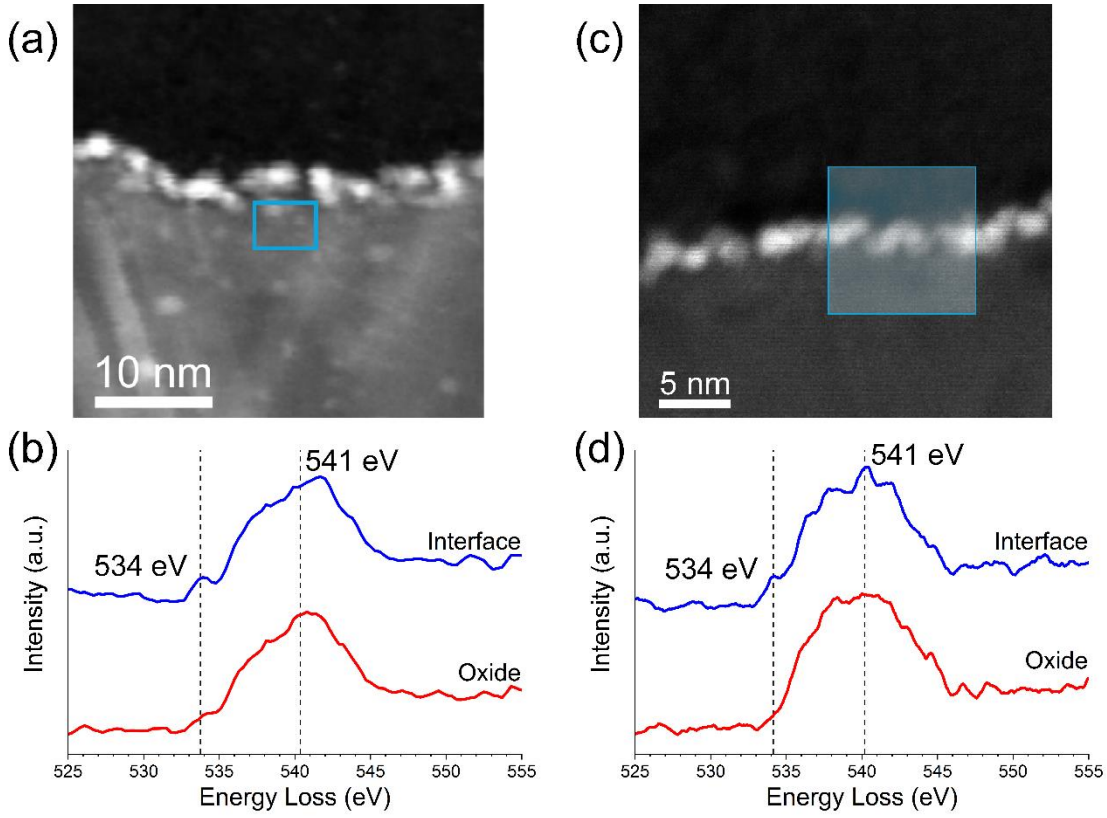

Appendix Figure 24. (a) Dark-field image with area of EELS acquisition highlighted with the blue box and (b) O-K edge spectrum collected from (a) at cryo temperature on an aberration-corrected JEOL 2100F STEM showing the 534 eV interfacial pre-peak. (c) Dark-field image with area of EELS acquisition highlighted with the blue box and (d) O-K edge spectrum collected from (c) at cryo temperature on a monochromated FEI Titan STEM showing the 534 eV interfacial pre-peak.

Appendix E.3 Confirmation of Beam Damage Suppression and Damage-Induced O-K ELNES Features

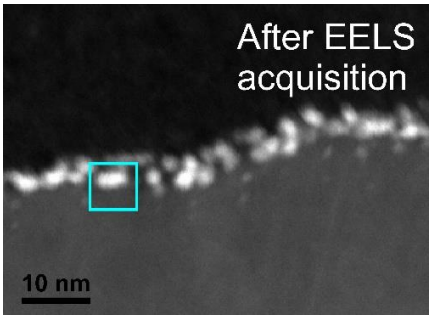

Appendix Figure 25. High-angle annular dark-field (HAADF) survey image of the Pt/γ-Al_2O_3(111) model catalyst after EELS acquisition, with the area of EELS spectrum image acquisition shown with the box. There are no visible signs of electron beam damage after the EELS acquisition.

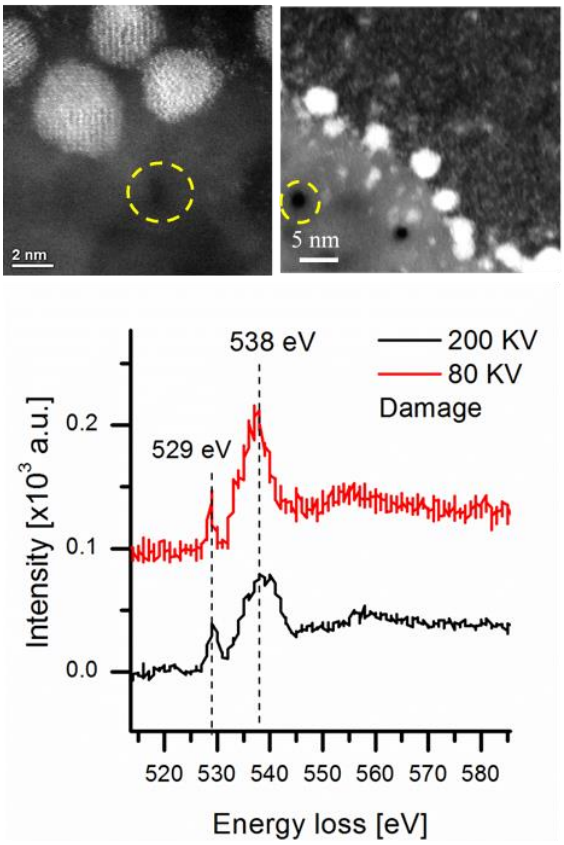

Appendix Figure 26. STEM-EELS of the Pt/γ-Al_2O_3 interface with clearly visible holes caused by electron beam damage. The O-K edge EELS spectra shown in (c) were acquired from the areas highlighted with yellow circles in (a) 80 kV and (b) 200 kV. The O-K edge pre-peak associated with beam damage appears at 529 eV.

Appendix E.4 Pt/γ-Al_2O_3 (111) Bonding Model Development

In general, the energy penalty for creating an oxygen vacancy in the first two rows of oxygen atoms (O1-O6) is ~6eV, with the exception of O4, which can be attributed to the better flexibility of ion relaxation around O4 site after removing the oxygen atom (see Appendix Figure 27 for the configurations after geometry optimization of oxygen vacancy models), while the energy penalty is around 4.5 eV for the third row of oxygen atoms (O7-O9). Finally, creating an oxygen vacancy on the last row (O10-O12) results in either a 5.87 eV energy penalty (O11 and O12), or the lowest energy penalty among all at 3.77 eV (O10). Examination of the V_O^{10} configuration after geometry optimization (Appendix Figure 27j) shows the most flexible ion relaxation process, which can be attributed to the flexible bonding allowed by the Al^t (I) atom neighboring the O10 site.

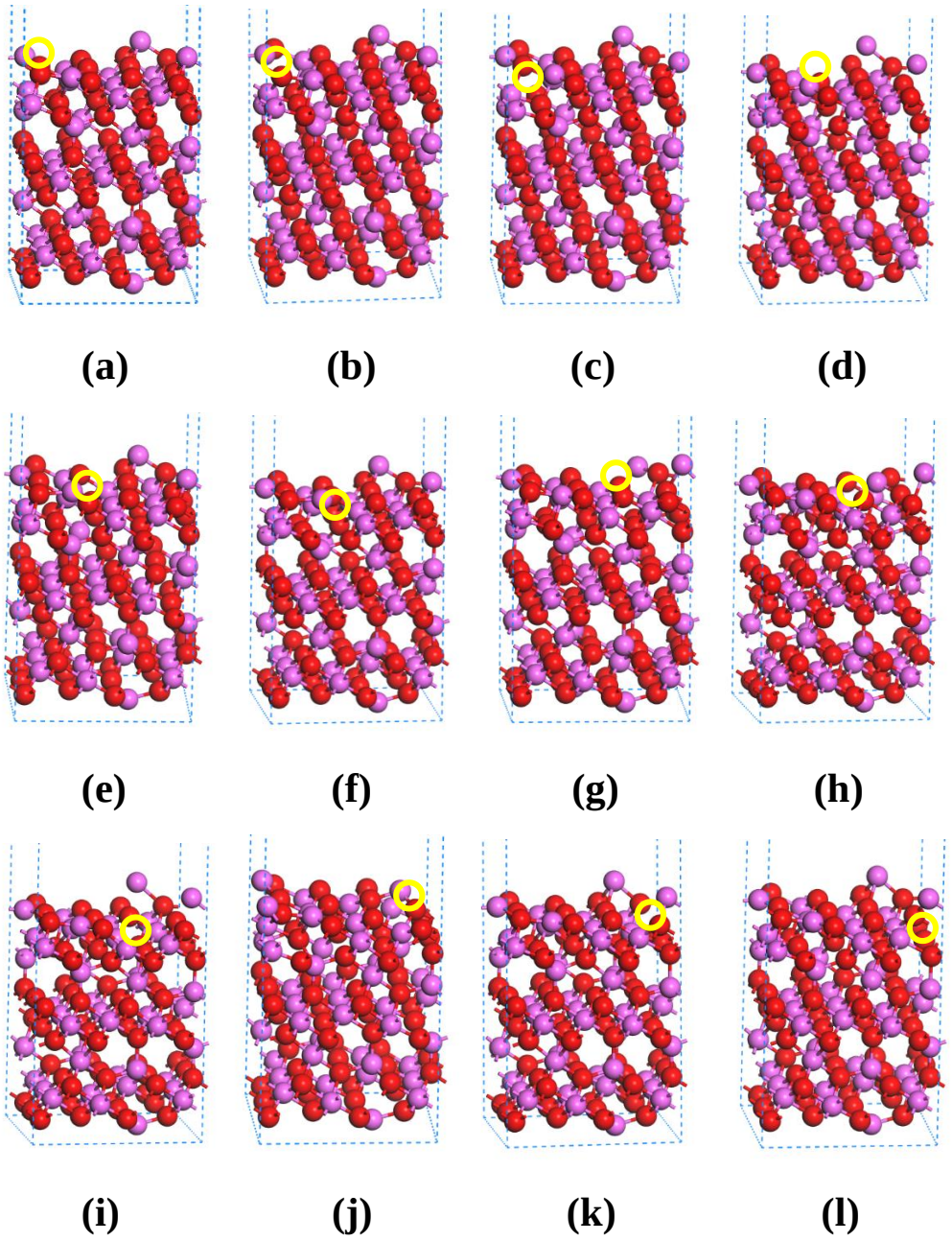

Appendix Figure 27. Configurations of oxygen vacancy models on the γ-Al_2O_3 (111) surface. (a)-(l) configurations correspond to the vacancy created on O1-O12 sites. The O vacancy position in each model is indicated with the yellow circles.

Appendix Table 7. Calculated oxygen vacancy formation energies on different γ-Al_2O_3 (111) surface sites showing a significant energy penalty to form oxygen vacancies on the pristine γ-Al_2O_3 (111) surface.

O vacancy Configurations	V_O^1	V_O^2	V_O^3	V_O^4	V_O^5	V_O^6	V_O^7	V_O^8	V_O^9	V_O^{10}	V_O^{11}	V_O^{12}
Formation Energy (eV)	5.92	5.92	5.87	4.79	6.02	6.02	4.28	4.28	4.77	3.77	5.87	5.87

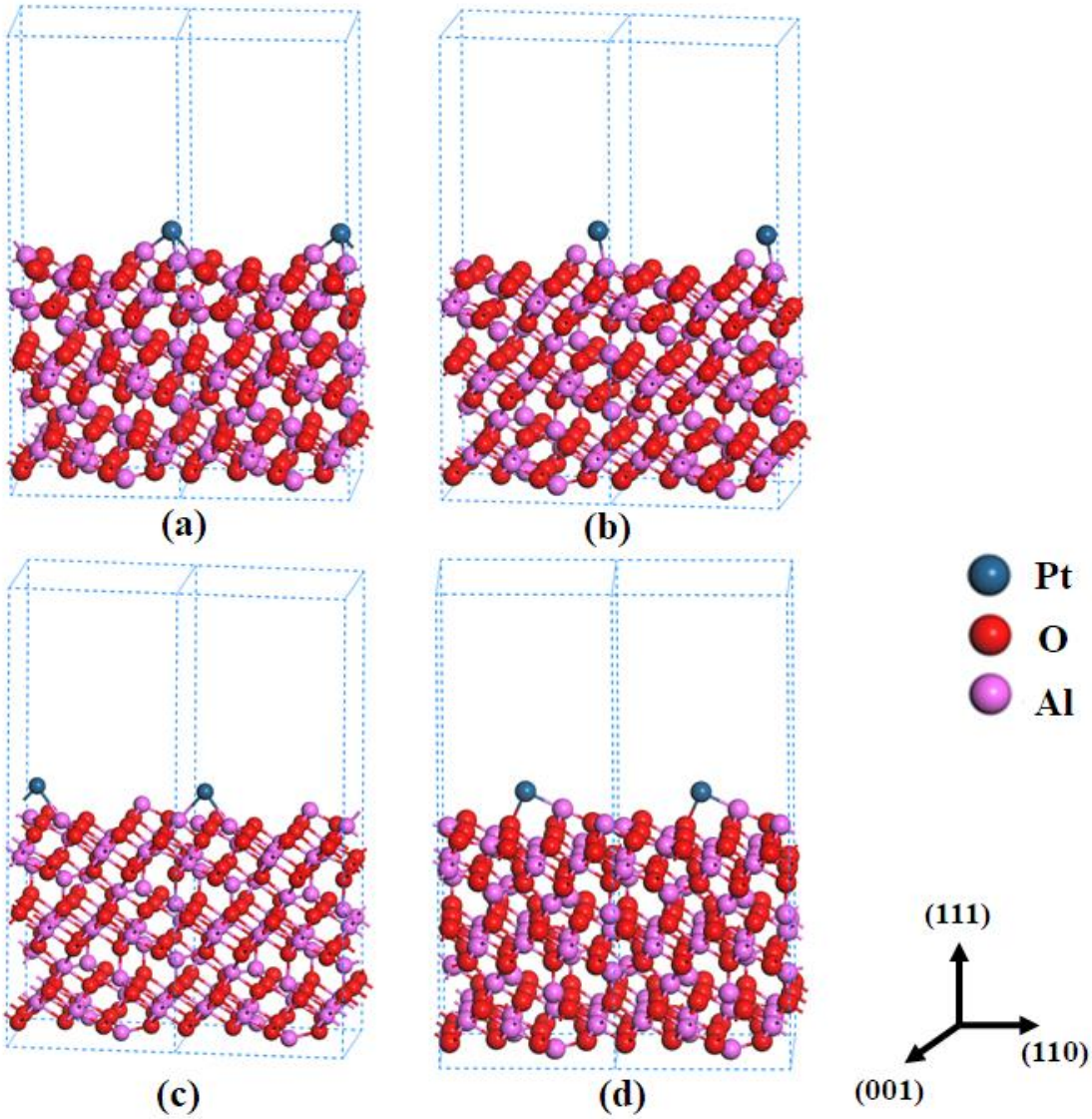

Appendix Figure 28. Configurations of Pt atom adsorption on the γ-Al_2O_3 (111) surface.

Appendix Table 8. Calculated Pt adatom adsorption energies on different γ-Al_2O_3 (111) surface sites.

Adsorption Configurations	Pt_a	Pt_b	Pt_c	Pt_d
Adsorption Energy (eV)	-2.40	-0.83	-1.21	0.03

Appendix F Publication List

Peer-reviewed journal articles and conference papers published as of May 1, 2020:

C.S. Bonifacio, Q. Zhu, D. Su, F. Vila, H.O. Ayoola, S.D. House, J. Kas, J.J. Rehr, E.A. Stach, W.A. Saidi, J.C. Yang, Investigation of the Structural and Electronic Properties of Pt/γ-Al2O3, a Model Catalyst System, Microscopy and Microanalysis, 21 (2015) 1655-1656.

J. Yang, Q. Zhu, C. Bonifacio, J. Kas, H. Ayoola, K. Kisslinger, D. Su, F. Vila, S. House, E. Stach, Multidisciplinary Investigation of the Structural and Electronic Properties of the Pt/gamma-Al2O3 interface, in: APS Meeting Abstracts, 2016.

H.O. Ayoola, C.S. Bonifacio, Q. Zhu, D. Su, J. Kas, J.J. Rehr, E.A. Stach, W.A. Saidi, J.C. Yang, Comparison of Spinel and Monoclinic Crystal Structures of γ-Al2O3 for Simulation of Electron Energy Loss Spectra, Microscopy and Microanalysis, 23 (2017) 2020-2021.

H.O. Ayoola, Q. Zhu, C.S. Bonifacio, M.P. McCann, M.T. Curnan, S.D. House, J. Kas, J.J. Rehr, E.A. Stach, W.A. Saidi, J.C. Yang, Correlative Structure-Bonding and Stability Studies of Pt/γ-Al2O3 Catalysts, Microscopy and Microanalysis, 24 (2018) 1644-1645.

M. McCann, H. Ayoola, J.C. Yang, Preparation of a Model Platinum/Gamma-Alumina Catalyst for in situ Environmental TEM Experiments, Microscopy and Microanalysis, 24 (2018) 1096-1097.

H.O. Ayoola, C.S. Bonifacio, M.T. Curnan, S.D. House, M. Li, J. Kas, J.J. Rehr, E.A. Stach, W.A. Saidi, J.C. Yang, Determination of the Crystal Structure of Gamma-Alumina by Electron

Diffraction and Electron Energy-Loss Spectroscopy, Microscopy and Microanalysis, 25 (2019) 2036-2037.

H.O. Ayoola, S.D. House, C.S. Bonifacio, K. Kisslinger, W.A. Saidi, J.C. Yang, Evaluating the accuracy of common γ-Al2O3 structure models by selected area electron diffraction from high-quality crystalline γ-Al2O3, Acta Materialia, 182 (2020) 257-266.

H.O. Ayoola, C.S. Bonifacio, Q. Zhu, C.-H. Li, S.D. House, J.J. Kas, J. Jinschek, J.J. Rehr, W.A. Saidi, J.C. Yang, Probing the Local Bonding at the Pt/γ-Al2O3 Interface, The Journal of Physical Chemistry C, (2020).

H.O. Ayoola, C.-H. Li, S.D. House, C.S. Bonifacio, K. Kisslinger, J. Jinschek, W.A. Saidi, J.C. Yang, Origin and Suppression of Beam Damage-Induced Oxygen-K Edge Artifact from γ-Al_2O_3 using Cryo-EELS, Ultramicroscopy, *Accepted*.

Papers in preparation:

H.O. Ayoola, C.-H. Li, M. McCann, S.D. House, J. Jinschek, W.A. Saidi, J.C. Yang, Determination of the vacancy distribution over Al cation sites in γ-Al_2O_3.

H.O. Ayoola, C.-H. Li, M. McCann, S.D. House, J. Jinschek, W.A. Saidi, J.C. Yang, Assessing nonspinel γ-Al_2O_3 models through EELS experiments and simulations.

Bibliography

1. McNaught, A.D. and A. Wilkinson, *Compendium of chemical terminology*. Vol. 1669. 1997: Blackwell Science Oxford.

2. Gupta, M.K., *Chapter 7 - Hydrogenation*, in *Practical Guide to Vegetable Oil Processing (Second Edition)*, M.K. Gupta, Editor. 2017, AOCS Press. p. 171-215.

3. Busacca, C.A., et al., *The Growing Impact of Catalysis in the Pharmaceutical Industry.* Advanced Synthesis & Catalysis, 2011. **353**(11-12): p. 1825-1864.

4. Speight, J.G., *Chapter 2 - Refining Processes*, in *The Refinery of the Future*, J.G. Speight, Editor. 2011, William Andrew Publishing: Boston. p. 39-80.

5. Gross, R.A., A. Kumar, and B. Kalra, *Polymer Synthesis by In Vitro Enzyme Catalysis.* Chemical Reviews, 2001. **101**(7): p. 2097-2124.

6. Ouchi, M., T. Terashima, and M. Sawamoto, *Transition Metal-Catalyzed Living Radical Polymerization: Toward Perfection in Catalysis and Precision Polymer Synthesis.* Chemical Reviews, 2009. **109**(11): p. 4963-5050.

7. Busca, G., *Chapter 9 - Metal Catalysts for Hydrogenations and Dehydrogenations*, in *Heterogeneous Catalytic Materials*, G. Busca, Editor. 2014, Elsevier: Amsterdam. p. 297-343.

8. Chen, S., et al., *Chapter 2 - Electrochemical Dinitrogen Activation: To Find a Sustainable Way to Produce Ammonia*, in *Studies in Surface Science and Catalysis*, S. Albonetti, S. Perathoner, and E.A. Quadrelli, Editors. 2019, Elsevier. p. 31-46.

9. Heveling, J., *Heterogeneous Catalytic Chemistry by Example of Industrial Applications.* Journal of Chemical Education, 2012. **89**(12): p. 1530-1536.

10. Behr, A. and P. Neubert, *Applied homogeneous catalysis*. 2012: John Wiley & Sons.

11. Ma, Z. and F. Zaera, *Heterogeneous Catalysis by Metals.* Encyclopedia of Inorganic Chemistry, 2005.

12. Anastas, P.T., M.M. Kirchhoff, and T.C. Williamson, *Catalysis as a foundational pillar of green chemistry.* Applied Catalysis A: General, 2001. **221**(1): p. 3-13.

13. Sheldon, R.A., *Engineering a more sustainable world through catalysis and green chemistry.* Journal of The Royal Society Interface, 2016. **13**(116): p. 20160087.

14. Bowker, M., *The 2007 Nobel Prize in Chemistry for Surface Chemistry: Understanding Nanoscale Phenomena at Surfaces.* ACS Nano, 2007. **1**(4): p. 253-257.

15. Rayment, T., et al., *Structure of the ammonia synthesis catalyst.* Nature, 1985. **315**(6017): p. 311-313.

16. Bell, A.T., *The Impact of Nanoscience on Heterogeneous Catalysis.* Science, 2003. **299**(5613): p. 1688.

17. Ertl, G., et al., *Handbook of Heterogeneous Catalysis*. 2nd ed. 1997: Wiley-VCH.

18. Schlögl, R., *Heterogeneous Catalysis.* Angewandte Chemie International Edition, 2015. **54**(11): p. 3465-3520.

19. Rothenberg, G., *Catalysis: concepts and green applications*. 2017: John Wiley & Sons.

20. Cuenya, B.R., *Synthesis and catalytic properties of metal nanoparticles: Size, shape, support, composition, and oxidation state effects.* Thin Solid Films, 2010. **518**(12): p. 3127-3150.

21. Hansen, P.L., et al., *Atom-Resolved Imaging of Dynamic Shape Changes in Supported Copper Nanocrystals.* Science, 2002. **295**(5562): p. 2053.

22. Midgley, P.A., et al., *Probing the Spatial Distribution and Morphology of Supported Nanoparticles Using Rutherford-Scattered Electron Imaging.* Angewandte Chemie, 2002. **114**(20): p. 3958-3961.

23. Sharma, R., et al., *Observation of dynamic nanostructural and nanochemical changes in ceria-based catalysts during in-situ reduction.* Philosophical Magazine, 2004. **84**(25-26): p. 2731-2747.

24. Crozier, P.A. and S. Chenna, *In situ analysis of gas composition by electron energy-loss spectroscopy for environmental transmission electron microscopy.* Ultramicroscopy, 2011. **111**(3): p. 177-85.

25. Midgley, P.A., et al., *Nanotomography in the chemical, biological and materials sciences.* Chem Soc Rev, 2007. **36**(9): p. 1477-94.

26. Gai, P.L., R. Sharma, and F.M. Ross, *Environmental (S)TEM studies of gas-liquid-solid interactions under reaction conditions.* Mrs Bulletin, 2008. **33**(2): p. 107-114.

27. Vila, F., et al., *Dynamic structure in supported Pt nanoclusters: Real-time density functional theory and X-ray spectroscopy simulations.* Physical Review B, 2008. **78**(12): p. 121404.

28. Jorissen, K., J.J. Rehr, and J. Verbeeck, *Multiple scattering calculations of relativistic electron energy loss spectra.* Physical Review B, 2010. **81**(15): p. 155108.

29. Nørskov, J.K., et al., *Towards the computational design of solid catalysts.* Nature Chemistry, 2009. **1**: p. 37.

30. Roldan Cuenya, B. and F. Behafarid, *Nanocatalysis: size- and shape-dependent chemisorption and catalytic reactivity.* Surface Science Reports, 2015. **70**(2): p. 135-187.

31. Ahmadi, M., H. Mistry, and B. Roldan Cuenya, *Tailoring the Catalytic Properties of Metal Nanoparticles via Support Interactions.* J Phys Chem Lett, 2016. **7**(17): p. 3519-33.

32. St.Clair, T.P. and D.W. Goodman, *Metal nanoclusters supported on metal oxide thin films: bridging the materials gap.* Topics in Catalysis, 2000. **13**(1): p. 5-19.

33. Prieto, G. and F. Schüth, *Bridging the gap between insightful simplicity and successful complexity: From fundamental studies on model systems to technical catalysts.* Journal of Catalysis, 2015. **328**: p. 59-71.

34. Freund, H.J., *Model Systems in Heterogeneous Catalysis: Selectivity Studies at the Atomic Level.* Topics in Catalysis, 2008. **48**(1): p. 137-144.

35. Risse, T., et al., *Gold Supported on Thin Oxide Films: From Single Atoms to Nanoparticles.* Accounts of Chemical Research, 2008. **41**(8): p. 949-956.

36. Panayotov, D.A. and J.R. Morris, *Surface chemistry of Au/TiO2: Thermally and photolytically activated reactions.* Surface Science Reports, 2016. **71**(1): p. 77-271.

37. Wahlström, E., et al., *Bonding of Gold Nanoclusters to Oxygen Vacancies on Rutile $\mathrm{T}\mathrm{i}{\mathrm{O}}_{\mathrm{2}}(110)$.* Physical Review Letters, 2003. **90**(2): p. 026101.

38. Wörz, A.S., et al., *Charging of Au Atoms on TiO2 Thin Films from CO Vibrational Spectroscopy and DFT Calculations.* The Journal of Physical Chemistry B, 2005. **109**(39): p. 18418-18426.

39. Nolte, P., et al., *Shape Changes of Supported Rh Nanoparticles During Oxidation and Reduction Cycles.* Science, 2008. **321**(5896): p. 1654-1658.

40. Farmer, J.A. and C.T. Campbell, *Ceria Maintains Smaller Metal Catalyst Particles by Strong Metal-Support Bonding.* Science, 2010. **329**(5994): p. 933-936.

41. Matthey, D., et al., *Enhanced Bonding of Gold Nanoparticles on Oxidized TiO₂(110).* Science, 2007. **315**(5819): p. 1692-1696.

42. Silly, F., et al., *Growth shapes of supported Pd nanocrystals on ${\mathrm{SrTiO}}_{3}(001)$.* Physical Review B, 2005. **72**(16): p. 165403.

43. Wefers, K. and C. Misra, *Oxides and hydroxides of aluminum*, in *Alcoa Technical Paper No. 19*. 1987, Alcoa Laboratories: Pittsburgh, PA.

44. Liu, X. and R.E. Truitt, *DRFT-IR Studies of the Surface of γ-Alumina.* Journal of the American Chemical Society, 1997. **119**(41): p. 9856-9860.

45. Trueba, M. and S.P. Trasatti, *γ-Alumina as a Support for Catalysts: A Review of Fundamental Aspects.* European Journal of Inorganic Chemistry, 2005. **2005**(17): p. 3393-3403.

46. Busca, G., *The surface of transitional aluminas: A critical review.* Catalysis Today, 2014. **226**: p. 2-13.

47. López-Fonseca, R., et al., *Partial oxidation of methane to syngas on bulk NiAl2O4 catalyst. Comparison with alumina supported nickel, platinum and rhodium catalysts.* Applied Catalysis A: General, 2012. **437**(Supplement C): p. 53-62.

48. Pakharukova, V.P., et al., *Alumina-supported platinum catalysts: Local atomic structure and catalytic activity for complete methane oxidation.* Applied Catalysis A: General, 2014. **486**: p. 12-18.

49. Kang, M. and A. Bhan, *Kinetics and mechanisms of alcohol dehydration pathways on alumina materials.* Catalysis Science & Technology, 2016. **6**(17): p. 6667-6678.

50. Koleva, I.Z., H.A. Aleksandrov, and G.N. Vayssilov, *Decomposition behavior of platinum clusters supported on ceria and [gamma]-alumina in the presence of carbon monoxide.* Catalysis Science & Technology, 2017. **7**(3): p. 734-742.

51. Dixit, M., P. Kostetskyy, and G. Mpourmpakis, *Structure–Activity Relationships in Alkane Dehydrogenation on γ-Al2O3: Site-Dependent Reactions.* ACS Catalysis, 2018. **8**(12): p. 11570-11578.

52. Kostetskyy, P., et al., *Understanding Alkane Dehydrogenation through Alcohol Dehydration on γ-Al2O3.* Industrial & Engineering Chemistry Research, 2018. **57**(49): p. 16657-16663.

53. Abou-Ziyan, H., et al., *Performance characteristics of thin-multilayer activated alumina bed.* Applied Energy, 2017. **190**: p. 29-42.

54. Levin, I. and D. Brandon, *Metastable Alumina Polymorphs: Crystal Structure and Transition Sequences.* Journal of the American Ceramic Society, 1998. **81**(8): p. 1995-2012.

55. Zhou, R.S. and R.L. Snyder, *Structures and transformation mechanisms of the η, γ and θ transition aluminas.* Acta Crystallographica Section B Structural Science, 1991. **47**(5): p. 617-630.

56. Tsuchida, T., R. Furuichi, and T. Ishii, *Kinetics of the dehydration of boehmites prepared under different hydrothermal conditions.* Thermochimica Acta, 1980. **39**(2): p. 103-115.

57. Jayaram, V. and C.G. Levi, *The structure of δ-alumina evolved from the melt and the γ → δ transformation.* Acta Metallurgica, 1989. **37**(2): p. 569-578.

58. Kovarik, L., et al., *Structure of δ-Alumina: Toward the Atomic Level Understanding of Transition Alumina Phases.* The Journal of Physical Chemistry C, 2014. **118**(31): p. 18051-18058.

59. Pecharromán, C., et al., *Thermal Evolution of Transitional Aluminas Followed by NMR and IR Spectroscopies.* The Journal of Physical Chemistry B, 1999. **103**(30): p. 6160-6170.

60. Levin, I., et al., *Cubic to monoclinic phase transformations in alumina.* Acta Materialia, 1997. **45**(9): p. 3659-3669.

61. Samain, L., et al., *Structural analysis of highly porous γ-Al2O3.* Journal of Solid State Chemistry, 2014. **217**: p. 1-8.

62. Paglia, G., et al., *Tetragonal structure model for boehmite-derived γ-alumina.* Physical Review B, 2003. **68**(14).

63. Lee, M.H., et al., *Distribution of tetrahedral and octahedral A1 sites in gamma alumina.* Chemical Physics Letters, 1997. **265**(6): p. 673-676.

64. Rotole, J.A. and P.M.A. Sherwood, *Gamma-Alumina (γ-Al2O3) by XPS.* Surface Science Spectra, 1998. **5**(1): p. 18-24.

65. Paglia, G., et al., *Determination of the structure ofγ-alumina from interatomic potential and first-principles calculations: The requirement of significant numbers of nonspinel positions to achieve an accurate structural model.* Physical Review B, 2005. **71**(22).

66. Krokidis, X., et al., *Theoretical Study of the Dehydration Process of Boehmite to γ-Alumina.* The Journal of Physical Chemistry B, 2001. **105**(22): p. 5121-5130.

67. Wolverton, C. and K.C. Hass, *Phase stability and structure of spinel-based transition aluminas.* Physical Review B, 2000. **63**(2): p. 024102.

68. Gutiérrez, G., A. Taga, and B. Johansson, *Theoretical structure determination of γ−Al2O3.* Physical Review B, 2001. **65**(1).

69. Alvarez, L.J., et al., *Molecular dynamics studies of the structure of γ-alumina.* Chemical Physics Letters, 1992. **192**(5): p. 463-468.

70. Blonski, S. and S.H. Garofalini, *Molecular dynamics simulations of α-alumina and γ-alumina surfaces.* Surface Science, 1993. **295**(1): p. 263-274.

71. Ferreira, A.R., et al., *Direct comparison between two structural models by DFT calculations.* Journal of Solid State Chemistry, 2011. **184**(5): p. 1105-1111.

72. Peintinger, M.F., M.J. Kratz, and T. Bredow, *Quantum-chemical study of stable, meta-stable and high-pressure alumina polymorphs and aluminum hydroxides.* J. Mater. Chem. A, 2014. **2**(32): p. 13143-13158.

73. Verwey, E.J.W., *Electrolytic conduction of a solid insulator at high fields The formation of the anodic oxide film on aluminium.* Physica, 1935. **2**(1-12): p. 1059-1063.

74. Smrcok, L., V. Langer, and J. Krestan, *Gamma-alumina: a single-crystal X-ray diffraction study.* Acta Crystallogr C, 2006. **62**(Pt 9): p. i83-4.

75. Lippens, B.C. and J.H. de Boer, *Study of phase transformations during calcination of aluminum hydroxides by selected area electron diffraction.* Acta Crystallographica, 1964. **17**(10): p. 1312-1321.

76. Ealet, B., et al., *Electronic and crystallographic structure of γ-alumina thin films.* Thin Solid Films, 1994. **250**(1-2): p. 92-100.

77. Chandran, C.V., et al., *Alumina: discriminative analysis using 3D correlation of solid-state NMR parameters.* Chemical Society Reviews, 2019. **48**(1): p. 134-156.

78. Digne, M., *Use of DFT to achieve a rational understanding of acid?basic properties of ?-alumina surfaces.* Journal of Catalysis, 2004. **226**(1): p. 54-68.

79. Pinto, H.P., R.M. Nieminen, and S.D. Elliott, *Ab initio study of gamma-Al2O3 surfaces.* Physical Review B, 2004. **70**(12): p. 125402.

80. Sohlberg, K., S.J. Pennycook, and S.T. Pantelides, *Hydrogen and the Structure of the Transition Aluminas.* Journal of the American Chemical Society, 1999. **121**(33): p. 7493-7499.

81. Paglia, G., et al., *Boehmite-Derived γ-Alumina System. 2. Consideration of Hydrogen and Surface Effects.* Chemistry of Materials, 2004. **16**(10): p. 1914-1923.

82. Silaghi, M.-C., A. Comas-Vives, and C. Copéret, *CO2 Activation on Ni/γ–Al2O3 Catalysts by First-Principles Calculations: From Ideal Surfaces to Supported Nanoparticles.* ACS Catalysis, 2016. **6**(7): p. 4501-4505.

83. Xu, G., et al., *Insight into the origin of sulfur tolerance of Ag/Al2O3 in the H2-C3H6-SCR of NOx.* Applied Catalysis B: Environmental, 2019. **244**: p. 909-918.

84. Gonçalves, L.P.L., et al., *Combined experimental and theoretical study of acetylene semi-hydrogenation over Pd/Al2O3.* International Journal of Hydrogen Energy, 2019.

85. Khan, T.S., et al., *On the role of oxocarbenium ions formed in Brønsted acidic condition on γ-Al2O3 surface in the ring-opening of γ-valerolactone.* Applied Catalysis A: General, 2018. **560**: p. 66-72.

86. Honkanen, M., et al., *Regeneration of sulfur-poisoned Pd-based catalyst for natural gas oxidation.* Journal of Catalysis, 2018. **358**: p. 253-265.

87. Loyola, C., E. Menéndez-Proupin, and G. Gutiérrez, *Atomistic study of vibrational properties of γ-Al2O3.* Journal of Materials Science, 2010. **45**(18): p. 5094-5100.

88. Ayoola, H.O., et al., *Evaluating the accuracy of common γ-Al2O3 structure models by selected area electron diffraction from high-quality crystalline γ-Al2O3.* Acta Materialia, 2020. **182**: p. 257-266.

89. Sun, M., A.E. Nelson, and J. Adjaye, *Examination of Spinel and Nonspinel Structural Models for γ-Al2O3 by DFT and Rietveld Refinement Simulations.* The Journal of Physical Chemistry B, 2006. **110**(5): p. 2310-2317.

90. Paglia, G., C.E. Buckley, and A.L. Rohl, *Comment on "Examination of Spinel and Nonspinel Structural Models for γ-Al2O3 by DFT and Rietveld Refinement Simulations".* The Journal of Physical Chemistry B, 2006. **110**(41): p. 20721-20723.

91. Digne, M., et al., *Comment on "Examination of spinel and nonspinel structural models for gamma-Al2O3 by DFT and Rietveld refinement simulations".* J Phys Chem B, 2006. **110**(41): p. 20719-20; author reply 20724-6.

92. Liu, Y., et al., *Study of Raman spectra for γ-Al2O3 models by using first-principles method.* Solid State Communications, 2014. **178**: p. 16-22.

93. Cai, S.-H., et al., *Phase transformation mechanism between γ- and θ-alumina.* Physical Review B, 2003. **67**(22).

94. Ching, W.Y., et al., *Ab initiostudy of the physical properties ofγ-Al2O3: Lattice dynamics, bulk properties, electronic structure, bonding, optical properties, and ELNES/XANES spectra.* Physical Review B, 2008. **78**(1): p. 014106.

95. Li, Y., C.M. Lousada, and P.A. Korzhavyi, *The nature of hydrogen in γ-alumina.* Journal of Applied Physics, 2014. **115**(20): p. 203514.

96. Jensen, T.N., et al., *Atomic structure of a spinel-like transition Al2O3(100) surface.* Phys Rev Lett, 2014. **113**(10): p. 106103.

97. Coster, D., A. Blumenfeld, and J. Fripiat, *Lewis acid sites and surface aluminum in aluminas and zeolites: a high-resolution NMR study.* The Journal of Physical Chemistry, 1994. **98**(24): p. 6201-6211.

98. Grabke, H.J., *Oxidation of NiAl and FeAl.* Intermetallics, 1999. **7**: p. 1153-1158.

99. Yang, J.C., et al., *Electron Microscopy Studies of NiAl/γ-Al_2O_3 Interfaces.* Scripta Metallurgica et Materialia, 1995. **33**(7): p. 1043-1048.

100. Doychak, J., J.L. Smialek, and T.E. Mitchell, *Transient oxidation of Single-Crystal β-NiAl.* Metallurgical Transactions A, 1989. **20**(3): p. 499-518.

101. Yang, J.C., et al., *Transient oxidation of NiAl.* Acta Materialia, 1998. **46**(6): p. 2195-2201.

102. Jennison, D.R., et al., *\textbf{ \textit{Ab initio} } structural predictions for ultrathin aluminum oxide films on metallic substrates.* Physical Review B, 1999. **59**(24): p. R15605-R15608.

103. Stierle, A., et al., *X-ray diffraction study of the ultrathin Al2O3 layer on NiAl(110).* Science, 2004. **303**(5664): p. 1652-1656.

104. Jaeger, R.M., et al., *Formation of a well-ordered aluminium oxide overlayer by oxidation of NiAl(110).* Surface Science, 1991. **259**(3): p. 235-252.

105. Zhang, Z., L. Li, and J.C. Yang, *γ-Al2O3 thin film formation via oxidation of β-NiAl(110).* Acta Materialia, 2011. **59**(15): p. 5905-5916.

106. Schmidt, E., et al., *Shape-Selective Enantioselective Hydrogenation on Pt Nanoparticles.* Journal of the American Chemical Society, 2009. **131**(34): p. 12358-12367.

107. Nørskov, J.K., et al., *Origin of the Overpotential for Oxygen Reduction at a Fuel-Cell Cathode.* The Journal of Physical Chemistry B, 2004. **108**(46): p. 17886-17892.

108. Arenz, M., et al., *The Effect of the Particle Size on the Kinetics of CO Electrooxidation on High Surface Area Pt Catalysts.* Journal of the American Chemical Society, 2005. **127**(18): p. 6819-6829.

109. Hu, C.H., et al., *Modulation of catalyst particle structure upon support hydroxylation: Ab initio insights into Pd13 and Pt13/γ-Al2O3.* Journal of Catalysis, 2010. **274**(1): p. 99-110.

110. Shamsi, A., J.P. Baltrus, and J.J. Spivey, *Characterization of coke deposited on Pt/alumina catalyst during reforming of liquid hydrocarbons.* Applied Catalysis A: General, 2005. **293**: p. 145-152.

111. Manasilp, A. and E. Gulari, *Selective CO oxidation over Pt/alumina catalysts for fuel cell applications.* Applied Catalysis B: Environmental, 2002. **37**(1): p. 17-25.

112. Xiao, Y. and A. Varma, *Highly Selective Nonoxidative Coupling of Methane over Pt-Bi Bimetallic Catalysts.* ACS Catalysis, 2018. **8**(4): p. 2735-2740.

113. Arvajová, A., et al., *The impact of CO and C3H6 pulses on PtOx reduction and NO oxidation in a diesel oxidation catalyst.* Applied Catalysis B: Environmental, 2016. **181**: p. 644-650.

114. Park, E.D., D. Lee, and H.C. Lee, *Recent progress in selective CO removal in a H2-rich stream.* Catalysis Today, 2009. **139**(4): p. 280-290.

115. Sun, K., et al., *Studying the Metal-Support Interaction in Pd/γ-Al2O3 Catalysts by Atomic-Resolution Electron Energy-Loss Spectroscopy.* Catalysis Letters, 2002. **84**(3): p. 193-199.

116. Corral Valero, M., P. Raybaud, and P. Sautet, *Influence of the Hydroxylation of γ-Al2O3 Surfaces on the Stability and Diffusion of Single Pd Atoms: A DFT Study.* The Journal of Physical Chemistry B, 2006. **110**(4): p. 1759-1767.

117. Sharifi, N., C. Falamaki, and M.G. Ahangari, *DFT study of Au adsorption on pure and Pt-decorated γ-alumina (110) surface.* Applied Surface Science, 2017. **416**: p. 390-396.

118. Kwak, J.H., et al., *Coordinatively unsaturated Al3+ centers as binding sites for active catalyst phases of platinum on gamma-Al2O3.* Science, 2009. **325**(5948): p. 1670-3.

119. Nellist, P.D. and S.J. Pennycook, *Direct Imaging of the Atomic Configuration of Ultradispersed Catalysts.* Science, 1996. **274**(5286): p. 413.

120. Sanchez, S.I., et al., *The Emergence of Nonbulk Properties in Supported Metal Clusters: Negative Thermal Expansion and Atomic Disorder in Pt Nanoclusters Supported on γ-Al2O3.* Journal of the American Chemical Society, 2009. **131**(20): p. 7040-7054.

121. Robinson, A.P.L., et al., *Theory of fast electron transport for fast ignition.* Nuclear Fusion, 2014. **54**(5): p. 054003.

122. Williams, D.B. and C.B. Carter, *Transmission Electron Microscopy*. 2nd ed. 2009, New York: Springer US.

123. Mitchell, D.R.G., *DiffTools: Electron diffraction software tools for DigitalMicrograph™.* Microscopy Research and Technique, 2008. **71**(8): p. 588-593.

124. Egerton, R.F., *Electron Energy-Loss Spectroscopy in the Electron Microscope*. 1986, New York: Plenum Press.

125. Köstlmeier, S. and C. Elsässer, *\textit{Ab initio} calculation of near-edge structures in electron-energy-loss spectra for metal-oxide crystals.* Physical Review B, 1999. **60**(20): p. 14025-14034.

126. Egerton, R.F., *Electron energy-loss spectroscopy in the electron microscope*. 2011: Springer Science & Business Media.

127. van Benthem, K. and H. Kohl, *Methods for ELNES-quantification: characterization of the degree of inversion of Mg–Al-spinels.* Micron, 2000. **31**(4): p. 347-354.

128. Moreno, M.S., K. Jorissen, and J.J. Rehr, *Practical aspects of electron energy-loss spectroscopy (EELS) calculations using FEFF8.* Micron, 2007. **38**(1): p. 1-11.

129. Rehr, J.J. and R.C. Albers, *Theoretical approaches to x-ray absorption fine structure*. Reviews of Modern Physics, 2000. **72**(3): p. 621-654.

130. Jiang, N. and J.C.H. Spence, *In situ EELS study of dehydration of Al(OH)3 by electron beam irradiation.* Ultramicroscopy, 2011. **111**(7): p. 860-864.

131. Egerton, R.F., *Mechanisms of radiation damage in beam-sensitive specimens, for TEM accelerating voltages between 10 and 300 kV.* Microsc Res Tech, 2012. **75**(11): p. 1550-6.

132. Egerton, R.F., P. Li, and M. Malac, *Radiation damage in the TEM and SEM.* Micron, 2004. **35**(6): p. 399-409.

133. Hobbs, L.W., *Electron-beam sensitivity in inorganic specimens.* Ultramicroscopy, 1987. **23**(3): p. 339-344.

134. Jiang, N., *Electron beam damage in oxides: a review.* Reports on Progress in Physics, 2015. **79**(1): p. 016501.

135. Nord, M., et al., *Assessing electron beam sensitivity for SrTiO3 and La0.7Sr0.3MnO3 using electron energy loss spectroscopy.* Ultramicroscopy, 2016. **169**: p. 98-106.

136. Bouchet, D. and C. Colliex, *Experimental study of ELNES at grain boundaries in alumina: intergranular radiation damage effects on Al-L23 and O-K edges.* Ultramicroscopy, 2003. **96**(2): p. 139-152.

137. Ruckman, M.W., et al., *Interpreting the near edges of O2 and O2- in alkali-metal superoxides.* Phys Rev Lett, 1991. **67**(18): p. 2533-2536.

138. Otsuka, Y., Y. Shimizu, and I. Tanaka, *Beam damage suppression of low-κ porous Si–O–C films by cryo-electron-energy loss spectroscopy (EELS).* Journal of Electron Microscopy, 2009. **58**(2): p. 29-34.

139. Torruella, P., et al., *Assessing Oxygen Vacancies in Bismuth Oxide through EELS Measurements and DFT Simulations.* The Journal of Physical Chemistry C, 2017. **121**(44): p. 24809-24815.

140. Jiang, N. and J.C. Spence, *Interpretation of Oxygen K pre-edge peak in complex oxides.* Ultramicroscopy, 2006. **106**(3): p. 215-9.

141. Kresse, G. and J. Hafner, *Ab initio molecular dynamics for liquid metals.* Physical Review B, 1993. **47**(1): p. 558-561.

142. Kresse, G. and J. Hafner, *Ab-initio molecular-dynamics simulation of the liquid-metal amorphous-semiconductor transition in germanium* Physical Review B, 1994. **49**(20): p. 14251-14269.

143. John P. Perdew, K.B., Matthias Ernzerhof, *Generalized Gradient Approximation Made Simple.* Physical Review Letters, 1996. **77**(18): p. 4.

144. Tkatchenko, A. and M. Scheffler, *Accurate Molecular Van Der Waals Interactions from Ground-State Electron Density and Free-Atom Reference Data.* Physical Review Letters, 2009. **102**(7): p. 073005.

145. Al-Saidi, W., V.K. Voora, and K.D. Jordan, *An assessment of the vdW-TS method for extended systems.* Journal of Chemical Theory and Computation, 2012. **8**(4): p. 1503-1513.

146. Acikgoz, M., J. Harrell, and M. Pavanello, *Seeking a Structure–Function Relationship for γ-Al2O3 Surfaces.* The Journal of Physical Chemistry C, 2018. **122**(44): p. 25314-25330.

147. Jiang, N. and J.C.H. Spence, *On the dose-rate threshold of beam damage in TEM.* Ultramicroscopy, 2012. **113**: p. 77-82.

148. Berger, S.D., et al., *Electron Energy-Loss Spectroscopy Studies of Nanometer-Scale Structures in Alumina Produced by Intense Electron-Beam Irradiation.* Philosophical Magazine B-Physics of Condensed Matter Statistical Mechanics Electronic Optical and Magnetic Properties, 1987. **55**(3): p. 341-358.

149. Cazaux, J., *Correlations between ionization radiation damage and charging effects in transmission electron microscopy.* Ultramicroscopy, 1995. **60**(3): p. 411-425.

150. Egerton, R.F., *Limits to the spatial, energy and momentum resolution of electron energy-loss spectroscopy.* Ultramicroscopy, 2007. **107**(8): p. 575-586.

151. Egerton, R.F., *Scattering delocalization and radiation damage in STEM-EELS.* Ultramicroscopy, 2017. **180**: p. 115-124.

152. Taftø, J. and J. Zhu, *Electron energy loss near edge structure (ELNES), a potential technique in the studies of local atomic arrangements.* Ultramicroscopy, 1982. **9**(4): p. 349-354.

153. Salisbury, I.G., et al., *Nanometer scale electron beam lithography in inorganic materials.* Applied Physics Letters, 1984. **45**(12): p. 1289-1291.

154. Levin, I., et al., *Electron Energy-Loss Near-Edge Structure of Alumina Polymorphs.* Modern Developments and Applications in Microbeam Analysis, 2012. **15**: p. 93-96.

155. Egerton, R.F., *Choice of operating voltage for a transmission electron microscope.* Ultramicroscopy, 2014. **145**: p. 85-93.

156. Jiang, N. and J.C.H. Spence, *Electronic ionization induced atom migration in spinel MgAl2O4.* Journal of Nuclear Materials, 2010. **403**(1): p. 147-151.

157. Digne, M., et al., *Hydroxyl Groups on γ-Alumina Surfaces: A DFT Study.* Journal of Catalysis, 2002. **211**(1): p. 1-5.

158. Ramsier, R.D. and J.T. Yates, *Electron-stimulated desorption: Principles and applications.* Surface Science Reports, 1991. **12**(6): p. 246-378.

159. Pells, G.P. and A.Y. Stathopoulos, *Radiation damage in the cation sublattice of alpha-Al2O3.* Radiation Effects, 1983. **74**(1-4): p. 181-191.

160. Jiang, N., et al., *Nanoscale modification of optical properties in Ge-doped SiO2 glass by electron-beam irradiation.* Applied Physics Letters, 2002. **80**(11): p. 2005-2007.

161. McCartney, M.R., et al., *Electron-beam-induced reactions at transition-metal oxide surfaces.* Vacuum, 1991. **42**(4): p. 301-308.

162. Gu, H., et al., *Considerable knock-on displacement of metal atoms under a low energy electron beam.* Scientific Reports, 2017. **7**(1): p. 184.

163. Wilson, S.J., *The dehydration of boehmite, γ-AlOOH, to γ-Al2O3.* Journal of Solid State Chemistry, 1979. **30**(2): p. 247-255.

164. Morrissey, K.J., et al., *Transition alumina structures studied using HREM.* Ultramicroscopy, 1985. **18**(1-4): p. 379-385.

165. Weirich, T.E., et al., *A crystal structure determined with 0.02 Å accuracy by electron microscopy.* Nature, 1996. **382**(6587): p. 144-146.

166. Labar, J.L., et al., *Electron diffraction based analysis of phase fractions and texture in nanocrystalline thin films, part III: application examples.* Microsc Microanal, 2012. **18**(2): p. 406-20.

167. Lábár, J.L., *Electron Diffraction Based Analysis of Phase Fractions and Texture in Nanocrystalline Thin Films, Part I: Principles.* Microscopy and Microanalysis, 2008. **14**(04): p. 287-295.

168. Santos, P.S., H.S. Santos, and S.P. Toledo, *Standard transition aluminas. Electron microscopy studies.* Materials Research, 2000. **3**: p. 104-114.

169. Kilaas, R., *Optimal and near-optimal filters in high-resolution electron microscopy.* Journal of Microscopy, 1998. **190**(1-2): p. 45-51.

170. Kwak, J.H., et al., *Role of Pentacoordinated Al3+ Ions in the High Temperature Phase Transformation of γ-Al2O3.* The Journal of Physical Chemistry C, 2008. **112**(25): p. 9486-9492.

171. Paglia, G., E.S. Božin, and S.J.L. Billinge, *Fine-Scale Nanostructure in γ-Al2O3.* Chemistry of Materials, 2006. **18**(14): p. 3242-3248.

172. Kovarik, L., et al., *Tomography and High-Resolution Electron Microscopy Study of Surfaces and Porosity in a Plate-like γ-Al2O3.* The Journal of Physical Chemistry C, 2013. **117**(1): p. 179-186.

173. Ayoola, H.O., et al., *Probing the Local Bonding at the Pt/γ-Al2O3 Interface.* The Journal of Physical Chemistry C, 2020. **124**(18): p. 9876-9885.

174. Ankudinov, A., et al., *Real-space multiple-scattering calculation and interpretation of x-ray-absorption near-edge structure.* Physical Review B, 1998. **58**(12): p. 7565.

175. Kas, J., et al., *Many-pole model of inelastic losses in x-ray absorption spectra.* Physical Review B, 2007. **76**(19): p. 195116.

176. Palisaitis, J., et al., *Effect of strain on low-loss electron energy loss spectra of group-III nitrides.* Physical Review B, 2011. **84**(24): p. 245301.

177. Hou, P.Y., A.P. Paulikas, and B.W. Veal, *Stress development and relaxation in Al2O3 during early stage oxidation of β-NiAl.* Materials at High Temperatures, 2005. **22**(3-4): p. 535-543.

178. Hou, P.Y., A.P. Paulikas, and B.W. Veal, *Strains in Thermally Growing Alumina Films Measured In-Situ Using Synchrotron X-Rays.* Materials Science Forum, 2006. **522-523**: p. 433-440.

179. Martin, R., et al., *Thermally Induced Formation of Transition Aluminas from Boehmite* Advanced Engineering Materials, 2017. **19**(9): p. 1700141.

180. Docherty, F.T., et al., *ELNES investigations of the oxygen K-edge in spinels.* Ultramicroscopy, 2001. **86**(3–4): p. 273-288.

181. Köstlmeier, S., C. Elsässer, and B. Meyer, *Ab initio analysis of electron energy loss spectra for complex oxides.* Ultramicroscopy, 1999. **80**(2): p. 145-151.

182. Hansen, P.L., et al., *EELS fingerprint of Al-coordination in silicates.* Microsc. Microanal. Microstruct., 1994. **5**(3): p. 173-182.

183. Altay, A., et al., *Characterizing CA2 and CA6 using ELNES.* Journal of Solid State Chemistry, 2010. **183**(8): p. 1776-1784.

184. Brydson, R., *Multiple scattering theory applied to ELNES of interfaces.* Journal of Physics D: Applied Physics, 1996. **29**(7): p. 1699-1708.

185. Paglia, G., et al., *Boehmite Derived γ-Alumina System. 1. Structural Evolution with Temperature, with the Identification and Structural Determination of a New Transition Phase, γ'-Alumina.* Chemistry of Materials, 2004. **16**(2): p. 220-236.

186. Scheu, C., et al., *Electron Energy-Loss Near-Edge Structure of Metal-Alumina Interfaces.* Microsc. Microanal. Microstruct., 1995. **6**(1): p. 19-31.

187. BRYDSON, R., *Probing the local structure and bonding at interfaces and defects using EELS in the TEM.* Journal of Microscopy, 1995. **180**(3): p. 238-249.

188. Blochl, P.E., *Projector augmented-wave method.* Physical Review B, 1994. **50**(24): p. 17953-17979.

189. Kresse, G. and D. Joubert, *From ultrasoft pseudopotentials to the projector augmented-wave method.* Physical Review B, 1999. **59**(3): p. 1758-1775.

190. Ishizawa, N., et al., *A structural investigation of [alpha]-Al2O3 at 2170 K.* Acta Crystallographica Section B, 1980. **36**(2): p. 228-230.

191. Chen, P.-T., et al., *First-principle calculations analysis of ELNES splitting for Mn3O4 spinels related to atomic local symmetry.* Ultramicroscopy, 2014. **140**: p. 51-56.

192. Rahane, A.B., M.D. Deshpande, and V. Kumar, *Structural and Electronic Properties of (Al2O3)n Clusters with n = 1–10 from First Principles Calculations.* The Journal of Physical Chemistry C, 2011. **115**(37): p. 18111-18121.

193. Zhang, Z., L. Li, and J.C. Yang, *Adhesion of Pt Nanoparticles Supported on γ-Al2O3 Single Crystal.* The Journal of Physical Chemistry C, 2013. **117**(41): p. 21407-21412.

194. Kimoto, K., et al., *Coordination and interface analysis of atomic-layer-deposition Al2O3 on Si(001) using energy-loss near-edge structures.* Applied Physics Letters, 2003. **83**(21): p. 4306-4308.

195. Garvie, L.A.J. and P.R. Buseck, *Determination of Ce4+/Ce3+ in electron-beam-damaged CeO2 by electron energy-loss spectroscopy.* Journal of Physics and Chemistry of Solids, 1999. **60**(12): p. 1943-1947.

196. Ayoola, H.O., et al., *Determination of the Crystal Structure of Gamma-Alumina by Electron Diffraction and Electron Energy-Loss Spectroscopy.* Microscopy and Microanalysis, 2019. **25**(S2): p. 2036-2037.

197. Ayoola, H.O., et al., *Correlative Structure-Bonding and Stability Studies of Pt/γ-Al2O3 Catalysts.* Microscopy and Microanalysis, 2018. **24**(S1): p. 1644-1645.

198. Wischert, R., et al., *Visibility of Al Surface Sites of γ-Alumina: A Combined Computational and Experimental Point of View.* The Journal of Physical Chemistry C, 2014. **118**(28): p. 15292-15299.

199. Comas-Vives, A., et al., *Cooperativity between Al Sites Promotes Hydrogen Transfer and Carbon-Carbon Bond Formation upon Dimethyl Ether Activation on Alumina.* ACS Cent Sci, 2015. **1**(6): p. 313-9.

200. Filatova, E.O. and A.S. Konashuk, *Interpretation of the Changing the Band Gap of Al2O3 Depending on Its Crystalline Form: Connection with Different Local Symmetries.* The Journal of Physical Chemistry C, 2015. **119**(35): p. 20755-20761.

201. Wan, C., et al., *Investigating the Surface Structure of γ-Al2O3 Supported WOX Catalysts by High Field 27Al MAS NMR and Electronic Structure Calculations.* The Journal of Physical Chemistry C, 2016. **120**(40): p. 23093-23103.

202. Yang, T. and M. Ehara, *Probing the electronic structures of Con (n = 1-5) clusters on [gamma]-Al2O3 surfaces using first-principles calculations.* Physical Chemistry Chemical Physics, 2017. **19**(5): p. 3679-3687.

203. Aaron Deskins, N., D. Mei, and M. Dupuis, *Adsorption and diffusion of a single Pt atom on γ-Al2O3 surfaces.* Surface Science, 2009. **603**(17): p. 2793-2807.

204. Gu, J., J. Wang, and J. Leszczynski, *Structure and Energetics of (111) Surface of γ-Al2O3: Insights from DFT Including Periodic Boundary Approach.* ACS Omega, 2018. **3**(2): p. 1881-1888.

205. Tan, K., et al., *Predicting Metal–Support Interactions in Oxide-Supported Single-Atom Catalysts.* Industrial & Engineering Chemistry Research, 2019. **58**(44): p. 20236-20246.

206. Deng, H., Y. Yu, and H. He, *Discerning the Role of Ag–O–Al Entities on Ag/γ-Al2O3 Surface in NOx Selective Reduction by Ethanol.* The Journal of Physical Chemistry C, 2015. **119**(6): p. 3132-3142.

207. Sakaguchi, N., et al., *EELS and <I>Ab-Initio</I> Study of Faceted CSL Boundary in Silicon.* Materials Transactions, 2011. **52**(3): p. 276-279.

208. Kurata, H. and C. Colliex, *Electron-energy-loss core-edge structures in manganese oxides.* Physical Review B, 1993. **48**(4): p. 2102-2108.

209. Nyquist, S. and U. Hålenius, *An EELS study of near edge structures of the oxygen K-edge in spinels.* Physics and Chemistry of Minerals, 2014. **41**(4): p. 255-265.

210. Saidi, W.A., *Density Functional Theory Study of Nucleation and Growth of Pt Nanoparticles on MoS2(001) Surface.* Crystal Growth & Design, 2015. **15**(2): p. 642-652.

211. Shi, Y., et al., *Experimentally Validated Structures of Supported Metal Nanoclusters on MoS2.* J Phys Chem Lett, 2018. **9**(11): p. 2972-2978.

212. Feng, B., et al., *Direct Observation of Oxygen Vacancy Distribution across Yttria-Stabilized Zirconia Grain Boundaries.* ACS Nano, 2017. **11**(11): p. 11376-11382.

213. Willhammar, T., et al., *Structure and vacancy distribution in copper telluride nanoparticles influence plasmonic activity in the near-infrared.* Nature Communications, 2017. **8**: p. 14925.

214. Yao, L., S. Inkinen, and S. van Dijken, *Direct observation of oxygen vacancy-driven structural and resistive phase transitions in La2/3Sr1/3MnO3.* Nature Communications, 2017. **8**: p. 14544.

215. Kim, H., et al., *Direct Observation of Sr Vacancies inSrTiO3by Quantitative Scanning Transmission Electron Microscopy.* Physical Review X, 2016. **6**(4): p. 041063.

216. Li, W.-Z., et al., *Stable platinum nanoparticles on specific MgAl2O4 spinel facets at high temperatures in oxidizing atmospheres.* Nature Communications, 2013. **4**: p. 2481.

217. Croy, J.R., et al., *Support Dependence of MeOH Decomposition Over Size-Selected Pt Nanoparticles.* Catalysis Letters, 2007. **119**(3): p. 209-216.

218. Matos, J., et al., *In situ coarsening study of inverse micelle-prepared Pt nanoparticles supported on γ-Al2O3: pretreatment and environmental effects.* Physical Chemistry Chemical Physics, 2012. **14**(32): p. 11457-11467.

219. Mostafa, S., et al., *Shape-Dependent Catalytic Properties of Pt Nanoparticles.* Journal of the American Chemical Society, 2010. **132**(44): p. 15714-15719.

220. Behafarid, F., et al., *Electronic properties and charge transfer phenomena in Pt nanoparticles on [gamma]-Al2O3: size, shape, support, and adsorbate effects.* Physical Chemistry Chemical Physics, 2012. **14**(33): p. 11766-11779.

221. Merte, L.R., et al., *Correlating Catalytic Methanol Oxidation with the Structure and Oxidation State of Size-Selected Pt Nanoparticles.* ACS Catalysis, 2013. **3**(7): p. 1460-1468.

222. Roldan Cuenya, B., et al., *Solving the Structure of Size-Selected Pt Nanocatalysts Synthesized by Inverse Micelle Encapsulation.* Journal of the American Chemical Society, 2010. **132**(25): p. 8747-8756.

223. Cargnello, M., et al., *Efficient Removal of Organic Ligands from Supported Nanocrystals by Fast Thermal Annealing Enables Catalytic Studies on Well-Defined Active Phases.* Journal of the American Chemical Society, 2015. **137**(21): p. 6906-6911.

224. Krivanek, O.L., et al., *Progress in ultrahigh energy resolution EELS.* Ultramicroscopy, 2019. **203**: p. 60-67.

225. Senftle, T.P., et al., *The ReaxFF reactive force-field: development, applications and future directions.* npj Computational Materials, 2016. **2**(1): p. 15011.

226. Kresse, G. and J. Hafner, *Ab initio molecular dynamics for liquid metals.* Phys. Rev. B, 1993. **47**(1): p. 558-561.

227. Kresse, G. and J. Hafner, *Ab initio molecular dynamics for open-shell transition metals.* Physical Review B, 1993. **48**(17): p. 13115-13118.

228. Kresse, G. and J. Hafner, *Ab-initio molecular-dynamics simulation of the liquid-metal amorphous-semiconductor transition in germanium* Phys. Rev. B, 1994. **49**(20): p. 14251-14269.

229. Kurata, H., et al., *Electron-energy-loss near-edge structures in the oxygen K-edge spectra of transition-metal oxides.* Physical Review B, 1993. **47**(20): p. 13763-13768.